Loma Linda University Electronic Theses, Dissertations & Projects

9-2017

Conduction Plus Convection Heat Flow Modeling for the Linga Complex, Peruvian Coastal Batholith

Luciano Uriel González Olivares

LOMA LINDA UNIVERSITY
School of Medicine
in conjunction with the
Faculty of Graduate Studies

—————————————

Conduction Plus Convection Heat Flow Modeling for the Linga Complex,
Peruvian Coastal Batholith

by

Luciano Uriel González Olivares

—————————————

A Dissertation submitted in partial satisfaction of
the requirements for the degree
Doctor of Philosophy in Earth Science

—————————————

September 2017

Each person whose signature appears below certifies that this dissertation in his opinion is adequate, in scope and quality, as a dissertation for the degree Doctor of Philosophy.

_____ , Chairperson
Benjamin L. Clausen, Adjunct Associate Professor of Geology

_____
H. Paul Buchheim, Professor of Geology

_____
Gregory Holk, Professor of Geological Sciences, California State University, Long Beach

_____
Ronald Nalin, Adjunct Assistant Professor of Geology

_____
Kevin E. Nick, Associate Professor of Geology

_____
Ivan Rouse, Professor of Physics, La Sierra University

ACKNOWLEDGEMENTS

My journey to reach the PhD in Earth Science has been hard but rewarding. Reaching the goal would have been impossible by myself. First, I am thankful to God for giving me life, health, energy, and the courage to persevere, even though at times the journey was difficult.

I want to thank my beloved wife Edelina Clark, who has always been my strongest supporter, without her love and encouragement it would have been impossible to reach this goal. During the final stage of writing, her mother suddenly passed away, however, in spite of the heartbreaking circumstances, my wife was always willing to support me. I am also grateful to my children Haroldo and Melissa, whose help and motivation was significant in accomplishing my goal.

I am grateful to my advisor, Dr. Benjamin Clausen, for his research guidance, patience in reading and correcting my writing, and his effort to make me an independent researcher. My sincere gratitude to my committee members: Dr. Kevin Nick, Dr. Ronald Nalin, Dr. Paul Buchheim, Dr. Ivan Rouse, and Dr. Gregory Holk whose great support was invaluable in achieving this academic endeavor. To the Department of Earth and Biological Sciences, the Geoscience Research Institute, Montemorelos University, and donors for giving me the opportunity of pursuing the doctorate and for providing financial support during my stay at Loma Linda. I would also like to thank Dr. Juan Carlos Molano from the University of Bogotá in Colombia. During our fieldwork in Peru, he was always willing to teach me new things on hydrothermal alteration, which is an important part of this dissertation. I would also like to thank my colleagues, Ana

iv

CONTENT

viii

FIGURES

xiii

TABLES

ABBREVIATIONS

GMWL   Global Meteoric Water Line

INGEMMET   Instituto Geológico Minero y Metalúrgico

PCB   Peruvian Coastal Batholith

SMOW   Standard Mean Ocean Water

USGS   United State Geological Survey

REE   Rare Earth Elements

ABSTRACT OF THE DISSERTATION

Conduction Plus Convection Heat Flow Modeling for the Linga Complex,
Peruvian Coastal Batholith

by

Luciano Uriel González Olivares

Doctor of Philosophy, Graduate Program in Earth Sciences
Loma Linda University, September 2017
Dr. Benjamin L. Clausen, Chairperson

Factors affecting the thermal evolution of the Linga magmatic intrusion in the Ica-Pisco area of the Peruvian Coastal Batholith were studied using field work, petrography, geochemistry data, and computer modeling. Field work and petrography involved collecting samples for geochemical analysis and documenting widespread propylitic and potassic hydrothermal alteration. Major element geochemistry was used to estimate rock density, viscosity, liquidus temperature, and water content. The $\delta^{18}O$ values of seven fresh samples showed a slightly increasing west-east and old-young trend of approximately 7-8‰, indicating an increasing crustal component. The $\delta^{18}O$ and δD values for eleven altered samples indicated that alteration came mostly from magmatic fluids, with metamorphic and meteoric fluids contributing minimally. The water/rock ratio was mostly ≤30%. Using MATLAB, calculations for heat transfer by conduction from a one-dimensional 3km-thick horizontal "Linga-like magmatic dike" intruded instantaneously at 900°C and cooled from only the upper surface took about 210kyrs to fully crystallize at 600°C. Using two-dimensional HYDROTHERM interactive from the USGS to include convection of meteoric hydrothermal fluids, the simulation took 150kyrs for a $12\times3km^2$ pluton with top at 3km depth having a permeability of $10^{-15}m^2$ to

cool from 900°C to 600°C in a 25°C/km geothermal gradient. Compared to this, an 8×3km² pluton took 20% less and a 12×2km² pluton 50% less. Varying the permeability from 10^{-22} to 10^{-14}m² changed cooling time from 180 to 125kyrs. This range of permeabilities could reproduce conditions for 450-600°C potassic and 220-350°C propylitic alteration in the host rock. Decreasing intrusion temperature from 1000°C to 700°C decreased cooling time from 170 to 90kyrs. Varying geothermal gradient between 10 and 40°C/km and depth to top of intrusion between 3 and 4 km affected cooling time by ≤3%. Cooling below crystallization to 170°C took nearly 800kyrs. Stoping of 1-5% decreased cooling times by 3-13%. Further work is needed with more robust software such as COMSOL to check effects of a more realistic porosity, variation in thermal conductivity, correctly estimating latent heat, better use of alteration data, fluid inclusion data, fractures, multiple intrusions, lower crust intrusions, magma convection, magmatic fluids, fluid super-convection, large fluid volume, Ar-Ar age constraints, and 3D effects.

CHAPTER ONE

INTRODUCTION

The northern section of the Peruvian Coastal Batholith (PCB) was the subject of intense geological research during the 1970's and the 1980's. At that time Agar (1981), Agar and Le Bel (1985), Cobbing and Pitcher (1972), Moore (1979), and Pitcher (1985) among others, provided a better understanding of the geology of this section of the Peruvian Andes.

The PCB is made up of five segments (Figure 1). The Arequipa segment located between the Lima and the Toquepala segments is the longest. The Arequipa segment is made up of several elongate, parallel Super-units with the Linga Super-unit of our research interest in the northern Ica-Pisco area having been first studied and named in the Arequipa area.

In the research area, the Linga Super-unit does not consist of a single plutonic intrusion but is made up of 3 distinct units known as Humay, Auquish and Rinconada (Agar, 1981). Therefore, it will be referred to in the rest of this document as the Linga complex.

Research Objective

The main goal of this project is to model the cooling of the Linga complex using heat conduction as well as convective hydrothermal fluids in the cooling process. This research will test the hypothesis that including the action of convecting hydrothermal fluids
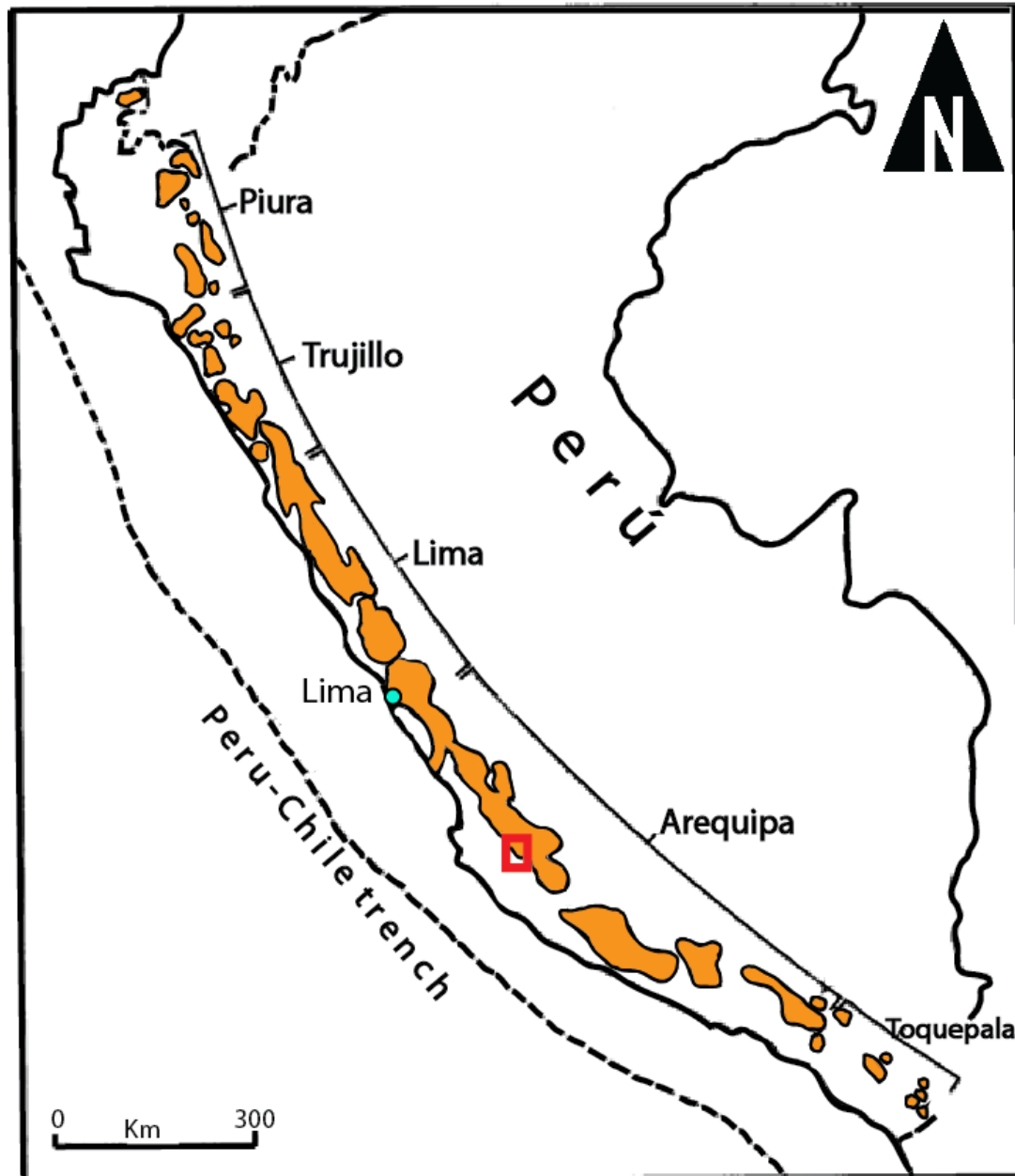
Figure 1. The five segments of the Peruvian Coastal Batholith and the study area in red. Adapted from Moore (1984).

in modeling the cooling of a magmatic body will significantly reduce the time for the batholith to reach its final temperature.

The thermal modeling includes information from field work observations of type and extent of hydrothermal alteration assemblages, lab data from $\delta^{18}O$ and δD values of fresh and altered samples, geochemistry of major and trace elements and thin sections, integrated with standard parameters used in the literature of thermal modeling. Computational modeling will be performed using the USGS software HYDROTHERM interactive (Kipp et al., 2008) and MATLAB (MATLAB, 2012).

The interaction between hydrothermal fluids and rocks produces different types of alteration depending on factors like fluid composition and temperature, as well as chemical composition of the magma and the country rock (Pirajno, 2009). Thus, results obtained from laboratory analysis of samples with different alteration assemblages are used in this research to understand temperature variations in the magma chamber and the country rock, as well as determining the source of the hydrothermal fluids and their role in the cooling process of the Linga complex (Bindeman, 2008; Hoefs, 1996).

Geologic Settings

The Peruvian Coastal Batholith

The Andes Cordillera is the largest active subduction-related orogeny on Earth (Schilling et al., 2006; Springer, 1999) and is the product of the subduction of the oceanic Farallon Plate and later the Nazca Plate under the continental crust of the South American Plate since the Cretaceous (Pfiffner and Gonzalez, 2013; Pilger, 1984; Polliand et al., 2005; Wortel, 1984). Convergence rates between these two plates increased dramatically

during the late Early to Late Cretaceous and shifted to a significant oblique component (Jaillard and Soler, 1996; McQuarrie et al., 2005; Mégard, 1984). This resulted in a trenchward motion of the South American plate, subduction erosion (Jaillard and Soler, 1996; Polliand et al., 2005), significant arc magmatism and the emergence of volcano-sedimentary basins of the Mesozoic Western Peruvian Trough (WPT) (Mégard, 1984; Pfiffner and Gonzalez, 2013). The development of the WPT was followed by intrusion of magmas between 100 Ma and 30 Ma that yielded numerous plutonic suites that comprise the Peruvian Coastal Batholith (PCB), shown in Figure 1 (Polliand et al., 2005; Soler and Bonhomme, 1990).

The PCB has a geometry and composite nature similar to other circum-Pacific batholiths, but is one of the largest. In addition, the PCB has preserved its integrity unlike the batholiths of western North America which have been partially disarticulated by later tectonic events, obscuring their relationships with the plate margin at the time of emplacement (Atwater, 1970; Schweickert and Cowan, 1975; Winter, 2010).

Abundant intrusions forming the Mesozoic-Cenozoic PCB constitute an exceptional example of long-lived plutonism related to a convergent margin. This batholith, parallel to the contemporary Peru-Chile trench along its almost 2000 km length, displays significant longitudinal differences in magma type and emplacement history and has been divided into five segments. From north to south these segments are termed Piura, Trujillo, Lima, Arequipa, and Toquepala (Figure 1). Each segment is characterized by its own particular intrusions, which can be grouped into Super-units and each Super-unit comprises a set of units closely related in space, time, chemistry, and petrology (Cobbing and Pitcher, 1972; Cobbing et al., 1977; Moore, 1984).

The 900 km-long Arequipa segment extends from Arequipa northward to the Lurín District in the Lima Province. This segment has been in mapped in detail, particularly in the Ica and Rio Pisco area, providing some of the most complete documentation of emplacement and petrologic processes for the PCB (Agar, 1978; Cobbing et al., 1977).

Brief Description of the Super-units in the Ica-Pisco Area

A number of Pre-PCB volcano-sedimentary units occur in the study area, with the Quilmana to the west and Yura to the East of the Ica-Pisco PCB being the two most important for this research. In this project all these units have been mapped as Pre-PCB (Figure 2). The Yura Group consists of dark shale and quartzites and has a thickness of approximately 3500 m near Arequipa, 2000 m in the Rio Ica, and up to 600 m to north-east in the Rio Pisco area (Moore, 1979). The Yura group in the eastern Rio Pisco also includes volcanics. The age of the Yura Group is constrained by geochronology to be between 216 Ma and 134 Ma (Boekhout et al., 2013).

The Quilmana volcanics (Figure 2) of middle Albian age (Mukasa, 1986) date to the emergence of the WPT (Aguirre and Offler, 1985). They are the youngest stratified rocks cut by the PCB and constitute a large part of its western and eastern envelope. The main lithology is metamorphic hornfels and the most abundant alteration minerals are biotite and epidote (Moore, 1979).

The Gabbros (Figure 2) that have been interpreted to correspond with the Patap gabbros in the Lima segment are broadly dispersed as minor plutons over a large part of the Arequipa segment. In the Rio Pisco area, the age of some of these gabbroic plutons
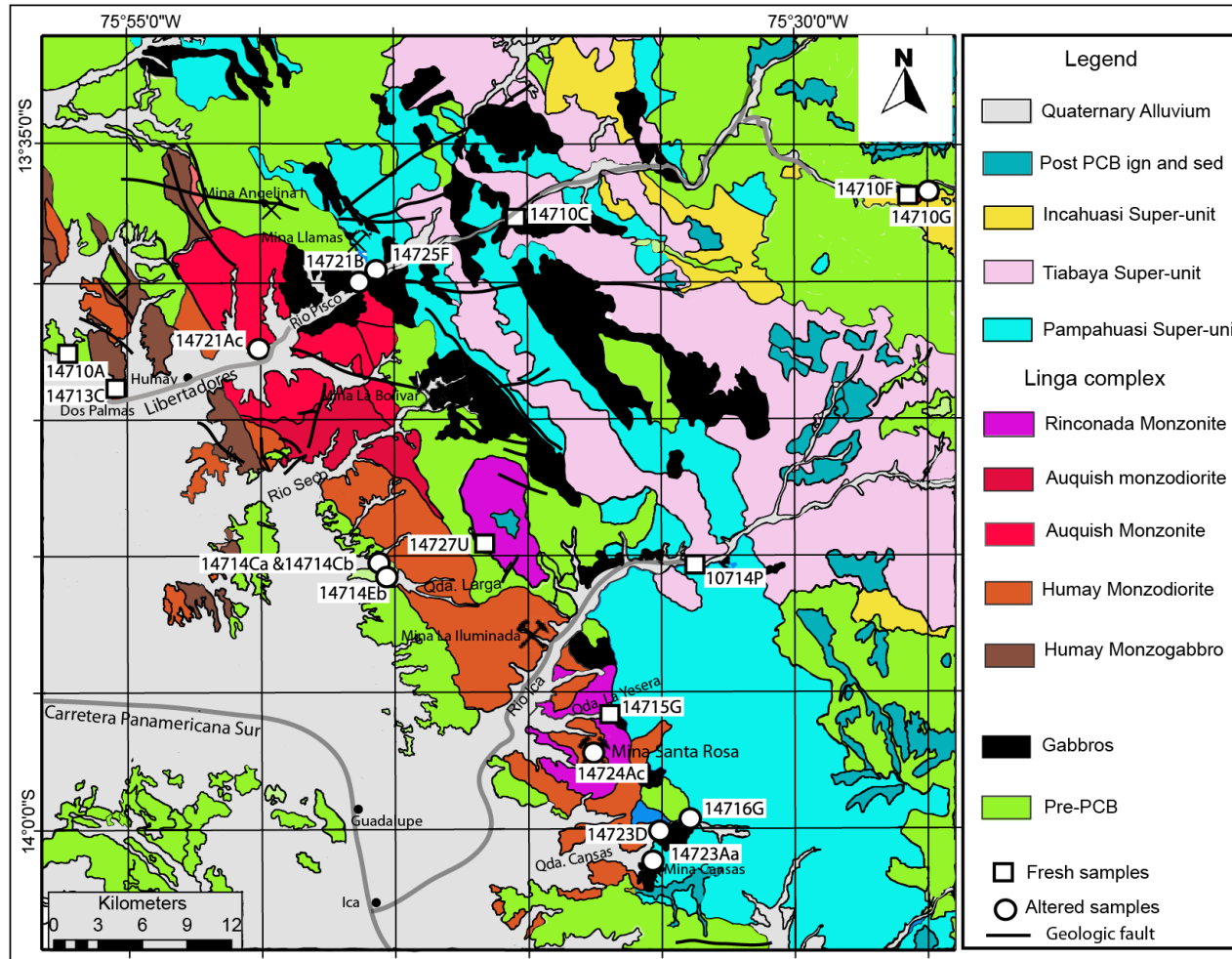
Figure 2. Simplified geologic map of the Ica-Pisco area in the Peruvian Costal Batholith. Sample locations and Super-units are indicated. The map includes the quadrangle 28-i (Guadalupe) and parts of quadrangles 28-m (Santiago de Chocorvos), 29-m (Cordova) and 29-i (Ica). Adapted from Instituto Geológico, Minero y Metalúrgico del Perú (INGEMMET, 1978).

can be constrained by the middle Albian volcaniclastics of the Quilmana volcanics, which they intrude, and by the 101.4 Ma concordant zircon crystallization ages of the oldest granitoids that cut the gabbros. Consequently, the gabbros are probably of late Albian age, i.e. <105 Ma but >101 Ma (Mukasa, 1986).

The Linga complex (Figure 2), which is the focus of this paper is at the western margin of the PCB. This unit is a group of monzonitic rocks ranging from monzogabbro to monzogranite. In the monzogabbros and monzodiorites, cumulose textures are well preserved whereas granophyric textures, which suggests rapid cooling at shallow depths, prevail in the monzogranitic units (Agar, 1981; Mukasa, 1986).

The Linga complex is a consanguineous suite of intrusive rocks originating from magmatic differentiation of a single parent magma (Agar, 1978). The zircon U-Pb age for this Super-unit is 101 Ma (Mukasa and Tilton, 1985). New U-Pb zircon ages of the Linga complex obtained by Martinez (2016) are between 105-98 Ma. Based on petrological considerations, this magmatic suite is divided into three units known as Humay, Auquish and Rinconada (Agar, 1981). The Humay unit is the most mafic of the three units and is comprised of quartz-monzodiorite, quartz-monzogabbro and monzogabbro. This elongate unit is exposed along the western edge of the Linga complex. The Auquish unit has a U-Pb zircon age of 104.8 ± 0.4 Ma (Martinez, 2016) and is mostly porphyritic monzogranites and quartz-monzodiorite. This unit is located northeast of the Humay unit and has a geometry of a ring complex. Finally, monzonites that belong to the Rinconada unit have a U-Pb zircon age of 98.3 ± 1.9 Ma (Martinez, 2016) and have an elliptical spatial distribution in the southern part of the Linga complex (Agar and Le Bel, 1985; Moore, 1979).

Large elongate and steep-walled plutons of the 94 Ma (Mukasa and Tilton, 1985) Pampahuasi Super-unit (Figure 2) in the Arequipa segment are made up of diorite to tonalite with well-developed mineral fabrics and localized shear banding (Moore, 1979; Mukasa, 1986). Plagioclase is coarse-grained and euhedral, and hornblende is present with poikilitic biotite. New U-Pb zircon ages of this Super-unit are between 98 and 92 Ma (Martinez, 2016).

The Tiabaya Super-unit (Figure 2) occurs throughout the Arequipa segment and was dated at 78 Ma (Mukasa and Tilton, 1985). This unit is made up of tonalite, granodiorite and quartz monzonite (Agar, 1978). New U-Pb zircon ages of this Super-unit are between 85 and 78 Ma (Martinez, 2016).

The Incahuasi Super-unit (Figure 2) is confined to the eastern margins of the batholith and was dated at 83 Ma by (Mukasa and Tilton, 1985). This unit is characterized by pervasive poikilitic hornblende and biotite in a framework of euhedral plagioclase. Its main lithology goes from quartz-diorite to monzogranite (Agar, 1978). New U-Pb zircon ages of the Incahuasi Super-unit are between 68 and 59 Ma (Martinez, 2016).

Geochemistry of Intrusive Rocks in the Ica-Pisco Area

This section briefly describes some aspects of the geochemistry in the study area. Geochemical data were obtained from 117 samples, most of which were collected in Peru field work during the summers of 2012 to 2014. GPS, geological unit and lithology of these samples are listed in Appendix 1. Information from the major elements (Appendix 2) yielded parameters like density and crystallization temperature, which were used in

modeling the heat flow of the Linga complex. Data from REE (Appendix 3) were used to establish the source depth of the Super-units in the research area as well as the extent of partial melting and fractional crystallization processes.

Chemical features of the Super-units in the Peruvian Coastal Batholith suggest that they evolved by fractionation from specific magma batches. However, a closer analysis (Agar, 1981; Moore, 1979) makes evident that some of the suites are composed of more than one magma batch, showing that petrological and geological features at the surface may disguise significant differences in the magma source. These compositional differences impact the heat flow model because of the different temperatures from felsic to mafic magmas (Belousov and Belousova, 2016). Most of the magmas evolved by crystallization of plagioclase (>40%) + hornblende $\pm$ pyroxene + biotite $\pm$ magnetite and probably K-feldspar and quartz in the greatly evolved ring complex Super-units (Atherton and Sanderson, 1985).

Magmatic differentiation may be displayed using a plot of a Mg Harker diagram (Figure 3). This plot illustrates the effect of Bowen's reaction series for the four Super-units in the study area, i.e. decreasing MgO with increasing SiO_2. This trend is congruent with the removal of MgO in early forming minerals, associated with olivine and pyroxene (Winter, 2010).

The Sr/Y ratio (Appendix 2) can discriminate deep from shallow fractionation processes due to differences in the partition coefficient between Sr and Y, a trace element in various residual phases and intermediate melt (Profeta et al., 2015; Rollinson, 1993). At lower pressures Sr is compatible and preferentially enters the solid phase substituting for Ca in plagioclase. In contrast, Y is incompatible at low pressures (Brown, 2013).

9
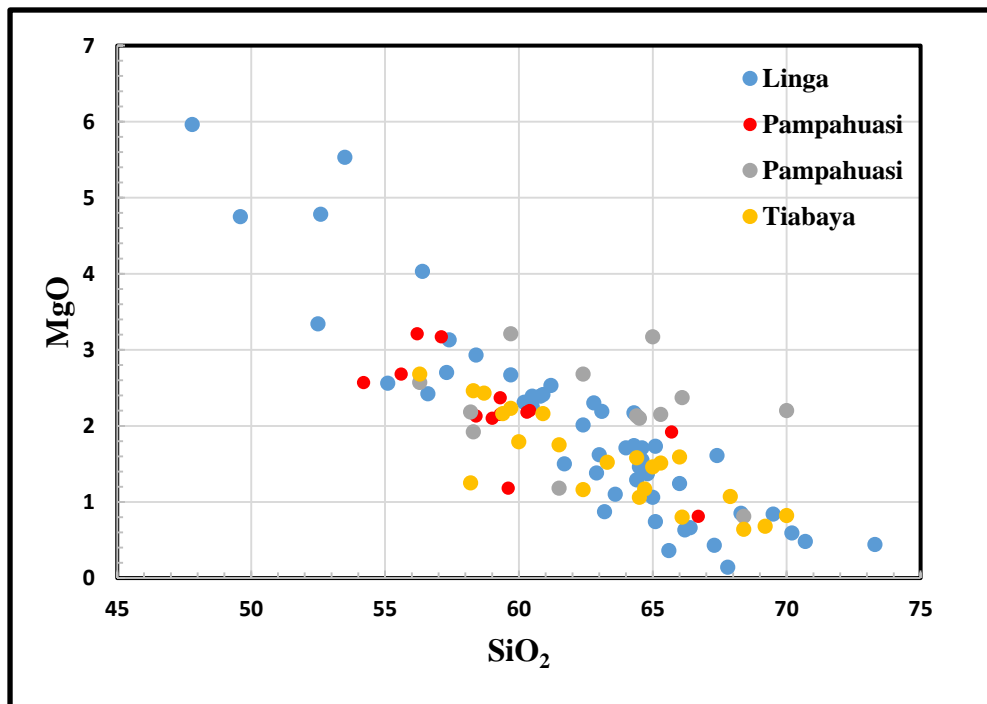
Figure 3: Variation of MgO with SiO2. Note the decreasing trend of MgO in the four Super-units. This trend is a result of fractional crystallization as MgO is incorporated into the early forming minerals.

At mid- to deep crustal levels where low density plagioclase does not preferentially crystallize, Sr is incompatible and preferentially enters the liquid phase.

However, due to the higher pressure small ionic radius Y is compatible with garnet (Carlson et al., 2014) and magma fractionation into amphibole ± garnet, leads to a relative Y depletion in magma coming from a deep source (Chiaradia, 2015; Profeta et al., 2015). The existence of more yttrium in the melt means that it is coming from a relatively shallow source. Conversely, if there is low yttrium in the melt, the magma can be interpreted as coming from a deep source. Figure 4 (based on data listed in appendix 2) shows that the Linga complex contains the most yttrium, which suggests the magma comes from a shallower source. Similarly, Figure 4 shows that magma from the Tiabaya Super-unit has less yttrium, suggesting a deeper magmatic source.

Figure 5 shows the REE concentrations in the Super-units of the Ica-Pisco area. Concentration values are normalized to chondrite meteorite concentration values of Boynton (1984). The REE pattern in Figure 5 displays the europium anomaly. This irregularity in the REE concentrations is a result of the substitution of Eu^{+2} for calcium in plagioclase. The anomaly can be positive or negative depending on whether plagioclase was removed or accumulated, respectively (Winter, 2010).

Figure 5 shows that the replacement of calcium by europium is stronger in the Linga complex, and shows less substitution in the Pampahuasi and Incahuasi Super-unit, and apparently no substitution of calcium by europium in the Tiabaya Super-unit. Figure 5 also shows that concentrations of the light rare elements (LREE), La-Sm, are greater than the concentration values of the heavier rare earth elements (HREE), Gd-Lu. The slope of the concentration values is lowest in the Linga and largest in the Tiabaya.
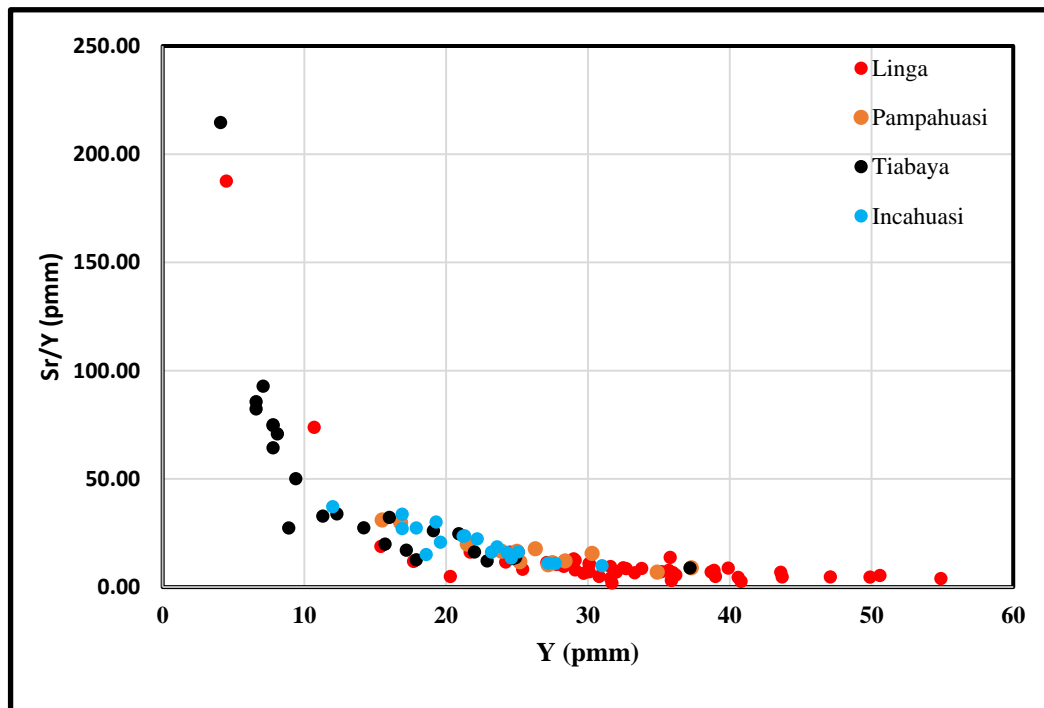
Figure 4. This is a plot of Sr/Y vs Y to determine relative depth of the magma source. The Linga complex has the shallower magma source and the Tiabaya has the deeper.
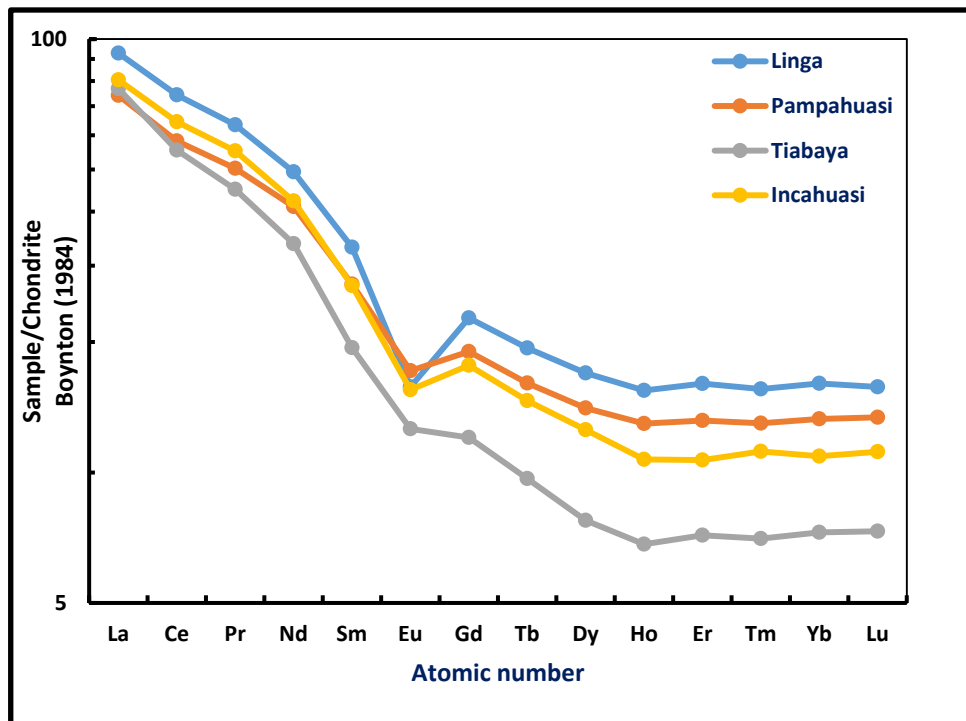
Figure 5. REE element spider diagram for the Super-units in the Ica-Pisco area of the PCB. Note the pronounced slope of Tiabaya, suggesting a deeper origin of the magmas.

This variation in slope is interpreted to be related to the depth of the magma source (Gromet and Silver, 1983), Thus, the Linga complex apparently has a shallower magma source and the Tiabaya a deeper source. The four Super-units are enriched in the light REEs and depleted in the heavy REEs. However, the difference in depletion is more notable in the Tiabaya Super-unit. This depletion of the heavy REE is probably due to their compatibility with garnet present in a deeper magma source (Rollinson, 1993).

Hydrothermal Alteration

Definition

Hydrothermal alteration is a process associated with mineralogical, chemical and textural changes, caused by the interaction of hot aqueous fluids with the rocks through which they circulate, under changing physico-chemical conditions (Pirajno, 2009; Rose and Burt, 1979). During hydrothermal alteration, hydrothermal fluids efficiently transport chemical components and heat (Rose and Burt, 1979).

Ore-forming solutions, which cause hydrothermal alteration, were previously thought to be mostly the product of magmatic sources (Criss and Taylor, 1986). However, now it is thought that meteoric or connate water may constitute a significant amount of hydrothermal solutions whose effects are observable at the outcrop, hand sample and microscopic scale (Gregory et al., 1989; Schwartz, 1959).

Hydrothermal Alteration in the Linga Complex

Most samples for hydrothermal alteration analysis were collected along south-west to north-east trending rivers that cut the Linga complex in the Ica-Pisco area.

Transects include the Rio Ica, Quebrada Larga, and Rio Pisco (Figure 2) with a focus on contact zones between Super-units to identify styles of hydrothermal alteration. Published geologic maps of the Guadalupe and Ica quadrangles (INGEMMET, 1978) guided these efforts. Rock samples selected for thin sections are representative of the Linga complex. Appendix 4 contains the GPS location, geologic unit, mineral association, alteration type and a brief description of the outcrop for 59 thin sections used in this study.

Alteration in Outcrop and Hand Sample Level

According to Agar (1981) the units of the Linga complex have their own sequence of alteration inside their particular envelope, which may be volcanic or an early part of the Linga complex. Three types of alteration are widespread, potassic, propylitic and sericitic. They are frequently distributed in zones around the parent pluton with the potassic zone in the center, followed by the sericitic and the propylitic zones. Following is a brief description of the main alteration types observed in the Linga complex, as well as the ranges of temperatures at which the alteration is estimated to occur. The ranges of temperature for the different types of alteration were used in the thermal modeling in order to estimate the possible conditions under which the alteration occurred.

Potassic Alteration

Potassic alteration results from potassium enrichment. This alteration is significant in porphyry and epithermal mineralizing systems, where it occurs in the high

temperature core zones. The distinguishing minerals of potassic alteration are K-feldspar, biotite and sericite (Damian, 2003) as observed in the outcrop showed in Figure 6. Potassic alteration is common in deeper plutonic settings, where orthoclase forms or in shallow volcanic settings where adularia is generated. Potassic alteration is the result of the replacement of plagioclase and mafic silicate minerals at temperatures from 450 to 600ºC (Pirajno, 2009). Figure 7 shows an outcrop containing specular hematite, a common alteration mineral associated with porphyry copper deposits where it occurs in veins with potassic alteration (Thomson and Thomson, 2011).

Propylitic Alteration

Propylitic alteration is characterized by the addition of H_2O and CO_2 with no substantial acidic metasomatism. It becomes more evident away from the heat/hydrothermal source of a hydrothermal deposit (Pirajno, 2009). Characteristic minerals of propylitic alteration are albite, chlorite, epidote, carbonates, sericite, pyrite and magnetite. Plagioclase crystals are replaced by aggregates of sericite, chlorite, epidote and calcite. Pyroxene crystals are replaced by carbonates and quartz and some alteration K-feldspar or albite may be added (Damian, 2003; Guilbert and Park, 1986). Existence of chlorite and epidote suggest temperatures of 220-340ºC and appearance of actinolite-tremolite indicates temperatures in the range of 280-350ºC (Damian, 2003). Figure 8 shows an outcrop at the border between the Linga complex and the Pampahuasi Super-unit displaying strong epidotization, indicative of propylitic alteration. Figure 9 shows another outcrop in the Rio Pisco with abundant tremolite, which suggests

.
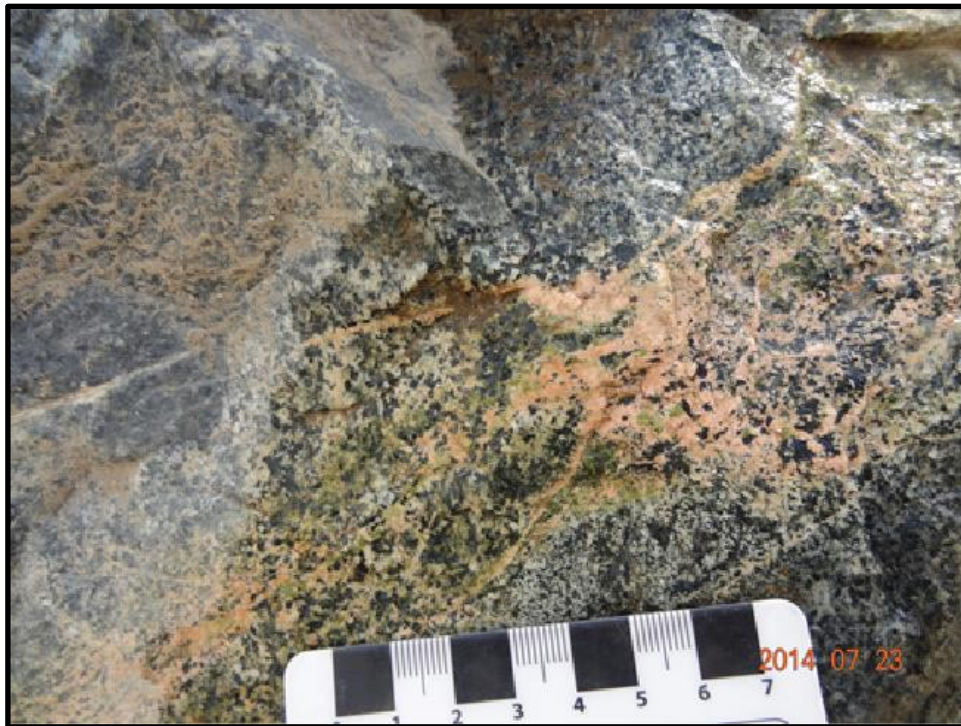
Figure 6. Outcrop with strong potassic alteration, suggesting interaction with hydrothermal fluids at temperatures from 450 °C to 600 °C. Outcrop located at the boundary between the Linga complex and the Pampahuasi Super-unit in the Quebrada Cansas transect.

Figure 7. Specular hematite in the Rio Pisco. Hematite is an alteration mineral common in several intrusion-related systems. In this region hematite seems to be associated with potassic alteration. In some outcrops it appears associated with high levels of sericite and chlorite.

Figure 8. Outcrop with strong epidotization, indicating propylitic alteration at temperatures in the range of 220 to 340ºC. Locality: Quebrada Cansas. (This picture is going to be referred to in chapter three as part of a paper for publication).

Figure 9. Tremolite belongs to the amphibole minerals and may weather to talc, chlorite and carbonates. The presence of tremolite suggests propylitic alteration from 280 up to 450 ºC. Locality: Rio Pisco transect.

propylitic alteration at temperatures from 280 to 350 ºC (Corbett and Leach, 1997; Ferry and Dipple, 1992)

Hydrothermal Alteration Observed in Thin Section from the Linga Complex

Mineral assemblages in thin section were studied to determine the type of hydrothermal alteration that occurred in different outcrops (Pirajno, 2009). Thin sections where qualitatively analyzed, using the petrographic microscope, to have a better understanding of the hydrothermal alteration processes in the Linga complex. Different mineral associations gave clues about the alteration type and therefore, the range of temperature that triggered the alteration. Alteration assemblages were also studied using TerraSpec, a mineral analyzer for geologic exploration and ore analysis (Goetz and Curtiss, 1990).

Mineralogical assemblages suggest potassic, phyllic, propylitic, and argillic alteration, although, propylitic and potassic seems to be the most abundant. These findings are in agreement with Agar and Le Bel (1985) who state that the Cu-Fe-Mo mineralization in the Rio Pisco section of the PCB is spatially associated with the Linga complex. Furthermore, Cu, Fe and Mo mineralization is associated with porphyry copper deposits in the area (Agar, 1981). Following is a brief description of some Linga complex thin sections, noting the evidence for various types of hydrothermal alteration.

Figure 10 displays potassic alteration characterized by the replacement of the primary minerals with secondary biotite, K-feldspar, and sericite in association with sulphides (pyrite, chalcopyrite) and magnetite. This mineral association suggests the presence of a "porphyry copper" system. Potassic feldspar replaces the plagioclase and

lamellar or crystalline biotite replaces plagioclase phenocrysts and mafic minerals (Damian, 2003). Characteristic minerals of propylitic alteration are chlorite, albite, epidote and sericite, some of which are observed in Figure 11. However, in general, other minerals like galena, sphalerite and chalcopyrite, as well as zeolites and smectites can also be present (Reed, 1997).

Sericitic alteration (Figure 12) is common in orthoclase and plagioclase feldspars in zones that have undergone hydrothermal alteration associated with copper, tin or other hydrothermal ore deposits. Sericite appears as a fine white mica that gives the sheen to phyllite and schistose metamorphic rocks (Reed, 1997; Thomson and Thomson, 2011).

Argillic alteration is characterized by the formation of clay minerals due to extreme base leaching of alumino-silicates (Damian, 2003). This alteration is associated with the upper parts of the vein fields and affects the volcanic rocks. Common clay minerals replacing plagioclases and mafic minerals are illite, kaolinite, and montmorillonite. Argillic alteration generally occurs below 200ºC (Meunier and Velde, 2004). Figure 13 shows a thin section displaying argillic alteration with kaolinite as the probable clay mineral.

Specific results about alteration assemblage parameters obtained and the application of them are detailed in chapters 3 and 5 of this dissertation.

Summary

This research aimed to model the cooling of the Linga complex, a group of magmatic intrusions located in the northern part of the Arequipa segment in the Peruvian
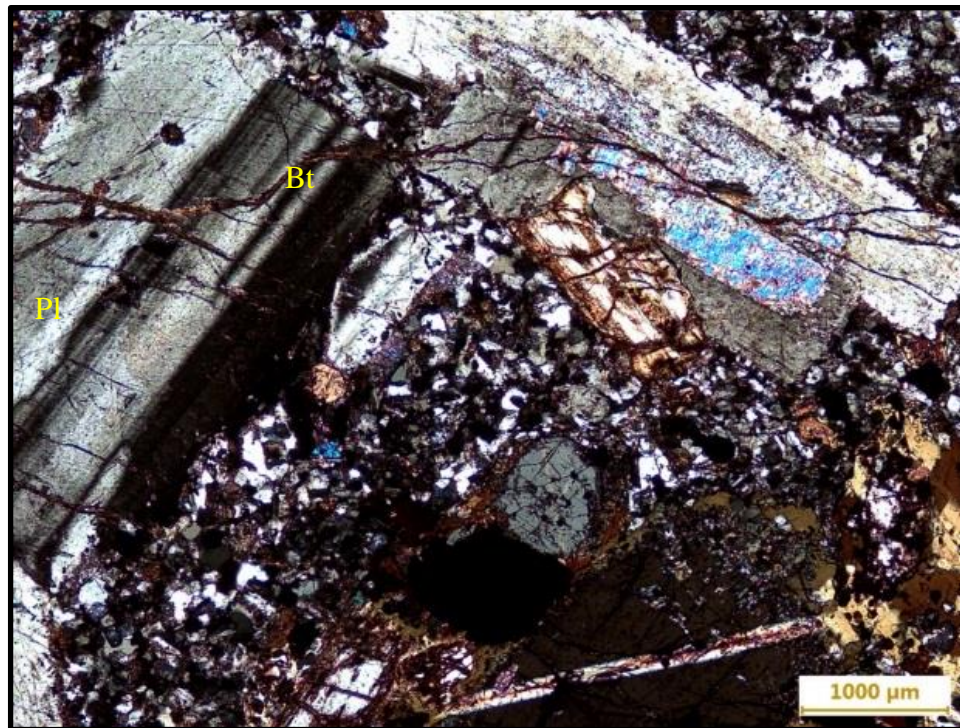
Figure 10. Thin section 13823A: Veinlets of secondary biotite (Bt) cutting plagioclase (Pl) crystals showing evidence of potassic alteration at temperatures from 350 °C to 550 °C. Location "Cabeza de Toro", northwest in the Linga complex.

Figure 11. Thin section 13822A: Epidote (Epi), chlorite (Chl), and sericite (Ser) suggesting propylitic alteration in an outcrop south of the Rio Pisco.

Figure 12. Thin section 13828A: Sericite is found throughout the Rio Pisco area. This thin section shows sericite replacing plagioclase, quartz and some opaque minerals (probably pyrite) which is indicative of phyllic alteration.
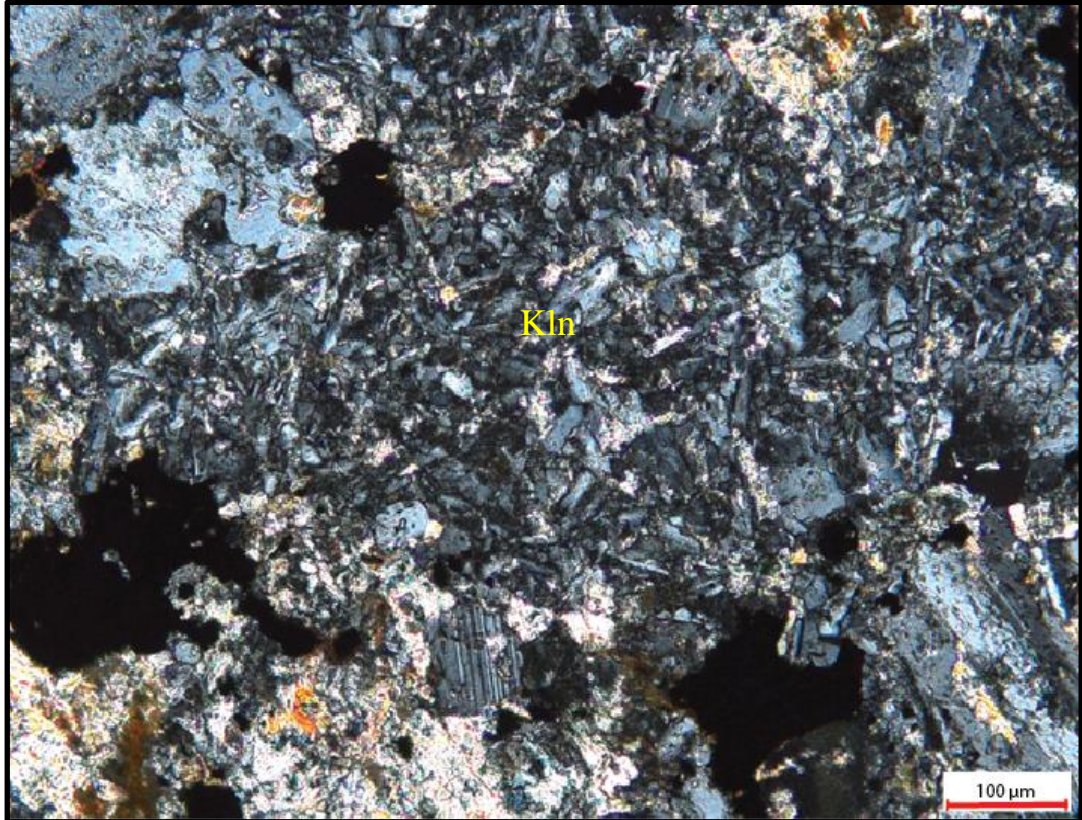
Figure 13. Thin section 14714Ca. This sample was taken at the contact zone between the Linga-Humay and the Quilmana volcanics in the Quebrada Larga transect. Note the clay mineral, probably kaolinite (Kln) replacing plagioclase. This indicates argillic alteration.

Coastal Batholith. The hypothesis to test is whether including the action of convective hydrothermal fluids to cool the magmatic body significantly reduces the time span for the batholith to reach its final temperature. The model includes data obtained from field work, geochemistry, thin sections, and stable isotope analysis. Field work provided information like areal extent and type of alteration. Geochemistry provided parameters like density and crystallization temperature to be used in the thermal modeling. Thin section analysis yielded information about the type and extent of alteration assemblages in the study area. Stable isotope analysis provided values for $\delta^{18}O$ and δD to determine magma source and apparent temperature for unaltered samples as well as sources of hydrothermal alteration for altered samples.

Outline of the Dissertation

In order to give an overview of the present research, this outline succinctly describes the dissertation chapters.

Chapter one states the research objectives and outlines geologic setting, major and trace elements geochemistry, and types of hydrothermal alteration of the Linga complex. These topics are addressed through maps, geochemistry plots and pictures of outcrops as well as thin sections summarizing the geology in the study area.

Chapter two is an introduction to and literature review of stable isotopes. The emphasis is on some mathematical relationships that govern isotopic fractionation processes, as well as their application to geothermometry, and as tracers for the origin and history of the hydrothermal fluids involved in alteration processes.

Chapter three is a paper to be submitted for publication in the Bulletin of the Peruvian Geological Society. This chapter presents oxygen and hydrogen isotope values obtained from 64 minerals separated from 18 samples collected in the Linga complex, 11 altered and 7 fresh. The study determined magma source and isotopic equilibrium temperatures for fresh samples as well as source of alteration and water/rock ratios for altered samples.

Chapter four is an introduction to and literature review of heat flow in Earth's rocks. This chapter begins with a summary of heat transfer processes and sources of Earth's internal heat. The topic of the geothermal gradient is addressed, as well as heat flow in hydrothermal systems. A brief historical background is then presented on some of the efforts to model heat flow over the last 150 years. The chapter ends by addressing the relationship between heat flow modeling and the use of geothermal energy.

Chapter five is focused on modeling heat flow in the Linga complex. The software MATLAB was used to simulate the cooling of a dyke by conduction. The modeling software was primarily HYDROTHERM interactive. The modeling with HYDROTHERM included parameters obtained from lab analysis and the literature. Several simulations display how varying parameters like permeability, size and initial temperature of the intrusion affect the thermal evolution of the Linga complex. The modeling investigates the possible thermal setting that triggered the hydrothermal alteration assemblages observed in some of the samples collected in the study area.

Chapter six summarizes the conclusions that emerged from the research as well as some suggestions for future work. Four appendices at the end summarize the data from which the conclusions are drawn.

References

Agar, R. A., 1978, The Peruvian Coastal Batholith: Its Monzonitic Rocks and their
Related Mineralization [Doctor of Philosophy]: University of Liverpool, 293 p.

-, 1981, Copper mineralization and magmatic hydrothermal brines in the Rio Pisco
section of the Peruvian Coastal Batholith: Economic Geology, v. 76, p. 677-693.

Agar, R. A., and Le Bel, L., 1985, The Linga Super-unit: High-K diorites of the Arequipa
segment, *in* W.S. Pitcher, M. P. Atherton, Cobbing, E. J., and Beckinsale, R. D.,
eds., Magmatism at a Plate Edge: The Peruvian Andes: New York, John Wiley
and Sons., p. 119-127.

Aguirre, L., and Offler, R., 1985, Burial metamorphism in the Western Peruvian Trough:
its relation to Andean magmatism and tectonics, *in* W.S. Pitcher, M. P. Atherton,
Cobbing, E. J., and Beckinsale, R. D., eds., Magmatism at a plate edge: The
Peruvian Andes: New York, John Wiley and Sons, p. 59-71.

Atherton, M. P., and Sanderson, M. L., 1985, The chemical variation and evolution of the
super-units of the segmented Coastal Batholith, *in* W.S. Pitcher, M. P. Atherton,
Cobbing, E. J., and Beckinsale, R. D., eds., Magmatism at a plate edge: The
Peruvian Andes: New York, John Wiley and Sons., p. 208-227.

Atwater, T., 1970, Implications of plate tectonics for the Cenozoic tectonic evolution of
western North America: GSA Bulletin, v. 81, no. 12, p. 3513-3536.

Belousov, V., I, and Belousova, I., V., 2016, Heat transfer in hydrothermal-magmatic
systems, Workshop on Geothermal Reservoir Engineering Stanford University,
Stanford, California, February 22-24 2016, p. 1-12.

Bindeman, I., 2008, Oxygen isotopes in mantle and crustal magmas as revealed by single

    crystal analysis: Reviews in Mineralogy and Geochemistry, v. 69, p. 445-478.

Boekhout, F., Sempere, T., Spikings, R., and Schaltegger, U., 2013, Late Paleozoic to

    Jurassic chronostratigraphy of coastal southern Peru: Temporal evolution of

    sedimentation along an active margin: Journal of South American Earth Sciences,

    v. 47, p. 179-200.

Boynton, W. V., 1984, Cosmochemistry of the rare Earth elements: Meteorite studies:

    Developments in Geochemistry, v. 2, p. 63-114.

Brown, M., 2013, Granite: From genesis to emplacement: GSA Bulletin, v. 125, no. 7-8,

    p. 1079-1113.

Carlson, W. D., Gale, J. D., and Kate, W., 2014, Incorporation of Y and REEs in

    aluminosilicate garnet: Energetics from atomistic simulation: American

    Mineralogist, v. 99, no. 5-6, p. 1022-1034.

Chiaradia, M., 2015, Crustal thickness control on Sr/Y signatures of recent arc magmas:

    an Earth scale perspective: Scientific Reports, v. 5, no. 8115, p. 1-5.

Cobbing, E. J., and Pitcher, W. S., 1972, The Coastal Batholith of Central Peru:

    Geological Society of London Journal, v. 128, no. 5, p. 421-460.

Cobbing, E. J., Pitcher, W. S., and Taylor, W. P., 1977, Segments and Super-units in the

    Coastal Batholith of Peru: Journal of Geology, v. 85, no. 5, p. 625-631.

Corbett, G., and Leach, T., 1997, Southwest Pacific rim gold-copper systems: Structure,

    alteration and mineralization, 1996 Society for Mining, Metallurgy, and

    Exploration Annual Meeting: Phoenix AZ.

Criss, R. E., and Taylor, H. P., 1986, Meteoric hydrothermal systems: Reviews in

    Mineralogy and Geochemistry, v. 16, no. 1, p. 373-424.

Damian, F., 2003, The mineralogical characteristics and the zoning of the hydrothermal

    types alteration from nistru ore deposit, Baia Mare metallogenetic district:

    Geologia, v. XLVIII, no. I, p. 101-112.

Ferry, J. M., and Dipple, G. M., 1992, Models for coupled fluid flow, mineral reaction,

    and isotopic alteration during contact metamorphism: The Notch Peak aureole,

    Utah: American Mineralogist, v. 77, p. 577-591.

Goetz, A., F.H, and Curtiss, B., 1990, TerraSpec: Boulder, Colorado, Analytical Spectral

    Devices Inc.

Gregory, R. T., Criss, R. E., and Taylor, H. P., 1989, Oxygen isotope exchange kinetics

    of mineral pairs in closed and open systems: applications to problems of

    hydrothermal alteration of igneous rocks and Precambrian iron formations:

    Chemical Geology, v. 75, no. 1-2, p. 1-42.

Gromet, L. P., and Silver, L. T., 1983, Rare earth element distributions among minerals

    in a granodiorite and their petrogentic implications: Geochimica et Cosmochimica

    Acta, v. 47, no. 5, p. 925-939.

Guilbert, J. M., and Park, C. F., 1986, The Geology of Ore Deposits, USA, W. H.

    Freeman and Company.

Hayba, D. O., and Ingebritsen, S. E., 1997, Multiphase groundwater flow near cooling

    plutons: Journal of Geophysical Research, v. 102, no. B6, p. 12235-12252.

Hoefs, J., 1996, Stable Isotope Geochemistry, Germany, Springer.

INGEMMET, 1978, Quadrangle 28-i (Guadalupe), and parts of quadrangles 28-m
(Santiago de Chocorvos) , 29-m (Cordova), and 29-i (Ica): Perú, Sector energía y
minas del Perú.

Jaillard, E., and Soler, P., 1996, Cretaceous to early Paleogene tectonic evolution of the
northern Central Andes (0-18ºS) and its relations to geodynamics:
Tectonophysics, v. 259, p. 41-53.

Martinez, A. M., 2016, Compositional diversity in arcs: A record of magmatic processes
in the Peru Coastal Batholith, Ica. [Doctor of Philosophy]: Loma Linda
University, 410 p.

McQuarrie, N., Horton, B., K, Zandt, G., Beck, S., and DeCelles, P., G., 2005,
Lithospheric evolution of the Andean fold-thrust belt, Bolivia, and the origin of
the central Andean plateau: Tectonophysics v. 399, p. 15-37.

Mégard, F., 1984, The Andean orogenic period and its major structures in central and
northern Peru: Journal of the Geological Society, v. 141, no. 5, p. 893-900.

Meunier, A., and Velde, B., 2004, Illite: Origins, Evolution and Metamorphism,
Germany, Springer.

Moore, N. D., 1979, The Geology and Geochronology of the Arequipa Segment of the
Coastal Batholith of Peru [Doctor in Philosophy]: Liverpool, 549 p.

-, 1984, Potassium-argon ages from the Arequipa segment of the Coastal Batholith of
Peru and their correlation with regional tectonic events: Journal of the Geological
Society, v. 141, no. 3, p. 511-519.

Mukasa, S. B., 1986, Zircon U-Pb ages of Super-units in the Coastal Batholith, Peru: Implications for magmatic and tectonic processes: GSA Bulletin, v. 97, p. 241-254.

Mukasa, S. B., and Tilton, G. R., 1985, Zircon U-Pb ages of Super-units in the Coastal Batholith of Peru, *in* W.S. Pitcher., M. P. Atherton., E. J. Cobbing., and Beckinsale, R. D., eds., Magmatism at a plate edge: The Peruvian Andes: New York, John Wiley and Sons., p. 203-207.

Norton, D., and Knight, J., 1977, Transport phenomena in hydrothermal systems: Cooling plutons: American Journal of Science, v. 277, p. 937-981.

Pfiffner, O. A., and Gonzalez, L., 2013, Mesozoic–Cenozoic evolution of the western margin of South America: Case study of the Peruvian Andes: Geosciences, v. 3, p. 262-310.

Pilger, R. H., 1984, Cenozoic plate kinematics, subduction and magmatism: South American Andes: Journal of the Geological Society, v. 141, no. 5, p. 793-802.

Pirajno, F., 2009, Hydrothermal Processes and Mineral Systems, Australia, Springer.

Pitcher, W. S., 1985, A multiple and composite batholith, *in* W.S. Pitcher, M. P. Atherton, Cobbing, E. J., and Beckinsale, R. D., eds., Magmatism at a plate edge: The Peruvian Andes: New York, John Wiley and Sons., p. 119-127.

Polliand, M., Schaltegger, U., Frank, M., and Fontbote, L., 2005, Formation of intra-arc volcanosedimentary basins in the western flank of the central Peruvian Andes during Late Cretaceous oblique subduction: field evidence and constraints from U-Pb ages and Hf isotopes: International Journal of Earth Sciences, v. 94, no. 2, p. 231-242.

Profeta, L., Ducea, M. N., Chapman, J. B., Paterson, S. R., Henriquez, S. M., Kirsch, M., Petrescu, L., and DeCelles, P. G., 2015, Quantifying crustal thickness over time in magmatic arcs: Scientific Reports, v. 4, no. 17786, p. 1-7.

Reed, M. H., 1997, Hydrothermal Alteration and its Relationship to Ore Fluid Composition, *in* Hubert L, B., ed., Geochemistry of Hydrothermal Ore Deposits: USA, John Wiley & Sons, Inc.

Rollinson, H. R., 1993, Using Geochemical Data: Evaluation, Presentation, Interpretation, UK, Pearson Prentice-Hall.

Rose, A. W., and Burt, D. M., 1979, Hydrothermal alteration, *in* Barnes, H. L., ed., Geochemistry of Hydrothermal Ore Deposits: New York, John Wiley & Sons, p. 173-227.

Schilling, F. R., Trumbull, R. B., Brasse, H., Haberland, C., Asch, G., Bruhn, D., Mai, K., Haak, V., Giese, P., Muñoz, M., Ramelow, J., Rietbrock, A., Ricaldi, E., and Vietor, T., 2006, Partial melting in the Central Andean crust: A review of geophysical, petrophysical, and petrologic evidence, *in* Oncken, O., Chong, G., Franz, G., Giese, P., Götze, H. J., Ramos, V. A., Strecker, M. R., and Wigger, P., eds., The Andes: Berlin, Springer, p. 459-474.

Schwartz, G. M., 1959, Hydrothermal alteration: Economic Geology, v. 54, no. 2, p. 161-183.

Schweickert, R. A., and Cowan, D. S., 1975, Early Mesozoic tectonic evolution of the western Sierra Nevada, California: GSA Bulletin, v. 86, no. 10, p. 1329-1336.

Sharp, Z. D., 2007, Principles of Stable Isotope Geochemistry, USA, Pearson Prentice-Hall.

Soler, P., and Bonhomme, M. G., 1990, Relation of magmatic activìty to plate dynamics

    ìn central Peru from Late Cretaceous to present: GSA Special Paper, v. 241, p.

    173-192.

Spera, F., 1980, Thermal evolution of plutons: a parameterized approach: Science, v. 207,

    no. 4428, p. 299-301.

Springer, M., 1999, Interpretation of heat-flow density in the Central Andes:

    Tectonophysics, v. 306, no. 3,4, p. 377-395.

Taylor, H. P., 1978, Oxygen and hydrogen isotope studies of plutonic granitic rocks:

    Earth and Planetary Science Letters, v. 38, no. 1, p. 177-210.

Thomson, A. J. B., and Thomson, J. F. H., 2011, Atlas of Alteration. A Field and

    Petrographic Guide to Hydrothermal Alteration Minerals, Canada, Geological

    Association of Canada.

Winter, J. D., 2010, Principles of Igneous and Metamorphic Petrology, New Jersey,

    Prentice Hall.

Wortel, M. J. R., 1984, Spatial and temporal variations in the Andean subduction zone:

    Journal of the Geological Society, v. 141, no. 5, p. 783-791.

CHAPTER TWO

STABLE ISOTOPES

This chapter provides an extended introduction to some principles of stable isotope geochemistry that apply to the petrology of pluton emplacement and associated hydrothermal alteration. The basis for using stable isotope for geothermometry is addressed, since stable isotopes data described in chapter three provide temperature constraints for the heat flow modeling presented in chapter five. This chapter also addresses the application of mineral $\delta^{18}O$ and δD values to identify sources of hydrothermal fluids and water/rock ratios. Thus, chapter two presents the mathematical relationships that rule mass dependence and temperature dependence of the isotopic fractionation factors. The concepts introduced are foundational to the heat flow modeling presented in chapter five.

Introduction

Stable isotope geochemistry is based on variations of the isotopic composition of light elements as a result of kinetic and physico-chemical processes and isotope exchange reactions (Hoefs, 1996; White, 2015). These changes, which are of a different nature than those triggered by radioactive decay, are known as isotopic fractionation (Rollinson, 1993). All isotopes of an element have the same electronic structure and consequently the same chemical properties, but the mass difference is the factor that causes the isotopic fractionation during different reactions (Faure and Mensing, 2009; Misra, 2012)

A large number of stable isotope variations arise naturally by isotopic fractionation; however, the elements most frequently analyzed for modern stable isotope geochemistry are H, Li, B, C, N, O, Si, S and Cl. Of these, O, H, C, N and S are undoubtedly the most important (Misra, 2012; White, 2015). These five elements 1) are rather common in the crust and mantle of the Earth and/or the atmosphere, 2) have a low atomic mass and therefore, a relatively large difference in mass between the rare (heavy) and the abundant (light) isotope, 3) have highly covalent chemical bonds, and 4) exist in more than one oxidation state (Faure, 1998; Hoefs, 1996). These properties allow them to fractionate readily, and therefore, these elements are appropriate for stable isotopic analysis (Fetter, 2001; Misra, 2012).

Stable Isotope Mathematical Relationships

Mass Dependence of Isotopic Fractionation

The relative atomic masses of an element's isotopes have a significant role in the process of isotopic fractionation. This fact can be demonstrated by taking the velocities of molecules in a gas at a specific temperature, and recalling that according to statistical mechanics, all molecules at the same temperature in an ideal gas have the same kinetic energy given by

$$K = \frac{1}{2}mv^2 \tag{1}$$

If there are two isotopic species of a molecule with different masses, but the same kinetic energy, it can be mathematically expressed as

$$\frac{1}{2}m_h v_h^2 = \frac{1}{2}m_l v_l^2 \tag{2}$$

where the subscripts h and l stand for heavy and light isotopes respectively. From (2) it is possible to obtain

$$\frac{v_l}{v_h} = \left(\frac{m_h}{m_l}\right)^{\frac{1}{2}}$$ (3)

Isolating v_l from (3) yields

$$v_l = v_h \left(\frac{m_h}{m_l}\right)^{\frac{1}{2}}$$ (4)

In (4) $\quad \frac{m_h}{m_l} > 1$, therefore

$$v_l > v_h$$ (5)

Inequality (5) indicates that the velocity of molecules containing the same element(s), but having the lighter isotope is greater than the velocity of the molecules containing the heavier isotope, if they are at the same temperature (White, 2015).

The difference in mass between molecules containing the heavy and light isotopes, as applied to water molecules, is the basis for the fractionation of the isotopes of H and O that take place during evaporation and condensation of water (Faure and Mensing, 2009; Larson and Zimmerman, 1991; Mysen, 2014). This mass difference regulates the differential isotopic evaporation of water from the surface of the oceans in the equatorial regions (more than at the poles) of the Earth, resulting in water vapor depleted in the heaviest ^{18}O and D (^{2}H) relative to seawater. As air mass move north or south from the equator, temperature decreases, and the air becomes saturated with water vapor causing condensation and precipitation of water. This condensate is enriched in the heavy isotopes of O and H (with respect to the water vapor) because condensation is the opposite of evaporation (Bowen and Revenaugh, 2003; Faure, 1998; Sharp, 2007).

Temperature Dependence of the Fractionation Factor

Stable isotope ratios are measured relative to a standard and are expressed in parts per thousand (‰). The isotope ratio is expressed as a δ value which, from a general perspective of isotopic fractionation between two phases a and b in isotopic equilibrium, can be respectively defined as

$$\delta_a = \left(\frac{R_a - R_{std}}{R_{std}}\right) \times 10^3 \tag{6}$$

and

$$\delta_b = \left(\frac{R_b - R_{std}}{R_{std}}\right) \times 10^3 \tag{7}$$

Negative and positive values of δ indicate respectively, depletion and enrichment of a particular isotope in the sample with respect to a determined standard. For example, meteoric water is depleted (takes more negative values) of $\delta^{18}O$ and δD with increasing latitude and altitude. Equations (6) and (7) can be respectively solved for R_a and R_b

$$R_a = \frac{R_{std}(\delta_a + 10^3)}{10^3} \tag{8}$$

$$R_b = \frac{R_{std}(\delta_b + 10^3)}{10^3} \tag{9}$$

The fractionation of an isotope between two compounds a and b is expressed by the fractionation factor α. This factor is defined as the ratio of the isotopic abundance of the heaviest chemical compound a divided by the analogous ratio for another lighter chemical compound b (Bindeman, 2008; Hoefs, 1996) which is mathematically expressed as

$$\alpha_b^a = \frac{R_a}{R_b} \tag{10}$$

Substituting (8) and (9) in (10) yields

$$\alpha_b^a = \frac{(\delta_a + 10^3)}{(\delta_b + 10^3)} \tag{11}$$

Equation (11) illustrates the relationship between the fractionation factor α and the δ values. Using this equation it is possible to calculate either α_b^a, δ_a or δ_b when any two of the three variables are known. Equation (11) is valid as long as isotopic equilibrium exists between phases a and b at a specified temperature (Faure and Mensing, 2009; Misra, 2012; White, 2015).

The temperature variation of isotopic fractionation factors for several exchange reactions is usually determined experimentally and can be mathematically expressed (Faure, 1998; Javoy, 1977) as

$$10^3 ln\, \alpha_b^a = A + \frac{B \times 10^6}{T^2} \tag{12}$$

where A and B are constants determined experimentally and T is the temperature in Kelvins.

To understand equation (12) it is necessary to remember that natural logarithms of a number with the general form 1.00x (where "x" is a digit in the third decimal place) have the property that

$$10^3 ln1.00x \approx x; x < 10 \tag{13}$$

The approximation (13) can be applied to oxygen fractionation in natural systems by means of the following equations

$$\alpha_b^a - 1 = \frac{R_a}{R_b} - 1 = \frac{R_a - R_b}{R_b} \tag{14}$$

Substitution of equations (8) and (9) in equation (14) yields

$$\alpha_b^a - 1 = \frac{\delta_a - \delta_b}{\delta_b + 10^3} \tag{15}$$

In general $\delta_b \ll 10^3$, which allows the approximation $\delta_b + 10^3 \approx 10^3$. Then, equation (15) yields the useful approximation

$$10^3(\alpha_b^a - 1) \approx \delta_a - \delta_b \qquad (16)$$

Based on the approximation (13) and equations (15) and (16), it can be established that

$$10^3(\alpha_b^a - 1) \approx 10^3 ln\, \alpha_b^a \approx \delta_a - \delta_b \qquad (17)$$

Now, defining $\delta_a - \delta_a = \Delta_b^a$ it can be established that

$$10^3 ln\, \alpha_b^a \approx \Delta_b^a \approx A + \frac{B \times 10^6}{T^2} \qquad (18)$$

Equation (18) indicates that the isotopic fractionation factor α in coexisting compounds in isotopic equilibrium decreases with increasing temperature and vice versa (Bindeman, 2008; Javoy, 1977; Turi, 1988).

Applications of Hydrogen and Oxygen Stable Isotopes

Among the elements O, H, C, N and S, oxygen and hydrogen are the most useful in petrologic studies (Guilbert and Park, 1986; Hoefs, 1996). The $^{18}O/^{16}O$ and D/H ratios, expressed in δ units of per thousand or per mil (‰) relative to the universal Standard Mean Ocean Water (SMOW), are presently one of the main tools for understanding several geologic problems. For example, they are useful in providing information about 1) the conditions and processes associated with mineral and rock formation, 2) the source and evolution of magmas, 3) chemical and isotopic exchange between magmas and country rocks, 4) the nature of the hydrothermal fluids involved in geological processes, 5) the record of the thermal history and the magnitude of fluid migration during metamorphic processes, and 6) the interaction between plutons and aqueous fluids of

different origins (Bindeman et al., 2008; Guilbert and Park, 1986; Sharp, 2007; Taylor, 1978; Turi, 1988).

These studies are important because of some properties inherent to isotopes in nature, for instance: 1) magmas derived from the upper mantle of the earth have very uniform and distinguishing isotopic compositions ($\delta^{18}O\approx$ +5.5‰ to +7.0‰ and $\delta D\approx$ −85‰ to −50‰) relative to SMOW (Taylor, 1978); 2) fractional crystallization of primary magmas is unable to produce significant variations in $\delta^{18}O$ and δD of subsequent differentiates, because the equilibrium isotopic fractionation between silicate fluids and minerals are negligible at magmatic temperatures (Sharp, 2007); 3) surface-derived ground-waters such as meteoric and connate formation waters, have characteristic $\delta^{18}O$ and δD values, different than the values found in deep-seated igneous rocks, which implies that significant isotopic changes are possible if meteoric water interacts with rocks (Hoefs, 1996); and 4) sedimentary rocks normally have higher $\delta^{18}O$ values than deep-seated igneous rocks (Guilbert and Park, 1986; Sheppard, 1986; Taylor, 1978).

Geothermometry

One of the first applications of oxygen isotope thermometry was in the calculation of the temperature of early oceans from measurements of oxygen isotopes ratios in carbonate minerals (calcite or aragonite) which make up the remains of marine organisms or limestone of known geologic ages (McSween et al., 2003; Misra, 2012). Later, a methodology was established for application to higher-temperature systems based on the distribution of ^{18}O between mineral pairs. Through this methodology, formation temperatures of rock, mineral, and gas systems are determined based on the temperature-

dependent fractionation of the isotopic ratios between two or more cogenetic phases (Sharp, 2007).

The analysis of high temperature rocks, minerals and fluids by means of stable isotopes is possible because: 1) isotopic fractionation factors decrease with increasing temperature, 2) a significant regularity is observed in the relative order of heavy isotope enrichment among coexisting phases, and 3) isotopic fractionation among high-temperature phases is still large when compared to analytical error. These facts, along with the lack of dependence of isotopic fractionation on pressure, makes the use of stable isotopic fractionation in high temperature thermometry possible (O'Neil, 1986; Turi, 1988). Theoretically, temperature can be estimated if minerals of interest record equilibrium conditions for a specific geologic event. The study of any two coexisting phases determines the isotopic fractionation and uniquely specifies the temperature of equilibration. In general, thermometry calculations assume these equilibrium conditions (Criss, 1999; Sharp, 2007).

Measured fractionations of D/H and $^{18}O/^{16}O$ ratios in rock are useful in resolving problems such as distinguishing between high and low temperature alteration assemblages, establishing the pressure and temperature conditions for plutonic and metamorphic rocks, and estimating the temperature of geothermal reservoirs (Clayton and Kieffer, 1991; O'Neil, 1986).

Comprehensive reviews of the mathematical theory and applications of oxygen isotope thermometry can be found in Javoy (1977), Faure and Mensing (2009) and White (2015). Specific examples of the application of equation (12) to some mineral pairs are given in chapter 3 of the present dissertation.

Determining the Source of Hydrothermal Fluids and Water-Rock Ratios

Another application of hydrogen and oxygen isotopes uses D/H and $^{18}O/^{16}O$ values as indicators of the origin and history of the H_2O in hydrothermal fluids (Best and Christiansen, 2001; Sheppard, 1986). Since H_2O is the main component of ore-forming hydrothermal fluids, determining its origin is fundamental to any theory of ore formation. The ultimate source of the H_2O can only be interpreted by analyzing some geochemical information encoded in the water molecules themselves (Criss, 1999; Taylor, 1974). Stable isotope analyses provide such information, because large reservoirs like the ocean and the mantle, as well as meteoric, metamorphic, magmatic, and formation waters have distinct stable isotope signatures that can be used to trace the origin of rocks and fluids. Their isotopic values display regular changes in their deuterium and ^{18}O contents (Sharp, 2007).

Hydrothermal alteration usually involves relatively large amount of fluids from different sources flowing through rocks of different permeability by way of fissures and connected pore space. Stable isotope analysis reveals that fluids involved in wall rock alteration have variable chemical properties. Consequently, interaction of different hydrothermal fluids with the wall rock in different geologic settings, has the potential to produce different types of alteration assemblages (Beane and Bodnar, 1995; Rose and Burt, 1979).

Oxygen isotope ratios of hydrothermally altered rocks can also be useful in investigating the mass of water which has interacted with the rocks (Larson and Zimmerman, 1991; Taylor, 1978). Mass balance of oxygen between a hydrothermal fluid and an altered rock can be used to calculate water/rock ratios if the temperature of

interaction, the initial $\delta^{18}O$ value of the rock, and the initial $\delta^{18}O$ value of the fluid are known (Hoefs, 1996; Taylor, 1978)

For specific explanations about the isotopic properties and distinguishing features of different hydrothermal fluids as well as water/rock ratios in specific geologic settings see chapter 3 of the present dissertation.

References

Beane, R. E., and Bodnar, R. J., 1995, Hydrothermal fluids and hydrothermal alteration in porphyry copper deposits, *in* Pierce, F. W., and Bohom, J. G., eds., Porphyry Copper Deposit of the American Cordillera, Volume 20: Tuczon, Az, Arizona Geological Society, p. 83-93.

Best, M., G, and Christiansen, E. H., 2001, Igneous Petrology, USA, Blackwell Science.

Bindeman, I., 2008, Oxygen isotopes in mantle and crustal magmas as revealed by single crystal analysis: Reviews in Mineralogy and Geochemistry, v. 69, p. 445-478.

Bindeman, I. N., Brooks, C. K., McBirney, A. R., and Taylor, H. P., 2008, The low-δ^{18}O late-stage ferrodiorite magmas in the Skaergaard intrusion: Result of liquid immiscibility, thermal metamorphism, or meteoric water incorporation into magma?: The Journal of Geology, v. 116, p. 571-586.

Bowen, G. J., and Revenaugh, J., 2003, Interpolating the isotopic composition of modern meteoric precipitation: Water Resources Research, v. 39, no. 10, 1299, p. 1-13.

Clayton, R. A., and Kieffer, S. W., 1991, Oxygen isotopic thermometer calibrations: The Geochemical Society, Special Publication, v. 3, p. 3-10.

Criss, R. E., 1999, Principles of Stable Isotope Distribution, New York, Oxford Univesity Press.

Faure, G., 1998, Principles and Applications of Geochemistry, USA, Prentice Hall.

Faure, G., and Mensing, T. M., 2009, Isotopes, Principles and Applications, India, Wiley.

Fetter, C. W., 2001, Applied Hydrogeology, USA, Prentice- Hall.

Guilbert, J. M., and Park, C. F., 1986, The Geology of Ore Deposits, USA, W. H. Freeman and Company.

Hoefs, J., 1996, Stable Isotope Geochemistry, Germany, Springer.

Javoy, M., 1977, Stable isotopes and geothermometry: Journal of the Geological Society, v. 133, no. 6, p. 609-636.

Larson, P. B., and Zimmerman, B. S., 1991, Variations in $\delta^{18}O$ values, water/rock ratios, and water flux in the Rico paleothermal anomaly, Colorado: The Geochemical Society, Special Publication, v. 3, p. 463-469.

McSween, H. Y., Richardson, S. M., and Uhle, M. E., 2003, Geochemistry Pathways and Preocesses, USA, Columbia University Press.

Misra, K., C, 2012, Introduction to Geochemistry: Principles and Applications, Malaysia, Wiley-Blackwell.

Mysen, B., 2014, Water-melt interaction in hydrous magmatic systems at high temperature and pressure: Progress in Earth and Planetary Science, v. 1, no. 1, p. 1-18.

O'Neil, J. R., 1986, Theoretical and experimental aspects of isotopic fractionation: Reviews in Mineralogy v. 16, p. 1-40.

Rollinson, H. R., 1993, Using Geochemical Data: Evaluation, Presentation, Interpretation, UK, Pearson Prentice-Hall.

Rose, A. W., and Burt, D. M., 1979, Hydrothermal alteration, *in* Barnes, H. L., ed., Geochemistry of Hydrothermal Ore Deposits: New York, John Wiley & Sons, p. 173-227.

Sharp, Z. D., 2007, Principles of Stable Isotope Geochemistry, USA, Pearson Prentice-Hall.

Sheppard, S. M. F., 1986, Characterization and isotopic variations in natural waters, *in* Valley, J. W., Taylor, H. P., and O'Neil, J. R., eds., Reviews in Mineralogy. Stable Isotopes in High Temperature Geological Processes, Volume 16: USA, Mineralogical Society of America p. 165-183.

Taylor, H. P., 1974, The application of oxygen and hydrogen isotope studies to problems of hydrothermal alteration and ore deposition: Economic Geology, v. 69, p. 843-883.

-, 1978, Oxygen and hydrogen isotope studies of plutonic granitic rocks: Earth and Planetary Science Letters, v. 38, no. 1, p. 177-210.

Turi, B., 1988, Stable isotopes in petrology: a brief survey: Rendiconti della Societa Italiana di Mineralogia e Petrologia, v. 43, p. 83-94.

White, W. M., 2015, Isotope Geochemistry, Singapore, Wiley Blackwell.

CHAPTER THREE

PETROLOGIC AND HYDROTHERMAL EVOLUTION OF THE CRETACEOUS LINGA COMPLEX OF THE PERUVIAN COASTAL BATHOLITH, NEAR ICA FROM STABLE ISOTOPES

Abstract

Oxygen and hydrogen isotope values obtained from 64 minerals separated from 18 samples are employed to determine the source of magma and hydrothermal fluids that caused potassic, propylitic, phyllic, and argillic alteration in the Linga complex, situated in the mid-to-late Cretaceous Peruvian Coastal Batholith near Ica. Calculated $\delta^{18}O$ plagioclase values in fresh samples are between +6.7‰ to +7.9‰ at equilibrium with $^{18}O/^{16}O$ crystallization temperatures between 588°C and 654°C. A slight west-east and from older to younger increasing trend in $\delta^{18}O$ values for fresh samples suggests a slightly greater crustal component to the east. Pervasive potassic and propylitic alteration assemblages yielded average values of $\delta^{18}O$ +7‰ and δD –50‰ suggesting the alteration was primarily caused by magmatic fluids. However, other fluids were also involved; for example, high plagioclase (+9.3‰) and hornblende (+6.3‰) $\delta^{18}O$ values from one sample near a pluton contact suggest interaction with metamorphic or low temperature fluids. High epidote δD values from altered diorite (–25.8‰) and monzonite (–36.1‰) suggest sea water infiltration west of the batholith. The average water/rock ratio of 0.1 suggests 1 part of external meteoric or metamorphic fluids to 10 parts rock or magmatic fluids, indicating the significant role of magmatic hydrothermal fluids in the alteration.

Resumen

Valores isotópicos de oxígeno e hidrógeno de 64 minerales separados de 18 muestras se usaron para conocer el origen de los fluidos hidrotermales que causaron alteración potásica, propilítica, fílica y argílica en el complejo Linga situado en el Batolito Costero Peruano del Cretácico medio-superior cerca de Ica. Valores de $\delta^{18}O$, roca fresca, varían de +6,7‰ a +7,9‰. La temperatura $^{18}O/^{16}O$ de cristalización para equilibrio isotópico varía desde 588°C a 654°C. Un leve incremento oeste-este y antiguos-recientes en los valores de $\delta^{18}O$ en muestras frescas sugiere contaminación por la corteza más marcada hacia el este. Asociaciones mineralógicas de alteración potásica y propilítica generaron valores promedio de + 7‰ en $\delta^{18}O$ y -50‰ en δD, sugiriendo alteración por fluidos magmáticos. Sin embargo, otros fluidos también causaron alteración, por ejemplo, altos valores de $\delta^{18}O$, +9.3‰, plagioclasa y +6.3‰, hornblenda, cerca de un contacto plutónico, sugieren interacción con fluidos metamórficos o a baja temperatura. Altos valores de δD, –25.8‰, diorita alterada y –36.1‰, monzonita, sugieren infiltración de agua marina desde el oeste del batolito. El valor promedio de 1/10 en la razón agua/roca indica una parte de agua meteórica o metamórfica por 10 partes de agua magmática, sugiriendo alteración principalmente por agua magmática.

Key Words

Stable isotopes, isotopic equilibrium, hydrothermal alteration, hydrothermal fluids.

Introduction

Earth, with its hydrosphere and active lithosphere and upper mantle, has enormous potential to trigger a variety of interactions between numerous aqueous fluids and rock reservoirs. Oxygen and hydrogen isotopes are especially valuable in understanding these interactions because they can help identify fluid sources and pathways, and estimate fluxes (Brandriss et al., 1995; Sharp, 2007; Taylor, 1978). Stable isotope studies of numerous igneous rock suites have dramatically transformed our perspective on the role of such fluids in the evolution of the crust (Gregory and Criss, 1986).

Magma experiences numerous changes in composition during transport from its source to the site of emplacement or eruption (Rutherford and Devine, 2003; Sykes, 1987). In particular, changes in stable isotopic composition occur as magmas are affected by partial melting (Williams et al., 2009), contamination (Garcia et al., 2008; Harris and Chaumba, 2001; Santo and Peccerillo, 2008), magma mixing (Bindeman, 2008; Johnson et al., 1996), fractional crystallization (DePaolo, 1981; Sparks and Huppert, 1984), degassing (Sparks, 2003), and hydrothermal alteration (Dilles et al., 1992; Harris and Golding, 2002).

Stable isotope studies have shown that subsolidus hydrothermal processes that affect plutons emplaced near Earth's surface are the result of water from different sources that include magmatic (Giachetti et al., 2015; Plank et al., 2013), metamorphic (Barnes, 1970; Yardley and Cleverley, 2013), oceanic (German and Lin, 2004; Humphris, 1976; Rohling, 2013), connate (Husband, 1998), and meteoric waters (Bowen and Revenaugh, 2003; Brandriss et al., 1995; Terzer et al., 2013). All can serve as ore-forming fluids (Guilbert

and Park, 1986; Hedenquist and Lowenstern, 1994; Jebrak, 1997; Robb, 2005). Other components in these solutions, such as dissolved ions and gasses, yield significant additional information about the P-T evolution of the solution, fluid pH and oxidation state (Markl and Baumgartner, 2002; Rose and Burt, 1979; Taylor, 1986). Lithologies with which the fluid has interacted along its flow path influence these variables through alteration reactions (Mysen, 2014; Seyfried et al., 1988).

The origin of hydrothermal fluids at the Linga complex in the northern Arequipa segment of the Cretaceous Peruvian Coastal Batholith near Ica is investigated with stable isotopes from the various alteration facies recorded in these rocks. Specifically, mineral rock $\delta^{18}O$ and δD values from unaltered rocks yield insight into magma sources and how they differ with location, age, composition, and apparent temperature. Style and temperatures of alteration, and the areal extent of alteration are identified in the field and in thin section. Hydrothermal fluid sources and water rock ratios are indicated by $\delta^{18}O$ and δD values from these altered rocks.

Geologic Setting

The Peruvian Coastal Batholith

The Andes Cordillera is the largest active subduction-related orogeny on Earth (Schilling et al., 2006; Springer, 1999) and is the product of the subduction of the oceanic Farallon Plate and later the Nazca Plate under the continental crust of the South American Plate since the Cretaceous (Martinod et al., 2010; Pfiffner and Gonzalez, 2013; Polliand et al., 2005).

52

Convergence rates between these two plates increased dramatically during the late Early to Late Cretaceous and shifted to a significant oblique component (Jaillard and Soler, 1996; McQuarrie et al., 2005; Mégard, 1984); this resulted in a trenchward motion of the South American plate, subduction erosion (Jaillard and Soler, 1996; Polliand et al., 2005), significant arc magmatism, and the emergence of volcano-sedimentary basins of the Mesozoic Western Peruvian Trough (Mégard, 1984; Pfiffner and Gonzalez, 2013). The development of the Western Peruvian Trough was followed by the intrusion of magmas that yielded the numerous plutonic suites that comprise the Peruvian Coastal Batholith (PCB), shown in Figure 14, between 100 Ma and 30 Ma ago (Polliand et al., 2005; Soler and Bonhomme, 1990).

The PCB has a geometry and composite nature similar to other circum-Pacific batholiths, but is one of the largest. In addition, the PCB has preserved its integrity unlike the batholiths of western North America which have been partially disarticulated by later tectonic events, obscuring their relationships with the plate margin at the time of emplacement (Atwater, 1970; Schweickert and Cowan, 1975; Winter, 2010).

The abundant intrusions that comprise the Mesozoic-Cenozoic PCB constitute an exceptional example of long-lived plutonism related to a convergent margin. This batholith parallel to the contemporary Peru-Chile trench along its almost 2000 km length displays significant longitudinal differences in magma type and emplacement history and has been divided into five segments. From north to south these segments are termed Piura, Trujillo, Lima, Arequipa and Toquepala (Figure 14). Each segment is characterized by its own particular intrusions, which can be grouped into Super-units and

53
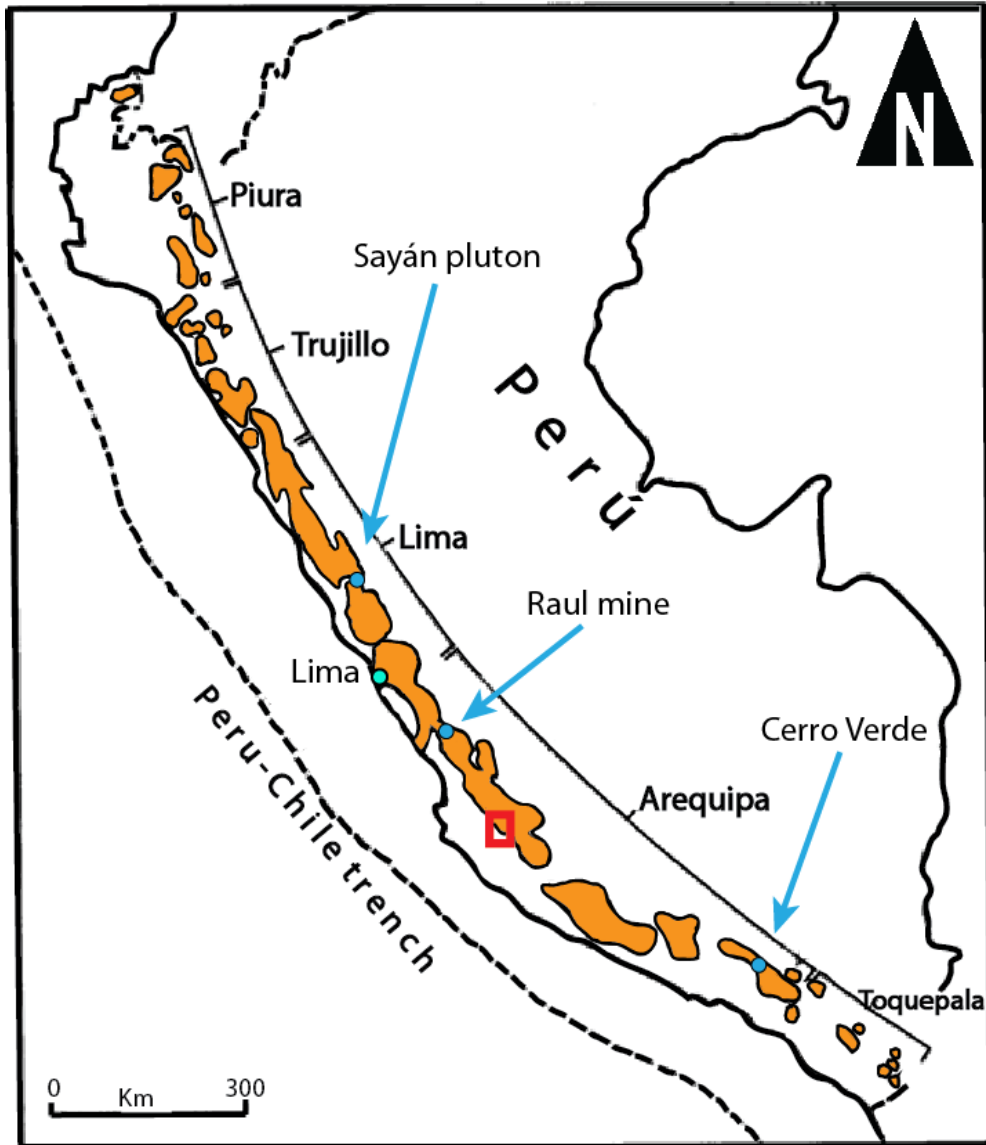
Figure 14. The five segments of the Peruvian Coastal Batholith with location of previous stable isotope studies indicated in blue and the study area in red. Adapted from Moore (1984).

each Super-unit comprises a set of units closely related in space, time, chemistry, and petrology (Cobbing and Pitcher, 1972; Cobbing et al., 1977; Moore, 1984).

The 900 km-long Arequipa segment, the longest of the PCB, extends from Arequipa northward to the Lurín District in the Lima Province. This segment has been broadly mapped, with the most meticulous mapping in the Rio Pisco and Ica area providing the most detailed documentation of emplacement and petrologic processes for the PCB (Agar, 1978; Cobbing et al., 1977).

Brief Description of Super-Units in the Ica-Pisco Section of the Arequipa Segment

There are two major Pre-PCB volcanic-sedimentary units, the Quilmana to the west and the Yura to the east. These units are indicated as Pre-PCB (Figure 15). The Yura group displays a thickness of 2000 m in the Rio Ica up to 600 m of quartzite with interbedded shales north-east in the Rio Pisco (Moore, 1979). The Yura group in the eastern Rio Pisco area also includes volcanics. The age of the Yura group is constrained to be between 216 Ma and 134 Ma (Boekhout et al., 2013). The Quilmana volcanics, whose origin dates back to the emergence of the Western Peruvian Trough (Aguirre and Offler, 1985), are the youngest stratified rocks cut by the PCB and constitute a large part of its western and eastern envelope. The main lithology is metamorphic hornfels and the most abundant alteration minerals are biotite and epidote (Moore, 1979).

Gabbros (Figure 15) that have been interpreted (Mukasa, 1986) to correspond to the Patap gabbros in the Lima segment are minor plutons broadly spread over a large part of the Arequipa segment. In the Rio Pisco area the age of some of these gabbroic plutons is bracketed to be between the middle Albian volcaniclastics of the Quilmana volcanics,
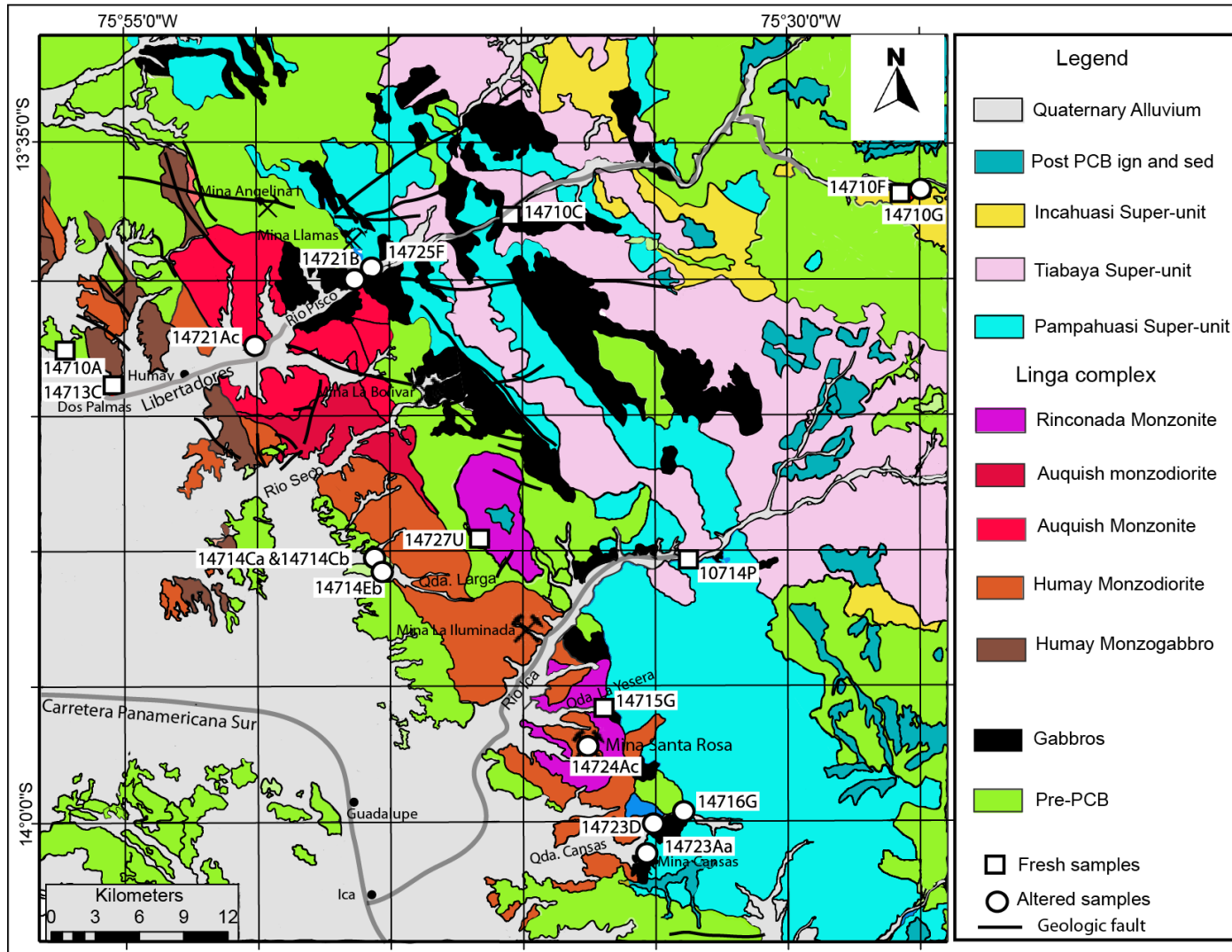
Figure 15. Simplified geologic map of the Ica-Pisco area in the Peruvian Costal Batholith. Sample locations and Super-units are indicated. The map includes the quadrangle 28-i (Guadalupe) and parts of quadrangles 28-m (Santiago de Chocorvos), 29-m (Cordova) and 29-i (Ica). Adapted from Instituto Geológico, Minero y Metalúrgico del Perú (INGEMMET, 1978).

which they intrude, and the 101.4 Ma concordant zircon crystallization ages of the oldest

granitoids that cut the gabbros. Therefore, the gabbros are probably of Albian age, i.e.

101-105 Ma (Mukasa and Tilton, 1985).

The Linga complex (Figure 15), the focus of this paper, is at the western margin

of the PCB. This unit ranges from monzogabbro to monzogranite in composition. In the

monzogabbro and monzodiorites, cumulose textures are well preserved whereas

granophyric textures, which suggests rapid cooling at shallow depths, prevail in the

monzogranitic units (Agar, 1981; Mukasa, 1986). This consanguineous suite of intrusive

rocks originated from magmatic differentiation of a single parent magma (Agar, 1978)

and is divided into three units : the Humay, Auquish and Rinconada (Agar, 1981).

The 101 Ma (Mukasa and Tilton, 1985) Humay unit (Figure 15) is the most mafic

unit and is comprised of quartz-monzodiorite, quartz-monzogabbro and monzogabbro.

Mafics are present as small clots and subhedral prisms of hornblende as well as small

flecks of biotite. This elongate unit is exposed along the western edge of the Linga

complex and follows the Andean trend.

The 104 Ma (Martinez, 2016) Auquish unit (Figure 15) is mostly porphyritic

monzogranites and quartz-monzodiorite. Mineralogy consists of hornblende, orthoclase

and quartz as well as varying proportions of accessory minerals. This unit is located

northeast of the Humay and has a geometry like a ring complex.

The 98 Ma (Martinez, 2016) Rinconada unit (Figure 15) is mostly monzogranite,

characterized by grey-pink feldspar, pale plagioclase and quartz as well as small prisms

of hornblende and sparse biotite. This unit outcrops in the southern part of the Linga

complex and has an elliptical spatial distribution (Agar and Le Bel, 1985; Moore, 1979).

Large elongate and steep-walled plutons of the 94 Ma (Mukasa and Tilton, 1985) Pampahuasi Super-unit (Figure 15) in the Arequipa segment are characterized by diorite-tonalite with well-developed mineral fabrics and localized shear banding (Moore, 1979; Mukasa, 1986). Plagioclase is coarse-grained and euhedral, and hornblende is present with poikilitic biotite.

The 83 Ma (Mukasa and Tilton, 1985) Incahuasi Super-unit (Figure 15) is characterized by pervasive poikilitic hornblende and biotite in a framework of euhedral plagioclase. Its main lithology goes from quartz-diorite to monzogranite (Agar, 1978).

The 78 Ma (Mukasa and Tilton, 1985) Tiabaya Super-unit (Figure 15) is distinguished by hornblende and biotite occurring as euhedral grains and plagioclase appearing as crystals of up to 1 cm long. Lithology is made up of tonalite, granodiorite and quartz monzonite. This unit occurs extensively throughout the Arequipa segment (Agar, 1978).

Previous Stable Isotopes Studies in the PCB

Few stable isotope data exist for the PCB. Beckinsale et al. (1985) report whole rock $\delta^{18}O$ values between +6.3‰ and +8.6‰ (n=11) in fresh samples from the Sayán pluton (Figure 14) 150 km north of Lima in the Lima segment. These data are interpreted to be the product of fractional crystallization (Taylor, 1978).

More data exist for portions of the PCB that have been affected by hydrothermal systems related to mineralization. Phengite δD values between $-67‰ < \delta D < -47‰$, and calcite $\delta^{18}O$ values between +15‰ and +30‰ (Le Bel, 1985) suggest a magmatic origin for alteration fluids at the Cerro Verde porphyry Cu deposit near Arequipa (Figure 14), but

high calcite $\delta^{18}O$ values at high structural levels suggest the involvement of meteoric hydrothermal fluids at low temperature ($<100°$).

Another study at the Raul mine, a complex metamorphosed stratabound vein-rich sulphur deposit (De Haller et al., 2006; Ripley and Ohmoto, 1979) 150 km south of Lima (Figure 14), revealed amphibole δD values between $-21‰$ and $-60‰$ (n = 15), whole rock $\delta^{18}O$ values from $+7.8‰$ to $+10.8‰$ (n = 11) and vein calcite $\delta^{18}O$ values of $+14.0‰$ to $+14.2‰$ (n = 2). These data suggest the involvement of seawater modified by evaporation and or shale membrane processes during mineralization (Ripley and Ohmoto, 1979).

Hydrothermal Alteration in the Linga Complex

Three types of alteration are common in the units of the Linga complex, potassic, sericitic and propylitic. The alteration patterns are frequently organized concentrically in areas surrounding the intrusion with the potassic alteration in the center and the propylitic alteration toward the outermost part of the pluton (Agar, 1981). Potassic alteration (Figure 16a) results from potassium enrichment. It is particularly abundant and significant in porphyry and epithermal mineralizing systems where it occurs in the high temperature core zones. Potassium silicate alteration is the result of the replacement of plagioclase and mafic silicate minerals with K-feldspar and secondary biotite/sericite (Figure 17a) at temperatures of 450 to 600°C (Pirajno, 2009). This type of alteration can occur before complete crystallization of magma. (Damian, 2003; Rose and Burt, 1979)

Propylitic alteration (Figure 16b) is characterized by the addition of H_2O and CO_2 with no substantial acidic metasomatism. It becomes more pervasive close to the

Figure 16. a) Outcrop at the Pampahuasi-Humay boundary with abundant K-feldspar, biotite and magnetite indicating potassic alteration probably at temperatures of 450 to 600°C. b) Outcrop at the Pampahuasi-Humay boundary with widespread epidote indicating propylitic alteration probably at temperatures of 250 to 350°C. Both outcrops are in the Rio Cansas transect. This information is part of preliminary results from field work observations first addressed in chapter 1.

heat-hydrothermal source of a hydrothermal deposit (Pirajno, 2009) and normally forms at 250°C to 350°C (Dilles et al., 1992; Hedenquist et al., 2000). Characteristic mineral assemblages of propylitic alteration are albite, chlorite, epidote, carbonates, sericite, pyrite and magnetite (Figure 17b), mostly replacing plagioclase (Rose and Burt, 1979).

Phyllic alteration is common in granitic intrusions related to porphyry copper and other vein-alteration ore deposits (Que and Allen, 1996). Both potassium feldspar and plagioclase are converted to sericite and minor amounts of clay minerals (Figure 17c; (Rose and Burt, 1979). Sericitization in the phyllic facies generally occurs between 200° and 350°C (Hedenquist et al., 2000; Meunier and Velde, 2004)

Argillic alteration (Figure 17d) results from the total conversion of feldspar and amphiboles to low temperature minerals (<200°C) (Meunier and Velde, 2004) dickite, kaolinite, and montmorillonite, along with sericite and other clay minerals. This style of alteration is related to leaching of calcium, sodium and magnesium by acidic fluids (Pirajno, 2009; Rose and Burt, 1979).

Analytical Techniques

Most samples were collected along south to west to north to east trending rivers that cut the Linga complex in the Ica-Pisco area. Transects include the Rio Ica, Quebrada Larga, and Rio Pisco (Figure 15) with a focus on contact zones between Super-units to identify styles of hydrothermal alteration. Published geologic maps of the Guadalupe and Ica quadrangles (INGEMMET, 1978) guided these efforts. Rock samples selected for isotopic analysis are representative of the Super-unit in this part of the PCB.
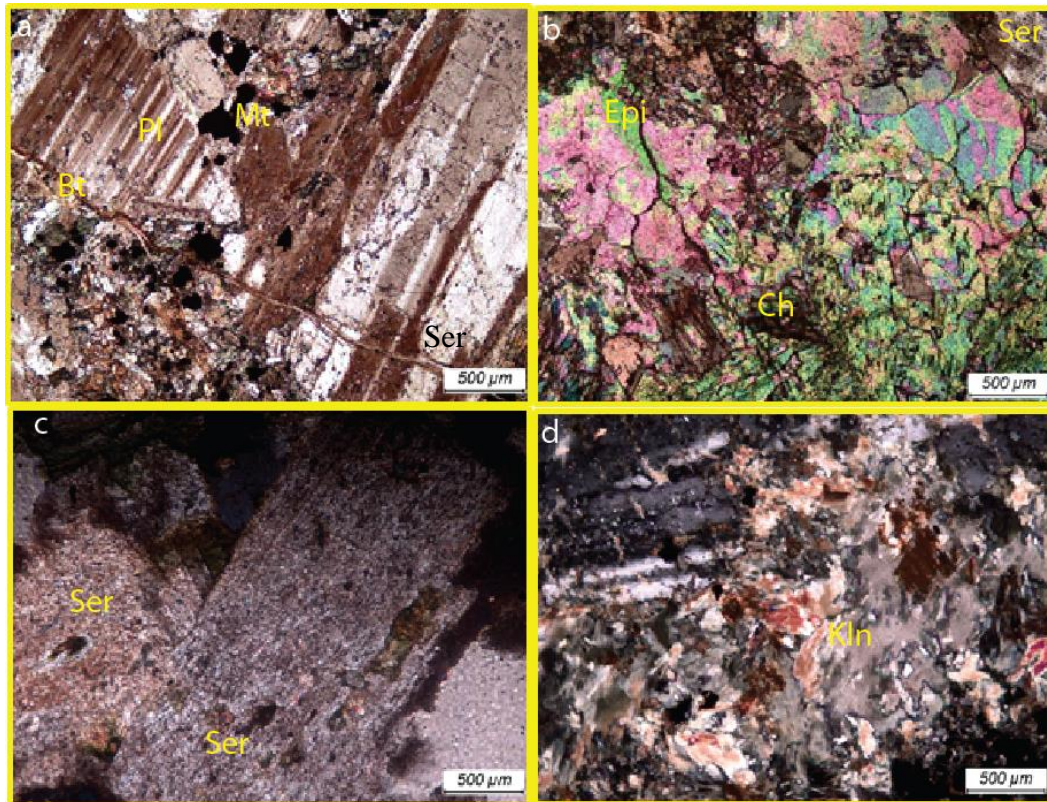
Figure 17. Thin sections (all cross-polars) of four types of alteration mentioned in the text and observed in the Linga complex. a) Potassic alteration in sample 14714Ca from the border between Humay and the volcanics in the Quebrada Larga transect. Note the secondary biotite (Bt) veinlets cutting plagioclase (Pl) crystals and the groundmass and magnetite (Mt). b) Propylitic alteration in sample 14723D from the border between Humay and Pampahuasi. Note the abundance of epidote (Epi) and chlorite (Ch). c) Phyllic alteration in sample 13828A in the Rio Pisco transect with sericite (Ser) replacing plagioclase (Pl). d) Argillic alteration in sample 14714Cb from the border between Humay and the volcanics in the Quebrada Larga transect with a clay mineral, probably kaolinite (Kln), replacing plagioclase.

Petrographic analysis identified the style of alteration and minerals available for isotope analysis. Minerals were separated from 18 samples by Yu-Neng Mineral Separation Co. Langfang, China.

All stable isotope measurements were performed using the ThermoFinnigan DeltaPlusXP mass spectrometer at the Institute for Integrated Research in Materials, Environments and Societies at California State University, Long Beach. Oxygen was extracted from silicate minerals using a modified version of the laser fluorination method (Sharp, 1990). Oxygen isotope values are reported relative to V-SMOW, where NBS-28 has $\delta^{18}O = +9.6‰$ on this scale. Replicate analyses of Caltech rose quartz working standard ($\delta^{18}O = +8.45‰$) have an analytical error of $\pm0.2‰$. Hydrogen was liberated from biotite, amphibole and epidote using the carbon reduction technique described by Sharp et al. (2001). Hydrogen isotope data are reported relative to V-SMOW. Multiple analyses of NBS-30 biotite standard ($\delta D = -65.7‰$) indicate an analytical error of $\pm2.0‰$. Water content of minerals analyzed for hydrogen isotopes was determined by comparing the area under the gas chromatograph peak for mass 2 to a calibration of area versus sample size for NBS-30 biotite (3.5‰ H_2O). Quality control and reproducibility is shown by duplicate measurements on 20% of samples analyzed for oxygen isotopes and all samples analyzed for hydrogen isotopes.

Results

Table 1 shows 48 $\delta^{18}O$ values and 16 δD values acquired from 18 samples from the Ica-Pisco section of the PCB. Seven samples are fresh and 11 are altered. Table 1 also

Table 1. Oxygen and hydrogen isotope values in units of per mil for fresh and altered samples, represented by a (*). Blue color means estimated values with the estimation based on the $\delta^{18}O$ values of other minerals in the same mineralization assemblage (Bottinga and Javoy, 1975). Biotite (Bt), hornblende (Hbl), epidote (Epi), actinolite (Act), magnetite (Mt), plagioclase (Pl), K-feldspar (Kfs), quartz (Qtz).

Unit	Sample	δD values				$\delta^{18}O$ values							
		Bt	Hbl	Epi	Act	Mt	Epi	Act	Bt	Hbl	Pl	Kfs	Qtz
Incahuasi													
	14710F	-78.2	-74.9						3.9	6.2	7.5	8.2	9.1
Tiabaya													
	10714P	-80.8	-76.4						5.5	5.9	7.9	8.2	9.8
Pampahuasi													
	14723Aa*									8.4			8.9
	14725F*		-89.2							3.6	*6.9*		8.9
	14715G	-74.5	-73.7						5.4	5.5	7.2		9.1
	14723D*			-25.6	-78.6		3.5	4.2			*6.8*		
	14716G*		-83.7							6.3	9.3		
Linga-Rinconada													
	14727U	-80.6	-86.7			1.5			4.6	5.8	7.5	7.4	9.2
	14724Ac*	-73.8							3.3		5.7		7.3
Linga-Auquish													
	14721Ac*					0.5					*5.5*	5.6	5.5
	14721B*			-36.1			3.2				*7.1*		
Linga-Humay													
	14714Eb*										8.2	8.5	8.2
	14714Ca*										7.6	7.6	
	14713C					1.6					6.7		
Gabbro													
	14710C		-63.9							5.7	7.4		
Quilmana (Pre-PCB)											7.4		
	14714Cb*												
	14710A										7.6		
Yura Group (Pre-PCB)													
	14710G*	-86.5							0.1		2.6		

shows four estimated $\delta^{18}O$ values for plagioclase. Sample locations are indicated in Figure 15.

Unaltered Intrusive Rocks

Quartz (+9.1 to +9.8‰, n = 4), K-feldspar (+7.4 to +8.2‰, n = 3), plagioclase (+6.7 to +7.9‰, n = 7), hornblende (+5.5 to +6.2‰, n = 5), biotite (+3.9 to 5.5‰, n = 4) $\delta^{18}O$ values (Table 1) from unaltered rocks that belong to each of the Super-units are consistent with a continental magmatic arc origin (Taylor and Sheppard, 1986). Likewise, biotite (−80.8 to −74.5‰, n = 4) and hornblende (−86.7 to −63.9‰, n = 5) δD values are primary magmatic values.

Primary Magma Sources

Plagioclase $\delta^{18}O$ values from unaltered rocks increase from approximately +7‰ to +8‰ in a west-to-east direction (Figure 18). The same data is displayed in Figure 19 by decreasing age from approximately +7‰ at 130 Ma to +8‰ at 70 Ma. These increasing values indicate the incorporation of more crustal material from west to east and with time. Since the $\delta^{18}O$ scale is so small error bars of ±0.2‰ are included.

The west-east increase (+6.7 to +7.9‰) is smaller than that for the Peninsular Ranges Batholith whole rock $\delta^{18}O$ values (+6‰ to +12‰; Silver et al., 1979). Contaminated mantle melts display a rise in $\delta^{18}O$ values in correlation with increasing SiO_2 (Hoefs, 1996). The trend of $\delta^{18}O$ in the Peninsular Ranges Batholith indicates a
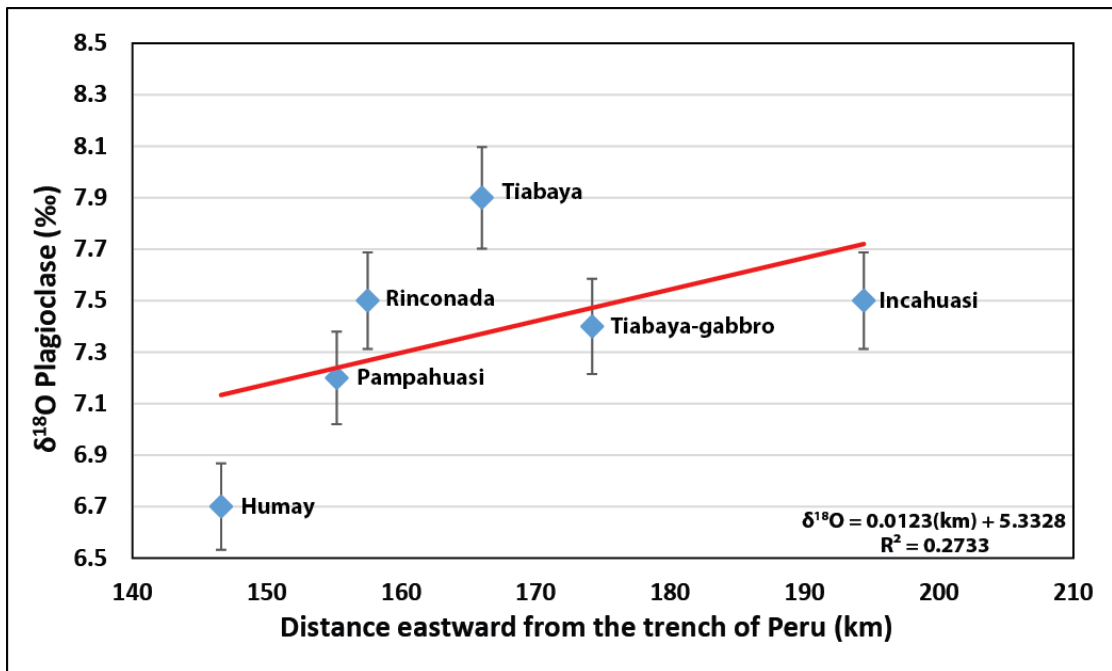
Figure 18. Values of $\delta^{18}O$ for fresh samples ordered from west to east. Note the slight increasing trend resembling that in the Peninsular Ranges Batholith of California (Clausen et al., 2014; Schmidt and Paterson, 2002; Silver et al., 1979). The error bars are $\pm0.2‰$. Errors come from the CSULB isotope laboratory.
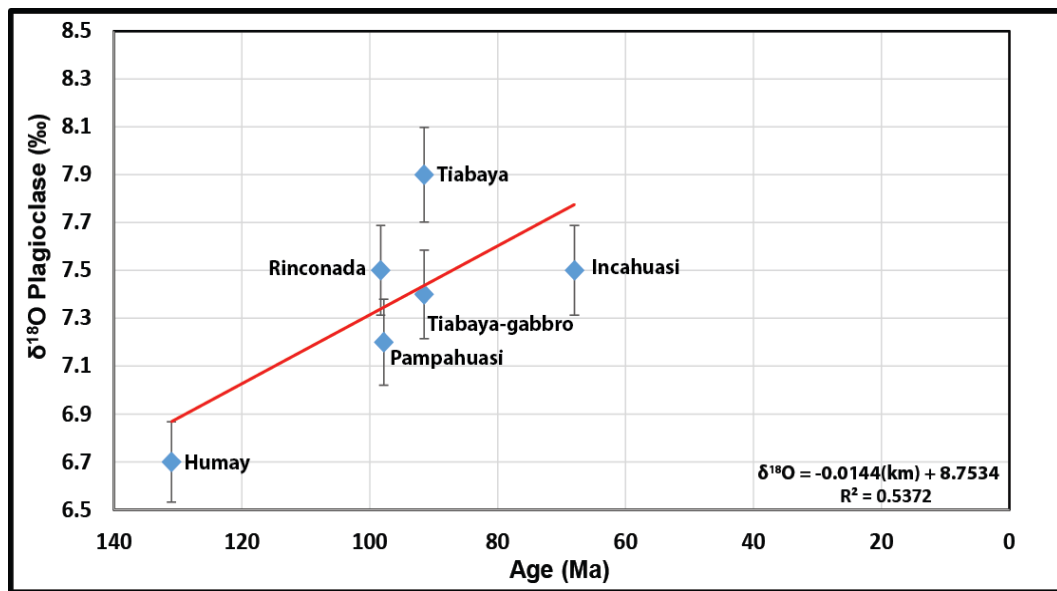
Figure 19. Values of $\delta^{18}O$ for fresh samples ordered from older to younger. Note the slight increasing trend as the rocks become younger, which corresponds to the west-to-east trend in Figure 18. The error bars are ± 0.2‰. Errors come from the CSULB isotope laboratory.

mantle magma source in the west contaminated by an ^{18}O source increasing eastward. In contrast, our data indicate only slight degrees of contamination of primary magma from a mantle source for the PCB in the Ica-Rio Pisco area. This is consistent with the restricted range of depleted mantle initial $^{87}Sr/^{86}Sr$ values (0.7036-0.7043) observed at this northernmost part of the Arequipa segment with slight increases of Sr_i toward the east and with increasing SiO_2.

To the south, magmas related to the Arequipa segment intruded Precambrian cratonal rocks of the Arequipa massif, as well as Pre-PCB volcanic and sedimentary units. Increased contamination of crustal material is reflected by a much larger range of initial $^{87}Sr/^{86}Sr$ ratios 0.7036 and 0.7084 (Beckinsale et al., 1985) and a slightly higher $\delta^{18}O$ value of +9‰ (Le Bel, 1985) from a pluton related to the Cerro Verde porphyry Cu deposit. In comparison, this range of Sr_i values are similar to those from the Peninsular Ranges Batholith (0.703 to 0.709; (Langenheim et al., 2004; Silver et al., 1979), another batholith displaying an eastward increasing crustal component as magmatism shifted in that direction due to shallowing subduction. This trend is not as pronounced in the Peruvian batholith.

A Test of $^{18}O/^{16}O$ Equilibrium and Geothermometry for Unaltered Rocks

Closure temperatures can be estimated by measurements of oxygen isotopic fractionations among coexisting minerals of igneous rocks (Bottinga and Javoy, 1975; Faure and Mensing, 2009).

The temperature dependence of the isotopic fractionation factors of oxygen and oxide minerals are given by equations (Bottinga and Javoy, 1975) with the form

$$10^3 \ln \alpha_b^a = A + \frac{B \times 10^3}{T^2} \qquad (19)$$

where α is the isotopic fractionation factor between two coexisting minerals a and b, T is the temperature in Kelvins, and A and B are experimentally determined constants. Equation (19) is linear at temperatures >300°C (Sharp, 2007) when plotted with $10^6/T^2$ as the x-axis and can be expressed as

$$\delta_a - \delta_b = \Delta_b^a = 10^3 \ln \alpha_b^a = A + \frac{B \times 10^3}{T^2} \qquad (20)$$

where $\delta_a - \delta_b = \Delta_b^a$ applies at temperatures >300°C (Gregory et al., 1989). By designating quartz as mineral a the B coefficient (Table 2) for each other mineral (b) is used to calculate equilibrium temperatures. If a and b are non-hydrous minerals then $A = 0$. However, if the minerals contain hydroxyl groups, particularly amphibole and biotite, then the A values are -0.30 and -0.60 respectively (Javoy, 1977). The importance of equation (20) is that knowing the differences $\delta_a - \delta_b$ between various pairs of minerals, it is possible to determine the equilibrium temperature of coexisting minerals (Bindeman, 2008; Javoy et al., 1970; Turi, 1988).

The resulting equilibrium temperature is equal to or less than the temperature of crystallization since the minerals may have continued exchanging oxygen isotopes while the rock was cooling after crystallization (Giletti and Hess, 1988). The oxygen-isotope temperature is valid under the assumption that minerals are in equilibrium when isotope exchange ceased and that the mineral assemblage was not disturbed by interaction with sub-solidus external aqueous fluids (Faure and Mensing, 2009; Guilbert and Park, 1986).

Oxygen isotopic equilibrium can be tested graphically using the "isotherm method" of (Javoy et al., 1970) that uses the experimentally and theoretically determined

Table 2. Values for the B coefficient in equation (20), according to Bottinga and Javoy (1975) considering quartz as the standard. b = mole fraction of anorthite in the feldspar. Blue color means an estimated value for epidote (Park and Ripley, 1999). Since quartz is the standard its value is set to zero in the third column.

Mineral	(Bottinga and Javoy, 1975) $B_{mineral}$	$B_{mineral}$-B_{quartz}
Quartz	−1.594	0
Feldspar	1.04(b − 0.6)	
If…		
anorthite = 0%	1.04(0 − 0.6)	0.97
anorthite = 35%	1.04(0.35-0.6)	1.33[1]
anorthite = 50%	1.04(0.5-0.6)	1.49
anorthite = 100%	1.04(1-0.6)	2.01
Amphibole	1.554	3.15
Actinolite	1.754	3.348
Biotite	2.096	3.69
Epidote		5
Magnetite	3.976	5.57

[1] Plagioclase value used in calculations

A and B parameters of equation (20). According to this method, individual minerals from a rock that are in isotopic equilibrium fall on a straight line that crosses the zero-zero point (representing quartz), and whose slope $10^6/T^2$, yields apparent equilibrium temperature. Most unaltered samples display isotopic equilibrium at temperatures that range between 588° and 654°C (Figure 20). The highest equilibrium temperature was for the Incahuasi granodiorite (654^{0}C) and not for the more mafic Pampahuasi diorite (639°C), a rock that produced only three minerals for this analysis.

This "isotherm method" yields better results if the number of mineral $\delta\,^{18}$O values is maximized and cover as large a range of δ^{18}O values as possible, such as covering the range between quartz and magnetite (Holk et al., 2016).

Altered Samples

Disequilibrium quartz (+8.9‰), K-feldspar (+5.6 to +8.5‰, n = 3), plagioclase (+2.6 to +9.3, n = 11), hornblende (+3.6 to +6.3‰, n = 2), biotite (+0.1 to +3.3‰, n = 2), actinolite (+4.2‰), epidote (+3.2 to 3.5‰, n = 2), and magnetite (+0.5‰) δ^{18}O values (Table 1) from altered samples suggest interaction with external fluids. Biotite (–86.5 to –73.8‰, n = 2), hornblende (–89.2 to –83.7‰, n = 2), actinolite (–78.6‰), and epidote (–36.1 to –25.6‰, n = 2) δD values also suggest a complex fluid history for these rocks.

Identification of Fluid Sources Using Isotope Data Based on Altered Samples

Stable isotopes values from altered samples can be used to determine the source of the hydrothermal fluids causing alteration. Possible alteration fluids include
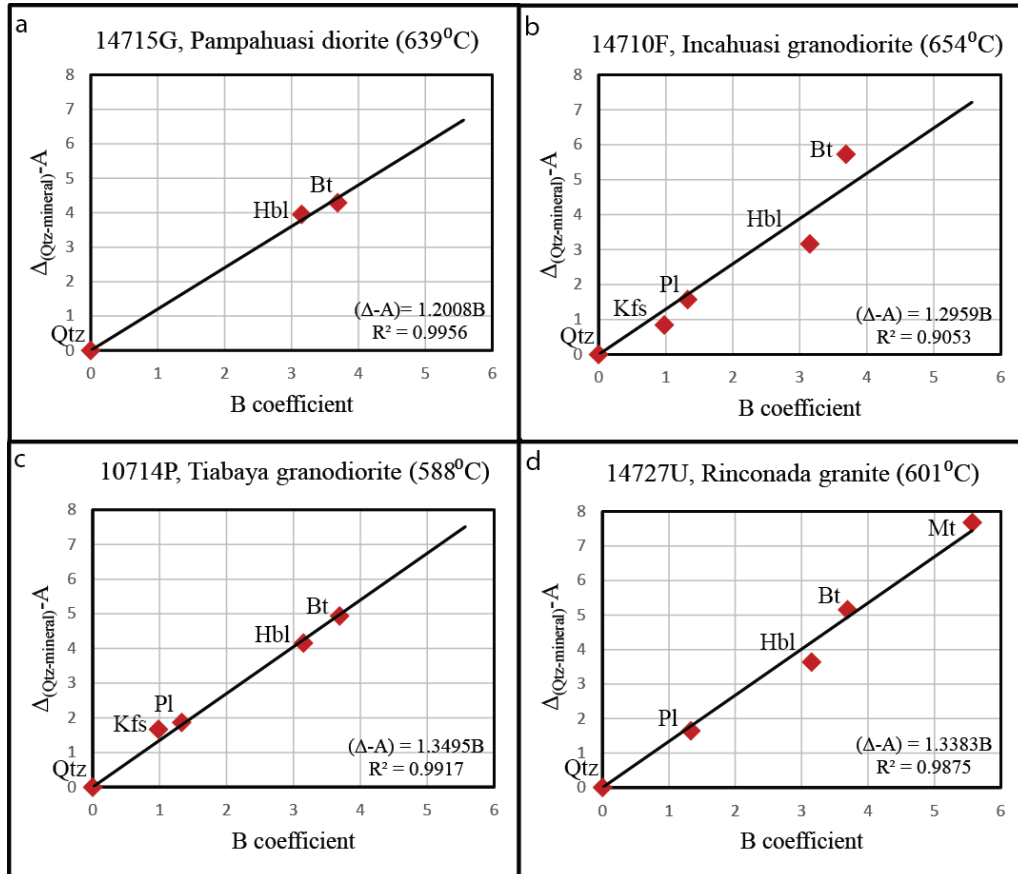
Figure 20. Thermometry plots for four fresh samples from the Linga complex. Values of R^2 greater than 0.9 suggest isotopic equilibrium between minerals. Temperatures were obtained using equation (20) in the text. Quartz (Qtz), K-feldspar (Kfs), plagioclase (Pl), hornblende (Hbl), biotite (Bt), magnetite (Mt).

seawater ($\delta^{18}O \sim 0‰$, $\delta D \sim 0‰$, Faure, 1998; Rollinson, 1993), magmatic water

($\delta^{18}O \sim +6$ to $+10‰$, $\delta D \sim -80$ to $-40‰$, Sheppard, 1986), metamorphic waters

($\delta^{18}O \sim +3$ to $+25‰$, $\delta D \sim -65$ to $-20‰$, Guilbert and Park, 1986; Rollinson, 1993), and

meteoric hydrothermal water (low and variable $\delta^{18}O$ and δD values).

Isotopic values of meteoric water are governed by the Global Meteoric Water

Line (GMWL) equation (Faure and Mensing, 2009; Yeh et al., 2014) whose

mathematical expression is equation (21). The values of δD and $\delta^{18}O$ displayed by

meteoric water are a function of geographic location, becoming increasingly lighter going

from the equator to the poles and from coastal to inland areas (Bowen and Revenaugh,

2003; Ohmoto, 1986; Sharp, 2007).

$$\delta D = 8\delta^{18}O + 10 \tag{21}$$

Meteoric water in the Ica-Pisco section of the PCB has an average $\delta^{18}O$ value of

approximately $-5‰$ (Bowen and Revenaugh, 2003). Thus, according to equation (3), δD

is $-30‰$. However, the interaction of this low $\delta^{18}O$ meteoric water with plutonic

intrusions in subduction environments causes an increase in water temperature (Ohmoto,

1996; Pirajno, 2009; Sharp, 2007; Taylor, 1979; Turi, 1988), which brings about a

depletion of ^{18}O in both the pluton and the country rock and a corresponding ^{18}O

enrichment or "^{18}O shift" in the meteoric water. This process causes plutonic rock to

achieve very low and even negatives values for $\delta^{18}O$ (Criss and Taylor, 1986; Taylor,

1978; Turi, 1988).

A graphical summary of waters mentioned above is illustrated in Figure 21,

displaying their isotopic composition and their relationship with the Ica area meteoric

Water, the GMWL, and the SMOW as stated by Rollinson (1993).
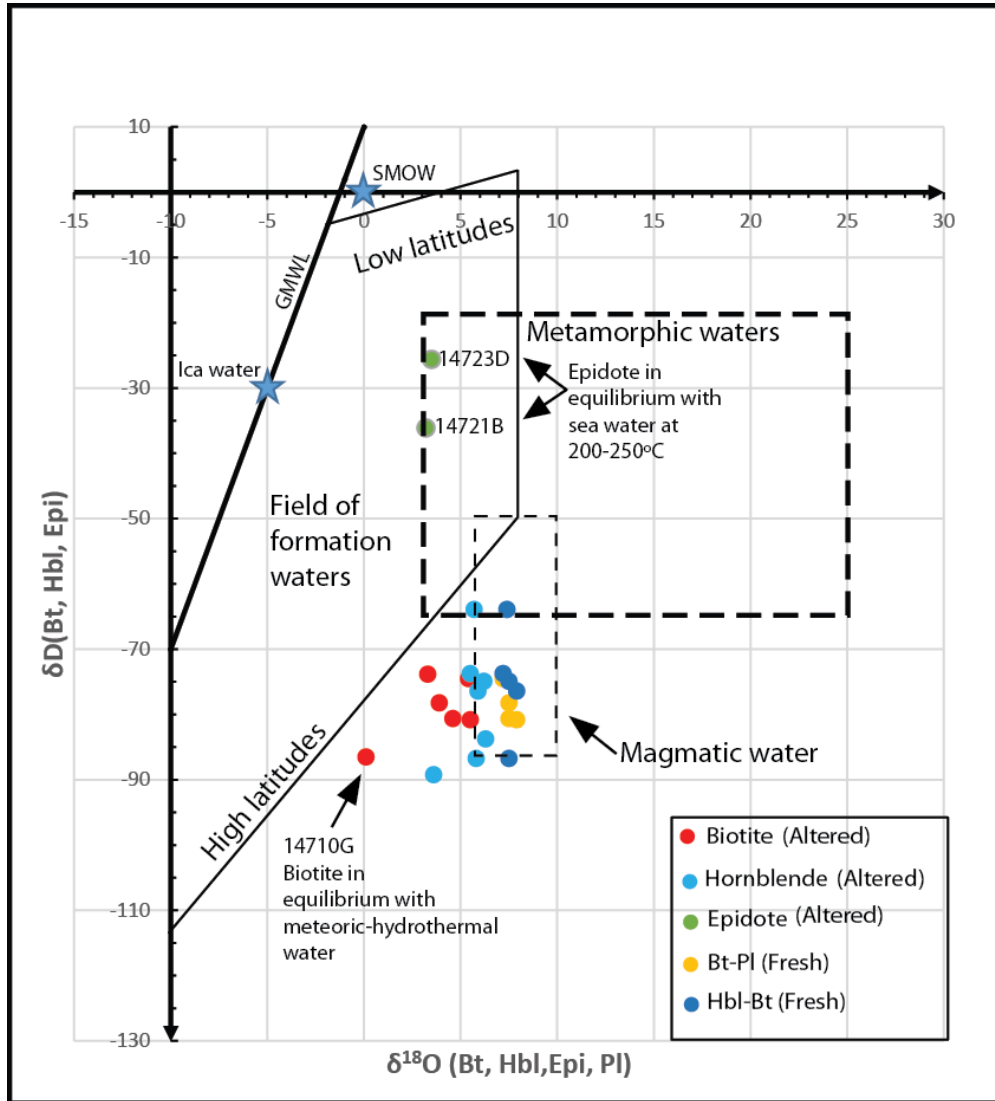
Figure 21. Location of δD and δ¹⁸O values of biotite (Bt), hornblende (Hbl), plagioclase (Pl) and Epidote (Epi), for fresh and altered samples and their values with respect to different water sources (Rollinson, 1993).

Water/Rock Ratio and Intensity of Fluid-Rock Interaction

When epizonal igneous intrusions interact with meteoric water, these igneous intrusions work as gigantic "heat engines" that produce the energy necessary to support a long- lasting convective circulation system of any mobile H_2O in the country rocks surrounding the igneous body. This interaction changes the $\delta^{18}O$ and δD values of both water and rock (Taylor, 1974). Nevertheless, unaltered igneous rocks have a definite range of isotopic values (Bindeman, 2008; Rollinson, 1993; Sharp, 2007) that can be used for comparison to determine the effects of any processes that considerably alter their $\delta^{18}O$ values (Taylor, 1974).

Oxygen isotope ratios of hydrothermally altered igneous rocks are useful data for determining the amount of water which has interacted with the rock (Larson and Zimmerman, 1991; Taylor, 1977). A first estimate of the amount of water involved in a closed meteoric hydrothermal system can be determined by the material balance equation (Gregory et al., 1989; Taylor, 1974).

$$W\delta^i_{H_2O} + R\delta^i_{rock} = W\delta^f_{H_2O} + R\delta^f_{rock} \tag{22}$$

where i =initial value, f =final value after reaction, W =atom percent of meteoric water oxygen in the whole system and $R =$ atom percent of rock oxygen in the total system. The water/rock ratio can be calculated rearranging equation (22) to the form

$$\frac{W}{R} = \frac{\delta^f_{rock} - \delta^i_{rock}}{W\delta^i_{H_2O} - (\delta^i_{rock} - \Delta)} \tag{23}$$

where $\Delta = \delta^f_{rock} - \delta^f_{H_2O}$

Values of $\delta^{18}O$ for fresh and altered samples are compared in Table 3, where equation (23) was used to estimate the water/rock ratio involved in the alteration.

Table 3. $\delta^{18}O$ values for plagioclase in altered samples with respect to fresh samples, displaying direction and magnitude of the alteration, probable fluid involved, and water/rock ratio calculated using equation (23) in the text.

Unit	Sample	$\delta^{18}O$ (‰)	W/R	Type of fluid
Pampahuasi	14716G	7.2 •──────→ 9.3	0.2	Metamorphic
Pampahuasi	14723D	6.8 ←• 7.2	0.05	Meteoric-magmatic
Pampahuasi	14725F	6.9 ←• 7.2	0.04	Meteoric-magmatic
Pampahuasi	14723Aa	7.2 •──→ 8.4	0.1	Metamorphic
Rinconada	14724Ac	5.7 ←──────• 7.5	0.3	Meteoric?
Auquish	14721B	7.1 ←• 7.5	0.05	Meteoric-magmatic
Auquish	14721Ac	5.5 ←──────• 7.5	0.3	Meteoric?
Humay	14714Ca	6.7 •──→ 7.6	0.08	Metamorphic
Humay	14714Eb	6.7 •────→ 8.2	0.1	Metamorphic
Quilmana	14714Cb	7.4 ←• 7.6	0.03	Meteoric-magmatic
Yura Group	14710G	2.6 ←──────────• 7.5	1.6	Meteoric

Equation (23) was also used to determine the magnitude of change undergone by the $\delta^{18}O$ values of fresh samples during the alteration process as well as the type of fluid that probably caused the alteration.

Discussion

To better understand the discussion below, it is important to remember that $\delta^{18}O$ values of coexisting minerals in isotopically normal granitic (fresh) rocks, increase in the following order: magnetite-biotite-amphibole-muscovite-plagioclase-K-feldspar-quartz (Taylor, 1978), and they show a general increase in $\delta^{18}O$ values with increasing wt % Si. The relative values with respect to quartz for the minerals mentioned above, as suggested by Bottinga and Javoy (1975) are summarized in Table 2. Park and Ripley (1999) suggest the estimated value of 5 for epidote in Table 2.

Classification of Fresh Samples Based on Their $\delta^{18}O$ Values

Based on their whole rock $\delta^{18}O$ values, plutonic rocks can be classified into three types (Taylor, 1978): a) low $\delta^{18}O$ granitic rocks with $\delta^{18}O < +6‰$, b) normal $\delta^{18}O$ granitic rocks with $+6‰ < \delta^{18}O < +10‰$, and c) high $\delta^{18}O$ granitic rocks with $\delta^{18}O > +10‰$. Since plagioclase is the most abundant mineral in igneous rocks, isotopic $\delta^{18}O$ values of plagioclase are the closest values to the $\delta^{18}O$ whole rock value. The normal range of hydrogen isotope values for granitic rocks is $-85‰ < \delta D < -50‰$ (Taylor, 1978).

Considering the plagioclase $\delta^{18}O$ isotopic value as a good representative of the whole rock $\delta^{18}O$ isotopic value, it is clear from Table 1 that all $\delta^{18}O$ values for fresh samples are in the normal range of $+6‰$ to $+10‰$ (Taylor, 1978). Table 1 also shows that

the variation in $\delta^{18}O$ values for different minerals in fresh samples is in general as expected from Taylor (1974), i.e. increasing from magnetite to quartz. These facts suggest that the minerals were in isotopic equilibrium at the time of crystallization, and unaffected by later alteration events. A plot of biotite and hornblende δD values vs plagioclase $\delta^{18}O$ values (Figure 21) shows that most of these samples lie within the rectangular area labeled as the primary magmatic zone of Taylor (1974).

$\delta^{18}O$ Values of Altered Samples

Hydrothermal alteration is an intricate process involving mineralogical, chemical and textural changes caused by the interaction of hydrothermal fluids with the rocks through which they circulate, under changing physico-chemical conditions (Pirajno, 2009; Rose and Burt, 1979).

The circulation of hydrothermal fluids is greatly accelerated by faults whose occurrence enhances permeability (Fetter, 2001). Joints and faults provide conduits that allow hydrothermal fluids to quickly migrate until they cool and precipitate their mineral content or react with and replace dissolvable country rocks, a process able to produce a variety of alteration types (Guilbert and Park, 1986). In accordance with the previous statements, Agar (1981) mentions that hydrothermal alteration observed in the Ica-Pisco section is associated with the circulation of hydrothermal fluids along faults. Figure 22 shows some of the faults in the Ica-Pisco section as well as the area affected by different types of alteration.

Table 1 shows the δD and $\delta^{18}O$ values for the 11 altered samples. Note that 5 out of 7 $\delta^{18}O$ plagioclase values from altered samples belong to the normal range proposed
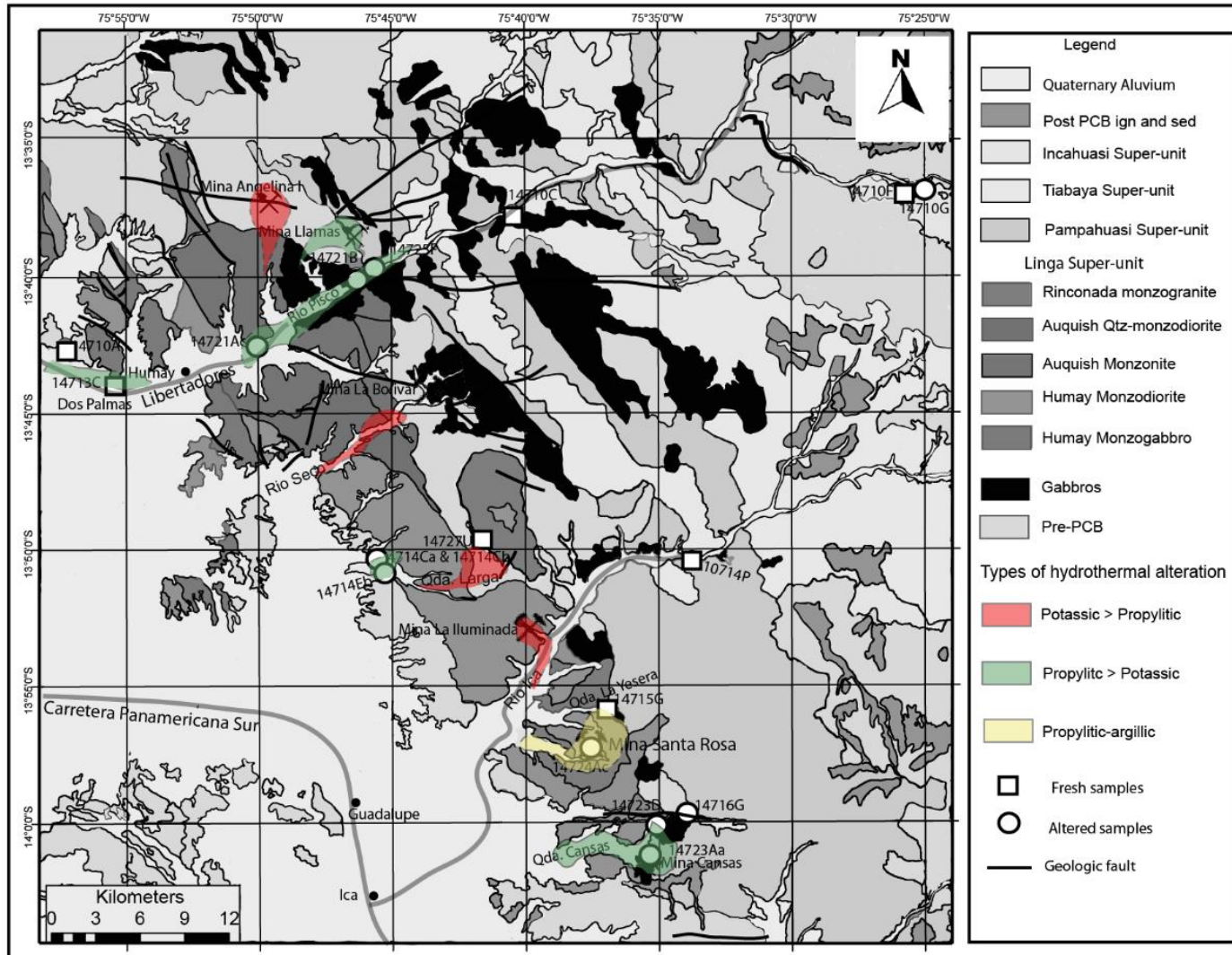
Figure 22. Approximate areal extent of the different types of hydrothermal alteration observed in the Linga complex. Quadrangles 28-i (Guadalupe) and parts of quadrangles 20-m (Santiago de Chocorvos), 29-m (Cordova) and 29-i (Ica). Adapted from Instituto Geológico, Minero y Metalúrgico del Perú (INGEMMET, 1978). This information is based on field observations and on the records in my field book.

by Taylor (1978). This suggests that the alteration of most samples was caused by hydrothermal fluid of magmatic origin (Sharp, 2007; Sheppard, 1986).

Altered samples whose plagioclase $\delta^{18}O$ show values below those in equilibrium with magmatic fluids are from the Yura volcanics (14710G, $\delta^{18}O$ = +2.6‰) and a sample near copper mineralization (14724Ac, $\delta^{18}O$ = +5.7‰). These $\delta^{18}O$ values are probably due to $^{18}O/^{16}O$ exchange with heated meteoric-hydrothermal water (Sharp, 2007; Taylor, 1978).

According to Table 3, the lowest water/rock ratio involved in the change of $\delta^{18}O$ values is 0.03. This value belongs to the Quilmana volcanics sample 14714Cb whose variation is from +7.6‰ to +7.4‰. Since this is a decrease from the original value, the change may just be due to margin error in measurement (a 3% percent error introduces error bars of ±0.2‰ in the calculations), but could also be caused by a very small contribution of meteoric water. However, the decrease from +7.6‰ to +7.4‰ still remains in the interval of magmatic fluids, which suggests that the main interaction was with magmatic hydrothermal fluids.

The biggest increase in $\delta^{18}O$ values from +7.2‰ to +9.3‰ belongs to sample 14716G from the metamorphic aureole where the Pampahuasi intrudes the Quilmana volcanics in the Rio Cansas transect. The water/rock ratio of 0.2 in Table 3 suggests that the increase may have resulted from the interaction of 1 part external metamorphic fluids with 5 parts rock or magmatic fluids. And in fact that the $\delta^{18}O$ value for this altered sample remains in the range of magmatic hydrothermal fluids.

The biggest decrease in $\delta^{18}O$ values in Table 3 is from +7.5‰ to +2.6‰ and belongs to the sample from the Yura group 14710G. The direction of the isotopic change

as well as the high water/rock ratio of 1.6 suggest that large amounts of meteoric fluids may have been involved in the alteration. The dominance of meteoric hydrothermal fluids interacting with this sample is supported by the low $\delta^{18}O$ value of biotite +0.1‰.

δD for Fresh and Altered Samples

Hydrothermal fluids are a major source of various components of hydrothermal ore deposits formed in volcanic arcs. These components, including metals and their ligands, become concentrated in magmas in various ways from various sources, including subducted oceanic crust and leaching of rocks (Hedenquist and Lowenstern, 1994). Thus, the fact that most of the samples in Table 1, either fresh or altered, have δD values in the normal isotopic range for plutonic rocks, i.e. −85‰ < δD < −50‰, can be explained by noting that most primary magmatic water may have originated from OH^--bearing minerals (clays, micas, amphiboles) of subducted sediments and altered volcanic rocks that have been introduced into the lower crust or the upper mantle through geologic time. These subducted materials are directly melted or dehydrated at high temperatures in the upper mantle, and the resulting hydrothermal fluid is incorporated into the calc-alkaline magmas produced in subduction-zone environments, like those producing the Linga complex of the PCB (Burnham, 1979; Hoefs, 1996; Stakes, 1991; Taylor, 1979; Wilson, 1989). Nevertheless, the high δD −25.6‰ epidote value of sample 14723D, and −36‰ for sample 14721B, do not fit in the normal interval for δD values of Taylor (1974). These values could be the result of interaction between the rock and seawater probably coming from the western side of the batholith.

Conclusions

The present study examined the stable isotopic composition δD and $\delta^{18}O$ for 18 igneous samples, 7 fresh and 11 with alteration. The data indicate that fresh rock of the Linga complex were mainly in isotopic equilibrium with magma. The approximate interval of closure temperature at which isotopic exchange ceased in fresh samples was from about 590°C to 650°C. There is a slight increase in $\delta^{18}O$ for fresh samples from west to east, suggesting the magmatic source has a slightly greater crustal component to the east. The same increase is observed from older to younger samples, which matches the younging trend toward the east.

Field observations suggest that potassic alteration at approximately 450-600°C is more abundant at the center of the Linga complex, while propylitic alteration at approximately 250-350°C is more abundant at the south-east and north-west extremes of the Linga complex. Phyllic alteration, around 200-350°C and argillic alteration around 100-200°C, although present, are not as abundant as potassic and propylitic.

The main source of hydrothermal fluids in the Linga complex was magmatic, which is in agreement with the findings of some of the studies referred to earlier in the text. However, meteoric fluids, metamorphic fluids and seawater were also involved to a small degree in the interaction with the rocks. The water/rock ratio of approximately 1/10 suggests 1 part external meteoric or metamorphic hydrothermal fluids to 10 parts rock or magmatic fluids.

Acknowledgments

References

Agar, R. A., 1978, The Peruvian Coastal Batholith: Its Monzonitic Rocks and their
 Related Mineralization [Doctor of Philosophy]: University of Liverpool, 293 p.

-, 1981, Copper mineralization and magmatic hydrothermal brines in the Rio Pisco
 section of the Peruvian Coastal Batholith: Economic Geology, v. 76, p. 677-693.

Agar, R. A., and Le Bel, L., 1985, The Linga Super-unit: High-K diorites of the Arequipa
 segment, *in* W.S. Pitcher, M. P. Atherton, Cobbing, E. J., and Beckinsale, R. D.,
 eds., Magmatism at a Plate Edge: The Peruvian Andes: New York, John Wiley
 and Sons., p. 119-127.

Aguirre, L., and Offler, R., 1985, Burial metamorphism in the Western Peruvian Trough:
 its relation to Andean magmatism and tectonics, *in* W.S. Pitcher, M. P. Atherton,
 Cobbing, E. J., and Beckinsale, R. D., eds., Magmatism at a plate edge: The
 Peruvian Andes: New York, John Wiley and Sons, p. 59-71.

Atwater, T., 1970, Implications of plate tectonics for the Cenozoic tectonic evolution of
 western North America: GSA Bulletin, v. 81, no. 12, p. 3513-3536.

Barnes, I., 1970, Metamorphic waters from the Pacific Tectonic Belt of the West Coast of
 the United States: Science, v. 168, no. 3934, p. 973-975.

Beckinsale, R. D., Sanchez-Fernandez, A. W., Brook, M., Cobbing, E. J., Taylor, W. P.,
 and Moore, N. D., 1985, Rb-Sr whole rock isochron and K-Ar age determinations
 for the Coastal Batholith of Peru, *in* W.S. Pitcher, M. P. Atherton, Cobbing, E. J.,
 and Beckinsale, R. D., eds., Magmatism at a plate edge: The Peruvian Andes:
 New York, John Wiley and Sons, p. 177-202.

Bindeman, I., 2008, Oxygen isotopes in mantle and crustal magmas as revealed by single

    crystal analysis: Reviews in Mineralogy and Geochemistry, v. 69, p. 445-478.

Boekhout, F., Sempere, T., Spikings, R., and Schaltegger, U., 2013, Late Paleozoic to

    Jurassic chronostratigraphy of coastal southern Peru: Temporal evolution of

    sedimentation along an active margin: Journal of South American Earth Sciences,

    v. 47, p. 179-200.

Bottinga, Y., and Javoy, M., 1975, Oxygen isotope partitioning among the minerals in

    igneous and metamorphic rocks: Reviews of Geophysics and Space Physics, v.

    13, no. 2, p. 401-418.

Bowen, G. J., and Revenaugh, J., 2003, Interpolating the isotopic composition of modern

    meteoric precipitation: Water Resources Research, v. 39, no. 10, 1299, p. 1-13.

Brandriss, M. E., Nevle, R. J., Bird, D. K., and O'Neil, J. R., 1995, Imprint of meteoric

    water on the stable isotope compositions of igneous and secondary minerals, Kap

    Edvard Holm Complex, East Greenland: Contributions to Mineralogy and

    Petrology, v. 12, no. 1, p. 74-86.

Burnham, C. W., 1979, Magmas and hydrothermal fluids, *in* Barnes, H. L., ed.,

    Geochemistry of Hydrothermal Ore Deposits: New York, John Wiley & Sons, p.

    71-136.

Clausen, B. L., Morton, D. M., Kistler, R. W., and Lee, C. A., 2014, Low-initial-Sr felsic

    plutons of the northwestern Peninsular Ranges batholith, southern California, and

    the role of mafic-felsic magma mixing in continental crust formation, *in* Morton,

    D. M., and Miller, F. K., eds., Peninsular Ranges Batholith, Baja California and

    Southern California: GSA Memoir 211, p. 317-344.

Cobbing, E. J., and Pitcher, W. S., 1972, The Coastal Batholith of Central Peru: Geological Society of London Journal, v. 128, no. 5, p. 421-460.

Cobbing, E. J., Pitcher, W. S., and Taylor, W. P., 1977, Segments and Super-units in the Coastal Batholith of Peru: Journal of Geology, v. 85, no. 5, p. 625-631.

Criss, R. E., and Taylor, H. P., 1986, Meteoric hydrothermal systems: Reviews in Mineralogy and Geochemistry, v. 16, no. 1, p. 373-424.

Damian, F., 2003, The mineralogical characteristics and the zoning of the hydrothermal types alteration from nistru ore deposit, Baia Mare metallogenetic district: Geologia, v. XLVIII, no. I, p. 101-112.

De Haller, A., Corfu, F., Urs, L. F., Barra, F., Chiaradia, M., Frank, M., and Julio, Z., 2006, Geology, geochronology, and Hf and Pb isotope data of the Raúl-Condestable iron oxide-copper-gold deposit, Central Coast of Peru: Economic Geology, v. 101, no. 2, p. 281-310.

DePaolo, D. J., 1981, Trace element and isotopic effects of combined wallrock assimilation and fractional crystallization: Earth and Planetary Science Letters, v. 53, p. 189-202.

Dilles, J. H., Solomon, G. C., Taylor, H. P., and Einaudi, M. T., 1992, Oxygen and hydrogen isotope characteristics of hydrothermal alteration at the Ann-Mason Porphyry Copper Deposit, Yerington, Nevada: Economic Geology, v. 87, p. 44-63.

Faure, G., 1998, Principles and Applications of Geochemistry, USA, Prentice Hall.

Faure, G., and Mensing, T. M., 2009, Isotopes, Principles and Applications, Delhi, Wiley India Pvt. Ltd.

Fetter, C. W., 2001, Applied Hydrogeology, USA, Prentice- Hall.

Garcia, M. O., Ito, E., and Eiler, A. M., 2008, Oxygen isotope evidence for chemical interaction of Kilauea historical magmas with basement rocks: Journal of Petrology, v. 49, no. 4, p. 757-769.

German, C. R., and Lin, J., 2004, The thermal structure of the oceanic crust, ridge-spreading and hydrothermal circulation: How well do we understand their inter-connections?, *in* German, C. R., Lin, J., and Parson, L. M., eds., Mid-Ocean Ridges, Volume 148, p. 1-18.

Giachetti, T., Gonnermann, H. M., Gardner, J. E., Shea, T., and Gouldstone, A., 2015, Discriminating secondary from magmatic water in rhyolitic matrix-glass of volcanic pyroclasts using thermogravimetric analysis: Geochimica et Cosmochimica Acta, v. 148, p. 457-476.

Giletti, B. J., and Hess, K. C., 1988, Oxygen diffusion in magnetite: Earth and Planetary Science Letters, v. 89, no. 1, p. 115-122.

Gregory, R. T., and Criss, R. E., 1986, Isotopic exchange in open and closed systems *in* Valley, J. W., Taylor H P, J., and O'Neil, J. R., eds., Reviews in Mineralogy, Volume 16: USA, p. 91-127.

Gregory, R. T., Criss, R. E., and Taylor, H. P., 1989, Oxygen isotope exchange kinetics of mineral pairs in closed and open systems: applications to problems of hydrothermal alteration of igneous rocks and Precambrian iron formations: Chemical Geology, v. 75, no. 1-2, p. 1-42.

Guilbert, J. M., and Park, C. F., 1986, The Geology of Ore Deposits, USA, W. H. Freeman and Company.

Harris, A. C., and Golding, S. D., 2002, New evidence of magmatic-fluid–related phyllic

    alteration: Implications for the genesis of porphyry Cu deposits: Geology, v. 30,

    no. 4, p. 335-338.

Harris, C., and Chaumba, J., 2001, Crustal contamination and fluid-rock interaction

    during the formation of the Platreef, northern limb of the Bushveld complex,

    South Africa: Journal of Petrology, v. 42, no. 7, p. 1321-1347.

Hedenquist, J. W., Arribas, A., and Gonzalez, E., 2000, Exploration for epithermal gold

    deposits: SEG reviews, v. 13, p. 245-277.

Hedenquist, J. W., and Lowenstern, J. B., 1994, The role of magmas in the formation of

    ore deposits: Nature, v. 370, p. 519-527.

Hoefs, J., 1996, Stable Isotope Geochemistry, Germany, Springer.

Holk, G. J., Grove, M., Jacobson, C. E., and Haxel, G. B., 2016, A two-stage fluid history

    for the Orocopia Schist and associated rocks related to flat subduction and

    exhumation, southeastern California: International Geology Review, v. 59, no. 5-

    6, p. 639-663.

Humphris, S. E., 1976, The Hydrothermal Alteration of Oceanic Basalts by Seawater

    [Doctor of Philosophy: Massachusetts Institute of Technology, 248 p.

Husband, M. E., 1998, Modeling the Mobilization of Connate Water while Injecting

    Water to Displace Oil [Doctor of Philosophy]: Texas Tech University, 202 p.

INGEMMET, 1978, Quadrangle 28-i (Guadalupe), and parts of quadrangles 28-m

    (Santiago de Chocorvos) , 29-m (Cordova), and 29-i (Ica): Perú, Sector energía y

    minas del Perú.

Jaillard, E., and Soler, P., 1996, Cretaceous to early Paleogene tectonic evolution of the
northern Central Andes (0-18ºS) and its relations to geodynamics:
Tectonophysics, v. 259, p. 41-53.

Javoy, M., 1977, Stable isotopes and geothermometry: Journal of the Geological Society,
v. 133, no. 6, p. 609-636.

Javoy, M., Fourcade, S., and Allegre, C. J., 1970, Graphical method for examination of
$^{18}O/^{16}O$ fractionations in silicate rocks: Earth and Planetary Science Letters, v. 10,
p. 12-16.

Jebrak, M., 1997, Hydrothennal breccias in vein-type ore deposits: A review of
mechanisms, morphology and size distribution: Ore Geology Reviews, v. 12, p.
111-134.

Johnson, K. E., Harmon, R. S., Richardson, J. M., Moorbath, S., and Strong, D. F., 1996,
Isotope and trace element geochemistry of Augustine Volcano, Alaska:
Implications for magmatic evolution: Journal of Petrology, v. 37, no. 1, p. 95-115.

Langenheim, V. E., Jachens, R. E., Morton, D. M., Kistler, R. W., and Matti, J. C., 2004,
Geophysical and isotopic mapping of preexisting crustal structures that influenced
the location and development of the San Jacinto fault zone, southern California:
GSA Bulletin, v. 116, no. 9-10, p. 1143-1157.

Larson, P. B., and Zimmerman, B. S., 1991, Variations in $\delta^{18}O$ values, water/rock ratios,
and water flux in the Rico paleothermal anomaly, Colorado: The Geochemical
Society, Special Publication, v. 3, p. 463-469.

Le Bel, L. M., 1985, Mineralization in the Arequipa segment: The porphyry-Cu deposit
of Cerro Verde/Santa Rosa, *in* W.S. Pitcher, M. P. Atherton, Cobbing, E. J., and

Beckinsale, R. D., eds., Magmatism at a plate edge: The Peruvian Andes: New York, John Wiley and Sons, p. 250-260.

Markl, G., and Baumgartner, L., 2002, pH changes in peralkaline late-magmatic fluids: Contributions to Mineralogy and Petrology, v. 144, no. 3, p. 331-346.

Martinez, A. M., 2016, Compositional Diversity in Arcs: A Record of Magmatic Processes in the Peru Coastal Batholith, Ica. [Doctor of Philosophy]: Loma Linda University, 410 p.

Martinod, J., Husson, L., Roperch, P., Guillaume, B., and Espurt, N., 2010, Horizontal subduction zones, convergence velocity and the building of the Andes: Earth and Planetary Science Letters, v. 299, p. 299-309.

McQuarrie, N., Horton, B., K, Zandt, G., Beck, S., and DeCelles, P., G., 2005, Lithospheric evolution of the Andean fold-thrust belt, Bolivia, and the origin of the central Andean plateau: Tectonophysics v. 399, p. 15-37.

Mégard, F., 1984, The Andean orogenic period and its major structures in central and northern Peru: Journal of the Geological Society, v. 141, no. 5, p. 893-900.

Meunier, A., and Velde, B., 2004, Illite: Origins, Evolution and Metamorphism, Germany, Springer.

Moore, N. D., 1979, The Geology and Geochronology of the Arequipa Segment of the Coastal Batholith of Peru [Doctor in Philosophy]: Liverpool, 549 p.

-, 1984, Potassium-argon ages from the Arequipa segment of the Coastal Batholith of Peru and their correlation with regional tectonic events: Journal of the Geological Society, v. 141, no. 3, p. 511-519.

Mukasa, S. B., 1986, Zircon U-Pb ages of Super-units in the Coastal Batholith, Peru: Implications for magmatic and tectonic processes: GSA Bulletin, v. 97, p. 241-254.

Mukasa, S. B., and Tilton, G. R., 1985, Zircon U-Pb ages of Super-units in the Coastal Batholith of Peru, *in* W.S. Pitcher., M. P. Atherton., E. J. Cobbing., and Beckinsale, R. D., eds., Magmatism at a plate edge: The Peruvian Andes: New York, John Wiley and Sons., p. 203-207.

Mysen, B., 2014, Water-melt interaction in hydrous magmatic systems at high temperature and pressure: Progress in Earth and Planetary Science, v. 1, no. 1, p. 1-18.

Ohmoto, H., 1986, Stable isotope geochemistry of ore deposits: Reviews in Mineralogy and Geochemistry, v. 16, no. 1, p. 491-559.

-, 1996, Formation of volcanogenic massive sulfide deposits: The Kuroko perspective: Ore Geology Reviews, v. 10, p. 135-177.

Park, Y.-R., and Ripley, E. M., 1999, Hydrothermal flow systems in the Midcontinent Rift: Oxygen and hydrogen isotopic studies of the North Shore Volcanic Group and related hypabyssal sills, Minnesota: Geochimica et Cosmochimica Acta, v. 63, no. 11-12, p. 1787-1804.

Pfiffner, O. A., and Gonzalez, L., 2013, Mesozoic–Cenozoic evolution of the western margin of South America: Case study of the Peruvian Andes: Geosciences, v. 3, p. 262-310.

Pirajno, F., 2009, Hydrothermal Processes and Mineral Systems, Australia, Springer.

Plank , T., Kelley , K. A., Zimmer , M. M., Hauri , E. H., and Wallace, P. J., 2013, Why do mafic arc magmas contain ~4 wt% water on average?: Earth and Planetary Science Letters, v. 364, p. 168-179.

Polliand, M., Schaltegger, U., Frank, M., and Fontbote, L., 2005, Formation of intra-arc volcanosedimentary basins in the western flank of the central Peruvian Andes during Late Cretaceous oblique subduction: field evidence and constraints from U-Pb ages and Hf isotopes: International Journal of Earth Sciences, v. 94, no. 2, p. 231-242.

Que, M., and Allen, A. R., 1996, Sericitization of plagioclase in the Rosses Granite Complex, Co. Donegal, Ireland Mineralogical Magazine, v. 60, p. 927-936.

Ripley, E. M., and Ohmoto, H., 1979, Oxygen and hydrogen isotopic studies of ore deposition and metamorphism at the Raul mine, Peru: Geochimica and Cosmochimica Acta, v. 43, p. 1633-1643.

Robb, L., 2005, Introduction to ore-forming processes, Victoria, Australia, Blackwell Science Ltd.

Rohling, E. J., 2013, Oxygen isotope composition of seawater, *in* Elias, S. A., ed., The Encyclopedia of Quaternary Science, Volume 2: Amsterdan, Elsevier, p. 915-922.

Rollinson, H. R., 1993, Using Geochemical Data: Evaluation, Presentation, Interpretation, UK, Pearson Prentice-Hall.

Rose, A. W., and Burt, D. M., 1979, Hydrothermal alteration, *in* Barnes, H. L., ed., Geochemistry of Hydrothermal Ore Deposits: New York, John Wiley & Sons, p. 173-227.

Rutherford, M. J., and Devine, J. D., 2003, Magmatic conditions and magma ascent as indicated by hornblende phase equilibria and reactions in the 1995-2002 Soufriere Hills magma: Journal of Petrology, v. 44, no. 8, p. 1433-1454.

Santo, A. P., and Peccerillo, A., 2008, Oxygen isotopic variations in the clinopyroxene from the Filicudi volcanic rocks (Aeolian Islands, Italy): Implications for open-system magma evolution: The Open Mineralogy Journal, v. 2, p. 22-33.

Schilling, F. R., Trumbull, R. B., Brasse, H., Haberland, C., Asch, G., Bruhn, D., Mai, K., Haak, V., Giese, P., Muñoz, M., Ramelow, J., Rietbrock, A., Ricaldi, E., and Vietor, T., 2006, Partial melting in the Central Andean crust: A review of geophysical, petrophysical, and petrologic evidence, *in* Oncken, O., Chong, G., Franz, G., Giese, P., Götze, H. J., Ramos, V. A., Strecker, M. R., and Wigger, P., eds., The Andes: Berlin, Springer, p. 459-474.

Schmidt, K. L., and Paterson, S. R., 2002, A doubly vergent fan structure in the Peninsular Ranges batholith: Transpression or local complex flow around a continental margin buttress?: Tectonics, v. 21, no. 5, p. 1-19.

Schweickert, R. A., and Cowan, D. S., 1975, Early Mesozoic tectonic evolution of the western Sierra Nevada, California: GSA Bulletin, v. 86, no. 10, p. 1329-1336.

Seyfried, W. E., Berndt, M. E., and Seewald, J. S., 1988, Hydrothermal alteration processes at mid-ocean ridges: Constraints from diabase alteration experiments hot-spring fluids and composition of the oceanic crust: Canadian Mineralogist, v. 26, p. 787-804.

Sharp, Z. D., 1990, A laser-based microanalytical method for the in situ determination of oxygen isotope ratios of silicates and oxides: Geochimica et Cosmochimica Acta, v. 54, p. 1353-1357.

-, 2007, Principles of Stable Isotope Geochemistry, USA, Pearson Prentice-Hall.

Sharp, Z. D., Atudorei, V., and Durakiewicz, T., 2001, A rapid method for determination of hydrogen and oxygen isotope ratios from water and hydrous minerals: Chemical Geology, v. 178, p. 197-210.

Sheppard, S. M. F., 1986, Characterization and isotopic variations in natural waters, *in* Valley, J. W., Taylor, H. P., and O'Neil, J. R., eds., Reviews in Mineralogy. Stable Isotopes in High Temperature Geological Processes, Volume 16: USA, Mineralogical Society of America p. 165-183.

Silver, L. T., Taylor, H. P., and Chappell, B., 1979, Some petrological, geochemical and geochronological observations in the Peninsular Ranges batholith near the international border of the USA and Mexico, *in* Abbott, P. L., and Todd, B. R., eds., Mesozoic Crystalline Rocks: San Diego State University, Department of Geological Sciences, p. 83-110.

Soler, P., and Bonhomme, M. G., 1990, Relation of magmatic activìty to plate dynamics ìn central Peru from Late Cretaceous to present: GSA Special Paper, v. 241, p. 173-192.

Sparks, R. S. J., 2003, Dynamics of magma degassing: Geological Society, London, Special Publications, v. 213, p. 5-22.

Sparks, R. S. J., and Huppert, H. E., 1984, Density changes during the fractional

  crystallization of basaltic magmas: fluid dynamic implications: Contributions to

  Mineralogy and Petrology, v. 85, p. 300-309.

Springer, M., 1999, Interpretation of heat-flow density in the Central Andes:

  Tectonophysics, v. 306, no. 3,4, p. 377-395.

Stakes, D. S., 1991, Oxygen and hydrogen isotope compositions of oceanic plutonic

  rocks: High-temperature deformation and metamorphism of oceanic layer 3: The

  Geochemical Society, v. 3, p. 77-90.

Sykes, M. L., 1987, Evolution of granitic magmas during ascent: A phase equilibrium

  model: The Geochemical Society, Special Publication, v. 1, p. 447-462.

Taylor, B. E., 1986, Magmatic volatiles: Isotopic variation on C, H, and S *in* Valley, J.

  W., Taylor H P, J., and O'Neil, J. R., eds., Stable Isotopes in High Temperature

  Geological Processes: USA, Mineralogical Society of America.

Taylor, H. P., 1974, The application of oxygen and hydrogen isotope studies to problems

  of hydrothermal alteration and ore deposition: Economic Geology, v. 69, p. 843-

  883.

-, 1977, Water/rock interactions and the origin of H_2O in granitic batholiths: Thirtieth

  William Smith lecture: Journal of the Geological Society, v. 133, no. 6, p. 509-

  558.

-, 1978, Oxygen and hydrogen isotope studies of plutonic granitic rocks: Earth and

  Planetary Science Letters, v. 38, no. 1, p. 177-210.

-, 1979, Oxygen and hydrogen isotope relationships in hydrothermal mineral deposits *in* Barnes, H. L., ed., Geochemistry of Hydrothermal Ore Deposits: New York, John Wiley & Sons, p. 236-277.

Taylor, H. P., and Sheppard, S. M. F., 1986, Igneous rocks: I. Processes of isotopic fractionation and isotope systematics, *in* Valley, J. W., Taylor, H. P., and O'Neil, J. R., eds., Reviews in Mineralogy. Stable Isotopes in High Temperature Geological Processes, Volume 16: USA, Mineralogical Society of America, p. 227-271.

Terzer, S., Wassenaar, L. I., Araguás, A. L. J., and Aggarwal, P. K., 2013, Global isoscapes for $\delta^{18}O$ and δ^2H in precipitation: Improved prediction using regionalized climatic regression models: Hydrology and Earth System Sciences, v. 17, p. 4713–4728.

Turi, B., 1988, Stable isotopes in petrology: a brief survey: Rendiconti della Societa Italiana di Mineralogia e Petrologia, v. 43, p. 83-94.

Williams, H. M., Nielsen, S. G., Renac, C., Griffin, W. L., O'Reilly, S. Y., McCammon, C. A., Pearson, N. R., Viljoen, F., Alt, J. C., and Halliday, A. N., 2009, Fractionation of oxygen and iron isotopes by partial melting processes: Implications for the interpretation of stable isotope signatures in mafic rocks: Earth and Planetary Science Letters, v. 283, p. 156-166.

Wilson, M., 1989, Igneous Petrogenesis, The Netherlands, Springer.

Winter, J. D., 2010, Principles of Igneous and Metamorphic Petrology, New Jersey, Prentice Hall.

Yardley, B. W. D., and Cleverley, J. S., 2013, The role of metamorphic fluids in the formation of ore deposits: Geological Society, London, Special Publications, v. 393, p. 1-18.

Yeh, H. F., Lin, H. I., Lee, C. H., Hsu, K. C., and Wu, C. S., 2014, Identifying seasonal groundwater recharge using environmental stable isotopes: Water, v. 6, p. 2849-2861.

CHAPTER FOUR

HEAT FLOW BASICS

This chapter provides a general perspective about heat flow as it applies to modeling the cooling of a batholith, and serves as an extended introduction to chapter five. This chapter describes the different mechanisms, like fluid convection, and variables like geothermal gradient, involved in heat transfer processes that have an impact on the cooling process of the Linga complex. Since the novel aspect in chapter five is modeling heat flow by convection of hydrothermal fluids, this chapter briefly analyzes some computational tools capable of simulating cooling by fluid convection. This chapter also reviews some history of previous efforts to model heat flow by conduction and convection. This provides a context for the use of HYDROTHERM interactive software in chapter five, that uses a mixed approach of cooling by conduction and convection involving hydrothermal fluids.

Introduction

The ability to do work is called potential energy which can be transformed to a motive power termed kinetic energy (Best and Christiansen, 2001). Energy can be transformed into many additional forms like chemical, electrical, light, wind and thermal energy (Bhattacharyya, 2011).

Heat is a form of energy which becomes apparent when two bodies in contact at different temperatures spontaneously reach thermal equilibrium (Carslaw and Jaeger, 1959) which means that in the absence of loss to other objects, they will arrive at a

common temperature due to heat transfer (Martinez and Zuloaga, 2010). This energy

transfer from hotter to colder bodies is commonly termed heat flux or the flow of heat per

unit area per second (Jaupart and Mareschal, 2011; McGeary et al., 2001).

Brief Descriptions of Heat Transfer Mechanisms

Heat transfers naturally from hotter to colder bodies through four physical

processes termed conduction, convection, radiation and advection (Fowler, 2005;

McKnight and Hess, 2000). These processes play different roles at different depths in the

Earth and may occur separately or in combination (Turcotte and Schubert, 2014). The

basic heat transfer equation (24) is presented by Serway and Jewett (2014)

$$Q = mC_p \Delta T \tag{24}$$

where Q is heat added or subtracted, m is mass, C_p is specific heat (the amount of heat

per unit mass required to raise the temperature by one degree Celsius) and ΔT is the

change in temperature.

To change the phase of a substance it is necessary to add or subtract heat from it.

This heat does not change the temperature of the substance, for this reason it is termed

latent heat (Sang, 2014). The heat needed to change a liquid into a gas is called the latent

heat of vaporization, and the heat needed to change a solid into a liquid is called latent

heat of fusion (Serway and Jewett, 2014) which is mathematically expressed by

$$Q = Lm \tag{25}$$

Where L is the latent heat of fusion or vaporization and m is mass.

Conduction

Conduction is the process by which thermal energy is transferred within solids and non-flowing fluids, if a temperature gradient exists (Lowrie, 1997). Heat in the hot object is the result of energetic collisions of rapidly vibrating molecules which collide with the less active molecules in the cold substance, causing them to vibrate more rapidly. These rapid molecular vibrations are the heat which transfers from hot to cold objects (Smith and Pun, 2006).

Thermal conductivity (k) and thermal diffusivity (κ) are two parameters related to different materials capability for heat transmission by conduction (Huang and Liu, 2009; Whittington et al., 2009). Thermal conductivity (k) is a measure of the rate at which heat is conducted in a material in response to temperature differences (Chekhonin et al., 2012; Midttomme et al., 1998). It is a coefficient that quantifies the steady-state rate of heat transfer along the direction of a temperature gradient, governed by Fourier's law of heat conduction (Clauser and Huenges, 1995; Mottaghy, 2007). Thermal conductivity is denoted by equation (26) with ρ and C_p representing density and specific heat respectively.

$$k = \kappa \rho C_p \qquad\qquad (26)$$

Thermal diffusivity (κ), in equation (26), is the ratio of the thermal conductivity to the product of density and heat capacity of a material. It quantifies the ability of a material to store thermal energy during heat transfer processes (Clauser and Huenges, 1995; Huang and Liu, 2009; Whittington et al., 2009). Thermal diffusivity is the controlling thermal property during transient conductive heating processes. It is the rate

at which thermal energy diffuses by conduction through a material (Chekhonin et al., 2012; Lienhard IV and Lienhard V, 2011).

In a steady-state situation, thermal conductivity is significant. However, in transient heat flow problems, thermal diffusivity measures the material's ability to conduct thermal energy relative to its ability to store thermal energy. Both of these properties are dependent on temperature (Navelek et al., 2012; Whittington et al., 2009).

Convection

Convection, which is a much faster way of transferring heat than conduction (Bejan, 2013; Fowler, 2005), is a process associated with the motion of a medium, and is the main mechanism for heat transfer in liquids and gases (Cengel, 2008; Jaupart and Mareschal, 2011). In this process, molecules move from one location to another within the material due to temperature gradients (Fowler, 2005; Turcotte and Schubert, 2014).

Radiation

All bodies whose temperature is above absolute zero constantly emit heat through electromagnetic waves, by a process termed radiation (Lienhard IV and Lienhard V, 2011; Winter, 2010). This explains why radiant energy from the Sun provides the necessary energy for life to thrive on planet Earth, and it is the principal way by which the Earth loses heat from its surface into space (Dayou, 2015; Fowler, 2005).

Advection

Advection, in the context of this study, is a special form of convection which involves the transfer of heat by bodies of rock that are in motion. It is manifested in the earth when a hot volume of rocks is uplifted by the action of tectonic forces, induced flow, or erosion and isostatic rebound (Fowler, 2005; Winter, 2010). Advection of mantle material is the main source of global and local tectonics, where advecting fluids accelerate and activate tectonic processes (Carlson, 1998; Pavlenkova, 2012).

Sources of Earth's Internal Heat

Two types of heat interact at the Earth's surface. The first is Earth's internal energy which accounts for most geological phenomena such as igneous intrusions, metamorphism, and tectonics. The second is external energy, which is predominantly the result of energy output from the Sun plus a small amount of cosmic energy (Fowler, 2005; Murphy et al., 2009). The Earth's internal energy has three sources, two of them related to its formation as a planet and its internal layering, with the third source attributed to radioactive decay. What follows is a brief description of these sources.

Gravitational Accretion and Gravitational Collapse

Except for the Sun, all solar system bodies are assumed to have accreted from the condensates of the solar nebular gases about 4.5 billion years ago (Li, 2000; Lowrie, 1997). This accretion process constitutes the first source of Earth's internal energy. The accretion triggered a massive amount of heat which caused large-scale melting, allowing the heavy elements, such as iron and nickel, to sink toward the center of the Earth, and

lighter elements, such as silicon and aluminum to rise toward the surface (Li, 2000; Murphy et al., 2009). This density separation of the heaviest elements into the Earth's core and lighter elements into the mantle and crust, is known as gravitational collapse, and constitutes the second source for the Earth's internal energy (Lowrie, 1997; Murphy et al., 2009). Starting from an initial temperature at a liquidus state, the Earth gradually solidified and has been cooling down through geologic time (Davies, 1980; Pollack, 1982).

Decay of Radioactive Isotopes

The third source of energy is the heat caused by the decay of radioactive isotopes (Davies, 1980; Fowler, 2005; McKnight and Hess, 2000). The radiogenic heat generation rate in rocks mainly depends on the abundances of the elements uranium, thorium, rubidium and potassium. Only the naturally occurring radioactive isotopes contribute appreciably to heat generation (Fowler, 2005; Turcotte and Schubert, 2014).

Heat Flow Inside the Earth

The thermal evolution of the Earth manifested in volcanoes, earthquakes, magmatic intrusions, mountain building and metamorphism, reveals a history of heat flow from its mantle and molten core to its surface (Lister, 1980; McGeary et al., 2001; Murphy et al., 2009). This heat flow, or loss of heat from the interior of the Earth through its entire surface, is mainly sustained by the essential mechanisms of plate tectonics and performed by conduction via continental lithosphere, hotspot volcanism

and magma convection (Pavlenkova, 2012; Schubert and Stevenson, 1980; Turcotte and Schubert, 2014).

Geothermal Gradient

It has long been recognized that the Earth's interior constitutes a great heat reservoir and that temperature varies directly with depth (Jaupart and Mareschal, 2011; Patiño, 2011). This variation with depth, termed the geothermal gradient, is due to outward heat flow by heat conduction from a hot core (Davies, 2013; Jaupart and Mareschal, 2007; McGeary et al., 2001).

Numerous references to and calculations of the geothermal gradient (Backus, 1975; Beal, 1920; Chekhonin et al., 2012; Elbeze, 2013; Fahnestock et al., 2001; Fanchi, 2010; Head and Solomon, 1981; Jupp and Schultz, 2000; Marsh and Kaufan, 2013; Millot et al., 2015; Palmer et al., 2011; Vacquier, 1998; Van der Hilst et al., 2007; Wetherill and Drake, 1980) appear in the scientific literature, dating back at least to Robert Boyle (1671). During the twentieth century, heat flow measurements were performed in the continental lithosphere by Benfield (1939) and Bullard (1939) who carried out studies on heat flow in continental lithosphere in Great Britain and South Africa respectively.

The geothermal gradient is an essential parameter of the dynamic solid Earth, which provides an understanding of Earth's internal state in the mantle, and its evolution and geochemistry. The geothermal gradient also provides insight on the thermal structure of the crust and lithospheric mantle and hence to lithospheric rheology, which is sensitive to temperature (Davies, 2013; McGeary et al., 2001; Plummer et al., 2007).

The primary directly observable quantity for heat flow is temperature (Lenardic and Kaula, 1995; Stacey 1992). Away from tectonic plate boundaries, the normal geothermal gradient is around 25–30°C/km of depth in most of the world, which roughly corresponds to a heat flow of from 40 to 90 mW/m^{-2} (Lowrie, 1997; Montgomery, 1990; Tarbuck et al., 2011).

The geothermal gradient varies with location and is typically measured by determining the bottom open-hole temperature after borehole drilling (Beardsmore and Cull, 2001; De Lima and Mannathal, 2005; Tanaka et al., 2004). Measurements from at least 300 m in depth are necessary because climatic variation in Earth's surface temperature influence the temperature in near surface rocks. The Continental Deep Drilling Project is an actual example of the importance of a reliable estimation of deep temperatures (Behr, 1988; Clauser et al., 1997; McGeary et al., 2001).

Temperatures at the surface of the earth are controlled by the Sun and the atmosphere, except for areas such as hot springs and lava flows (Condie, 2016; McKnight and Hess, 2000; Tarbuck et al., 2011). Then, from shallow depths to about 60 m below the surface, the temperature is constant at about 11°C (Thomson, 1992). Below that zone, temperature almost always increases with depth. However, the rate of increase with depth varies considerably with both tectonic setting and the thermal properties of the rock (Chi and Reed, 2008; Montgomery, 1990; Springer, 1999).

High gradients of up to 200°C/km are observed along the oceanic spreading centers, such as the Mid-Atlantic Ridge and along island arcs, such as the Aleutian subduction area (Condie, 2016; Dott and Batten, 1988; Frish et al., 2011; Lister, 1980; Lowrie, 1997; McDonald, 1983; Monroe et al., 2007; Russell, 1992; Van Andel, 1992).

These high gradients are due to magma rising to the surface. Low gradients are observed in tectonic subduction zones where cold lithosphere descends into the mantle (Ernst, 2005; Frish et al., 2011; Lister, 1980).

As seen in Figure 23, the geothermal gradient decreases sharply at a short depth below the Earth's surface (Condie, 2016; Coumou et al., 2008; Turcotte and Schubert, 2014). A geothermal gradient of 25°C/km would result in a temperature of 2500°C at a depth of 100 km, which is above the melting point of all rocks at that depth. Based on mantle density calculations from seismic analysis, it is suggested that the geothermal gradient in the mantle must drop to values as low as 1°C/km (Bercovici, 2010; Davies, 2011; Plummer et al., 2007). In addition, new estimates of Earth's internal temperature have yielded 3800°C at the core/mantle boundary, 6200±800°C at the inner-core/outer-core boundary and 6400±600°C at the Earth's center (McGeary et al., 2001; Plummer et al., 2007; Pollack, 1982).

Oceanic heat flow varies in proportion to the inverse square root of its age (Sclater and Francheteau, 1970; Stacey 1992; Tarbuck et al., 2011; Van Andel, 1992) which according to Stein and Stein (1992) can be mathematically expressed as

$$Q = \frac{510}{\sqrt{t}} \; for \; t \leq 55 \; Ma \tag{27}$$

and

$$Q = 48 + 96 \exp\left(-\frac{t}{36}\right) \; for \; t > 55 \; Ma \tag{28}$$

where Q is heat flow and t is time.

Cooling and contraction of the lithosphere produce a gradual growth in the depth to the top of the lithosphere away from the ocean ridges (Frish et al., 2011; Kearey et al., 2009) along with a reduction in heat flow. Equations (29) and (30) express d (depth to the
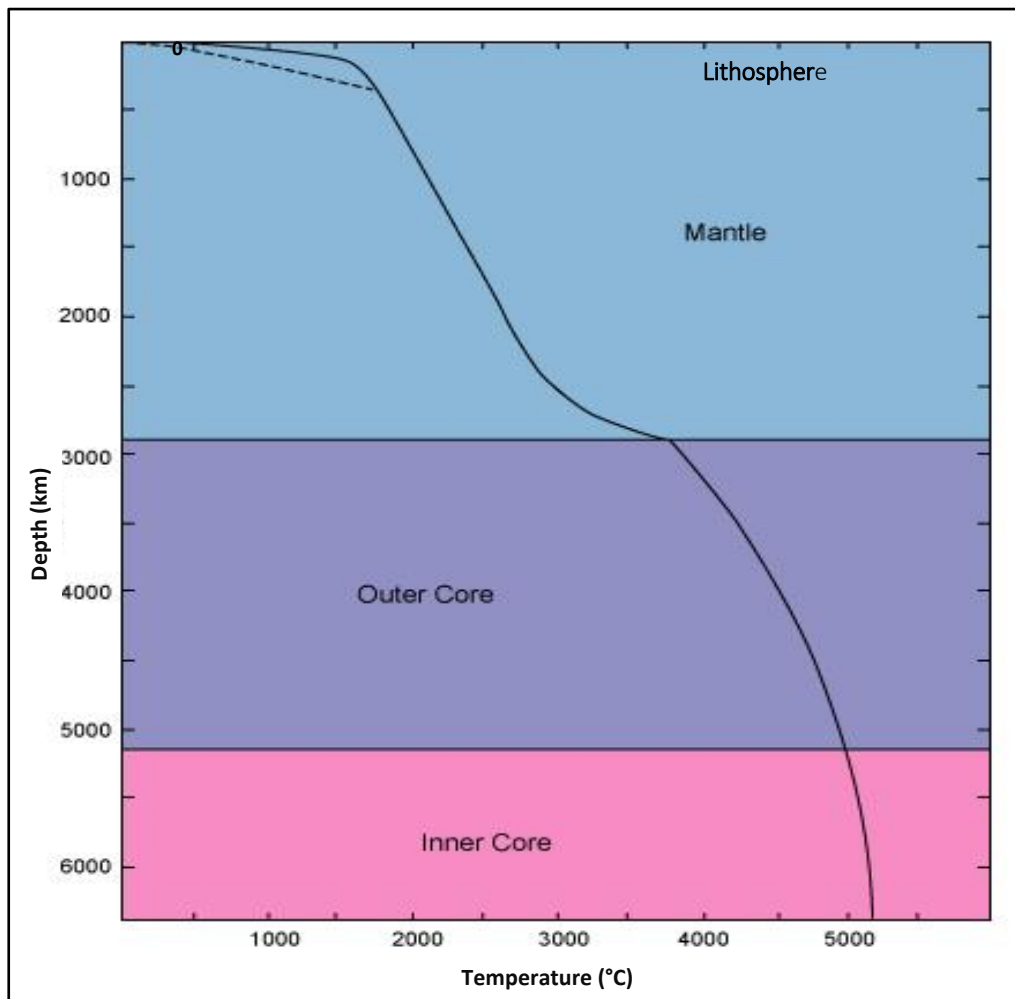
Figure 23. Approximate geothermal gradient to the center of the Earth (according to Stacey (1992)). The dashed geotherm is suggested by Jaupart and Mareschal (2011). Adapted from Winter (2010).

top of the lithosphere) as a function of t (age) (Lowrie, 1997; Stein and Stein, 1992).

$$d = 2,600 + 365\sqrt{t} \; for \; t < 20 \tag{29}$$

$$d = 5,651 - 2473\exp(-0.0278t) \; for \; t \geq 20 \tag{30}$$

Assuming a uniform sea-floor spreading rate, the age of the oceanic crust is proportional to the distance from the ridge axis, and so heat flow decreases with increasing age (Condie, 2016; Dott and Batten, 1988; Sclater and Francheteau, 1970).

Mantle Convection

The theory of mantle convection was first developed to understand the thermal history of the Earth and to propose a reasonable mechanism for Alfred Wegener's theory of Continental Drift in the 1930s (Bercovici, 2007; McGeary et al., 2001; McKnight and Hess, 2000). Interest in mantle convection declined for about 30 years as Wegener's theory was strongly criticized and apparently discredited (Belousov and Belousova, 2016; Stanley, 2005).

However, abundant magnetic information from sea-floor sounding during World War II and improvements in paleomagnetic techniques were significant in the discovery of sea-floor spreading and the emergence of the theory of Plate Tectonics in the 1960s (Belousov and Belousova, 2016; Prothero and Dott, 2010). This theory unified several areas in geology and revived the interest in mantle convection as a mechanism for plate motions and in non-plate tectonic volcanism such as that happening in hot spots like the Hawaiian Islands and Yellowstone (Anderson et al., 1992; Bird et al., 2005; Burke, 2011).

Nowadays it is generally accepted that thermally driven convection takes place in the Earth's mantle. The condition for convection to occur reflects a balance between causal forces due to thermal expansion and resistive effects due to viscosity and thermal diffusivity (Gilbert et al., 2003; Kennedy and van Soest, 2007; Weeraratne and Manga, 1998).

Thermal mantle convection transfers mass and heat extracted from the cooling outer core through the overlying rocky mantle to the surface of the Earth (Davies, 1980; Gubbins et al., 2011; Sparks, 1992). The sluggish and massive mantle controls the cooling of the core by regulating heat flux across the core-mantle boundary (Backus, 1975; Fowler, 2005; Murphy et al., 2009). Thermal mantle-convection impacts a wide range of geodynamic processes including: continental drift, earthquakes, heat flow, mountain building, and changes in sea level (Fowler, 2005; Stein and Stein, 1992; Turcotte and Schubert, 2014).

Heat Flow and Hydrothermal Systems

Definition

A hydrothermal system is essentially a natural mechanism by which heat is transferred from the upper crust to the cooler surface of the Earth (Belousov, 1970; Guilbert and Park, 1986). The physical and chemical processes taking place in these systems redistribute heat and mass by circulating water fluids either in liquid or vapor state (Belousov and Belousova, 2016; Foustoukos and Seyfried, 2007; Hedenquist and Lowenstern, 1994; Norton, 1984). Hot springs, geysers, mud pots, and fumaroles are features at the Earth's surface that represent the final stage of interacting subterranean

systems of water, heat, and rocks, which are the essential components of a hydrothermal system (Dobran and Papale, 1993; Heasler et al., 2009; Wohletz, 1986).

Hydrothermal Systems in the Continental Crust

Hydrothermal systems driven by magmatic intrusions rule fluid movements in the upper crust and are capable of transporting a significant proportion of Earth's internal heat to the surface (Criss and Taylor, 1986; Norton and Knapp, 1977; Taylor, 1974). In areas of active volcanism and hydrothermal activity, heat flow is mainly due to convection of hydrothermal-magmatic systems (Dini, 2014; Norton and Cathless, 1979). Hydrothermal convection in the Earth's continental crust is aided by the movement of heated magmas with a high thermal capacity and water as a main component (Guilbert and Park, 1986; Rose and Burt, 1979; Taylor, 1979).

Hydrothermal fluid circulation within a porous or fractured host rock more efficiently transfers heat when magma is emplaced into water-bearing host rock (Furbish, 1997; German et al., 1998; Guilbert and Park, 1986; Pirajno, 2009). In this system igneous intrusions work as gigantic "heat engines" that produce the energy necessary to support a durable convective circulation system of any mobile hydrothermal fluid in the country rock surrounding the igneous intrusion (Davies and Davies, 2010; Heasler et al., 2009; Taylor, 1974).

Hydrothermal fluids originated from cooling magma, metamorphic processes, and meteoric sources circulate through the continental crust (Guilbert and Park, 1986; Norton, 1984). These fluids are involved in many chemical reactions (Cathless, 1997; Spera, 1980; Stein, 1995) changing the original composition of the surrounding magma and country

rock (Beane and Bodnar, 1995; Rose and Burt, 1979). Through this hydrothermal

alteration (Guilbert and Park, 1986; Pirajno, 2009) the primary minerals are substituted

by secondary minerals due to a change in the surrounding conditions. These changes

could be in temperature, pressure, or chemical conditions or any combination of them

(Pirajno, 2009; Rose and Burt, 1979; Thomson and Thomson, 2011).

Hydrothermal Systems in the Oceanic Crust

The mid-ocean ridge spreading and convective system is located at the sea

bottom, where the Earth's tectonic plates are spreading apart. This system is volcanically

active and the place of abundant hydrothermal systems that cause circulation of seawater

through the permeable oceanic crust. Approximately the equivalent of an entire ocean's

worth of water flows through the mid-ocean ridge hydrothermal systems every 10 million

years (Humphris and McCollom, 1998).

Hydrothermal circulation through fresh oceanic crust is one of the main methods

of heat loss from the Earth (Davies, 1980; Davis et al., 1997; German and Lin, 2004;

Ohmoto, 1996). This circulation occurs due to convection currents originated as new

oceanic lithosphere cools as it moves away from the ridges (Lowrie, 1997). Thus

hydrothermal circulation is a consequence of the plate tectonic cycle (Mayer and Reitz,

2014; Smith and Pun, 2006; Stein et al., 2013).

As seawater penetrates through the oceanic crust, complex physical and chemical

reactions occur between seawater and volcanic rocks. These reactions affect the chemical

composition of seawater and the rocks and influence the whole composition of the

oceanic crust (Guilbert and Park, 1986; Humphris and McCollom, 1998).

Mathematical and Computational Modeling Tools

The dynamic and complex behavior of hydrothermal systems can be mathematically modeled by numerical methods (Cathless, 1997; Ingebritsen et al., 2010; Spera, 1980) which is an area in which computer modeling constitutes an essential tool (Adam, 2003; Prusinkiewicz, 1998). Mathematical modeling involves a steady construction of a cognitively useful, yet simplified and idealized, image of analyzed phenomena (Lave and March, 1995; Paul, 2004; Prusinkiewicz, 1998; Quarteroni, 2009). As this image frequently takes the form of an abstract description, modeling is better performed in formal sciences such as mathematics, physics, chemistry, and computer sciences (Hestenes, 1987; Stacewicz and Włodarczyk, 2010).

Mathematical models are abstractions of the physical world and constitute a scientific tool to mathematically describe diverse phenomena occurring in nature (Hestenes, 1987; Hofleitner, 2013; Stacewicz and Włodarczyk, 2010). They can be based on physical laws or built empirically, using collected measurements, which are termed data-driven models, like the present study (Carrejo and Marshall, 2007; Hofleitner, 2013). The physical properties involved in the natural phenomena, expressed as different variables in the model, directly impact the complexity, interpretability, scalability, accuracy and closeness to reality of the model (Beardsmore and Cull, 2001; Hofleitner, 2013; White, 2004).

Mathematical modeling is by itself one of the pillars of science and engineering that complements the achievements of theoretical analysis and experimentation (Chatuverdi, 2010; Gerya, 2010; Quarteroni, 2009; Velten, 2009). Nowadays, mathematical modeling plays an important role in diverse fields such as geodynamics,

electricity, mechanics, optics, magnetism, environment and industry, while its potential

contribution in many other areas is becoming more and more evident (Farlow, 1993;

Gerya, 2010; Lee, 2014; Morton and Mayers, 2005; Paul, 2004; Quarteroni, 2009;

Schiesser and Griffiths, 2009).

One of the reasons for this increasing success is certainly the amazing progress of

scientific computation, a discipline that permits the transformation of a mathematical

model, which can rarely be solved analytically, into algorithms that can be treated and

solved numerically by increasingly powerful computers and sophisticated scientific

computing and simulation software (Beardsmore and Cull, 2001; Green, 2014; Johnson,

2009; Shen, 2007; Thomas, 1995; Weerawarana, 1994; Yasar and Landau, 2003).

Examples include MATLAB (Matlab, 2012), Heat3D (Wohletz, 2015), HYDROTHERM

(Kipp et al., 2008) and COMSOL Multiphysics (COMSOL Multiphysics, 2015)**,** several

of which are specifically for doing heat flow modeling**.** Through successive modifications

to the model and subsequent computations it is possible to gain some insights into the

phenomenon under consideration (Beardsmore and Cull, 2001; Gerya, 2010; Quarteroni,

2009; White, 2004).

The construction of a mathematical model requires the correct identification of

the variables responsible for changing the system (Carrejo and Marshall, 2007;

Chatuverdi, 2010; Jensen, 2010) as well as the selection of the level of resolution of the

model by choosing the appropriate grid size in order to reach as close as possible a

representation of the model to reality (Jensen, 2010; Klee, 1987; Schiesser and Griffiths,

2009; Shen, 2007; Velten, 2009; Zill and Cullein, 1997).

There are three important steps in the construction of mathematical models of physical processes: problem definition, mathematical representation of the model, and computer simulation (Carrejo and Marshall, 2007; Jensen, 2010; Peiro and Sherwin, 2005). The first step involves defining and idealizing the problem of interest in terms of a set of relevant quantities which can be measured (Jensen, 2010; Peiro and Sherwin, 2005; Soetjahjo, 2006; Yasar and Landau, 2003; Zill and Cullein, 1997). This idealization is expected to yield a well-posed problem, i.e., a problem that has a unique solution for a given set of parameters. It might not always be possible to guarantee the fidelity of the idealization since, in some instances, the physical process is not totally understood (Jensen, 2010; Soetjahjo, 2006; Velten, 2009).

The second step of the modeling process is to represent our idealization of the physical reality by a mathematical model or the governing equations of the system (Chatuverdi, 2010; Gerya, 2010; Peiro and Sherwin, 2005). Thus, the model frequently is going to be in the form of a system of ordinary or partial differential equations (PDE) (Ibragimov, 2004; Johnson, 2009; Schiesser and Griffiths, 2009; Vichnevetsky, 1977).

Solving partial or ordinary differential equations analytically is a challenging task, so it has long been a productive area of research in applied mathematics (Ibragimov, 2004; Johnson, 2009; Lee, 2014; Morton and Mayers, 2005; Thomas, 1995; Vichnevetsky, 1977). As a result many numerical techniques are commonly used to find numerical solutions to different types of partial differential equations (Farlow, 1993; Gockenbach, 2011; Lapidus and Pinder, 1999; Meis and Marcowitz, 1981). Of these techniques, the most frequently used are probably finite difference and finite element methods (Li and Chen, 2009; Morton and Mayers, 2005; Peiro and Sherwin, 2005).

Finite difference techniques compute the solution and possibly its derivatives at points regularly distributed over a grid in the domain. The approach involves replacing the continuous derivatives in the PDE operator by difference quotients, which are approximations to the derivatives at a point using values at nearby points. The resulting system of differential equations can be solved and the solutions plotted by computational mathematical software (Larsson and Thomee, 2009; Mazumder, 2016).

Finite element techniques compute the solution on small regions of the domain, which are called "elements", by expanding the unknown functions in terms of a set of basis functions. Solving the resulting system of algebraic equations gives the coefficients of the expansion (Gockenbach, 2011; Larsson and Thomee, 2009; Ruas, 2016; Solin, 2006).

The final step of the computational modeling process consists of transforming the mathematical model to a computational program. The computer simulation can be performed when the system is set with suitable initial and boundary conditions, (Farlow, 1993; Jensen, 2010; Johnson, 2009; Peiro and Sherwin, 2005; Soetjahjo, 2006).

The resulting mathematical model should be tested against observations of the physical system. If the agreement is considered acceptable, the model is then taken as a representation of the physical system, at least until further research leads to improvements of the model under study (Jensen, 2010; Salsa, 2015; Schiesser and Griffiths, 2009; Weerawarana, 1994).

Modeling Earth's Heat Flow

Thermal models allow one to study complex geologic processes such as

magma intrusions (dikes, sills and plutons), magma convection, and temperature profiles (Annen, 2009; Burchardt, 2009; Copeland et al., 1995; Crawford et al., 1999; Flores et al., 2001; Tarnmemagi and Wheildon, 1974). Other features in thermal modeling are initial and boundary conditions, thermal parameters such as heat conductivity and diffusivity, heat capacity, density, latent heat, radiogenic heat production and geometry (Clauser et al., 1997; Flores et al., 2001; Jaupart and Mareschal, 2007).

One of the first scientists to address the issue of modeling Earth's cooling history was William Thomson, or Lord Kelvin (1864). He calculated the rate for thermal diffusion from a gradually solidifying crust on an originally liquid, magma-like earth. He concluded that the earth could have reached its present state after at most 100 m.y., later reduced to 20 m.y. (Beardsmore and Cull, 2001; Jaupart and Mareschal, 2011; Smith and Pun, 2006). His conclusion had such a strong influence on studies of earth heat flow issues that it restricted geological thinking for the rest of that century. However, this temporal frame was extended to about 4.5 billion years when a new source of heat was discovered, radioactivity (Davies, 1980; England et al., 2007; Mayer and Reitz, 2014; Pollack, 1982).

History of Modeling Cooling of Batholiths

Cooling by Conduction

Modeling the cooling histories of plutons dates back to at least Ingersoll and Zobel (1913) and Lovering (1935, 1936). These researchers principally used analytical solutions to model the cooling history by heat conduction in different magma intrusions.

Later pioneering research aimed at modeling heat flow in batholiths was performed by Larsen (1945) who built an analytical model for the cooling process of the Batholith of Southern and Baja California. A fundamental assumption for building the model was that the main process for heat transfer was conduction. He proposed several scenarios, for example, cooling by conduction through the walls, cooling by loss of heat from the surface once the batholith reached the surface and cooling from the surface with a cover. The mathematical tool to do the modeling was the one-dimensional heat equation, presented in equation (26) (Gockenbach, 2011; Johnson, 2009; Li and Chen, 2009).

$$\frac{\partial T}{\partial t} = \kappa \frac{\partial^2 T}{\partial x^2} \tag{31}$$

Under the initial and boundary conditions

$$i)\ T(0) = T_0\ \text{ for -w} \leq \text{x} \leq \text{w} \tag{32}$$

$$ii)\ T = 0\ at\ t = 0\ for\ |x| > w \tag{33}$$

One solution for equation (31) is the Lovering equation (Carslaw and Jaeger, 1959; Turcotte and Schubert, 2014).

$$T(x,t) = \frac{T_0}{2}\left(erf\left(17.8\frac{w-x}{2\sqrt{\kappa t}}\right) + erf\left(17.8\frac{w+x}{2\sqrt{\kappa t}}\right)\right) \tag{34}$$

where

T_0 = initial temperature
κ = thermal diffusivity
w = width of the intrusion
x = distance from the bottom of the intrusion

and

$$erf\left(17.8\frac{w-x}{2\sqrt{\kappa t}}\right) \tag{35}$$

is the error function, whose values can be found in tables (Fowler, 2005).

Using equation (34), with T_0=820°C as the initial temperature of the intrusion, w =100 km and κ =0.005 m^2/s, Larsen (1945) determined that the central part of the southern California batholith required around 70 Ma for crystallization.

Later research was performed by Birch (1950) on the flow of heat in the Front Range of Colorado. Revelle and Maxwell (1952) performed studies of heat flow by conduction in oceanic lithosphere through the floor of the eastern North Pacific Ocean. Jaeger (1961) who considered only conduction, modeled temperature variation for several types of cooling magma sheets assuming similarity in the thermal properties of liquid and solid magma and the country rock.

Yoshinobu et al. (1998) built a two-dimensional finite difference model simulating the conductive thermal flow associated with the creation and conservation of a continental magma chamber originated by the intrusion of granitic dikes into granodiorite host rocks. The study showed that if the intrusion arises intermittently through time, the thermal and mechanical behavior of the intruded host rock are different from that of rapid intrusions.

Annen and Sparks (2002) made a one-dimensional thermal conduction model, using a finite difference approach, to simulate the frequent intrusion of basalt sills into the deeper parts of the crust. The model took into account the collective effects of multiple intrusions of mafic magma over millions of years, and analyzed several as-sumptions about the composition and water contents for crust and basalt, and about the depth and spacing of basalt intrusions. With this model they studied the simultaneous generation of evolved melt from basalt crystallization and crustal partial melting caused

by repetitive intrusions of basalt into the crust through a long period of time. The study revealed that the main controls on melt generation are magma intrusion rate, the composition and water content of the pre-existing crustal rocks, and temperature and water content of the intruding basalt magma.

Paterson et al. (2011) used the finite difference approach to develop a 2-D heat conduction model for the Tuolumne batholith in the eastern Sierra Nevada in California, USA. This model simulated the thermal change of incrementally growing intrusions created through the combination of pulses with changing properties. They concluded that the spatial distribution of volumetric additions of magma was a more important controlling factor on magma chamber sizes and durations than size or shape of individual rhythms.

Cooling by Conduction Plus Convection of Hydrothermal Fluids

Papers by Norton and Knight (1977) and Cathles (1977) about density driven groundwater flow have had a significant impact on the modern understanding of the role that the convection of magmatic hydrothermal systems has on the cooling of batholiths. Taking into account the limitations in computational technology at that time, the work they did represents an enormous effort to understand how fluids convection and heat conduction combine to cool down small and massive magmatic intrusions in the Earth's crust (Hayba and Ingebritsen, 1997).

Using the hydrothermal fluid convection mechanism Spera (1980) modeled thermal evolution of plutons using a parametrized approach. The study led to the conclusion that depth of emplacement and the scale of the hydrothermal circulatory system are first-order parameters in ruling the thermal evolution of plutons.

Later, with the development of HYDROTHERM, Hayba and Ingebritsen (1997) continued the pioneering work of Norton and Knight (1977) and Cathles (1977) in the cooling of magmatic bodies by modeling the cooling history of some simple generic plutons.

Hurwitz et al. (2003) using a modified version of HYDROTHERM modeled the magma-hydrothermal and volcano-hydrothermal systems of the Cascade Range volcanoes in the USA. The model improved the understanding of how the location of underground waters in volcanic edifices influences the thermal regimes in the system.

Fujimitsu et al. (2005) using HYDROTHERM modeled the hydrothermal system after the 1990-95 Eruption near the Lava Dome of Unzen Volcano in Japan. The analysis suggested first, that there are two dominant flows, the upflow of high temperature gas in the conduit and the downflow of permeating rainwater. Second that there is little possibility of geothermal fluid convection at a scale of a few hundred meters in Unzen Volcano in 13 years since the commencement of the 1990-95 eruption.

Saibi et al. (2006) using HYDROTHERM developed a numerical simulation of the Obama geothermal field in the Kyushu Island, southwestern Japan. The model showed that in the transitory state the central part of the field undergoes a hot upflow of geothermal fluid at a depth associated with the faults of the Obama geothermal field. Faults allow a larger cross downflow of meteoric and cold groundwater, coming from the east of the geothermal field at different levels.

Gutierrez and Parada (2010) built a time-dependent numerical model to simulate the dynamics of magma in the Hudson Volcano, Chile. The model simulated the physical processes of heat transfer, liquid convection, phase exsolution and segregation in a closed

basaltic chamber in the upper crust. The model considered melt formation, magma composition, and dissemination of phases at any time and location during a period of 10 kyr. In building the model they used the finite element method (FEM), the software MELTS (Ghiorso and Sack, 1995), and COMSOL Multiphysics (COMSOL Multiphysics, 2015). The model revealed that stock-like chambers would be more eruptible and would display a broader compositional spectrum of eruptive materials than sill-like chambers.

Verma et al. (2012) used the computer program TCHEMSYS (Thermal and CHEmical Modeling of a Volcanic-Geothermal SYStem) (Verma and Andaverde, 2007) to describe simulation results of three-dimensional thermal modeling for the hydrothermal circulation caused by the magma chamber underlying the La Primavera caldera, Jalisco, Mexico. The equations they used simulated temperatures as a function of age, volume, and depth of the magma chamber. They found that both depth and age of the magma chamber are more important parameters than its volume.

Over time the modeling of heat flow has been important in modeling magma chambers and the resulting plutons. The approaches and computational technology have improved significantly. Today it is possible to perform different tasks more efficiently by including more variables, considering different initial and boundary conditions and varying geometries.

Magma Convection and Stoping

Although the style and strength of magma convection has been subject to uncertainty and controversy (Marsh 1989) numerical simulations (Annen, 2009; Bea, 2010; Gutierrez and Parada, 2010) indicate that convection in magma chambers is a

common process (Bea, 2010; Bindeman and Simakin, 2014; Huppert et al., 1982). Magma convection triggers crystallization, partial melting and differentiation (Brandeis and Jaupart, 1986; Gutierrez and Parada, 2010; Worster et al., 1990) and plays an essential role in the cooling rates which can be determined by Ar-Ar data (Miggins et al., 2014) and are governed by heat flux mainly through the roof of the magma chamber (Martin et al., 1987; Worster et al., 1990). Convection in the filled magma chamber is ruled by the shape and size of the chamber, the viscosity of the magma, and by processes at the chamber boundary which produce lighter or denser fluid than that in the interior of the chamber (Bergantz and Dawes, 1994; Brown, 2013; Turner and Campbell, 1986).

Mechanisms of magma emplacement in the upper crust, like stoping (detaching and engulfing pieces of the country rock that fall down and are assimilated by magma), diapirism and ballooning, ring faulting and cauldron subsidence (Burchardt, 2009; Burov and Jaupart, 2003) represent material and heat transfer processes mainly controlled by the brittle deformation of the host rock (Yoshinobu et al., 1998). Magma stoping results from a continued fracturing of wall and roof rocks around a magma body due to high fluid pressures in the pluton and high strain-rates in the country rock (Cruden, 1998; Farris and Paterson, 2007) causing the inclusion and ascent or sinking of the detached blocks (Burchardt, 2009; Paterson et al., 2008).

The large temperature gradients between the rock at the roof of the magma chamber and the intruding magma makes magma stoping and recycling important processes of magma cooling in the Earth's crust (Bindeman and Simakin, 2014; Burchardt, 2009; Turner and Campbell, 1986; Zak et al.). Glazner (2007) presents the following example on magma heat loss by assimilation of wall rock: The incorporation of

25% granite at 400 °C into basaltic magma at 1125 °C produces a hybrid magma at 1050 °C with >50% crystals; if the granite disaggregates without melting, the crystal content is 65% -70%. Once the crystal content reaches is about 50% the viscosity of the magma is too high to allow further magma movement or xenolith incorporation.

Geothermal Energy and Thermal Modeling

Thermal modeling is important for many reasons, such as its reliable use in the hydrocarbon industry and the information it provides on the available geothermal energy in the lithosphere (Townend, 1999). Projects aimed at using the Earth's internal heat for beneficial purposes can be improved by geothermal models developed from qualitative and quantitative data collected during the exploration phase of the project. In its simplest form modeling geothermal energy may involve rough ideas about depth and areal extension of the reservoir as well as its temperature and permeability (Pruess, 1990). Geothermal energy can be efficiently used for power generation when the vertical geothermal gradient is able to cause surface temperatures of about 180°C. Constructive and destructive plate boundaries provide such conditions, as demonstrated by the geothermal power plants in Iceland and the North Island of New Zealand, respectively. High geothermal gradients can also be found in intra-plate zones where they are typically related to granitic plutons (Kearey et al., 2009). Today, geothermal energy has much to offer in generating power and heat for industry, medicine, tourism and recreation. Geothermal energy is also a great asset and a source of possibilities for sustainable development (Kepinska, 2003).

Summary

Thermal energy can be transferred by conduction, convection, radiation and advection. Earth's internal energy is due to gravitational accretion and gravitational collapse as well as the decay of radioactive isotopes. Earth's internal heat is transferred mainly by convection in the mantle and conduction through the lithosphere. The geothermal gradient is an important factor in providing an understanding of Earth's internal heat, its evolution and geochemistry. A hydrothermal system provides an additional mechanism for heat loss beyond conduction and convection. The physical and chemical processes taking place in these systems reallocate heat and mass in response to circulating water fluids either in liquid or vapor state.

For more than 150 years, the modeling of heat flow in the earth has been a continuing scientific endeavor leading to a deeper understanding of temperature distribution in the planet. Modeling the cooling of plutons and their associated hydrothermal systems has provided insight into the interplay between convection and conduction as well as their efficiency as heat transfer mechanisms. Thermal modeling is a valuable tool in understanding and using geothermal energy for the benefit of humanity.

References

Adam, J. A., 2003, Mathematics in Nature: Modeling Patterns in the Natural World, New
   Jersey, Princeton University Press.

Anderson, D. L., Tanimoto, T., and Shang, Y. S., 1992, Plate tectonics and hotspots: the
   third dimension: Science, v. 256, p. 1645-1651.

Annen, C. J., 2009, From plutons to magma chambers: Thermal constraints on the
   accumulation of eruptible silicic magma in the upper crust: Earth and Planetary
   Science Letters, v. 284, no. 3,4, p. 409-416.

Annen, C. J., and Sparks, R. S. J., 2002, Effects of repetitive emplacement of basaltic
   intrusions on thermal evolution and melt generation in the crust: Earth and
   Planetary Science Letters, v. 203, no. 3,4, p. 937-955.

Backus, G. E., 1975, Gross thermodynamics of heat engines in deep interior of Earth:
   Proceedings of the National Academy of Sciences of the United States of
   America, v. 72, no. 4, p. 1555-1558.

Bea, F., 2010, Crystallization dynamics of granite magma chambers in the absence of
   regional stress: Multiphysics modeling with natural examples: Journal of
   Petrology, v. 51, no. 7, p. 1541-1569.

Beal, W. O., 1920, Note on the temperature of the Earth's interior: Popular Astronomy, v.
   28, p. 387-388.

Beane, R. E., and Bodnar, R. J., 1995, Hydrothermal fluids and hydrothermal alteration in
   porphyry copper deposits, *in* Pierce, F. W., and Bohom, J. G., eds., Porphyry
   Copper Deposit of the American Cordillera, Volume 20: Tuczon, Az, Arizona
   Geological Society, p. 83-93.

Beardsmore, G. R., and Cull, J. P., 2001, Crustal Heat Flow. A Guide to Measurement and Modelling, USA, Cambridge University Press.

Behr, H. J., 1988, Objectives and organization of the German continental deep drilling project (KTB): Annales de la Société Géologuique de Belgique, v. 111, p. 203-216.

Bejan, A., 2013, Convection Heat Transfer, USA, Wiley.

Belousov, V., I, and Belousova, I., V., 2016, Heat transfer in hydrothermal-magmatic systems, Workshop on Geothermal Reservoir Engineering Stanford University, Stanford, California, February 22-24 2016, p. 1-12.

Belousov, V. V., 1970, Against the hypothesis of ocean-floor spreading: Tectonophysics, v. 9, no. 6, p. 489-511.

Benfield, A. E., 1939, Terrestrial heat flow in Great Britain: Proceedings of the Royal Society of London A, v. 173, no. 955, p. 428-450.

Bercovici, D., 2007, Mantle dynamics past, present and future: An overview, *in* Gerald, S., ed., Treatise on Geophysics: UK, Elsevier.

Bercovici, D., 2010, Mantle Convection, *in* Harsh, G., ed., Encyclopedia of Solid Earth Geophysics, Volume 1: The Netherlands, Springer, p. 1-27.

Bergantz, G. W., and Dawes, R., 1994, Aspects of magma generation and ascent in continental lithosphere, *in* Ryan, M. P., ed., Magmatic Systems: UK, Academic Press Limited.

Best, M., G, and Christiansen, E. H., 2001, Igneous Petrology, USA, Blackwell Science.

Bhattacharyya, S. C., 2011, Energy Economics, London, Springer.

Bindeman, I. N., and Simakin, A. G., 2014, Rhyolites-hard to produce, but easy to

    recycle and sequester: Integrating microgeochemical observations and numerical

    models: Geosphere, v. 10, no. 5, p. 1-27.

Birch, F., 1950, Flow of heat in the Front Range, Colorado: GSA Bulletin, v. 61, no. 6, p.

    567-630.

Bird, D., E, Burke, K., Hall, S. A., and Casey, J. F., 2005, Gulf of Mexico tectonic

    history: Hotspot tracks, crustal boundaries, and early salt distribution: AAPG

    Bulletin, v. 89, no. 3, p. 311-328.

Boyle, R., 1671, Of the temperature of subterranean regions as to heat and cold, *in*

    Robert, B., ed., The Works London, G. Ohlms.

Brandeis, G., and Jaupart, C., 1986, On the interaction between convection and

    crystallization in cooling magma chambers: Earth and Planetary Science Letters,

    v. 77, no. 3,4, p. 345-361.

Brown, M., 2013, Granite: From genesis to emplacement: GSA Bulletin, v. 125, no. 7-8,

    p. 1079-1113.

Bullard, E. C., 1939, Heat flow in South Africa: Proceedings of the Royal Society of

    London, v. 173, no. 955, p. 474-502.

Burchardt, S., 2009, Mechanisms of Magma Emplacement in the Upper Crust

    [Doktorgrades]: Georg-August-Universität zu Göttingen, 125 p.

Burke, K., 2011, Plate tectonics, the Wilson cycle, and mantle plumes: Geodynamics

    from the top: Annual Review of Earth and Planetary Sciences, v. 39, p. 1-29.

Burov, E., and Jaupart, C., 2003, Ascent and emplacement of buyoant magma bodies in brittle-ductile upper crust: Journal of Geophysical Research, v. 108, no. B4, p. 1-20.

Carlson, W. D., 1998, Petrologic constraints of the tectonic evolution of the Llano uplift *in* Hogan, J. P., and Gilbert, M. C., eds., Basement Tectonics 12: USA, Springer Science+Business Media, B. V., p. 3-28.

Carrejo, D. J., and Marshall, J., 2007, What is mathematical modelling? Exploring prospective teachers' use of experiments to connect mathematics to the study of motion: Mathematics Education Research Journal, v. 19, no. 1, p. 45-76.

Carslaw, H. S., and Jaeger, J. C., 1959, Conduction of Heat in Solids, Great Britain, Oxford.

Cathles, L., M., 1977, An analysis of the cooling of intrusives by ground-water convection which includes boiling: Economic Geology, v. 72, no. 5, p. 804-826.

Cathless, L., M., 1997, Thermal aspects of ore deposition, *in* Barnes, H. L., ed., Geochemistry of Hydrothermal Ore Deposits: USA, John Wiley and Sons, Inc, p. 191-223.

Cengel, Y., A, 2008, Introduction to Thermodynamics and Heat Transfer, USA, McGraw-Hill.

Chatuverdi, D. K., 2010, Modeling and Simulation of Systems Using Matlab and Simulink, USA, Taylor and Francis Group.

Chekhonin, E., Parshin, A., Pissarenko, D., Popov, Y., Romushkevich, R., Safonov, S., Spasenykh, M., Chertenkov, M. V., and Stenin, V. P., 2012, When rocks get hot: thermal properties of reservoirs rocks: Oilfield Review, v. 24, no. 3, p. 20-37.

Chi, W. C., and Reed, D. L., 2008, Evolution of shallow, crustal thermal structure from

    subduction to collision: An example from Taiwan: GSA Bulletin, v. 120, no. 5/6,

    p. 679-690.

Clauser, C., Giese, P., Huenges, E., Kohl, T., Lehman, H., Ryach, L., Saafanda, J.,

    Wilhel, H., Windloff, K., and Zoth, G., 1997, The thermal regime of the

    crystalline continental crust: Implications from the KTB: Journal of Geophysical

    Research, v. 102, no. B8, p. 18417-18441.

Clauser, C., and Huenges, E., 1995, Thermal conductivity of rocks and minerals, Rock

    Physics and Phase Relations. A Hand Book of Physical Constants: Germany,

    American Geophysical Union, p. 105-127.

COMSOL Multiphysics, 2015, COMSOL Multiphysics® The platform for physics-

    based modeling and simulation.

Condie, K. C., 2016, Earth as an Evolving Planetary System, UK, Academic Press.

Copeland, P., Harrison, T. M., Yun, P., Kidd, W. S. F., Roden, M., and Yuquan, Z., 1995,

    Thermal evolution of the Gangdese Batholith, southern Tibet: A history of

    episodic unroofing: Tectonics, v. 14, no. 2, p. 223-236.

Coumou, D., Driesner, T., and Heinrich, C. A., 2008, The structure and dynamics of mid-

    ocean ridge hydrothermal systems: Science, v. 321, no. 5897, p. 1825-1828.

Crawford, M. L., Klepeis, K. A., Gehrels, G., and Clark, I., 1999, Batholith emplacement

    at mid-crustal levels and its exhumation within an obliquely convergent margin:

    Tectonophysics, v. 312, p. 57-78.

Criss, R. E., and Taylor, H. P., 1986, Meteoric hydrothermal systems: Reviews in

    Mineralogy and Geochemistry, v. 16, no. 1, p. 373-424.

Cruden, A. R., 1998, On the emplacement of tabular granites: Journal of the Geological
Society, v. 155, p. 853-862.

Davies, G. F., 1980, Thermal histories of convective earth models and constraints on
radiogenic heat production in the Earth: Journal of Geophysical Research, v. 85,
no. B5, p. 2517-2530.

Davies, G. F., 2011, Mantle Convection for Geologists, UK, Cambridge University Press.

Davies, J. H., 2013, Global map of solid Earth surface heat flow: Geochemistry,
Geophysics, Geosystems, v. 14, no. 10, p. 4608–4622.

Davies, J. H., and Davies, D. R., 2010, Earth's surface heat flux: Solid Earth, v. 1, p. 5-
24.

Davis, E. E., Fisher, A. T., and Firth, J. V., 1997, Introduction and summary:
Hydrothermal circulation in the oceanic crust and its consequences on the eastern
flank of the Juan de Fuca ridge: Proceedings of the Ocean Drilling Program,
Initial Reports, v. 168, p. 7-31.

Dayou, C., 2015, A study of fundamental law of thermal radiation and thermal
equilibrium process: International Journal of High Energy Physics, v. 2, no. 3, p.
38-46.

De Lima, A. J., and Mannathal, V., 2005, Geothermal gradient and heat flow in the state
of Rio De Janeiro: Revista Brasileira de Geofísica, v. 23, no. 4, p. 325-347.

Dini, A., 2014, Sequential emplacement of sheeted plutons and sill-dyke complexes:
implication on crustal anatexis and lifespan of hydrothermal/geothermal systems,
Abstract V24D-05 presented at 2014 Fall Meeting AGU, San Francisco CA.

Dobran, F., and Papale, P., 1993, Magma-water interaction in closed systems and

    application to lava tunnels and volcanic conduits: Journal of Gephysical Research

    v. 98, no. B8, p. 14041–14058.

Dott, R. H., and Batten, R. L., 1988, Evolution of the Earth, USA, McGraw-Hill Book

    Company.

Elbeze, A. C., 2013, On the existence of another source of heat production for the earth

    and planets, and its connection with gravitomagnetism: SpringerPlus, v. 2, no.

    513, p. 2-13.

England, P., Molnar, P., and Ritcher, F. M., 2007, Kelvin, Perry and the Age of the Earth:

    American Scientist, v. 95, p. 342-349.

Ernst, W. G., 2005, Alpine and Pacific styles of Phanerozoic mountain building:

    subduction-zone petrogenesis of continental crust: Terra Nova, v. 17, p. 165-188.

Fahnestock, M., Abdalati, W., Joughin, I., Brozena, J., and Gogineni, P., 2001, High

    geothermal heat flow, Basal melt, and the origin of rapid ice flow in central

    Greenland: Science, v. 294, no. 5550, p. 2338-2342.

Fanchi, J. R., 2010, Integrated Reservoir Asset Management. Principles and Best

    Practices, USA, Elsevier Inc.

Farlow, S. J., 1993, Partial Differential Equations for Scientist and Engineers, USA, John

    Wiley & Sons.

Farris, D. W., and Paterson, S. R., 2007, Contamination of silicic magmas and fractal

    fragmentation of xenoliths in Paleocene plutons on Kodiak island, Alaska: The

    Canadian Mineralogist, v. 45, p. 107-129.

Flores, E. L., Prol, R. M., and Royer, J. J., 2001, Boundary conditions in thermal models: An application to the KTB site, Germany: Geofísica Internacional, v. 40, no. 2, p. 97-109.

Foustoukos, D. I., and Seyfried, W. E., 2007, Fluid phase separation processes in submarine hydrothermal systems: Reviews in Mineralogy and Geochemistry, v. 65, no. 1, p. 213-239.

Fowler, C. M. R., 2005, The Solid Earth: An Introduction to Global Geophysics, UK, Cambridge University Press.

Frish, W., Meschede, M., and Blakey, R., 2011, Plate Tectonics Continental Drift and Mountain Building, New York, Springer.

Fujimitsu, Y., Kanou, R., Nishijima, Jun, and Ehara, S., 2005, Hydrothermal system after the 1990-95 eruption near the lava dome of Unzen Volcano, Japan, Proceedings World Geothermal Congress , 24-29 April 2005: Antalya, Turkey.

Furbish, D. J., 1997, Fluids Physics in Geology. An Introduction to Fluid Motions on Earth's Surface and within its Crust, USA, Oxford University Press.

German, C. R., Baker, E. T., Mevel, C., Tamaki, K., and Team, F. S., 1998, Hydrothermal activity along the southwest Indian ridge: Nature, v. 395, no. 6701, p. 490-493.

German, C. R., and Lin, J., 2004, The thermal structure of the oceanic crust, ridge-spreading and hydrothermal circulation: How well do we understand their inter-connections?, *in* German, C. R., Lin, J., and Parson, L. M., eds., Mid-Ocean Ridges, Volume 148, p. 1-18.

Gerya, T. V., 2010, Introduction to Numerical Geodynamic Modeling, USA, Cambridge University Press.

Ghiorso, M. S., and Sack, R. O., 1995, Chemical mass transfer in magmatic processes IV. A revised and internally consistent thermodynamic model for the interpolation and extrapolation of liquid-solid equilibria in magmatic systems at elevated temperatures and pressures: Contributions to Mineralogy and Petrology, v. 119, no. 2, p. 197-212.

Gilbert, B., Seipold, U., Tommasi, A., and Mainprice, D., 2003, Thermal diffusivity of upper mantle rocks: Influence of temperature, pressure, and the deformation fabric: Journal of Geophysical Research, v. 108, no. B8, p. 1-15.

Glazner, A. F., 2007, Thermal limitations on incorporation of wall rock into magma: Geology, v. 35, no. 4, p. 319-322.

Gockenbach, M. S., 2011, Partial Differential Equations, Analitical and Numerical Methods, USA, Society for Industrial and Applied Mathematics.

Green, D., 2014, One Hundred Physics Visualizations Using Matlab, Singapore, World Scientific Co.

Gubbins, D., Sreenivasan, B., Mound, J., and Rost, S., 2011, Melting of the Earth's inner core: Nature, v. 473, no. 7347, p. 361-364.

Guilbert, J. M., and Park, C. F., 1986, The Geology of Ore Deposits, USA, W. H. Freeman and Company.

Gutierrez, F., and Parada, M. A., 2010, Numerical modeling of time-dependent fluid dynamics and differentiation of a shallow basaltic magma chamber: Journal of Petrology, v. 51, no. 3, p. 731-762.

Hayba, D. O., and Ingebritsen, S. E., 1997, Multiphase groundwater flow near cooling

      plutons: Journal of Geophysical Research, v. 102, no. B6, p. 12235-12252.

Head, J. W., and Solomon, S. C., 1981, Tectonic evolution of the terrestrial planets:

      Science, v. 213, no. 4503, p. 62-76.

Heasler, H. P., Jaworowsky, C., and Foley, D., 2009, Geothermal systems and monitoring

      hydrothermal features, *in* Young, R., and Norvy, L., eds., Geological Monitoring:

      Boulder, Colorado: USA, GSA, p. 105-140.

Hedenquist, J. W., and Lowenstern, J. B., 1994, The role of magmas in the formation of

      ore deposits: Nature, v. 370, p. 519-527.

Hestenes, D., 1987, Toward a modeling theory of physics instruction: American Journal

      of Physics, v. 55, no. 5, p. 440-454.

Hofleitner, A., 2013, A Hybrid Approach of Physical Laws and Data-Driven Modeling

      for Estimation: The Example of Queuing Networks [Doctor of Philosophy]:

      University of California, Berkeley, 198 p.

Huang, L., and Liu, L.-S., 2009, Simultaneous determination of thermal conductivity and

      thermal diffusivity of food and agricultural materials using a transient plane-

      source method: Journal of Food Engineering, v. 95, p. 179-185.

Humphris, S., and McCollom, T., 1998, The cauldron beneath the seafloor: Oceanus, v.

      41, no. 2, p. 18-21.

Huppert, H. E., Turner, J. S., and Sparks, R. S., 1982, Replenished magma chambers:

      effects of compositional zonation and input rates: Earth and Planetary Science

      Letters, v. 57, p. 345-357.

Hurwitz, S., Kipp, K. L., Ingebritsen, S. E., and Reid, M. E., 2003, Groundwater flow, heat transport, and water table position within volcanic edifices: Implications for volcanic processes in the Cascade Range: Journal of Geophysical Research, v. 108, no. B12, p. 1-19.

Ibragimov, N. H., 2004, A Practical Course in Differential Equations and Mathematical Modelling, Sweden, ALGA Publications.

Ingebritsen, S. E., Geiger, S., Hurwitz, S., and Driesner, T., 2010, Numerical simulation of magmatic hydrothermal systems: Reviews of Geophysics, v. 48, p. 1-33.

Ingersoll, L. R., and Zobel, O., J. , 1913, An Introduction to the Mathematical Theory of Heat Conduction, with Engineering and Geological Applications, USA, Ginn and Company.

Jaeger, J. C., 1961, The cooling of irregularly shaped igneous bodies: American Journal of Science, v. 259, no. 10, p. 721-734.

Jaupart, C., and Mareschal, J. C., 2007, Heat flow and thermal structure of the lithosphere, *in* Gerald, S., ed., Treatise on Geophysics: Oxford, Elsevier, p. 217-253.

-, 2011, Heat Generation and Transport in the Earth, New York, Cambridge University Press

Jensen, J. C., 2010, Elements of Model-Based Design: University of California at Berkeley, Technical Report No. UCB/EECS-2010-19.

Johnson, C., 2009, Numerical Solutions of Partial Differential Equations by the Finite Element Method, USA, Cambridge University Press.

Jupp, T., and Schultz, A., 2000, A thermodynamic explanation for black smoker temperatures: Nature, v. 403, no. 6772, p. 880-883.

Kearey, P., Klepeis, K. A., and Vine, F. J., 2009, Global Tectonics, UK, Wiley-Blackwell.

Kelvin, L., 1864, On the secular cooling of the Earth: Transaction of the Royal Society of Edimburg, v. 23, p. 167-169.

Kennedy, B. M., and van Soest, M. C., 2007, Flow of mantle fluids through the ductile lower crust: helium isotope trends: Science, v. 318, no. 5855, p. 1433-1436.

Kepinska, B., 2003, Geothermal energy in human history, culture, and practices-selected highlights: Reports, v. 2, p. 1-27.

Kipp, K. L., Hsieh, P. A., and Charlton, S. R., 2008, Guide to the revised ground-water flow and heat transport simulator: HYDROTHERM-Version 3: USA, United State Geological Survey.

Klee, H. H., 1987, Mathematical modeling of continuous dynamic systems: Mathematical Modelling, v. 8, p. 468-471.

Lapidus, L., and Pinder, G., F, 1999, Numerical Solution of Partial Differential Equations in Science and Engineering, USA, John Wiley & Sons, Inc.

Larsen, E. S., 1945, Time required for the crystallization of the Great Batholith of Southern and Lower California: American Journal of Science, v. 243A, p. 399-416.

Larsson, S., and Thomee, V., 2009, Partial Differential Equations with Numerical Methods, Germany, Springer.

Lave, C., and March, J. J., 1995, An Introduction to Models in the Social Sciences, USA, Longman Publishers.

Lee, C, O, 2014, Computational imaging and partial differential equations: Asia Pacific Mathematics Newsletter, v. 4, no. 2, p. 1-5.

Lenardic, A., and Kaula, W. M., 1995, Mantle dynamics and the heat-flow into the Earth's continents: Nature, v. 378, no. 6558, p. 709-711.

Li, J., and Chen, Y. T., 2009, Computational Partial Differential Equations Using Matlab, USA, CRC Press.

Li, Y.-H., 2000, A Compendium of Geochemistry, USA, Princenton University Press.

Lienhard IV, J. H., and Lienhard V, J., H. , 2011, A heat Transfer Text Book, USA, Phlogiston Press.

Lister, C. R. B., 1980, Heat flow and hydrothermal circulation: Annual Review of Earth and Planetary Sciences, v. 8, p. 95-117.

Lovering, T. S., 1935, Theory of heat conduction applied to geological problems: GSA Bulletin, v. 46, no. 1, p. 69-94.

-, 1936, Heat conduction in dissimilar rocks and the use of themal models: GSA Bulletin, v. 47, no. 1, p. 87-100.

Lowrie, W., 1997, Fundaments of Geophysics, UK, Cambridge University Press.

Marsh , B. D., 1989, Magma chambers: Annual Review Earth and Planetary Sciences, v. 17, p. 439-474.

Marsh, W. M., and Kaufan, M. M., 2013, Physical Geography, Great Systems and Global Environments, USA, Cambridge University Press.

Martin, D., Griffiths, R., W, and Campbell, I. H., 1987, Compositional and thermal
convection in magma chambers: Contributions to Mineralogy and Petrology, v.
96, p. 465-475.

Martinez, L. F., and Zuloaga, C. A., 2010, Thermal modeling of pluton emplacement and
associated contact metamorphism: Parashi stock emplacement in the Serranía de
Jarara (Alta Guajira, Colombia): Earth Sciences Research Journal, v. 14, no. 2, p.
145-152.

Matlab, 2012, Mathworks the language of technical computing, USA, The MathWorks,
Inc.

Mayer, F. J., and Reitz, J. R., 2014, Thermal energy generation in the Earth: Nonlinear
Processes in Geophysics, v. 21, p. 367-378.

Mazumder, S., 2016, Numerical Methods for Partial Differential Equations. Finite
Differences and Finite Volume Methods, UK, Academic Press.

McDonald, K. C., 1983, A geophysical comparison between fast and slow-spreading
centers: Constraints in magma chambers formation and hydrothermal activity, *in*
Peter, A. R., Bostrom, K., Laubier, L., and Kenneth L, S., eds., Hydrothermal
Processes at Seafloor Spreading Centers: New York, Springer Science +Business
media, p. 27-52.

McGeary, D., Plumer, C. C., and Carlson, D. H., 2001, Physical Geology, Earth
Revealed, New York, McGraw-Hill.

McKnight, T. L., and Hess, D., 2000, Physical Geography, USA, Prentice Hall.

Meis, T., and Marcowitz, U., 1981, Numerical Solutions of Partial Differential Equations,
USA, Springer-Verlag.

Midttomme, K., Roaldset, E., and Aagaard, P., 1998, Thermal conductivity claystones and mudstones of selected from England: Clay Minerals, v. 33, p. 131-145.

Miggins, D. P., Premo, W. R., Snee, L. W., Yeoman, R., Naeser, N., D, Naeser, C., W, and Morton, D. M., 2014, Thermochronology of Cretaceous batholithic rocks in the northern Peninsular Ranges batholith, southern California: Implications for the Late Cretaceous tectonic evolution of southern California *in* Morton, D. M., and Miller, F. K., eds., Peninsular Ranges Batholith, Baja California and Southern California: USA, GSA Memoir 211, p. 199-261.

Millot, M., Dubrovinskaia, N., Cernok, A., Blaha, S., Dubrovinsky, L., Braun, D. G., Celliers, P. M., Collins, G. W., Eggert, J. H., and Jeanloz, R., 2015, Planetary science. Shock compression of stishovite and melting of silica at planetary interior conditions: Science, v. 347, no. 6220, p. 418-420.

Monroe, J. S., Wicander, R., and Hazlett, R., 2007, Physical Geology Exploring the Earth, China, Brooks/Cole.

Montgomery, C. W., 1990, Physical Geology, USA, W. C. Brown Publishers.

Morton, K. W., and Mayers, D., 2005, Numerical Solutions of Partial Differential Equations, USA, Cambridge University Press.

Mottaghy, D. C., 2007, Heat Transfer Processes in the Upper Crust: Influence of Structure, Fluid Flow, and Palaeoclimate [Doctor of Science]: Rheinisch-Westphalian Technical University of Aachen.

Murphy, J. B., Dostal, J., and Nance, R. D., 2009, Mass and energy: Interactions of the Earth systems, *in* Cilek, V., ed., Earth System: History and Natural Variability, Volume IV: Oxford, UK, Eolss Publishers Co.

Navelek, P. I., Hofmeiser, A. M., and Whittington, A. C., 2012, The influence of
temperature-dependent thermal diffusivity on the conductive cooling rates of
plutons and temperature-times paths in contact aureoles: Earth and Planetary
Science Letters, v. 317-318, p. 157-164.

Norton, D., and Cathless, L., M., 1979, Thermal aspects of ore deposition, *in* Barnes, H.
L., ed., Geochemistry of Hydrothermal Ore Deposits: New York, John Wiley &
Sons, p. 611-631.

Norton, D., and Knapp, R., 1977, Transport phenomena in hydrothermal systems: The
nature of porosity: American Journal of Science, v. 277, no. 8, p. 913-936.

Norton, D., and Knight, J., 1977, Transport phenomena in hydrothermal systems: Cooling
plutons: American Journal of Science, v. 277, p. 937-981.

Norton, D. L., 1984, Theory of hydrothermal systems: Annual Review of Earth and
Planetary Sciences, v. 12, p. 155-177.

Ohmoto, H., 1996, Formation of volcanogenic massive sulfide deposits: The Kuroko
perspective: Ore Geology Reviews, v. 10, p. 135-177.

Palmer, M. D., McNeall, D. J., and Dunstone, N. J., 2011, Importance of the deep ocean
for estimating decadal changes in Earth's radiation balance: Geophysical
Research Letters, v. 38, no. L13707, p. 1-5.

Paterson, S. R., Okaya, D., Memeti, V., Economos, R., and Miller, R. B., 2011, Magma
addition and flux calculations of incrementally constructed magma chambers in
continental margin arcs: Combined field, geochronologic, and thermal modeling
studies: Geosphere, v. 7, no. 6, p. 1439-1468.

Paterson, S. R., Pignotta, G. S., Farris, D., Memeti, V., Miller, R. B., Vernon, R. H., and Zak, J., 2008, Is stoping a volumetrically significant pluton emplacement process?: Discussion: GSA Bulletin, v. 120, no. 7-8, p. 1075-1079.

Patiño, A., 2011, Thermodynamics of the Earth and Planets, UK, Cambridge University Press.

Paul, B. J., 2004, Modelling Approaches to Geodynamic Processes [Doctor of Natural Sciences]: Swiss Federal Institute of Technology, 259 p.

Pavlenkova, N. I., 2012, The Earth's degassing, rotation and expansion as sources of global tectonics: New Concepts in Global Tectonics Newsletter, v. 63, p. 31-53.

Peiro, J., and Sherwin, S., 2005, Finite difference, finite element and finite volume methods for partial differential equations, *in* S, Y., ed., Handbook of Materials Modeling, Volume 1: Methods and Models: Netherlands, Springer, p. 1-32.

Pirajno, F., 2009, Hydrothermal Processes and Mineral Systems, Australia, Springer.

Plummer, C. C., Carlson, D. H., and McGeary, D., 2007, Physical Geology, New York, McGraw-Hill.

Pollack, H. N., 1982, The heat flow from the continents: Annual Review of Earth and Planetary Sciences, v. 10, p. 459-481.

Prothero, D. R., and Dott, R. H., 2010, Evolution of the Earth, New York, McGraw-Hill.

Pruess, K., 1990, Modeling of geothermal reservoirs: Fundamental processes, computer simulation and field applications: Geothermics, v. 19, no. 1, p. 3-15.

Prusinkiewicz, P., 1998, In search of the right abstraction: The synergy between art, science, and information technology in the modeling of natural phenomena, *in*

Sommerer, C., and Mignonneau, L., eds., Art @ Science: Wien, Springer, p. 60-68.

Quarteroni, A., 2009, Mathematical models in science and engineering: Notices of the AMS, v. 56, no. 1, p. 10-19.

Revelle, R., and Maxwell, A. E., 1952, Heat flow through the floor of the eastern north Pacific Ocean: Nature, v. 170, p. 199-200.

Rose, A. W., and Burt, D. M., 1979, Hydrothermal alteration, *in* Barnes, H. L., ed., Geochemistry of Hydrothermal Ore Deposits: New York, John Wiley & Sons, p. 173-227.

Ruas, V., 2016, Numerical Methods for Partial Differential Equations: An Introduction, UK, John Wiley & Sons.

Russell, M. J., 1992, Plate tectonics and hydrothermal ore deposits, *in* Brown, G. C., Hawkesworth, C., J, and Wilson, C. L., eds., Understanding the Earth, a New Synthesis: Great Britain, Cambridge University Press.

Saibi, H., Ehara, S., Fujimitsu, Y., and Fukuoka, K., 2006, Hydrothermal numerical simulation model of Obama geothermal field: Geothermal and Volcanological Research Report of Kyushu University, v. 15, p. 49-57.

Salsa, S., 2015, Partial Differential Equations in Action: From Modelling to Theory, Switzerland, Springer.

Sang, D., 2014, Physics Coursebook, UK, Cambridge University Press.

Schiesser, W. E., and Griffiths, G. W., 2009, A Compendium of Partial Differential Equation Models: Method of Lines Analysis with Matlab, USA, Cambridge University Press.

Schubert, G., and Stevenson, D., 1980, Whole planet cooling and the radiogenic heat
source contents of the Earth and Moon: Journal of Geophysical Research, v. 85,
no. B5, p. 2531-2538.

Sclater, J. G., and Francheteau, J., 1970, The implications of terrestrial heat flow
observations on current tectonic and geochemical models of the crust and upper
mantle of the Earth: Proceedings of the Royal Society of London, v. 20, no. 5, p.
509-542.

Serway, R. A., and Jewett, J. W., 2014, Physics for Scientist and Engineers, USA,
Brooks/Cole Cengage Learning.

Shen, W., 2007, Computer Simulation and Modeling of Physical and Biological
Processes using Partial Differential Equations [Doctor of Philosophy]: University
of Kentucky, 153 p.

Smith, G. A., and Pun, A., 2006, How does Earth work?, USA, Pearson Prentice-Hall.

Soetjahjo, A. T. M. J., 2006, Mathematical Analysis of Dynamic Process Models Index,
Inputs and Interconnectivity [Doctor]: Technische Universiteit Delft, 201 p.

Solin, P., 2006, Partial Differential Equations and the Finite Element Method, USA, John
Wiley & Sons.

Sparks, S. J., 1992, Magma generation in the Earth, *in* Brown, G. C., Hawkesworth, C., J,
and Wilson, C. L., eds., Undesrtanding the Earth, a New Synthesis: Great Britain,
Cambridge University Press.

Spera, F., 1980, Thermal evolution of plutons: a parameterized approach: Science, v. 207,
no. 4428, p. 299-301.

Springer, M., 1999, Interpretation of heat-flow density in the Central Andes: Tectonophysics, v. 306, no. 3,4, p. 377-395.

Stacewicz, P., and Włodarczyk, A., 2010, Modeling in the context of computer science - a methodological approach: Studies in Logic, Grammar and Rhetoric, v. 20, no. 33, p. 155-179.

Stacey , F. D., 1992, Physics of the Earth, Australia, Brookfield Press.

Stanley, S. M., 2005, Earth System History, USA, W. H. Freeman and Company.

Stein, C. A., 1995, Heat flow of the Earth, *in* Ahrens, T. J., ed., Global Earth Physics: A Handbook of Physical Constants: Florida, American Geophysical Union, p. 144-158.

Stein, C. A., and Stein, S., 1992, A model for the global variation in oceanic depth and heat-flow with lithospheric age: Nature, v. 359, no. 6391, p. 123-129.

Stein, C. A., Stein, S., and Pelayo, A. M., 2013, Heat flow and hydrothermal circulation, *in* Humphris, S. E. Z., R. A. , Mullineaux, L. S. Thomson, R. E. , ed., Seafloor Hydrothermal Systems: Physical, Chemical, Biological, and Geological Interactions, Volume 425-445: U.S.A., American Geophysical Union.

Tanaka, A. R., Yamano, M., Yano, Y., and Saasada, M., 2004, Geothermal gradient and heat flow data in and around Japan (I): Appraisal of heat flow from geothermal gradient data: Earth Planets Space, v. 56, p. 1191-1194.

Tarbuck, E. J., Lutgens, F. K., and Tasa, D., 2011, Earth, an Introduction to Physical Geology, USA, Pearson Prentice Hall.

Tarnmemagi , H. Y., and Wheildon, J., 1974, Terrestrial heat flow and heat generation in south-west England: Proceedings of the Royal Society of London, v. 38, p. 86-94.

Taylor, H. P., 1974, The application of oxygen and hydrogen isotope studies to problems of hydrothermal alteration and ore deposition: Economic Geology, v. 69, p. 843-883.

-, 1979, Oxygen and hydrogen isotope relationships in hydrothermal mineral deposits *in* Barnes, H. L., ed., Geochemistry of Hydrothermal Ore Deposits: New York, John Wiley & Sons, p. 236-277.

Thomas, J. W., 1995, Numerical Partial Differential Equations: Finite Differences Method, USA, Springer.

Thomson, A. B., 1992, Metamorphism and fluids, *in* Brown, G. C., Hawkesworth, C., J, and Wilson, C. L., eds., Understanding the Earth: Great Britain Cambridge University Press.

Thomson, A. J. B., and Thomson, J. F. H., 2011, Atlas of Alteration. A Field and Petrographic Guide to Hydrothermal Alteration Minerals, Canada, Geological Association of Canada.

Townend, J., 1999, Heat flow through the West Coast, South Island, New Zealand: New Zealand Journal of Geology & Geophysics, v. 42, p. 21-31.

Turcotte, D., and Schubert, G., 2014, Geodynamics, UK, Cambridge University Press.

Turner, J. S., and Campbell, I. H., 1986, Convection and mixing in magma chambers: Earth-Science Reviews, v. 23, p. 255-352.

Vacquier, V., 1998, A theory of the origin of the Earth's internal heat: Tectonophysics, v. 291, no. 1-4, p. 1-7.

Van Andel, T. H., 1992, Sea floor spreading and plate tectonics, *in* Brown, G. C.,
Hawkesworth, C., J, and Wilson, C. L., eds., Understanding the Earth System, a
New Synthesis: Great Britain, Cambridge University Press.

Van der Hilst, R. D., de Hoop, M. V., Wang, P., Shim, S. H., Ma, P., and Tenorio, L.,
2007, Seismostratigraphy and thermal structure of Earth's core-mantle boundary
region: Science, v. 315, no. 5820, p. 1813-1817.

Velten, K., 2009, Mathematical Model and Simulation Introduction for Scientist and
engineers, Federal Republic of Germany, Wiley-VCH.

Verma, S. P., and Andaverde, J., 2007, Coupling of thermal and chemical simulations in
a 3-D integrated magma chamber-reservoir model: A new geothermal energy
research frontier, *in* Ueckermann, H. I., ed., Geothermal energy research trends:
New York, Nova Science Publishers, p. 149-189.

Verma, S. P., Arredondo, U. C., Andaverde, J., Gomez, E., and Guerrero, F. J., 2012,
Three-dimensional temperature field simulation of a cooling of a magma
chamber, La Primavera caldera, Jalisco, Mexico: International Geology Review,
v. 54, no. 7, p. 833-843.

Vichnevetsky, R., 1977, Partial Differetial Equations in Mathematical Modeling, First
International Conference of Mathematical Modeling, September 1977: St. Louis,
Mo.

Weeraratne, D., and Manga, M., 1998, Transitions in the style of mantle convection at
high Rayleigh numbers: Earth and Planetary Science Letters, v. 160, p. 563-568.

Weerawarana, S., 1994, Problem Solving Environments for Partial Differential Equation
Based Applications [Doctor of Philosophy]: Purdue University, 127 p.

Wetherill, G. W., and Drake, C. L., 1980, The Earth and planetary sciences: Science, v. 209, no. 4452, p. 96-104.

White, R. E., 2004, Computational Mathematics, USA, Chapman & Hall/CRC.

Whittington, A. G., Hofmeister, A., M, and Nabelek1, P. I., 2009, Temperature-dependent thermal diffusivity of the Earth's crust and implications for magmatism: Nature, v. 458, p. 319-321.

Winter, J. D., 2010, Principles of Igneous and Metamorphic Petrology, New Jersey, Prentice Hall.

Wohletz, K. H., 1986, Explosive magma-water interactions: Thermodynamics, explosion mechanisms, and field studies: Bulletin of Volcanology, v. 48, p. 245-264.

-, 2015, Heat3D, Los Alamos National Laboratory.

Worster, M. G., Huppert, H. E., and Sparks, R. S., 1990, Convection and crystallization in magma cooled from above: Earth and Planetary Science Letters, v. 101, no. 1, p. 78-89.

Yasar, O., and Landau, R. H., 2003, Elements of computational science and engineering education: Society for Industrial and Applied Mathematics Review, v. 45, no. 4, p. 787-805.

Yoshinobu, A. S., Okaya, D., A, and Paterson, S. R., 1998, Modeling the thermal evolution of fault-controlled magma emplacement models: Implications for the solidification of granitoid plutons: Journal of Structural Geology, v. 20, no. 9,10, p. 1205-1218.

Zak, J., Holub, F. V., and Kachlik, V., Magmatic stoping as an important emplacement mechanism of Variscan plutons: Evidence from roof pendants in the Central

Bohemian plutonic complex (Bohemian Massif): International Journal of Earth Sciences, v. 95, p. 771-789.

Zill, D. G., and Cullein, M. R., 1997, Differential Equations with Boundary-Value Problems, USA, Brooks/Cole Publishng Company.

CHAPTER FIVE

MODELING HEAT FLOW FROM THE LINGA COMPLEX USING

CONDUCTION PLUS HYDROTHERMAL FLUID FLOW

Abstract

This research modeled the cooling history of the Linga complex, located in the Ica-Pisco section of the Peruvian Coastal Batholith. Parameters used in the modeling were obtained from field work, literature review, and laboratory analysis of samples collected in the field. The modeling was performed using the USGS software HYDROTHERM interactive that can handle fluid temperatures from 0 to 1200°C, and fluid pressures from 0.05 to 10^3 MPa. Simulations were completed to examine the variation on the time for crystallization of the Linga complex caused by variations in permeability, initial temperature of the intrusion, geothermal gradient, depth of emplacement, and size of the pluton. Possible conditions for yielding potassic and propylitic hydrothermal assemblages were also investigated. Results suggest that the permeability of both the country rock and the intrusion, as well as the size and initial temperature of the intrusion could have been important factors affecting the thermal history of the Linga complex.

Introduction

Modeling is a basic tool in the empirical sciences (Adam, 2003; Longo, 2003; Prusinkiewicz, 1998) that involves a steady construction of a cognitively useful, yet simplified and idealized image of the phenomena under analysis (Lave and March, 1995;

149

Paul, 2004; Prusinkiewicz, 1998; Quarteroni, 2009). Since this image frequently takes the form of an abstract description, modeling is better performed in formal sciences such as mathematics, physics, and computer science (Hestenes, 1987; Stacewicz and Włodarczyk, 2010; Wolfram, 1984).

Thermal models are useful in studying complex geologic processes such as magma intrusions (dikes, sills and plutons), magma convection, and temperature profiles (Annen, 2009; Burchardt, 2009; Copeland et al., 1995; Crawford et al., 1999; Flores et al., 2001; Tarnmemagi and Wheildon, 1974). When building thermal models, initial and boundary conditions like temperature and pressure, and thermal parameters such as heat conductivity, heat diffusivity, heat capacity, density, latent heat and geometry are essential input needed to accurately model the phenomena (Clauser et al., 1997; Flores et al., 2001; Jaupart and Mareschal, 2007).

Emplacement of magma bodies into the Earth's crust causes enormous thermal anomalies. These anomalies cause energy transfer by an interplay of heat conduction and density-driven groundwater flow, activating massive convection currents that take away (Clauser et al., 1997; Flores et al., 2001; Jaupart and Mareschal, 2007) the heat of the pluton (Hayba and Ingebritsen, 1997; Norton and Knight, 1977). These mechanisms of heat transfer from the Earth's internal heat sources to its surface can be complex and challenging to model. The complexity arises because there are many unknowns, such as the depth range of water circulation and how heat is conveyed from the groundwater to the magma bodies. Modeling challenges are also due to the variable spatial distribution of heat sources and the emergence of supercritical temperatures (Magnusdottir, 2014). Numerical solutions are also a challenge due to the great nonlinearity presented by the

relative-permeability functions and disparities in fluid properties at high pressures and temperatures (Ingebritsen and Sanford, 1998).

The aim of this chapter is to model two-dimensional cooling for the Linga complex that was described in chapters one and three. The thermal modeling will include heat transfer by conduction as well as by convection of hydrothermal fluids. The hypothesis to test is whether the inclusion of convecting hydrothermal fluids significantly reduces the time for batholith cooling with respect to cooling by conduction only (Hayba and Ingebritsen, 1997; Norton and Knight, 1977). Heat transfer by magma convection will not be included in the model, since the modeling software just allows modeling of groundwater convection.

Brief Description of the HYDROTHERM Equations

HYDROTHERM is the computer modeling software used in this project. It estimates the multiphase flow of pure water and heat in a temperature range from 0 to 1200°C and a pressure range of 0.5 to 10 kbars (Harmoko et al., 2007; Kipp et al., 2008). The range of these values is appropriate for simulating the performance of such processes as deep and shallow hydrothermal systems, volcanic systems with shallow magma intrusions, magmatic hydrothermal systems, cooling plutons and crustal-scale heat transport (Kipp et al., 2008).

Using the software HYDROTHERM interactive is a challenging task because of its high sensitivity to small changes in parameters. This subject is addressed later in this dissertation. However, a major issue is that a bug in the original code of the software has been found (Magnusdottir, 2014) in the section addressing the step function for the

dependence of heat capacity with temperature. This problem significantly complicates the modeling.

HYDROTHERM considers pressure and enthalpy as independent variables and uses a finite differences approach to solve chiefly two partial differential equations. The first is called the Ground-Water Flow Equation which is mathematically expressed as:

$$\frac{\partial}{\partial t}[\emptyset(\rho_w S_w + \rho_s S_s)] - \nabla \cdot \frac{kk_{rw}\rho_w}{\mu_w} - \nabla \cdot \frac{kk_{rs}\rho_s}{\mu_s}[\nabla p_g + \rho_s g\hat{e}_z] - q_{sf} = 0 \qquad (36)$$

where

ϕ is porosity (dimensionless)

ρ is fluid density (kg/m^3)

S_p is saturation of water in phase p; p = w (water) or s (steam) (dimensionless)

k is porous-medium permeability tensor (m^2)

k_r is relative permeability (dimensionless)

μ is viscosity (Pa-s)

p is fluid pressure in the liquid phase (Pa)

p_g is fluid pressure in the gas phase (Pa)

g is acceleration of gravity (m/s^2)

$\hat{e}_z$ is a unit vector in the z-coordinate direction (dimensionless)

q_{sf} is flow-rate intensity of a fluid-mass source (positive is into the region) (kg/s-m^3)

t is time (s)

∇ is spatial gradient (m^{-1}), (vector)

Equation (36) establishes a relationship between the rate of change of the total water mass in the liquid and gas phases with the net source flow rate.

The second equation is called the Thermal-Energy Transport Equation. It is based on the conservation of enthalpy in both the fluid phases and the solid phase of the porous medium in a volume element of the region. Its mathematical expression is

$$\frac{\partial}{\partial t}[\phi(\rho_w h_w S_w + \rho_s h_s S_s + (1 - \phi)\rho_r h_r)] - \nabla \cdot K_a I \nabla T + \nabla \cdot \emptyset(S_w \rho_w h_w V_w + S_s \rho_s h_s V_s) - q_{sh} = 0 \quad (37)$$

where

h is specific enthalpy of the fluid phase (J/kg)

h_r is specific enthalpy of the porous-matrix solid phase (rock or sediment) (J/kg)

ρ_r is density of the porous-matrix solid phase (rock or sediment) (kg/m³)

K_a is effective thermal conductivity of the bulk porous medium (combined liquid, gas, and solids phases) (W/m-°C)

I is the identity matrix of rank 3 (dimensionless)

T is temperature

q_{sh} is flow-rate intensity of an enthalpy source (positive is into the region) (W/m³).

In equation (36) and (37) water and steam phases are represented respectively by the *w* and *s* subscripts. This equation establishes a relationship between the change of fluid and porous-medium enthalpy, the net conductive enthalpy flux, the net advective enthalpy flux and the heat source.

Input Parameters from the Literature

Thickness of the Intrusion

Modeling heat flow from a batholith requires an estimate of its size and shape. It is only an estimate because erosion reveals only a part of most magmatic bodies. Based on data from geophysical and mining studies on several plutons, it is possible to classify

batholiths in two broad groups, tabular or sheet like-bodies and non-tabular ones

(Cruden, 1998). Gravity profiles on three traverses across the PCB indicate that its

geometry is essentially that of a flat slab with average thickness of 2.0-3.2 km. Granitic

material does not extend to depths greater than 3 km below sea level datum. The study

agrees with gravity work, which suggests that PCB plutons are commonly 5 km or less in

thickness. (Couch et al., 1981; Haederle and Atherton, 2001).

Depth to the Top of the Intrusion

Fluid inclusions analysis (Agar, 1981) revealed that the boiling of the fluids from

which the quartz of the Linga complex crystallized originated from a low-salinity vapor

phase and a high-salinity vapor phase. The salt concentration of each phase as well as the

homogenization temperature of the fluid inclusion depends strongly on the pressure at the

time of boiling. The analysis of this factor suggests a pressure between 800 and 900 bars,

which indicates a depth to the top of the intrusion and crystallization for quartz from 2.9

to 3.2 km (Agar, 1981; Agar and Le Bel, 1985). Thus, in the modeling done here the

thickness of the Linga complex varied from 2 to 3 km and the depth to top of the pluton

used values of 3 and 4 km.

Porosity and Permeability

The total porosity in a rock is determined by equation

$$\phi_T = 1 - \frac{\rho_\beta}{\rho_\gamma} \qquad (38)$$

where ρ_β is the dry rock bulk density of a typical sample obtained by usual immersion

methods, and ρ_γ is the grain density obtained in a finely ground sample with a grain size

less than the minimum pore diameter. The porosity determined in this manner is a measure of the total pore volume in the rock. The flow porosity of fractured rocks is related to the entire rock that constitutes rock permeability. Continuous pore features in pluton settings are made up of planar structures such as faults, joints, fissures, or bedding planes in layered host rocks. A simple flow porosity model created on open-smooth-walled cracks seems to be a useful primary approach to permeability. For example, The Sherman Granite, Wyoming, has a flow porosity and a total porosity of 5×10^{-6} and 10^{-2}, respectively (Norton and Knapp, 1977).

Permeability which is controlled by fracture density and porosity, aperture and connectivity (Ranjram et al., 2015; Schwartz, 1959) is an important rock property in thermal modeling. It is a measure of the interactions between fracture surfaces and fluid as it moves through interconnected systems. However, in spite of being an important property, permeability is far from being well understood (Norton and Knapp, 1977; Norton, 1984).

A unit of measure for permeability is the "darcy", in honor of the French engineer, Henry Darcy, who made the first systematic study of permeability (Fetter, 2001). However, the SI unit of permeability used in this modeling is m^2, where the equivalence is 1 darcy = 10^{-12} m^2 (Criss, 1999). Permeability regulates the entrance and flow of thermal fluids into the rocks, and heat flow is directly related to the magnitude of hydrothermal fluid circulation (Norton and Knight, 1977). Consequently permeability influences the transfer of heat from the pluton to the Earth's surface and the time for cooling (Hayba and Ingebritsen, 1997; Spera, 1980).

In general, in situ measurements of permeability on fractured rock yield values in the interval from 10^{-16} to 10^{-12} m^2. For example, an in situ experiment

performed on the Sherman Granite, Wyoming, determined the permeability of this rock to be 10^{-15} m^2, whereas the permeability found on intact core samples is 2 to 3 orders of magnitude less. Laboratory measurements of intact core samples of granites provided a value of 10^{-18} -10^{-21} m^2 (Norton and Knapp, 1977).

Permeability of fractured rock increases significantly, with in situ values of 10^{-15} to 10^{-11} m^2. Fine-scale cracking is closely connected to faulting, as is revealed from studies of fault zones showing that micro- and macro-fracture density increases permeability by at least an order of magnitude near faults (Curewitz and Karson, 1977). Thus, the factor that is most important in controlling diffusion of hydrothermal fluids is not depth under the surface, but high fracture concentration and interconnectivity that permit hydrothermal fluids to diffuse and change the composition of the igneous rocks (Jerram and Petford, 2011).

Hayba and Ingebritsen (1997) used the temperature-dependent permeability function illustrated in Figure 24 to build a thermal model of a generic intrusion. Permeability of the country rock was constant for each simulation, taking its value from the set $10^{-13.5}$, 10^{-14}, $10^{-14.5}$, 10^{-15}, $10^{-15.5}$, 10^{-16}, and 10^{-17} m^2. Porosity of the intrusion and the country rock took values of 5 and 10% respectively, which are bigger than the porosity of the Sherman granite (Norton and Knapp, 1977). The assumption of temperature-dependent permeability, reduces one of the effects of the pure water assumption used by Cathles (1977), Hayba and Ingebritsen (1997) and also used in this project. This is so because of the small difference in fluid properties under supercritical conditions (Hayba and Ingebritsen, 1997; Yardley and Bodnar, 2014). The temperature-dependent function for permeability of the intrusion in Figure 24 shows that 1) at
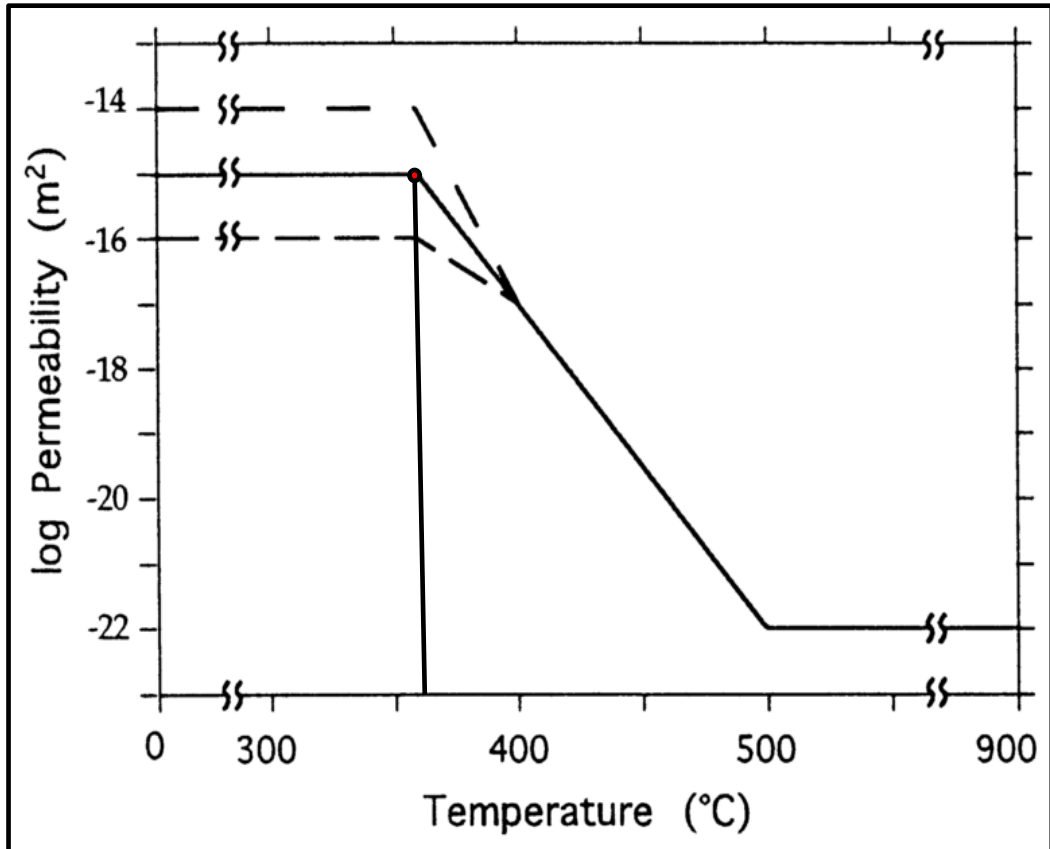
Figure 24. Variation in permeability of the intrusion as a function of temperature showing the effect of the brittle/ductile transition at about 360°C (Hayba and Ingebritsen, 1994).

temperatures greater than 500°C permeability has a value of 10^{-22}m^2, which indicates that the pluton is almost impermeable, 2) from 500°C to 400°C permeability increases log linearly from 10^{-22} m^2 to 10^{-17}m^2, and 3) from 400°C to 360°C the pluton reaches the brittle-ductile transition (Dobson et al., 2017). This is the temperature where the pluton experiences substantial fracturing and consequently its permeability increases, equaling the permeability of the neighboring country rock (Brown, 2013; Hayba and Ingebritsen, 1997). Consequently, there is an increase in the amount of heat transferred from the intrusion into the country rock and from there to the Earth's surface.

In this project, permeability of the pluton varied according to the function depicted in Figure 24, and country rock permeability took values from the set 10^{-14}, 10^{-15}, 10^{-16}, 10^{-17}, 10^{-22} m^2. The modeling used a porosity of 5% for the pluton and 10% for the host rock because that is the range that Hayba and Ingebritsen (1997) used and it allowed HYDROTHERM to run without crashing. This assumed a 0.5% initial aqueous content by mass for the simulated pluton and porous sedimentary host rock. They also mention host rock porosities of 0.1%, 1%, and 4% under other conditions. From other references (Jamtveit et al., 2011; Manning and Bird, 1995; Siratovich et al., 2016), we find the porosity of basaltic andesite type rocks to be on the order of 0.1-11%. The porosity is difficult to measure in present-day host rocks and can be very different than the porosity at the time of magma intrusion. Factors affecting porosity are hydrothermal dissolution and precipitation, burial pressure, and fractures from tectonic events. For the basaltic andesite host rock in the Ica-Pisco area, the porosity may have been significantly less than 10%, so cooling due to hydrothermal fluids could have been significantly slower than that from our calculations.

Thermal Conductivity, Thermal Diffusivity and Heat Capacity

The thermal conductivity coefficient of a material describes its capacity to transmit heat. Thermal conductivity of rocks is a function of temperature, pressure, porosity, composition, and properties of pore-filling fluids and gases. Samples saturated with water show much higher values of heat conductivity than dry samples (Eppelbaum et al., 2014). As reported by Cho et al. (2009) heat conductivity of dry granites ranges from 2.12 W/(m-K) for rocks with high porosity to 3.12 W/(m-K) for rocks with low porosity, showing how porosity strongly affects values of heat conductivity. Stein (1995) found thermal conductivity values from 1 to 5 W/(m-K) for continental rocks in the Earth's surface.

In their thermal model Hayba and Ingebritsen (1997) used a thermal conductivity value of 2W/(m-K) for both the intrusion and the country rock. Similarly, the hydrothermal modeling of the Linga complex used a thermal conductivity of 2 W/(m K). From the literature Annen (2009) and Bea (2010) estimates for this value are 1.8-2.5 W/(m K), or a 17% average variation. To estimate the variation in cooling rate, if the thermal conductivity changes, we use the simple solution to the heat flow equation listed in chapter 4 as equation (34). If the initial and final temperatures and dike thickness remain constant in this equation, the cooling time varies inversely with the thermal conductivity. Thus, for example, the cooling time would decrease by 17%, if the thermal conductivity used in the calculations were to increase by 17%.

Thermal diffusivity κ is mathematically defined by equation (39), where k is the thermal conductivity, ρ is density and C_p is heat capacity

$$\kappa = \frac{k}{\rho C_p} \tag{39}$$

Thermal diffusivity describes the capacity of a material to conduct heat relative to its capacity to store thermal energy. It is about 10^{-6} to 10^{-7} m^2/s for melts and typical dry rocks, but it is somewhat less for rocks that contain water or air in pore spaces (Best and Christiansen, 2001).

The laser-flash thermal diffusivity measurement technique consists of applying uniform laser (heat) pulse heating on the sample face and observing the progressive evolution of the temperature on the other side (Oksanen et al., 1996). Applying this technique to upper and middle crustal rock, it was found that thermal diffusivity κ significantly decreases from 1.5 to 2.5×10^{-6} m^2/s in upper crustal rocks to approximately 0.5×10^{-6} m^2/s at mid-crustal temperatures. The second value is about half that normally expected, so hot middle to lower crust is a much more efficient thermal insulator than formerly thought (Whittington et al., 2009).

Specific heat capacity C_P (J/kg-K) is defined as the amount of heat required to raise the temperature of a unit mass (1 kg) of a substance by a unit temperature increase (1 K). This parameter is related to the thermal conductivity (k) and the thermal diffusivity (κ) by equation (39).

The temperature dependence of C_P can be mathematically expressed through a second order polynomial in equation

$$C_p = \sum_{i=0}^{2} A_i T^i \tag{40}$$

where the A_i coefficients can be experimentally determined (Mottaghy et al., 2007). Heat capacity indicates the ability of the rocks to store heat. Scharli and Rybach (2001) reported values of specific heat for some igneous rocks as: granodiorite, 752 J/(kg-K); diorite, 775 J/(kg-K); granite, 720 J/(kg-K), and peridotite, 827-855 J/ (kg-K). In their

thermal model Hayba and Ingebritsen (1997) used a constant heat capacity value of 1000 J/(kg-K) for the country rock. Heat capacity of the intrusion varied according to a piecewise constant function with values of 1000 J/(kg-K) for temperatures up to 750°C, and 2000 J/(kg-K) for temperatures between 750 and 900°C. This difference in values was meant to substitute the effects of latent heat of magma, which HYDROTHERM does not quantify directly. In the cooling model of the Linga complex, heat capacity of the country rock and the intrusion took a value of 1000 J/(kg-K). Similar values for heat capacity of the country rock have been used in other modeling. For example, both Annen (2009) and Caricchi et al. (2012) used 1000 J/(kg-K) as heat capacity for the country rock and the magma. Norton and Cathles (1979) argue that assuming equal heat capacities for the solid and the melt will not lead to substantial errors in the calculations since geologic evidence suggests that most plutonic bodies were emplaced at temperatures below their liquidus. Furthermore, during 90% of their cooling history in the upper crust, magmatic intrusions were dominantly crystalline bodies.

Geothermal Gradient and Basal Heat

The subject of geothermal gradient was addressed in chapter 4 of this dissertation. Ernst (2005) says that for typical subduction zones the geothermal gradient is approximately 8°C/km. Kearey et al. (2009) indicate that some metamorphic transformations in subduction zones reflect abnormally low geothermal gradients of 10°C/km; however, in subduction zones the geothermal gradient can also vary from 25 up to 50°C/km (Frish et al., 2011; Tarbuck et al., 2011). In modeling the cooling of generic plutons, Hayba and Ingebritsen (1997) used a geothermal gradient of 20°C/km.

The thermal modeling done here used a geothermal gradient for the Linga complex of 10, 20, 25, 30, and 40 °C/km, where 25°C/km was chosen as the standard value. These values encompass the common range of geothermal gradient values observed in subduction zones (Frish et al., 2011; Tarbuck et al., 2011).

Turcotte and Schubert (2014) say that basal heat flow at subduction zones takes an average value of 67 mW/m^2. In their model Hayba and Ingebritsen (1997) used a basal heat flow into the host rock of 63 mW/m^2. In modeling the Linga complex a basal heat flow of 65 mW/m^2 into the host rock was used.

Initial Temperature of the Intrusion

According to Belousov and Belousova (2016), the temperature of granitic magma intrusions in the Earth's crust can vary from 600 to 1000°C. Murphy et al. (1998) suggested that the temperature in the reservoir of the Soufrière Hills andesitic magma was in the range of 810 to 880°C. In another study, Nakada et al. (1999) estimated temperatures of the 1990-1992 Unzen dacite lavas to be in the range of 850 to 900°C. In modeling heat flow of hypothetical plutons, Norton and Knight (1977) used 870 and 920°C as initial temperatures of the intrusion while Hayba and Ingebritsen (1997) used 900°C. The present modeling used initial temperatures of the granitic intrusion of 700, 800, 900 and 1000°C, a range that encompass the wide range of values presented in the literature, 900°C is the standard value. This range of temperatures includes from granitic to the low extreme of basaltic magmas (Plummer et al., 2007; Yokoyama, 2005) since the Linga complex includes the more felsic Rinconada unit and the more mafic Humay unit (Agar, 1981; Moore, 1984).

Density and Volatiles from Batholith Geochemistry

Magmas are complex multiphase fluids that include solids, dissolved gas and bubbles transported in a continuous liquid (melt) phase. The physical properties of magma significantly control their capacity to flow and mix during ascent and emplacement (Jerram and Petford, 2011). These magmatic melts and water-rich fluids are the main transport of mass and energy in the Earth. Their transport properties are dependent on their water and silica content. Consequently, experimental characterization of solubility and solution mechanisms of water and silica components are essential to unraveling the magmatic and metasomatic processes in the Earth's interior (Mysen, 2014).

The main volatile components of magma are water and carbon dioxide, most of which are liberated during crystallization (Cathles, 1977; Cho et al., 2009; Mysen, 2014). Therefore, magma emplacement at depth in the crust causes both heating of surrounding host rock (contact aureole formation) and fluxing of these same rocks with exsolved magmatic volatiles (Blundy and Annen, 2016; Mysen, 2014).

The study of volatiles in whole rocks has traditionally drawn less attention from igneous petrologists than major and trace-elements and isotope analysis. In many recent publications, the LOI (Loss on Ignition) is the only available information related to volatiles in natural samples (Heide and Schmidt, 2005). LOI measures the total volatiles, i.e. H_2O, CO_2, F, Cl, S, etc. (Lechler and Desilets, 1987; Veres, 2002), and is one of the quickest and cheapest approaches used for knowing this parameter (Veres, 2002).

Two important properties for heat flow of the liquid (melt) part of a magma are viscosity and density (Jerram and Petford, 2011). Transport properties of silicate melts

like viscosity, diffusion and conductivity, depend strongly on their water content (Plank et al., 2013; Ushioda et al., 2014). For example, adding 2 wt % water to rhyolite melt at 1000°C lowers the viscosity from 10^7 to 10^5 Pa-s (Winter, 2010). This effect is strongly non-linear and decreases with increasing water content. Moreover, deviation of melt viscosity from Arrhenian behavior is greater the higher the water content.

The influence of water on viscosity is more evident the more felsic the melt. The influence of water is also more evident the higher the alkali/alkaline earth ratio. This implies that viscosity of rhyolitic melts is more affected by water content than basalt and that alkali basalt is more sensitive to water content than olivine tholeiite (Mysen, 2014). Water also has a major impact on the melting temperature of the mantle, crystallization pathways of generated magmas, and the explosivity of magmas (Ushioda et al., 2014).

Although magma viscosity is an important property in heat flow modeling, its value is not included in this research. Magma viscosity is not used because HYDROTHERM interactive considers just convection of pure water as a cooling mechanism.

Magma density is an important physical feature in several magmatic processes because the small variations of liquid density that happen during fractional crystallization can have a large effect on the dynamical processes of magma mixing, fractionation, volcanic activity and magmatic differentiation (Seifert et al., 2013; Sparks and Huppert, 1984).

Despite its importance, direct measurements of magma density at the high pressures and temperatures for magmatic processes are difficult due to experimental challenges. However, it is well known that the density and compressibility of hydrous

silicate melts may be affected by variations in the melt water content (Seifert et al., 2013). In their modeling, Hayba and Ingebritsen (1997) used a density of 2.5 g/cm^3 for density of both the intrusion and the country rock. In modeling the crystallization dynamics of the Stepninsk Uralian massif, Bea (2010) used a density of 2.29 g/cm^3 for the granitic magma. In modeling the cooling history of the Linga complex, the standard values for density of the intrusion and the country rock are 2.7 and 2.8 g/ cm^3 respectively, which are accepted values for granitic magma and volcanic rocks (Best and Christiansen, 2001; Plummer et al., 2007)

Table 4 shows values for the density, temperature and viscosity of the three main units that form the Linga complex, plus the Gabbros. Since there are three intrusions, the values for density and temperature were the average of the three units. These values resulted from major element geochemistry of 49 samples from the Linga complex, using the CIPW software. See Appendix 2 for a complete view of the data.

The inputs for this software are the geochemistry values of major elements. The outputs are estimated values of density, viscosity, liquidus temperature, and water content (Pruseth, 2009). These output data along with additional parameters obtained from the literature, were used as input to HYDROTHERM interactive to model the thermal history of the Linga complex.

Note in Table 4 the decreasing trend of liquid density from 2.74 to 2.55 g/cm^3, and liquidus temperature from 1190 to 969°C. This decreasing trend is as expected for the more mafic lithology of Humay to the more felsic lithology of Rinconada. Similarly, viscosity and water content increase, as expected, from the more mafic Humay to the more felsic Rinconada.

Table 4. Magma properties from the geochemistry of the Linga complex and the gabbros.

	Gabbros	Humay	Auquish	Rinconada
Calculated density (g/cm^3)	3.51	3.09	2.97	2.85
Calculated liquid density (g/cm^3)	3.05	2.74	2.64	2.55
Calculated viscosity dry (poises)	-0.2	2.5	3.7	5.5
Calculated viscosity wet (poises)	-0.2	2.4	3.4	4.7
Estimated liquidus temp (°C)	1516	1190	1091	969
LOI, Loss on ignition (%)	0.1	0.47	1.03	2.04

MATLAB Simulation of the Time Required for Crystallization of the Linga

Complex Just by Heat Conduction

Larsen (1945) mentioned in chapter 4 of this dissertation, performed one of the pioneering research studies on heat flow modeling using conduction as the main process for heat transfer. Since then, other researchers, such as Annen et al. (2006) and Paterson et al. (2011) have continued doing heat flow modeling in magmas by conduction. This section investigates the time required for cooling of the Linga complex following the Larsen (1945) approach and using Matlab (2012) as a programing language. Another solution for equation (31) in chapter 4 is given by (Fowler, 2005). This solution, which is just a variant with different units than equation (34) in chapter 4, is mathematically expressed as

$$T(x,t) = \frac{T_0}{2}\left(erf\left(\frac{w-x}{2\sqrt{\kappa t}}\right) + erf\left(\frac{w+x}{2\sqrt{\kappa t}}\right)\right) \tag{41}$$

Programing equation (41) as a MATLAB code results in a set of cooling curves (Figure 25) which give some insight about the conduction-only cooling history of the Linga complex. In programing equation (41), the Linga complex was considered as a magma body 3 km thick of infinite length, instantaneously intruding country rock at an initial temperature of 900°C Assuming no basal heat flow, the cooling is through only the top side of a 3 km thick slab. Substituting in equation (41) 3 km for w, 0 km for x, 900°C as initial temperature of the intrusion, 0.74×10-6 m2/s as thermal diffusivity, and time in seconds, yields the isotherms shown in Figure 25 that go from the bottom to the top of the slab.
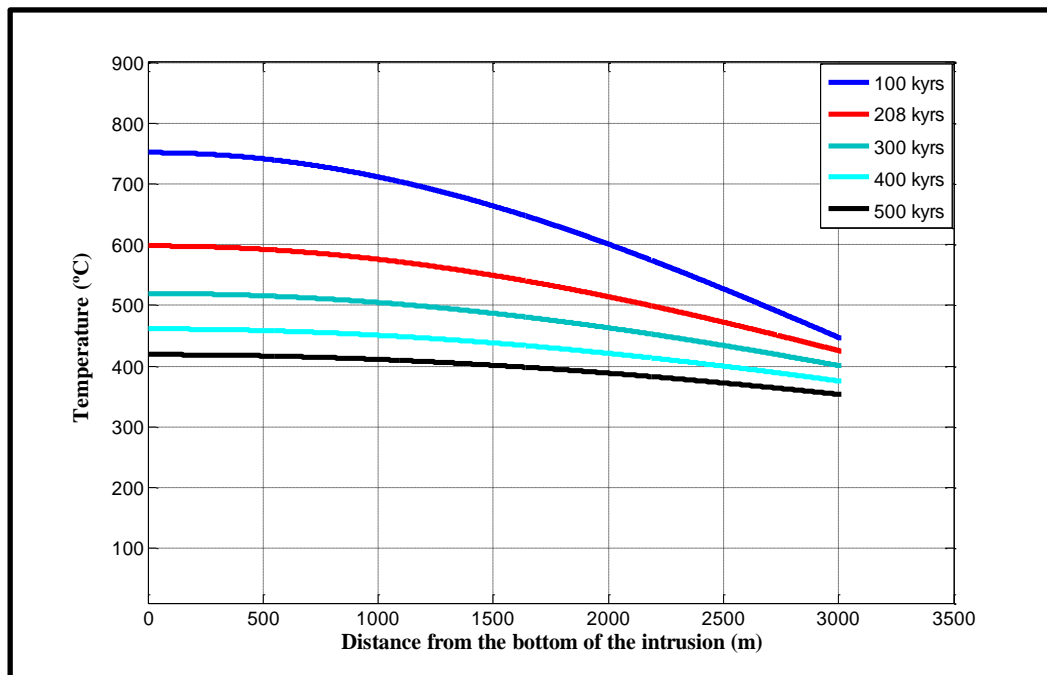
Figure 25. Distribution of temperature at different times considering the Linga complex as a dike 3km wide assuming heat transfer just by conduction.

According to these curves, the central part of the Linga complex, and therefore the whole magma body, was completely crystallized at 600°C approximately 206 kyrs after the intrusion. Here a very simple estimate is made for the quantitative cooling effects of stoping. Small pieces of roof rock falling into the magma chamber would quickly equilibrate in temperature with the magma by heating the stoped blocks and slightly cooling the magma. The heat exchange can be quantified by $\Delta Q = mc\Delta T$ to give an equilibrium temperature of $T = (RT_s + T_m) / (R+1)$, assuming that the specific heat for magma and stoped blocks is the same.

Using an R=1% by mass for assimilation, a 900°C magma intrusion would rapidly heat 25°C stoped blocks to an equilibrium temperature of 891°C. Redoing the calculations in the previous paragraph using an initial temperature of 891°C, would result in cooling to crystallization in 200 kyrs or about 3% faster than without stoping. For R=5% stoping, the equilibrium temperature would be 858°C and the time for cooling would be 180 kyrs or about 13% faster.

Time Required for the Crystallization of the Linga Complex by Conduction Plus Convection of Hydrothermal Fluids

Boundary and Initial Conditions

The Linga complex has an approximate length and width of 50 and 12 km respectively and an average depth to top of the pluton of about 3 km (Agar, 1981; Agar and Le Bel, 1985). Thus, the Linga complex can be represented as a parallelepiped with dimensions of 50×12×3 km. It is assumed that this volume of 1800 km^3 of granitic magma intruded instantaneously into the country rock.

In most of the simulations to follow the Linga complex was considered as a two-dimensional magmatic body of 12 km width and 3 km thickness and infinite length. Computer simulations were performed on just half of the pluton, for speed in computing. The modeling uses a body of country rock 20 km wide by 6 km deep, so that the effects of the right lateral boundary conditions in the Linga complex were negligible (Hayba and Ingebritsen, 1997).

The upper boundary of the conceptual model in Figure 26 represents the top of the water table (Hayba and Ingebritsen, 1997) with pressure and temperature held constant at 1 atmosphere and 20°C. The lower boundary allows the entrance of basal heat to the host rock at a rate of 65mW/m^2 (Springer and Forster, 1998; Turcotte and Schubert, 2014), but no basal heat is entering the pluton after the intrusion (Hayba and Ingebritsen, 1997).

The assumption of no basal heat flowing into the intrusion is an ideal situation that simplifies the modeling. The use of no basal heat flow allows one to consider the bottom as a closed boundary whose influence in the cooling process is negligible (Norton and Knight, 1977). Removing the restriction of no heat flow adds more variables to the system, making it closer to reality but more complex for modeling (Quarteroni, 2009). Another possibility is that heat is not flowing into the intrusion because of thermal equilibrium between the bottom of the pluton and the under crust.

The left boundary in Figure 26 represents an impermeable and insulating symmetry plane. The right boundary, located 14 km from the batholith, is set at a temperature gradient of 25°C/km and hydrostatic pressure, and does not have an influence on the temperature distribution (Magnusdottir, 2014). Table 5 is a summary of parameters used in the modeling of the Linga complex.

170
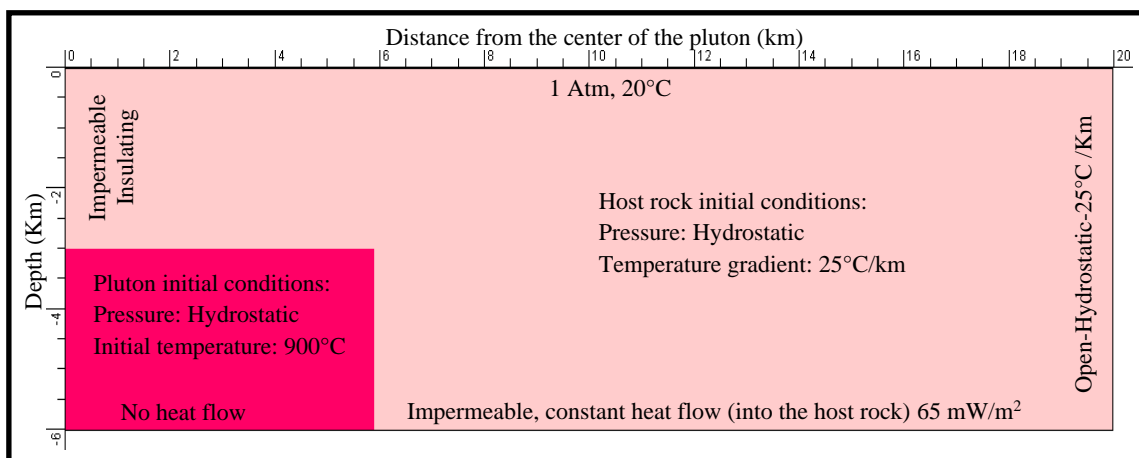
Figure 26. Cross-sectional conceptual model displaying geometry, boundary and initial conditions for the simulations of the cooling process of the Linga complex.

Table 5. Parameters used in the heat flow modeling of the Linga complex. (*) means a standard value with respect to which other results are going to be compared.

Property	Pluton	Host
Permeability-isotropic (m^2)	F(t)	10^{-14}, 10^{-15}, 10^{-16}*, 10^{-17}, 10^{-22}
Porosity (%)	5	10
Heat capacity (J/Kg-K)	1000	1000
Width (km)	12*,10,8	
Thickness (km)	3*,2	6
Depth to top of the pluton (km)		3*,4
Thermal conductivity (W/(m-K))	2	2
Rock density (g/cm^3)	2.7*, 2.64	2.8
Initial Temperature, (°C)	700,800,900*,1000, 1083	-----
Pressure (Atm)	Hydrostatic	Hydrostatic
Geothermal gradient (°C/km)		10,20,25*,30,40
Basal heat flow (mW/m^2)	0	65

Grid Spacing in HYDROTHERM

The grid spacing is a critical issue in HYDROTHERM interactive because of the high sensitivity of the software to small changes in parameters. For example, small changes of permeability for the intrusion or the country rock can cause substantial numerical instability if the grid size is not appropriately chosen. Yet, some modeling problems could require very small grid sizes to accurately represent spatial density variations of sharp saturation, which makes the simulation prohibitively demanding of computer memory (Kipp et al., 2008). These factors lead to a continual crashing of the software while performing the simulation. In modeling the cooling history of the Lina complex, the grid spacing that fit better with the used parameters was a grid variable in the x-axis from 200 to 1400 m, and uniform in the z-axis with cells 200 m thick.

Simulation and Discussion from HYDROTHERM Interactive Results

In the plots generated by HYDROTHERM interactive, mass flow vectors (liquid water) are drawn in black with their tails (little squares) at the centers of the cells. Steam-mass flux vectors are drawn in gray. These vectors point away from the tail in the direction of flow with a length that is proportional to the flux magnitude.

In most of the following simulations permeability of the pluton varies according to Figure 24 and country rock permeability remains constant at 10^{-16} m^2 or 10^{-15} m^2. These permeabilities for the country rock were used in previous heat flow modeling by Hayba and Ingebritsen (1997) and Norton and Knight (1977). These values give also more results regardless of the software limitations. The permeability of 10^{-16} m^2 marks

the transition between hydrothermal systems whose dynamic is governed by conduction and convection of hydrothermal fluids.

Thermal Pressurization

Thermal pressurization is a force that results from a significant pore pressure in the country rock. This force varies inversely with permeability of the country rock and directly with porosity, and the temperature contrast between the pluton and the country rock (Delaney, 1982). Thermal pressurization generates a repulsive pattern in the fluid distribution as that illustrated in Figure 27 for 1 kyr after the intrusion. Thermal pressurization significantly accelerates the heat transfer for a few hundreds of years after the intrusion, when there is a higher temperature contrast (Hayba and Ingebritsen, 1997; Yoshinobu et al., 1998).

500 kyrs of Cooling with a Country Rock Permeability of 10^{-16} m^2

Figures 28a-f display the cooling history of the Linga complex in 100 kyrs increments from the time of an instantaneous intrusion up to 500 kyrs later. Figure 28a displays the moment of the instantaneous intrusion of granitic magma. Figure 28b shows the temperature distribution of the Linga complex 100 kyrs years after the intrusion. At this time heat is transferred from the magma to the host rock through conduction and hydrothermal fluid convection. Steam is abundant at the top center of the intrusion, and temperature at the bottom center of the intrusion is about 700°C. After 200 kyrs (Figure 28c) the highest magmatic temperature at the bottom center of the pluton is around 600°C. This temperature will be assumed as the temperature of full magma crystallization
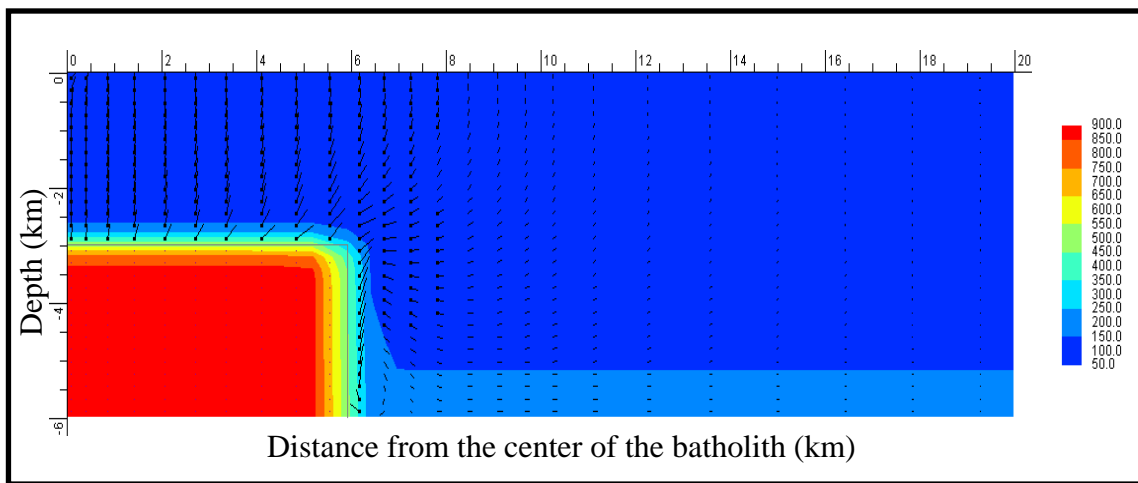
Figure 27. Fluids moving away from the intrusion due to thermal pressurization. The frame depicts the hydrothermal system 1 kyr after the intrusion.
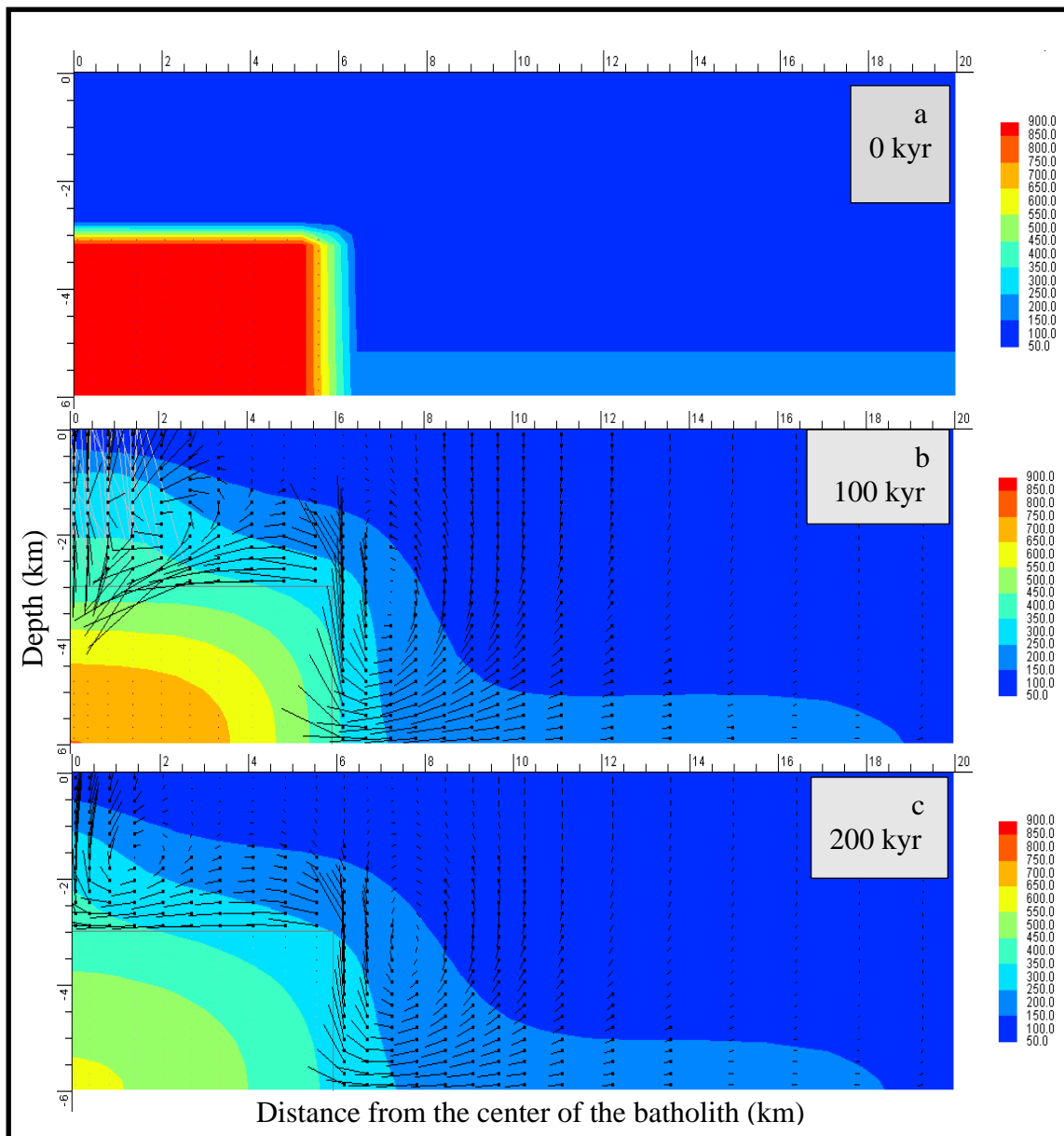
Figure 28. Simulation results for host rock permeability of 10^{-16} m^2 displaying temperature contours, fluid flow (black) and steam flow (gray) vectors in 100 kyrs increments up to 500 kyrs at the Linga complex. Flow vectors lengths are proportional to the intensity of the fluid. Permeability of the pluton varies according to Figure 24.
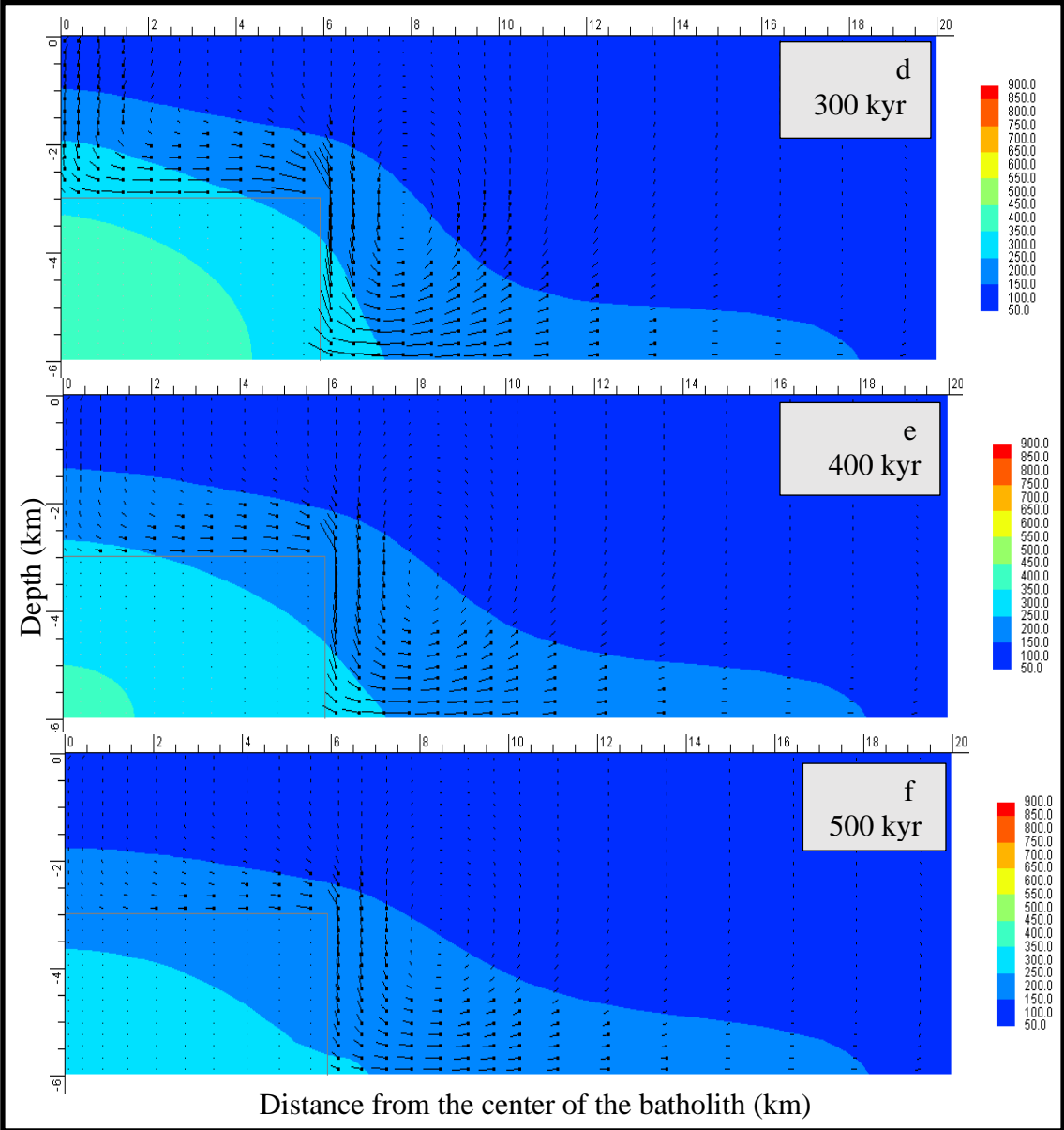
Figure 28. *Continued*

during the entire study (Harrison et al., 2007; Larsen, 1945). There are two notable convection patterns, one at the left edge close to the top center of the pluton, and the other at the right of the intrusion. After 300 kyrs (Figure 28d) the temperature in the whole magmatic complex is below 450°C and hydrothermal fluid convection currents are still removing heat from the intrusion.

After 400 kyrs (Figure 28e) convection currents are weaker. The remaining heat is transferred mainly by conduction through the country rock. Finally, at 500 kyrs (Figure 28f) the temperature of the whole magmatic body is below 350°C. At this time, water temperature is sufficiently high to produce hydrothermal alteration in both in the country rock and the intrusion.

Figure 29 displays some temperature-depth profiles using the same parameters as in Figure 28. At 20 kyrs after the intrusion there is still a large temperature contrast between the intrusion and the country rock, thus, a steep temperature gradient develops above the pluton. After 300 kyrs the temperature of the system continually decreases everywhere. At 800 kyrs after the intrusion, the highest temperature at the bottom center of the Linga complex is about 170°C.

Results of Varying Pluton Size

The dimensions of a magmatic intrusion are important factors in the thermal evolution of hydrothermal systems (Bowers et al., 1990; Parmentier and Schedl, 1981). Thus, this section presents the effect that varying dimensions of the Linga complex exert on its cooling history, especially in cooling until full magma crystallization.

The dimensions of the Linga complex were considered originally to be 12×3 km.
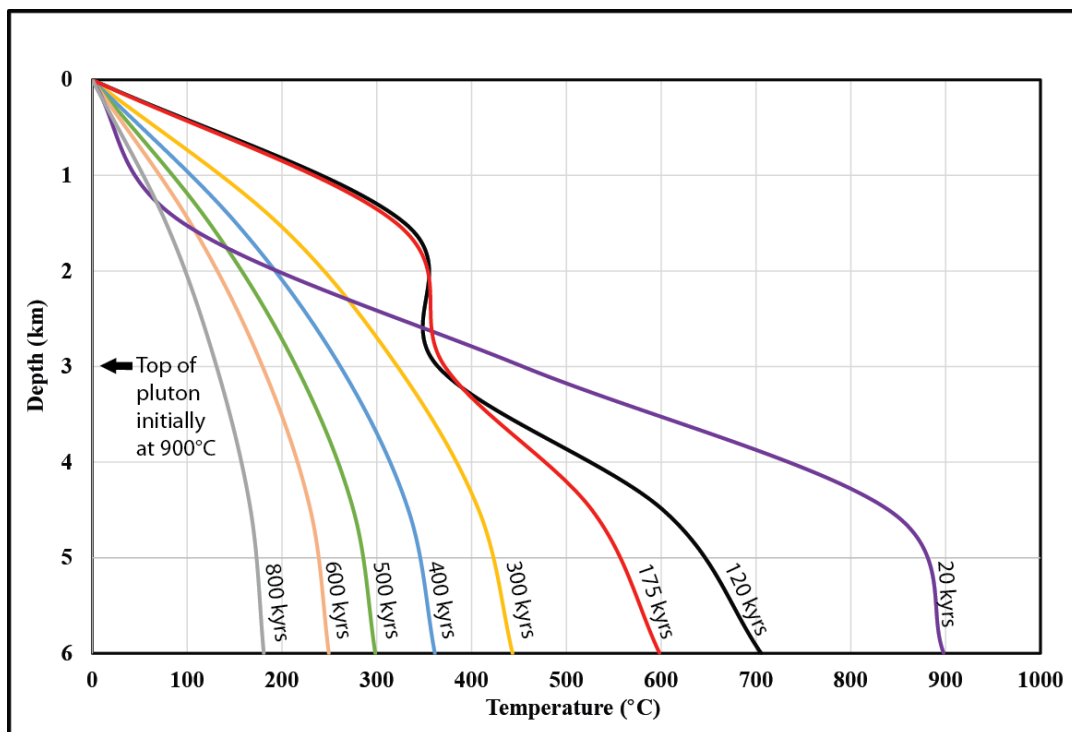
Figure 29. Temperature-depth profiles above the center of the pluton (along left boundary of the model) at different times for a host rock permeability of 10^{-16} m.

Now, Figures 30a-c illustrate the effect of changing the batholith size on the thermal and fluid distribution of the Linga complex.

In Figure 30a the batholith is 12×3 km, and the simulation was stopped at 174 kyrs when the center of the Linga complex was fully crystallized. In Figure 30b the batholith dimensions were 10×3 km and magma crystallized 166 kyrs after the intrusion. Finally, in Figure 30c where the batholith dimensions were 8×3 km, magma fully crystallized 138 kyrs after the intrusion. Thus, decreasing the width of the batholith by 33% reduces the time for magma crystallization by approximately 22%.

In Figure 30 the batholith dimensions were altered by changing only the width of the intrusion. Figure 31 illustrates the effect of reducing the thickness of the intrusion, from 3 to 2 km. Thus, assuming dimensions of 12×2 km for the Linga complex yields magma fully crystallized at 89 kyrs after the intrusion. As expected, there is a decreasing trend in the time for magma crystallization from 174 to 89 kyrs. Thus, decreasing the thickness of the batholith by 33% reduces the time for full magma crystallization by almost a 50%.

Note that although the batholiths of 8×3 km and 12×2 km have the same volume, (assuming the same third dimension) the time for magma crystallization is different, 138 and 89 kyrs respectively. An explanation for the difference is that the 12×2 km intrusion has a more contact surface area for top and sides with the country rock than the 8×3 km intrusion. Thus, the intrusion with a larger contact surface with the country rock cools faster (Martin et al., 1987; Worster et al., 1990).
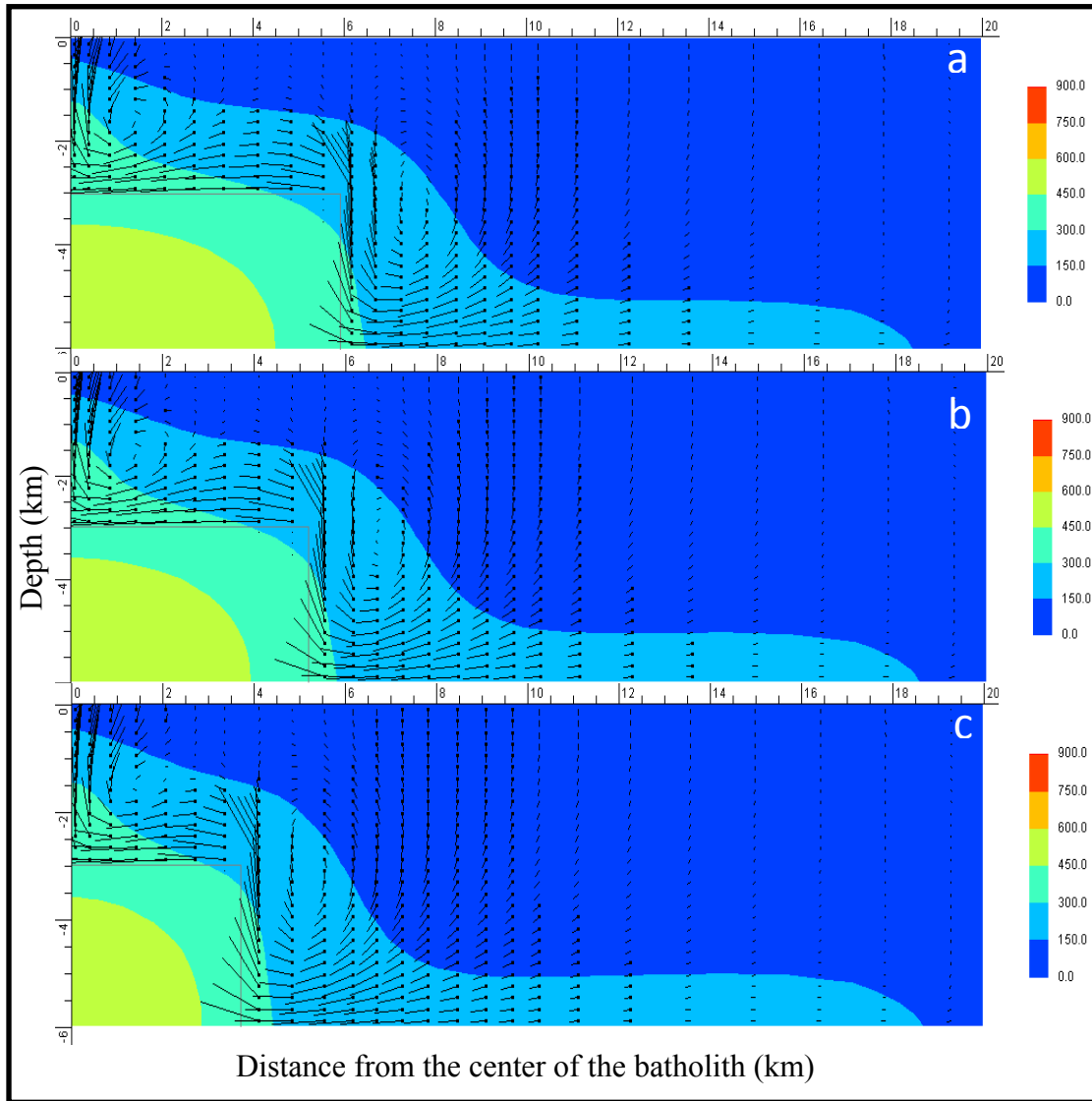
Figure 30. Temperature and fluid flux distribution for hydrothermal systems developed by three different intrusions with dimensions of a) 12km×3km b) 10km×3km and c) 8km×3km. Magma crystallization was reached at 174, 166 and 138 kyrs respectively. Depth to top of the pluton: 3km.
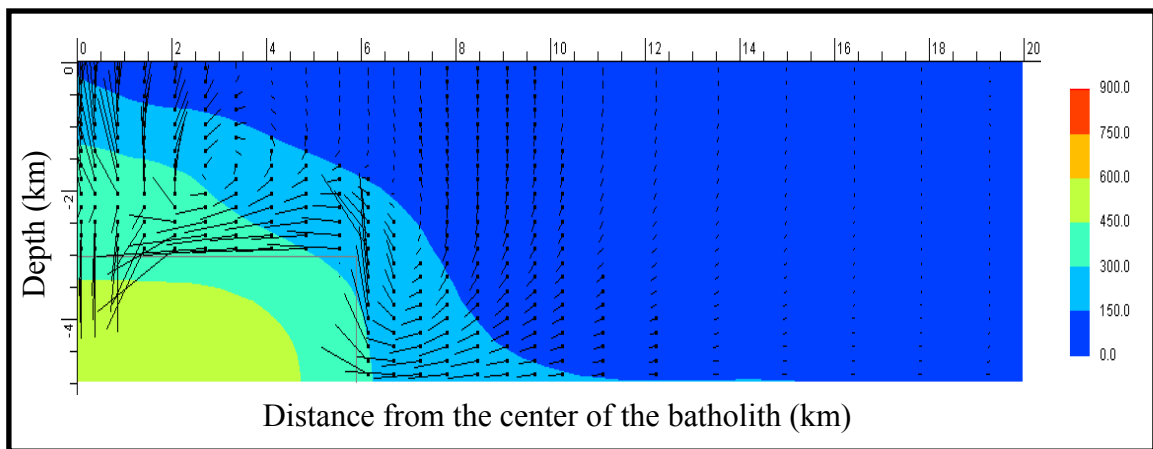
Figure 31. Temperature and fluid flux distribution for hydrothermal systems developed by a magmatic intrusion with dimensions of 12×2 km. Magma crystallization was reached 89 kyrs after the intrusion.

Results from Varying Permeability

The near-magma environment is characterized by high strain rates and extraordinary gradients in temperature and fluid composition, consequently there are significant variations in permeability over time in country rocks close to magmatic intrusions (Ingebritsen and Sanford, 1998). This section presents the effects that changing permeability in both the intrusion and the host rock exert on the thermal evolution of the Linga complex.

Figure 29 displays temperature-depth profiles above the center of the pluton for a host rock permeability of 10^{-16} m^2. Now, a comparison between Figure 29 and Figure 32 shows that while magma fully crystallized at about 175 kyrs after intrusion with a permeability of 10^{-16} m^2, it takes approximately 150 kyrs to crystallize with a permeability of 10^{-15} m^2. Thus, the time for full magma crystallization with a permeability of 10^{-15} m^2 is approximately 15% lower than the time for magma crystallization with a permeability of 10^{-16} m^2.

Figure 33 illustrates the cooling history at the center of the Linga complex, located at 6 km depth and 6 km horizontally from its border for permeabilities of 10^{-22}, 10^{-16}, 10^{-15} and 10^{-14} m^2. The modeled time for magma crystallization at the bottom center of the Linga complex was approximately 180 kyrs for a permeability of 10^{-22} m^2, 175 kyrs for 10^{-16} m^2, 150 kyrs for 10^{-15} m^2, and 125 kyrs for 10^{-14} m^2. Thus, the time for full magma crystallization with a permeability of 10^{-14} m^2 is about 71% of the time for full magma crystallization with permeability of 10^{-22} m^2.
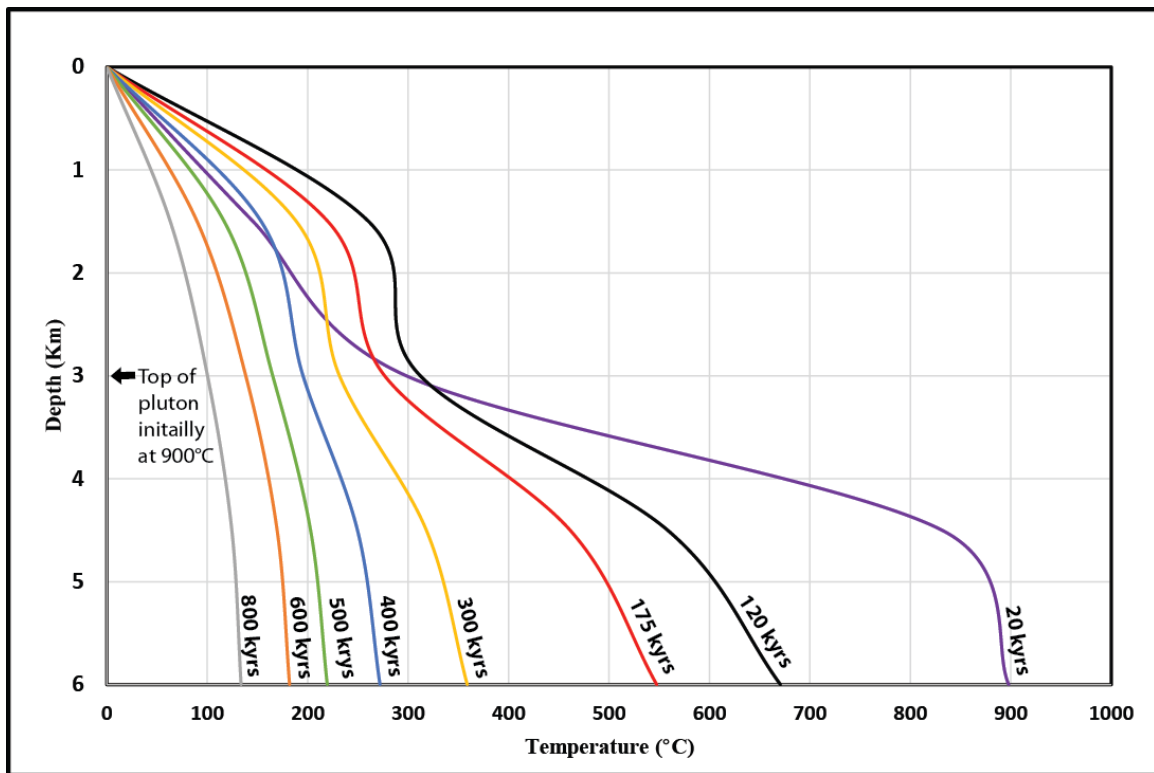
Figure 32. Temperature-depth profiles above the center of the pluton showing the thermal evolution of the Linga complex during 700 kyrs, assuming a permeability of 10^{-15} m^2.
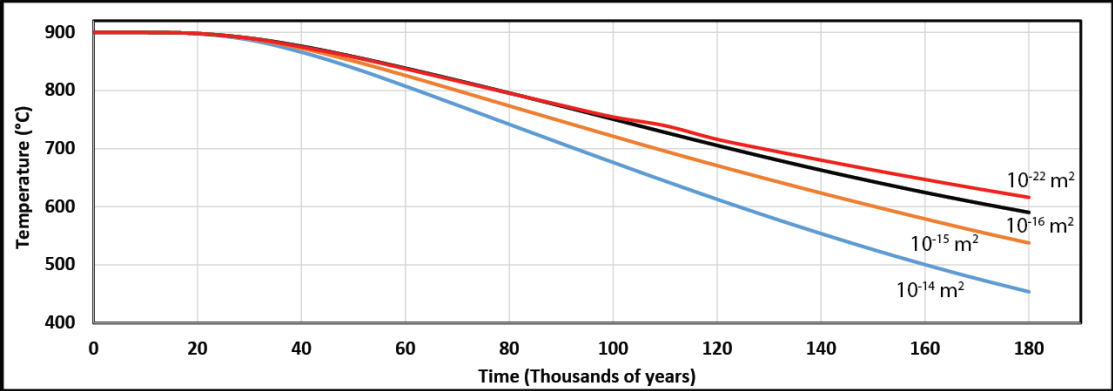
Figure 33. Cooling history for the center of the Linga complex 180 kyrs after the intrusion. Total crystallization occurs faster for the highest permeability: 10^{-14} m^2.

From Table 4 it is seen that the average value of the estimated liquidus temperature of Humay, Auquish and Rinconada, the three main units of the Linga complex is about 1083°C. Likewise, the average value of the calculated liquid density for the three units, is about 2.64g/cm^3. Figure 34 depicts magma crystallization using these parameters, which are the closest to the real parameters yielded from geochemistry of the study area. (See Appendix 2 for the whole set of geochemistry samples). Intrusion permeability varies according to Figure 24 and country rock permeability was 10^{-14} m^2. In Figure 34, magma is fully crystallized 153 kyrs after the intrusion. Software limitations did not allow using these parameters in the whole set of simulations performed in this project.

Results from Varying Geothermal Gradient

In this section, the effect of changing geothermal gradient on the cooling history of the Linga complex will be investigated. The values to be analyzed are 10, 20, 25, 30, and 40 °C/km. Figure 35 illustrates the influence of each one of these geothermal gradients during 400 kyrs of cooling of the Linga complex. These five temperature profiles correspond to bottom center of the batholith at 6 km depth using a permeability of 10^{-15} m^2. Thus, the five curves start at 900°C, the initial temperature of the intrusion.

By varying the geothermal gradient between 10 and 40 °C/km, the time for crystallization varied between 145 and 150 kyrs. According to the HYDROTHERM modeling, increasing the geothermal gradient in a stepwise fashion did not increase the crystallization time in a corresponding stepwise fashion as expected. This needs more study; however, we can conclude that at a depth of 3-6 km the cooling time to

186
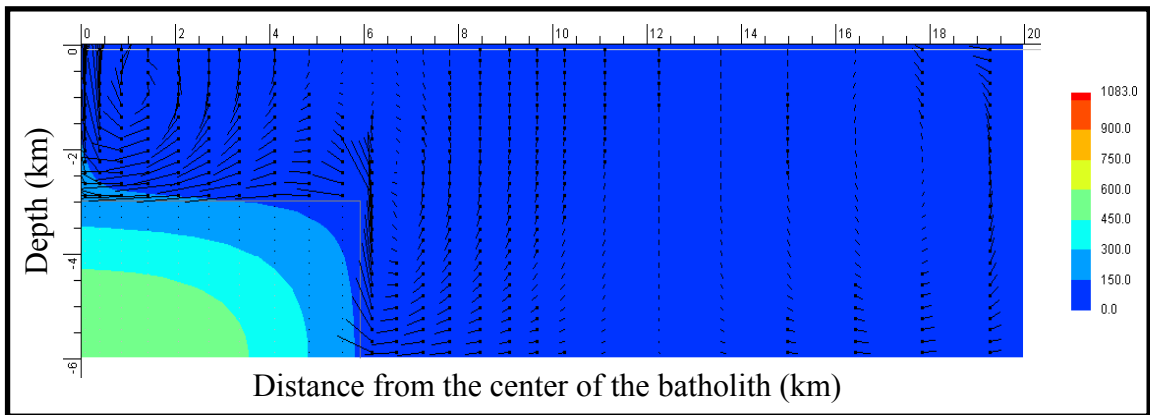
Figure 34. Magma crystallization at the Linga complex with density of 2.64 g/cm^3 and temperature of the intrusion of 1083°C. Permeability of the country rock 10^{-14} m^2.
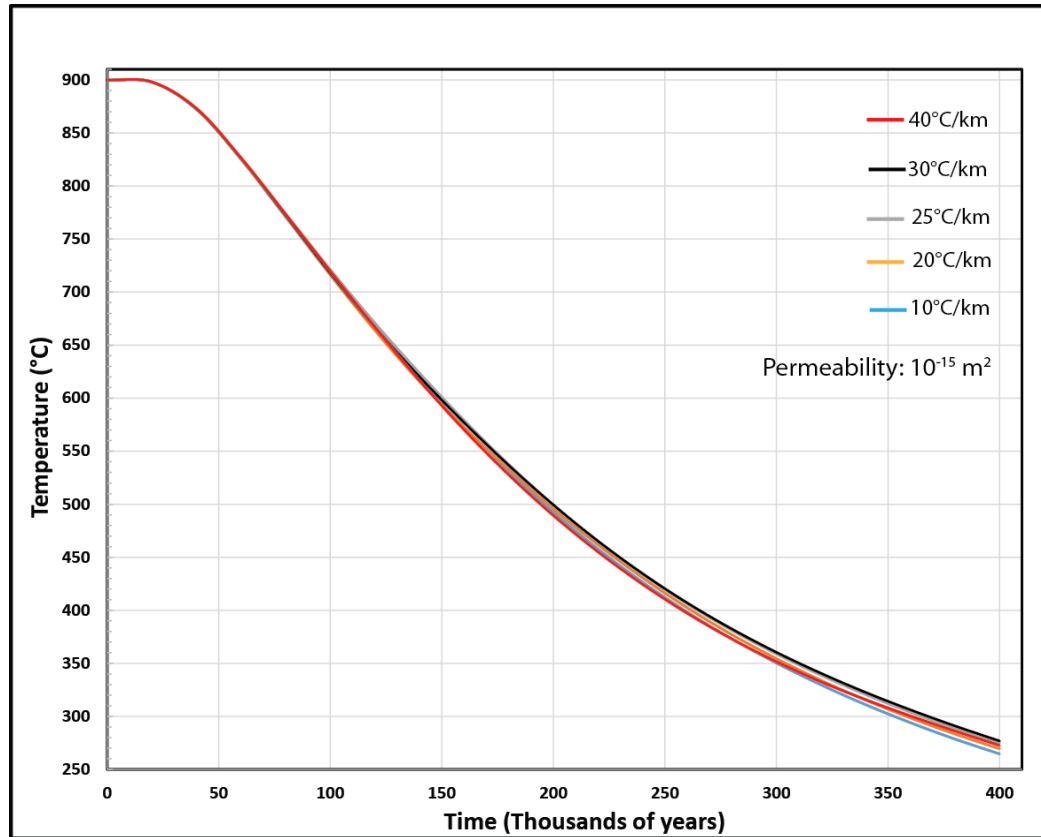
Figure 35. Cooling history at the center of the Linga complex using five different geothermal gradients for the country rock. The time for magma crystallization is approximately 150 kyrs. The difference between the highest and the lowest temperature after 400 kyrs of cooling is around 20°C.

crystallization changes by less than 3% over any reasonable variation in geothermal gradient. This result suggests that variation in geothermal gradient in the country rock had little effect on the cooling rate.

Results from Varying the Initial Temperature of the Intrusion

In modeling the temperature distribution during episodic intrusions of dykes, Yoshinobu et al. (1998) used 850°C as the initial temperature of the intrusion. The model suggested that a simultaneous change in composition of the intruding magma from felsic to mafic i.e. a higher temperature, and thermal diffusivity, would raise the heat content of the system, increasing its lifespan. Cathles (1977), in modeling the thermal history of a hypothetical hydrothermal system, used 700°C as the initial temperature of the intrusion.

In previous simulations of the thermal history of the Linga complex in this project, it has been assumed that the intruding magma has an initial temperature of 900°C. Now, the modeling in this section presents an analysis of the influence of the temperature of magma intrusions on the cooling history of the Linga complex.

Figures 36a-d compare the thermal history at 100 kyrs intervals for the center of the Linga complex (left boundary of the conceptual model) for four different initial temperatures of magmatic intrusions, i.e. for 700, 800, 900, and 1000°C, a range that includes granitic and the low extreme of basaltic magmas. The temperature-depth profiles in Figure 36a-d show that magma fully crystallizes respectively at about 90, 120, 150 and 170 kyrs after the intrusion. Note that the time for magma crystallization with an initial intrusion temperature of 700°C is about a half of the time for magma crystallization when the initial intrusion temperature of 1000°C.
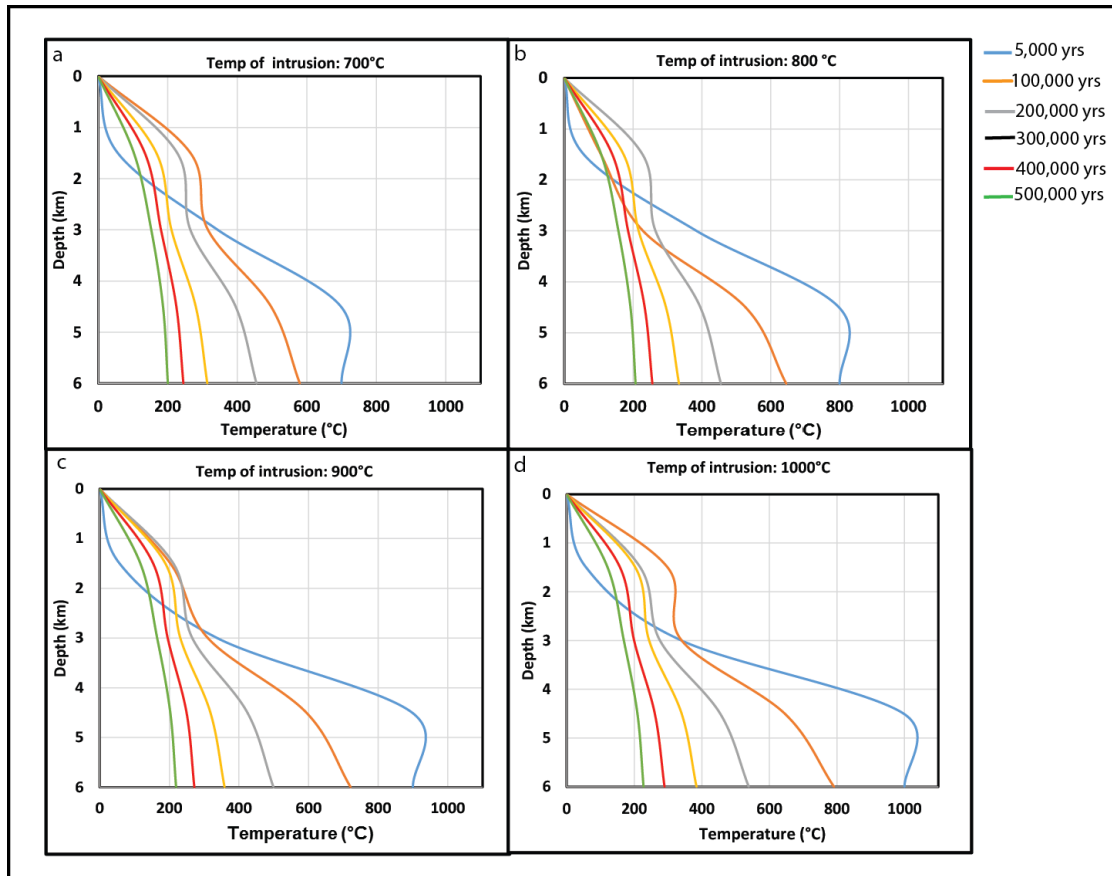
Figure 36. Temperature-depth profiles at the center of the Linga complex resulting from using different initial temperature of intruding magma. The time to crystallization at 6 km depth is about 90, 120, 150 and 170 kyrs respectively, after the intrusion. Country rock permeability: 10^{-15} m^2.

Thus, modeling suggests that varying the initial temperature of the intrusion can also exert a significant influence on the time for magma crystallization in the Linga complex. These results are also in agreement with the models from Yoshinobu et al. (1998) and Cathles (1977).

Results from Varying the Depth to Top of the Pluton

Depth to top of the intrusion is another parameter involved in the cooling history of magmatic intrusions. This section will investigate how changing this parameter affects the thermal evolution of the Linga complex.

Figures 37a-b illustrate the effect of increasing the depth to the top of the intrusion from 3 to 4 km using a permeability of 10^{-15} m^2. The simulation was performed until full crystallization which occurred 151 kyrs after the intrusion for the hydrothermal system in Figure 37a and at 153 kyrs for the hydrothermal system in Figure 37b. Thus, the effect of changing depth of emplacement by 1 km is negligible.

This is probably because the geothermal gradient produces only slightly hotter country rocks when going 1 km deeper. In similar studies, Bowers et al. (1990) built a two-dimensional conduction cooling model for the thermal evolution of the Cupsuptic pluton in Maine. The depth to top of the intrusion used in the modeling was from 11 to 12 km and had little influence on the cooling history of the pluton.

The pioneering heat flow model of Norton and Knight (1977) showed that intrusions with depth to top of the pluton < 2.2 km generate thermal distributions able to produce two phases i.e. water and vapor. Depths to top of the pluton > 2.2 km generate

191
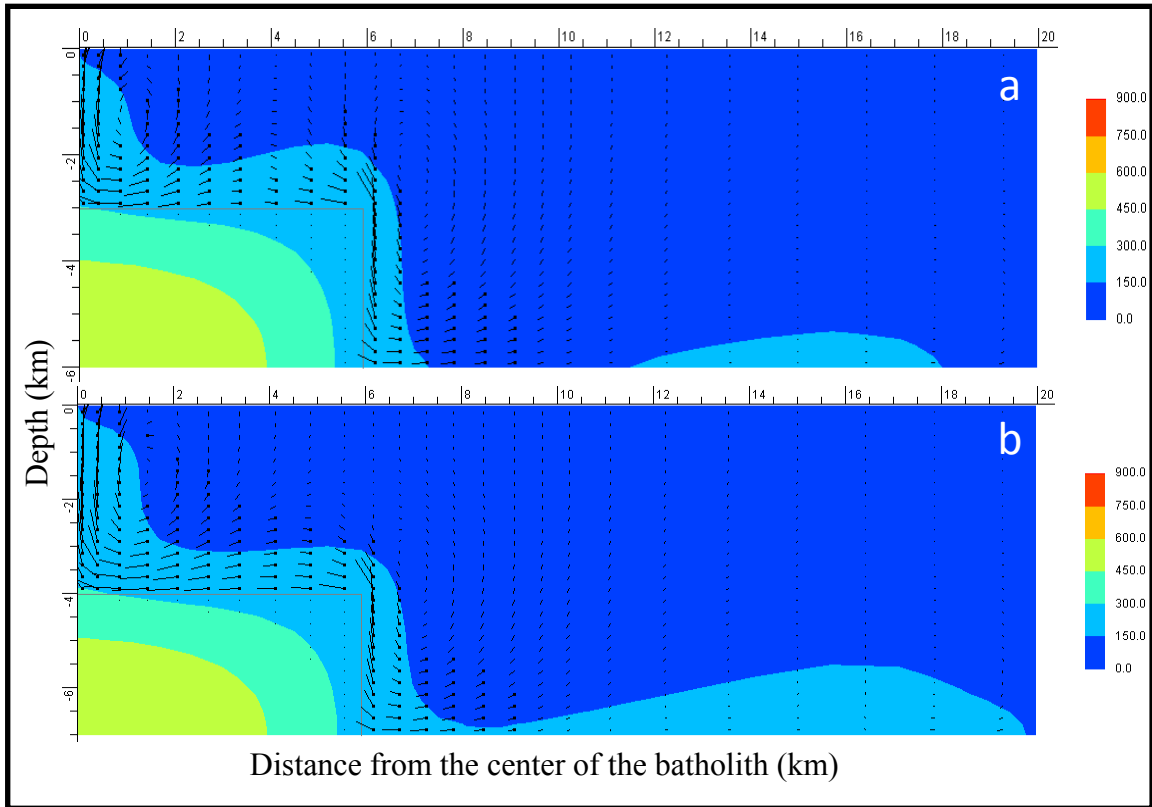
Figure 37. Temperature and fluid flux distribution for depths of emplacement to a) 3 km and b) 4 km. Permeability of the country rock: 10^{-15} m^2. Magma crystallization was reached at 151 kyrs in Figure 37a and 153 kyrs in Figure 37b.

thermal distributions with larger circulation cells that preserve the energy of the system

for a longer time.

In the modeling of Hayba and Ingebritsen (1997), depth to the top of the intrusion

was varied from 2 to 5 km. Their model indicated that deeper intrusions can develop two-

phase conditions and persist longer that shallower intrusions.

Using Stable Isotope Data to Constrain the Thermal Modeling

Alteration assemblages provide information about the temperature of interaction

between rocks and hydrothermal fluids from different sources (Guilbert and Park, 1986;

Rose and Burt, 1979). Hydrothermal fluid sources are indicated by $\delta^{18}O$ and δD values

from altered rocks (Criss, 1999; Sharp, 2007). This information is useful in modeling the

thermal history of the Linga complex by knowing under which circumstances of

permeability and temperature, the rocks in the Linga complex underwent hydrothermal

alteration.

Field observations along several transects across the Linga complex suggest that

propylitic and potassic alteration are the most abundant types of alteration in the area

(Figure 22). The ubiquity of potassic and propylitic alteration in the study area is noted

by Agar (1981) and Moore (1979). Isotopic values of $\delta^{18}O$ (see Chapter 3) suggested that

the alteration was mostly the result of the interaction between rock and magmatic water.

Table 6 summarizes GPS, main type of alteration, unit and location for each one

of the altered samples used in this analysis. These samples were all collected by the

author of this dissertation during summer of 2014. Figure 38 shows the geographic

location of the samples as well as their position with respect to an ideal rectangular

Table 6. Summary of hydrothermally altered samples from the Linga complex

Sample	GPS		Alteration	Unit	Location
14721Ac	13.70707S	75. 83489W	Potassic	Auquish	Rio Pisco transect
14721B	13.66606S	75.77181W	Propylitic	Auquish	Rio Pisco transect
14725F	13.66006	75.76045W	Potassic	Pampahuasi	Rio Pisco transect
14714Ca	13.84743S	75.75401W	Potassic	Humay	Quebrada Larga
14714Cb	13.84743S	75.75401W	Potassic	Quilmana	Quebrada Larga
14714Eb	13.83944S	75.76015W	Potassic	Humay	Quebrada Larga
14724Ac	13.9544S	75.62615W	Potassic	Rinconada	Mina Santa Rosa
14723Aa	14.01916S	75.58982W	Propylitic	Pampahuasi	Mina Cansas
14723D	14.00145S	75.58366W	Propylitic	Pampahuasi	Quebrada Cansas
14716G	13.99522S	75.56576W	Propylitic	Pampahuasi	Quebrada Cansas

Figure 38. Ideal geometry of the Linga complex (black rectangle) showing four linear cross sections (dashed lines) that contain the location of altered samples.
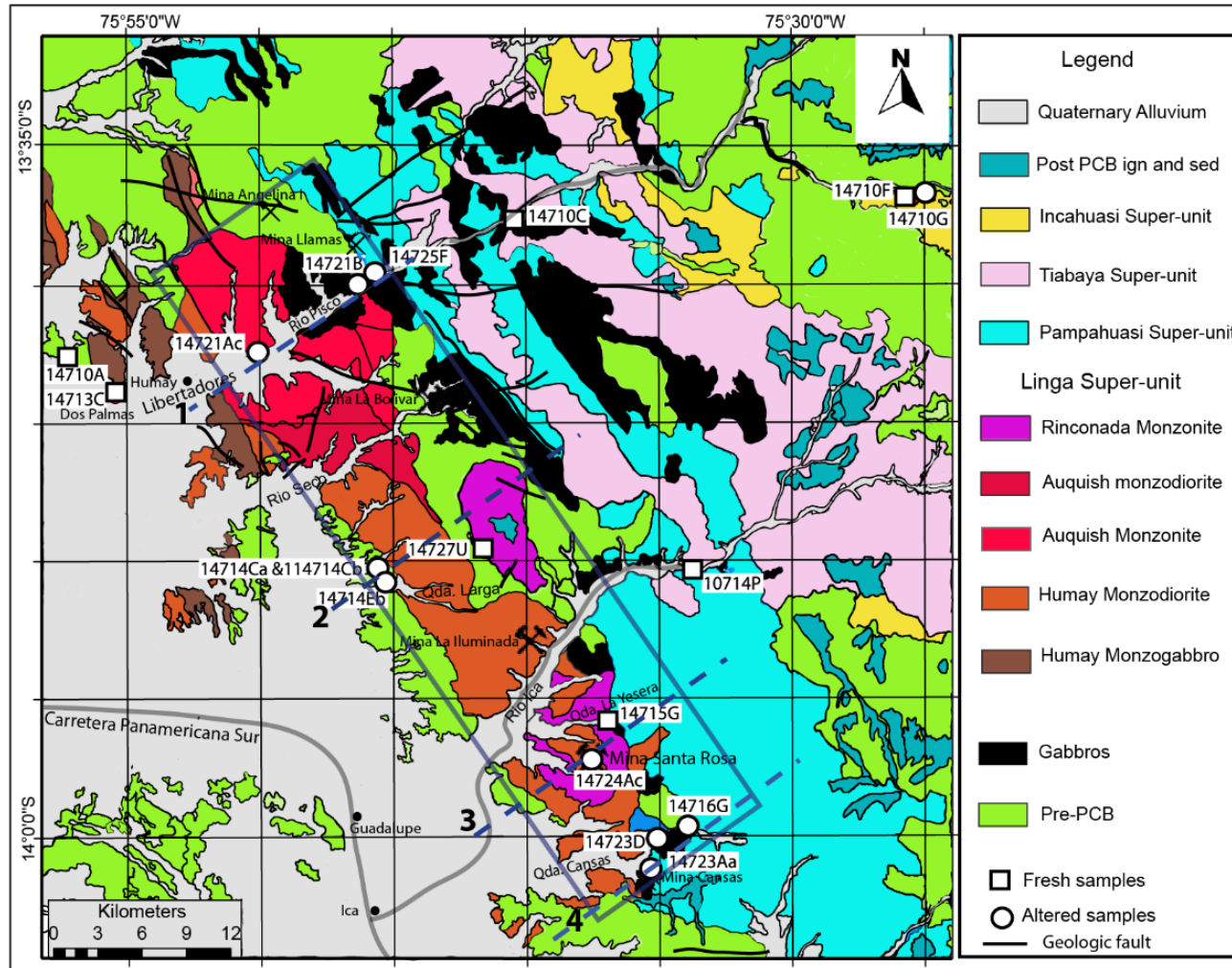
geometry of the Linga complex on four transects crossing the batholith. Potassic alteration, which occurs at temperatures from 450 to 600ºC (Pirajno, 2009), is widespread in 6 samples. Propylitic alteration, which occurs at temperatures from 250°C to 350°C (Dilles et al., 1992; Hedenquist et al., 2000) is notable in 4 samples.

Figure 39 presents a possible scenario to explain the potassic alteration assemblage displayed by sample 14721Ac. This sample was collected at the northwest extreme of the Linga complex in transect 1. At some point of its thermal history, this sample was under the influence of hydrothermal fluids in the range of temperature from 450 to 600°C. The fact that the potassic alteration assemblage remains in the sample implies that this rock was not subject to another alteration event. The simulation in Figure 39 reveals that a country rock permeability of 10^{-16} m^2 along with a temperature from 450 to 600°C were important factors in reaching potassic alteration assemblages.

Figure 40 presents a possible scenario to explain the potassic alteration assemblage displayed by sample 14724Ac. This sample was collected close to the center of the Linga complex on transect 3, at the south-east extreme of the Linga complex. At some point of its thermal history, this sample was under the influence of hydrothermal fluids in the range of temperature from 450 to 600°C. Temperature and potassic alteration of this sample were probably attained under a country rock permeability of 10^{-16} m^2 and a depth to top of the pluton of 3 km.
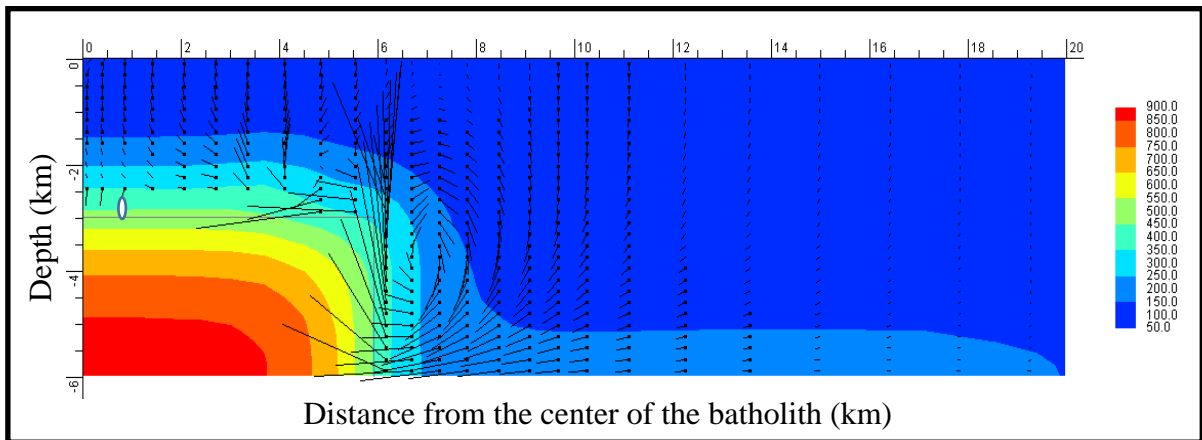
Figure 39. Probable thermal setting for the development of potassic alteration in samples 14724Ac and 14721Ac. Permeability of the country rock: 10^{-16} m^2, permeability of the intrusion is a function of temperature. Depth to top of the pluton: 3 km.
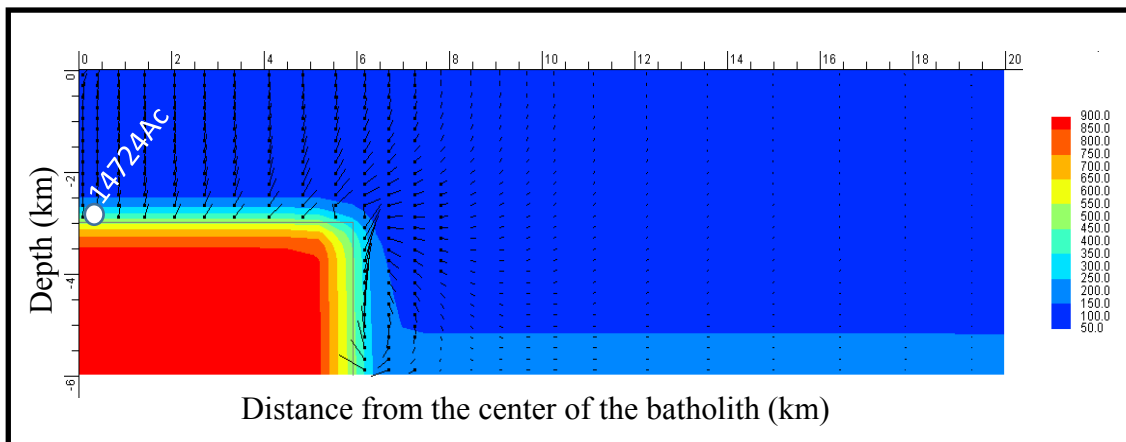
Figure 40. Probable thermal setting for the development of potassic alteration in samples 14724Ac. Permeability of the country rock: 10^{-16} m^2, permeability of the intrusion is a function of temperature. Depth to top of the pluton: 3 km.

Samples 14714Ca, 14714Cb and 14714Eb on transect 2 were under the influence of hydrothermal fluids with a temperature from 450 to 600ºC at the west side of the Linga complex. The interaction with these fluids produced potassic alteration. Figure 41 displays a possible thermal setting in which these rocks were altered. These temperature and fluid pattern distribution in the Linga complex was probably attained with a country rock permeability of 10^{-17} m^2 and a permeability of the intrusion varying as a function of temperature.

Figure 42 is a cross section of transect 2. This plot depicts the approximate location of samples 14714Ca, 14714Cb and 14714Eb at the S-W end of the cross section.

These samples were collected at the boundary between the Pre-PCB Quilmana and the Linga-Humay. Potassic alteration was probably caused by magmatic fluids exsolved from the intrusion of the monzodiorite of Humay into the volcanics. However, since HYDROTHERM interactive models just groundwater convection, another possibility for the emergence of potassic alteration is as follows: The magmatic intrusion that formed the Humay monzodiorite originated groundwater convection in the country rock. This convecting water reached at some point of the thermal history, temperatures from 450 to 600°C, which caused potassic alteration assemblages.

Samples 14721B and 14725F on transect 1 underwent propylitic and potassic alteration respectively. Figure 43 depicts the possible location and thermal setting in which these samples were altered. Permeability of the country rock was of 10^{-16} m^2 and permeability of the intrusion varied with temperature according to Figure 24.

Samples 14716G, 14723Aa and 14723D on transect 4, collected at the Southeast end of the Linga complex show propylitic alteration. Hydrothermal fluids that caused the

alteration were probably at a temperature from 250 to 350 ºC. Figure 44 shows a possible thermal setting in which these samples attained the alteration. Permeability of the country rock was in the order of 10^{-15} m^2, permeability of the intrusion varied with temperature and depth to top of the pluton of 3 km.

Conclusions

The present study modeled the cooling history of the Linga complex to understand how different parameters might in general affect the cooling of plutons in other places.

Different simulations were performed to explore how the variations in parameters affect the cooling rates. Two modeling software were used, MATLAB and the USGS software HYDROTHERM interactive.

The study revealed that decreasing the width of the Linga complex by 33% i.e. from 12 to 8 km, reduces the time for magma crystallization by 21%, i.e. from 174 kyrs to 138 kyrs. Decreasing thickness of the batholith by 33%, i.e. from 3 to 2 km, reduces the time for magma crystallization from 174 kyrs to 89 kyrs, almost by 50%.

Although there are many variables involved in the cooling history of the Linga complex, multiple simulations indicate that permeability of both the country rock and the intrusion played a significant role in cooling of the Linga complex. Thus, the time for magma crystallization at the bottom center of the Linga complex was approximately 180 kyrs for a permeability of 10^{-22} m^2, 175 kyrs for 10^{-16} m^2, 150 kyrs for 10^{-15} m^2, and 125 kyrs for 10^{-14} m^2. Thus, the time for magma crystallization decreases about 30% between the lowest and highest permeability.
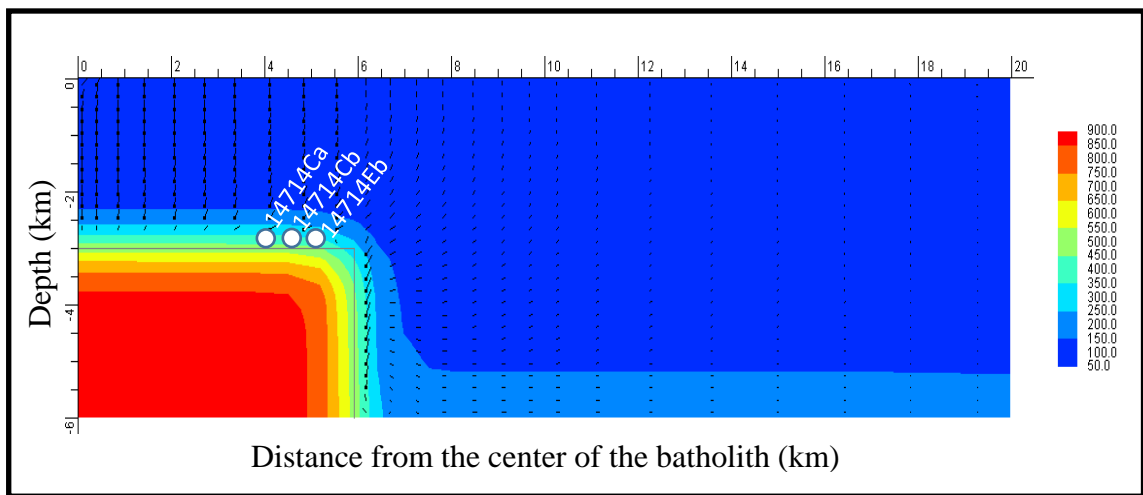
Figure 41. Probable thermal setting for the development of potassic alteration in samples 14714Ca, 14714Cb and 14714Eb. Permeability of the country rock: 10^{-17} m^2, permeability of the intrusion is a function of temperature. Depth to top of the pluton, 3 km.
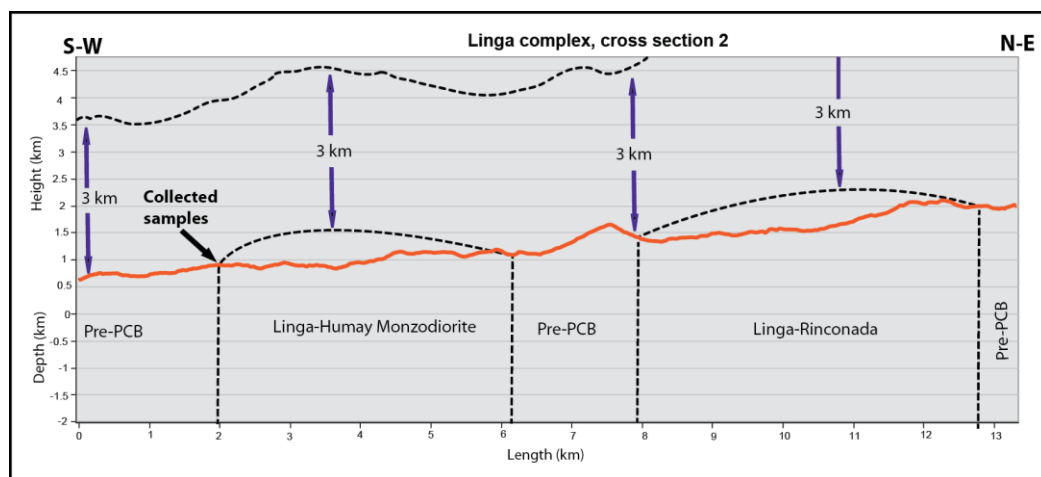
Figure 42. Cross section through transect 2 of Figure 38. Samples 14714Ca, 14714Cb and 14714Eb were collected to the S-W end of the cross section (black arrow) at the boundary between the Pre-PCB and the Linga-Humay Monzodiorite. Dashed lines beneath the profile indicate assumed edges of the different intrusions and the probable path for emergence to the Earth's surface. Dashed lines above the profile indicate the Pre-PCB volcanic or sedimentary cover that has been eroded away through geologic time.
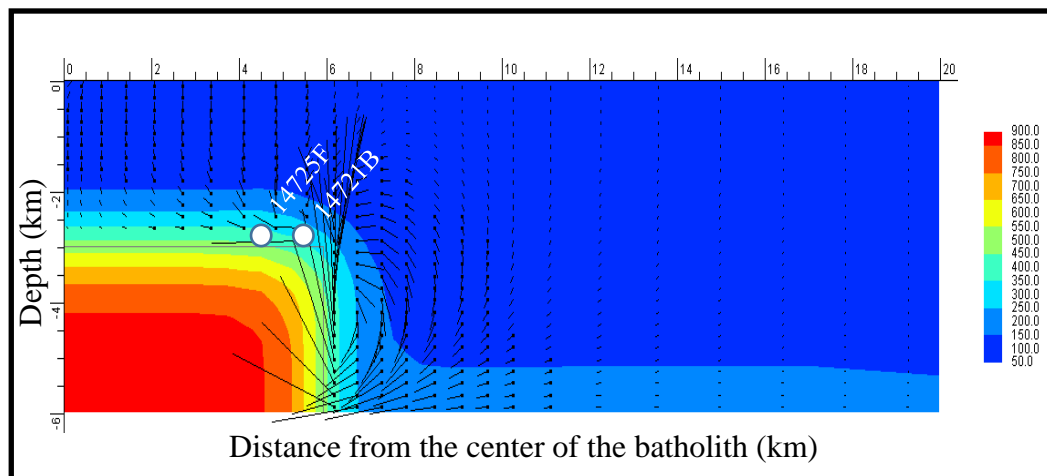
Figure 43. Probable thermal setting for the development of potassic alteration in sample 14725F, and propylitic alteration in sample 14721B. Permeability of the country rock: 10^{-16} m^2, permeability of the intrusion is a function of temperature. Depth to top of the pluton: 3 km.
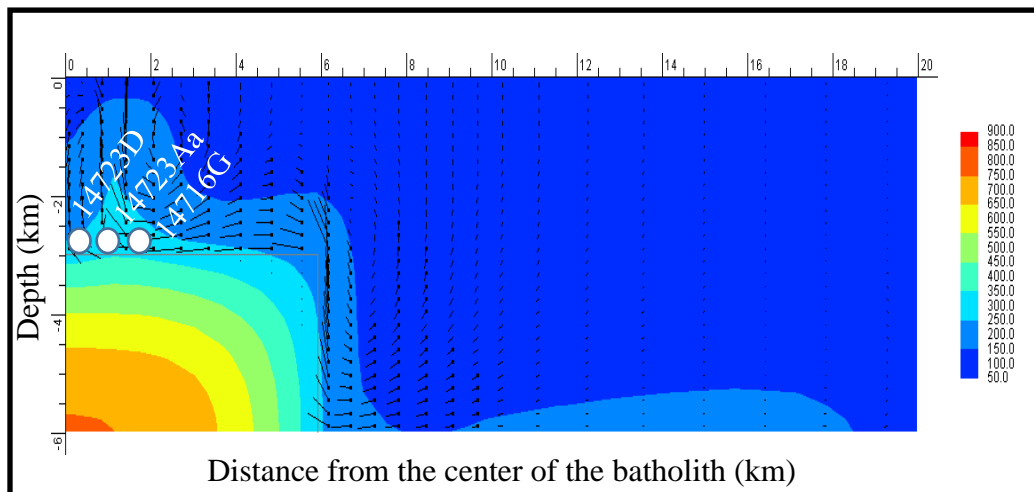
Figure 44. Probable thermal setting for the development of propylitic alteration in samples 14716G, 14723Aa and 14723D. Permeability of the country rock: 10⁻¹⁵ m², permeability of the intrusion is a function of temperature. Depth to top of the pluton: 3 km.

The time for magma crystallization decreased about 5 kyrs when the geothermal gradients was decreased from 40 and 10°C/km. Crystallization occurred at 152 and 147 kyrs. Thus, the difference in time of about 3% indicates that the geothermal gradient has little effect on the cooling rate.

Assuming initial temperatures for the intrusion of 700, 800, 900 and 1000°C, temperature-depth profiles show that magma fully crystallizes respectively at about 90, 120, 150 and 170 kyrs after the intrusion. Thus, the time for magma crystallization with an initial intrusion temperature of 700°C is about a half of the time for magma crystallization when the initial intrusion temperature is of 1000°C. This finding indicated that the initial temperature of the intrusion is a significant factor in the cooling history of the Linga complex.

Increasing the depth to top of the Linga complex from 3 to 4 km resulted in a time difference of 2 kyrs, from 151 kyrs to 153 kyrs, which represents roughly a 1.5% difference until magma crystallization at 600°C. Thus, a variation of 1 km in depth to top of the pluton did not affect significantly the time for magma crystallization.

Magma crystallization just by conduction occurred at about 208 kyrs after the intrusion, and by conduction plus convection of hydrothermal fluids in about 153 kyrs. Thus, the time for magma crystallization by conduction plus convection of hydrothermal fluids is about 74% of the time required for magma crystallization considering heat transfer only by conduction.

Hydrothermal alteration assemblages at the Linga complex were the result of the interplay among different factors. The modeling suggests that potassic alteration could occur if the permeability of the country rock is on the order of 10^{-17} to $10^{-16}\,m^2$, and

an intrusion permeability varying as a function of temperature. The modeling also suggests that propylitic alteration could occur if the permeability of the country rock in the order of 10^{-16} to 10^{-15} m^2 and permeability of the intrusion changing as a function of temperature. These simulations really needed to be done by varying permeability, intrusion temperature, and other parameters over a wide range of values to yield hydrothermal fluid temperatures at the sample locations that corresponded to the values expected for these two kinds of alteration; however, HYDROTHERM doesn't allow easy variation of these parameters to facilitate such modeling.

Summarizing, width and thickness of the intrusion, permeability of both the country rock and the intrusion as well as initial temperature of the intrusion are significant factors in the thermal history of the Linga complex. Whereas, geothermal gradient and depth to top of the intrusion have little effect on the cooling history of the Linga complex.

References

Adam, J. A., 2003, Mathematics in Nature: Modeling Patterns in the Natural World, New Jersey, Princeton University Press.

Agar, R. A., 1981, Copper mineralization and magmatic hydrothermal brines in the Rio Pisco section of the Peruvian Coastal Batholith: Economic Geology, v. 76, p. 677-693.

Agar, R. A., and Le Bel, L., 1985, The Linga Super-unit: High-K diorites of the Arequipa segment, *in* W.S. Pitcher, M. P. Atherton, Cobbing, E. J., and Beckinsale, R. D., eds., Magmatism at a Plate Edge: The Peruvian Andes: New York, John Wiley and Sons., p. 119-127.

Annen, C., Blundy, J. D., and Sparks, R. S. J., 2006, The genesis of intermediate and silicic magmas in deep crustal hot zones: Journal of Petrology, v. 47, no. 3, p. 505-539.

Annen, C. J., 2009, From plutons to magma chambers: Thermal constraints on the accumulation of eruptible silicic magma in the upper crust: Earth and Planetary Science Letters, v. 284, no. 3,4, p. 409-416.

Bea, F., 2010, Crystallization dynamics of granite magma chambers in the absence of regional stress: Multiphysics modeling with natural examples: Journal of Petrology, v. 51, no. 7, p. 1541-1569.

Belousov, V., I, and Belousova, I., V., 2016, Heat transfer in hydrothermal-magmatic systems, Workshop on Geothermal Reservoir Engineering Stanford University, Stanford, California, February 22-24 2016, p. 1-12.

Best, M., G, and Christiansen, E. H., 2001, Igneous Petrology, USA, Blackwell Science.

Blundy, J. D., and Annen, C. J., 2016, Crustal Magmatic Systems from the Perspective of
Heat Transfer: Elements, v. 12, p. 115-120.

Bowers, J. R., Kerrick, D. M., and Furlong, K. P., 1990, Conduction model for the
thermal evolution of the Cupsuptic aureole, Maine: American Journal of Science,
v. 290, p. 644-665.

Brown, M., 2013, Granite: From genesis to emplacement: GSA Bulletin, v. 125, no. 7-8,
p. 1079-1113.

Burchardt, S., 2009, Mechanisms of Magma Emplacement in the Upper Crust
[Doktorgrades]: Georg-August-Universität zu Göttingen, 125 p.

Caricchi, L., Annen, C., Rust, A., and Blundy, J., 2012, Insights into the mechanisms and
timescales of pluton assembly from deformation patterns of mafic enclaves:
Journal of Geophysical Research, v. 117, no. B11206, p. 1-18.

Cathles, L., M., 1977, An analysis of the cooling of intrusives by ground-water
convection which includes boiling: Economic Geology, v. 72, no. 5, p. 804-826.

Cho, W. J., Kwon, S., and Choi, J. W., 2009, The thermal conductivity for granite with
various water contents: Engineering geology, v. 107, no. 3-4, p. 167-171.

Clauser, C., Giese, P., Huenges, E., Kohl, T., Lehman, H., Ryach, L., Saafanda, J.,
Wilhel, H., Windloff, K., and Zoth, G., 1997, The thermal regime of the
crystalline continental crust: Implications from the KTB: Journal of Geophysical
Research, v. 102, no. B8, p. 18417-18441.

Copeland, P., Harrison, T. M., Yun, P., Kidd, W. S. F., Roden, M., and Yuquan, Z., 1995,
Thermal evolution of the Gangdese Batholith, southern Tibet: A history of
episodic unroofing: Tectonics, v. 14, no. 2, p. 223-236.

Couch, R., Whitsett, R., Huehn, B., and Briceno, L., 1981, Structures of the continental margin of Peru and Chile: GSA Memoir, v. 154, p. 703-726.

Crawford, M. L., Klepeis, K. A., Gehrels, G., and Clark, I., 1999, Batholith emplacement at mid-crustal levels and its exhumation within an obliquely convergent margin: Tectonophysics, v. 312, p. 57-78.

Criss, R. E., 1999, Principles of Stable Isotope Distribution, New York, Oxford Univesity Press.

Cruden, A. R., 1998, On the emplacement of tabular granites: Journal of the Geological Society, v. 155, p. 853-862.

Curewitz, D., and Karson, J. A., 1977, Structural settings of hydrothermal outflow: Fracture permeability maintained by fault propagation and interaction: Journal of Volcanology and Geothermal Research, v. 79, p. 149-168.

Delaney, P. T., 1982, Rapid intrusion of magma into wet rock: Groundwater flow due to pore pressure increases: Journal of Geophysical Research, v. 87, no. B9, p. 7739-7756.

Dilles, J. H., Solomon, G. C., Taylor, H. P., and Einaudi, M. T., 1992, Oxygen and hydrogen isotope characteristics of hydrothermal alteration at the Ann-Mason Porphyry Copper Deposit, Yerington, Nevada: Economic Geology, v. 87, p. 44-63.

Dobson, P., Asanuma, H., Huenges, E., Poletto, F., Reinsch, T., and Sanjuan, B., 2017, Supercritical geothermal systems-A review of past studies and ongoing research activities, Proceedings, 41st Workshop on Geothermal Reservoir Engineering: Stanford University, Stanford, California. February 13-15, 2017, p. 1-13.

Eppelbaum, L., Kutasob, I., and Pilchin, A., 2014, Applied Geothermics, USA, Springer-Verlag.

Ernst, W. G., 2005, Alpine and Pacific styles of Phanerozoic mountain building: subduction-zone petrogenesis of continental crust: Terra Nova, v. 17, p. 165-188.

Fetter, C. W., 2001, Applied Hydrogeology, USA, Prentice- Hall.

Flores, E. L., Prol, R. M., and Royer, J. J., 2001, Boundary conditions in thermal models: An application to the KTB site, Germany: Geofísica Internacional, v. 40, no. 2, p. 97-109.

Fowler, C. M. R., 2005, The Solid Earth: An Introduction to Global Geophysics, UK, Cambridge University Press.

Frish, W., Meschede, M., and Blakey, R., 2011, Plate Tectonics Continental Drift and Mountain Building, New York, Springer.

Guilbert, J. M., and Park, C. F., 1986, The Geology of Ore Deposits, USA, W. H. Freeman and Company.

Haederle, M., and Atherton, M. P., 2001, Shape and intrusion style of the Coastal Batholith, Peru: Tectonophysics, v. 345, p. 17-28.

Harmoko, U., Fujimitsu, Y., and Ehara, S., 2007, Shallow ground temperature anomaly and thermal structure of Merapi Volcano, Central Java, Indonesia: Journal of the Geothermal Research Society of Japan, v. 29, no. 1, p. 25-37.

Harrison, T. M., Watson, E. B., and Aikman, A. B., 2007, Temperature spectra of zircon crystallization in plutonic rocks: Geology, v. 35, no. 7, p. 635-638.

Hayba, D. O., and Ingebritsen, S. E., 1994, The computer model HYDROTHERM, a three-dimensional finite-difference model to simulate ground-water flow and heat

transport in the temperature range of 0 to 1200°C: USGS Geological Survey. Water-Resources Investigations. Report 94-4045.

-, 1997, Multiphase groundwate flow near cooling plutons: Journal of Geophysical Research, v. 102, no. B6, p. 12235-12252.

Hedenquist, J. W., Arribas, A., and Gonzalez, E., 2000, Exploration for epithermal gold deposits: SEG reviews, v. 13, p. 245-277.

Heide, K., and Schmidt, C. M., 2005, Determination of volatiles in volcanic rocks and minerals with a Directly Coupled Evolved Gas Analyzing System (DEGAS)-Part I: Interpretation of degassing profiles (DEGAS-profiles) of minerals and rocks on the basis of melting experiments: Annals of Geophysics, v. 48, no. 4-5, p. 719-729.

Hestenes, D., 1987, Toward a modeling theory of physics instruction: American Journal of Physics, v. 55, no. 5, p. 440-454.

Ingebritsen, S. E., and Sanford, W. E., 1998, Groundwater in Geologic Processes, USA, Cambridge University Press.

Jamtveit, B., Kobchenko, M., Austrheim, H., Malthe, A., Royne, A., and Svensen, H., 2011, Porosity evolution and crystallization-driven fragmentation during weathering of andesite: Journal of Geophysical Research, v. 116, no. B12204, p. 1-12.

Jaupart, C., and Mareschal, J. C., 2007, Heat flow and thermal structure of the lithosphere, *in* Gerald, S., ed., Treatise on Geophysics: Oxford, Elsevier, p. 217-253.

Jerram, D., and Petford, N., 2011, The Field Description of Igneous Rocks, Singapore, Wiley-Blackwell.

Kearey, P., Klepeis, K. A., and Vine, F. J., 2009, Global Tectonics, UK, Wiley-Blackwell.

Kipp, K. L., Hsieh, P. A., and Charlton, S. R., 2008, Guide to the revised ground-water flow and heat transport simulator: HYDROTHERM-Version 3: USA, United State Geological Survey.

Larsen, E. S., 1945, Time required for the crystallization of the Great Batholith of Southern and Lower California: American Journal of Science, v. 243A, p. 399-416.

Lave, C., and March, J. J., 1995, An Introduction to Models in the Social Sciences, USA, Longman Publishers.

Lechler, P. J., and Desilets, M. O., 1987, A review of the use of loss on ignition as a measurement of total volatiles in whole-rock analysis: Chemical Geology, v. 63, no. 3-4, p. 341-344.

Longo, G., 2003, Computer modelling and natural phenomena, Proceedings of the 9th European software engineering conference, ESEC/FSE-11, New York.

Magnusdottir, L., 2014, Modeling the deep roots of geothermal systems, Thirthy-Ninth Workshop on Geothermal Reservoirs Engineering, February 24-26, 2014: Stanford, CA.

Manning, C. E., and Bird, D. K., 1995, Porosity, permeability, and basalt metamorphism: GSA Special Paper, v. 296, p. 123-140.

Martin, D., Griffiths, R., W, and Campbell, I. H., 1987, Compositional and thermal
convection in magma chambers: Contributions to Mineralogy and Petrology, v.
96, p. 465-475.

Matlab, 2012, Mathworks the language of technical computing, USA, The MathWorks,
Inc.

Moore, N. D., 1979, The Geology and Geochronology of the Arequipa Segment of the
Coastal Batholith of Peru [Doctor in Philosophy]: Liverpool, 549 p.

-, 1984, Potassium-argon ages from the Arequipa segment of the Coastal Batholith of
Peru and their correlation with regional tectonic events: Journal of the Geological
Society, v. 141, no. 3, p. 511-519.

Mottaghy, D. C., Vosteen, H. D., and Schellschmidt, R., 2007, Temperature dependence
of the relationship of thermal diffusivity versus thermal conductivity for
crystalline rocks: International Journal of Earth Sciences, v. 97, no. 2, p. 1-435.

Murphy, M. D., Sparks, R. S. J., Barclay, J., Carroll, M. R., Lejeune, A. M., and Brewer,
T. S., 1998, The role of magma mixing in triggering the current eruption at the
Soufriere Hills Volcano, Montserrat, West Indies: Geophysical Research Letter,
v. 25, no. 18, p. 3433-3436.

Mysen, B., 2014, Water-melt interaction in hydrous magmatic systems at high
temperature and pressure: Progress in Earth and Planetary Science, v. 1, no. 1, p.
1-18.

Nakada, S., Shimizub, I., and Ohtab, K., 1999, Overview of the 1990-995 eruption at
Unzen Volcano: Journal of Volcanology and Geothermal Research, v. 89, no. 1-4,
p. 1-22.

Norton, D., and Cathles, L., M., 1979, Thermal aspects of ore deposition, *in* Barnes, H. L., ed., Geochemistry of Hydrothermal Ore Deposits: USA, John Wiley and Sons Inc.

Norton, D., and Knapp, R., 1977, Transport phenomena in hydrothermal systems: The nature of porosity: American Journal of Science, v. 277, no. 8, p. 913-936.

Norton, D., and Knight, J., 1977, Transport phenomena in hydrothermal systems: Cooling plutons: American Journal of Science, v. 277, p. 937-981.

Norton, D. L., 1984, Theory of hydrothermal systems: Annual Review of Earth and Planetary Sciences, v. 12, p. 155-177.

Oksanen, M., Volcan, A., and Fenici, P., 1996, Simulations on the accuracy of laser-flash data analysis: Review of Progress in Quantitative Nondestructive Evaluation, v. 15, p. 549-552.

Parmentier, E. M., and Schedl, A., 1981, Thermal aureoles of igneous intrusions: Some possible indications of hydrothermal convective cooling: The Journal of Geology, v. 89, no. 1, p. 1-22.

Paterson, S. R., Okaya, D., Memeti, V., Economos, R., and Miller, R. B., 2011, Magma addition and flux calculations of incrementally constructed magma chambers in continental margin arcs: Combined field, geochronologic, and thermal modeling studies: Geosphere, v. 7, no. 6, p. 1439-1468.

Paul, B. J., 2004, Modelling Approaches to Geodynamic Processes [Doctor of Natural Sciences]: Swiss Federal Institute of Technology, 259 p.

Pirajno, F., 2009, Hydrothermal Processes and Mineral Systems, Australia, Springer.

Plank, T., Kelley, K. A., Zimmer, M. M., Hauri, E. H., and Wallace, P. J., 2013, Why do mafic arc magmas contain ~ 4 wt% water on average?: Earth and Planetary Science Letters, v. 364, p. 168-179.

Plummer, C. C., Carlson, D. H., and McGeary, D., 2007, Physical Geology, New York, McGraw-Hill.

Pruseth, K. L., 2009, Calculation of the CIPW norm: New formulas: Journal of Earth System Science, v. 118, no. 1, p. 101-113.

Prusinkiewicz, P., 1998, In search of the right abstraction: The synergy between art, science, and information technology in the modeling of natural phenomena, *in* Sommerer, C., and Mignonneau, L., eds., Art @ Science: Wien, Springer, p. 60-68.

Quarteroni, A., 2009, Mathematical models in science and engineering: Notices of the AMS, v. 56, no. 1, p. 10-19.

Ranjram, M., Gleeson, T., and Luijendijk, T., 2015, Is the permeability of crystalline rock in the shallow crustrelated to depth, lithology or tectonic setting?: Geofluids, v. 15, p. 106-119.

Rose, A. W., and Burt, D. M., 1979, Hydrothermal alteration, *in* Barnes, H. L., ed., Geochemistry of Hydrothermal Ore Deposits: New York, John Wiley & Sons, p. 173-227.

Scharli, U., and Rybach, L., 2001, Determination of specific heat capacity on rock fragments: Geothermics, v. 30, p. 93-110.

Schwartz, G. M., 1959, Hydrothermal alteration: Economic Geology, v. 54, no. 2, p. 161-183.

Seifert, R., Malfait , W. J., Petitgirard, S., and Sanchez-Valle, C., 2013, Density of phonolitic magmas and time scales of crystal fractionation in magma chambers: Earth and Planetary Science Letters, v. 381, p. 12-20.

Sharp, Z. D., 2007, Principles of Stable Isotope Geochemistry, USA, Pearson Prentice-Hall.

Siratovich, P. A., Heap, M. J., Villeneuve, M. C., Cole, J. W., Kennedy, B. M., Davidson, J., and Reuschlé, T., 2016, Mechanical behaviour of the Rotokawa Andesites (New Zealand):Insight into permeability evolution and stress-induced behaviour inan actively utilised geothermal reservoir: Geothermics, v. 64, p. 163-179.

Sparks, R. S. J., and Huppert, H. E., 1984, Density changes during the fractional crystallization of basaltic magmas: fluid dynamic implications: Contributions to Mineralogy and Petrology, v. 85, p. 300-309.

Spera, F., 1980, Thermal evolution of plutons: a parameterized approach: Science, v. 207, no. 4428, p. 299-301.

Springer, M., and Forster, A., 1998, Heat-flow density across the Central Andean subduction zone: Tectonophysics, v. 298, p. 123-139.

Stacewicz, P., and Włodarczyk, A., 2010, Modeling in the context of computer science - a methodological approach: Studies in Logic, Grammar and Rhetoric, v. 20, no. 33, p. 155-179.

Stein, C. A., 1995, Heat flow of the Earth, *in* Ahrens, T. J., ed., Global Earth Physics: A Handbook of Physical Constants: Florida, American Geophysical Union, p. 144-158.

Tarbuck, E. J., Lutgens, F. K., and Tasa, D., 2011, Earth, an Introduction to Physical
Geology, USA, Pearson Prentice Hall.

Tarnmemagi , H. Y., and Wheildon, J., 1974, Terrestrial heat flow and heat generation in
south-west England: Proceedings of the Royal Society of London, v. 38, p. 86-94.

Turcotte, D., and Schubert, G., 2014, Geodynamics, UK, Cambridge University Press.

Ushioda, M., Takahashi, E., Hamada, M., and Suzuki, T., 2014, Water content in arc
basaltic magma in the Northeast Japan and Izu arcs: an estimate from Ca/Na
partitioning between plagioclase and melt: Earth, Planets and Space, v. 66, no.
127, p. 1-10.

Veres, D. S., 2002, A comparative study between loss on ignition and total carbon
analysis on minerogenic sediments: Studia Universitatis Babe-Bolyai, Geologia,
v. XLVII, no. 1, p. 171-182.

Whittington, A. G., Hofmeister, A., M, and Nabelek1, P. I., 2009, Temperature-
dependent thermal diffusivity of the Earth's crust and implications for
magmatism: Nature, v. 458, p. 319-321.

Winter, J. D., 2010, Principles of Igneous and Metamorphic Petrology, New Jersey,
Prentice Hall.

Wolfram, S., 1984, Computer software in science and mathematics: Scientific American,
v. 251, p. 188-203.

Worster, M. G., Huppert, H. E., and Sparks, R. S., 1990, Convection and crystallization
in magma cooled from above: Earth and Planetary Science Letters, v. 101, no. 1,
p. 78-89.

Yardley, B. W. D., and Bodnar, R. J., 2014, Fluids in the continetal crust: Geochemical

    Perspectives, v. 3, no. 1, p. 1-123.

Yokoyama, I., 2005, Growth rates of lava domes with respect to viscosity of magmas:

    Annals of Geophysics, v. 48, no. 6, p. 957-971.

Yoshinobu, A. S., Okaya, D., A, and Paterson, S. R., 1998, Modeling the thermal

    evolution of fault-controlled magma emplacement models: Implications for the

    solidification of granitoid plutons: Journal of Structural Geology, v. 20, no. 9,10,

    p. 1205-1218.

CHAPTER SIX

CONCLUSIONS

The present study was performed in the Ica-Pisco section of the Peruvian Coastal Batholith. Information obtained by field work observations, sample collection, thin sections, elemental geochemistry, and literature review yielded insight on the geology of the area. The study analyzed δD and $\delta^{18}O$ for 18 igneous samples, 7 fresh and 11 with alteration.

Field work observations mainly at contacts between different units and Super-units, revealed mineral associations indicating primarily propylitic and potassic alteration. These conclusions were sustained by the qualitative analysis of 59 thin section from the study area. The type of hydrothermal alteration gives insight about the geothermal and geochemical conditions that caused the alteration as well as the extent of the alteration, which were used to model the heat flow in the area.

Isotopic values of altered samples revealed that magmatic water was the main source of alteration in the Linga complex. The average water/rock ratio of about $1/10$ in the Linga complex implies 1 part of external meteoric or metamorphic hydrothermal fluids to 10 parts rock or magmatic fluids.

Data from fresh samples revealed an interval for reaching isotopic equilibrium from about 590°C to 650°C; a slight west to east increase in $\delta^{18}O$ values implying that the magmatic source has a slightly greater crustal component to the east; and a slight increase in $\delta^{18}O$ values going from older to younger samples which parallels the younging trend toward the east.

The study revealed that decreasing the width of the Linga complex from 12 to 8 km, causes a reduction in time for magma crystallization from 174 to 138 kyrs, which is a reduction of 33%. Decreasing thickness of the Linga complex from 3 to 2 km, reduces the time for magma crystallization from 174 to 89 kyrs, which is a reduction of about 50%.

Multiple simulations indicate that permeability of both the country rock and the intrusion played a significant role in cooling of the Linga complex. Thus, the time for magma crystallization at the bottom center of the Linga complex was approximately 180 kyrs for a permeability of 10^{-22} m^2, 175 kyrs for 10^{-16} m^2, 150 kyrs for 10^{-15} m^2, and 125 kyrs for 10^{-14} m^2. Thus, the decrease in time for magma crystallization is about 30% between the lowest and the highest permeability.

The time for magma crystallization was decreased about 5 kyrs when the geothermal gradient was decreased from 40 to 10°C/km. Crystallization occurred at 152 and 147 kyrs. Thus, the difference in time of about 3% indicate that the geothermal gradient has little effect on the cooling rate.

Assuming initial temperatures for the intrusion of 700, 800, 900 and 1000°C, temperature-depth profiles show that magma fully crystallizes respectively at about 90, 120, 150 and 170 kyrs after the intrusion. Thus, the time for magma crystallization with an initial intrusion temperature of 700°C is about a half of the time for magma crystallization when the initial intrusion temperature of 1000°C.

Increasing the depth to top of the Linga complex from 3 km to 4 km resulted in increasing the cooling rate by 2 kyrs, from 151 kyrs to 153 kyrs, which represents roughly a 1.5% of temporal difference until magma crystallization at 600°C. Thus, a

variation of 1 km in depth to top of the pluton did not affect significantly the time for magma crystallization.

Magma crystallization just by conduction occurred about 208 kyrs after the intrusion, and by conduction plus convection of hydrothermal fluids in about 153 kyrs. Thus, the time for magma crystallization by conduction plus convection of hydrothermal fluids is about 74% of the time required for magma crystallization considering heat transfer by conduction.

Potassic alteration probably resulted from the interaction between magmatic fluids at temperatures from 450 to 600°C, and country rock with a permeability in the order of 10^{-17} to 10^{-16} m^2. Similarly, propylitic alteration was probable the result of the interaction between magmatic fluids at temperatures from 220 to 350°C, and country rock with a permeability in the order of 10^{-16} to 10^{-15} m^2.

Future Work

A step forward in this research would be to model the cooling history of the Linga complex from the approach of multiple intrusions. This approach is important because the Linga complex is apparently the result of at least three different magmatic intrusions, chronologically called the Humay, Auquish and Rinconada. Thermal conditions imposed by the first intrusions will significantly influence later thermal and fluid flux distributions. To model the cooling history of the Linga complex it is important to know, beside the physical, geochemical and thermal parameters, the relative ages of each of the intrusions. New data from Ar-Ar ages constitutes valuable information in establishing appropriate initial and boundary conditions for each one of the simulations. However, it

might be that modeling of multiple intrusions will not be so relevant for the Linga complex. This is so because the cooling times in the order of 100 kyrs obtained in this dissertation for the whole complex are significantly shorter than the times intervals between individuals intrusions based on the new Ar-Ar ages.

Fluid inclusion data could be another method to complement the stable isotope data of the Linga complex. Fluid inclusion represent natural samples of water trapped at the time of mineral growth. Therefore, they have the potential to yield valuable information about the conditions in which water and minerals reached isotopic equilibrium.

The focus of this research was analyzing stable isotopes and modeling heat flow of just a small section of the Arequipa segment of the PCB. Future work could expand the research to a larger area of the Arequipa segment or other segments of the PCB.

Another step forward in modeling heat flow would be using the software COMSOL Multiphysics which is a modern and versatile software package to do heat flow modeling. An advantage of using COMSOL Multiphysics is that heat flow modeling could be done in 3D, which enhances the understanding of the thermal evolution of cooling plutons. It would also be possible to include in the modeling with COMSOL Multiphysics, information from stable isotopes involving water/rock ratio calculations.

More work needs to be done on using stable isotope data to constrain the thermal modeling. For example, in the present research it is not clear the interplay between permeability, temperature and hydrothermal alteration. Probably this task is going to be addressed more efficiently with another modeling software, like COMSOL Multiphysics.

The software HYDROTHERM interactive uses convection of pure water as the main mechanism of heat transfer. However, data from stable isotopes reveals that the alteration displayed by the samples collected at the Linga complex underwent alteration mainly by interaction with magmatic water. Future work needs to be done for modeling convection not just of pure water, but of magmatic water. In this matter, it is important to have modeling software with the capability of changing properties of convecting fluids so that magmatic fluids can be included in the simulations.

A future modeling project could also be done analyzing the advantages of super-convection in the cooling of magmatic bodies. This process apparently performed at pressure and temperatures bigger than the critical point of water, then the modeling software should have capabilities to do modeling in high pressure and temperature conditions. Probably COMSOL Multiphysics has these features.

While doing field work during the Summer of 2014 in Peru, I spent some hours working with the mineral spectrometer TerraSpec. Taking advantage of the capabilities of this devise could be another way to enhance this research in future work. This technology allows the straightforward analysis of samples in the field yielding information about mineral and fluid content of the rock, which are essential in determining the nature of hydrothermal alteration and the appropriate initial conditions for heat flow modeling.

APPENDIX A

LOCATION, UNIT AND ROCK TYPES OF GEOCHEMISTRY SAMPLES

FROM THE ICA-PISCO AREA OF THE PCB

Sample	Coordinates		Unit	Rock type
10714H	13.95362S	75.67537W	Linga-Humay	Granodiorite
10714J	13.92279S	75.67860W	Linga-Auquish	Granite
10714K	13.87099S	75.63913W	Linga-Humay	Quartz-monzodiorite
10714M	13.83710S	75.59167W	Pampahuasi	Monzodiorite
10714P	13.83987S	75.56205W	Tiabaya	Tonalite
10714Q	13.81248S	75.51926W	Tiabaya	Granodiorite
10715B	13.73208S	75.92461W	Humay	Quartz-diorite
10715C	13.71041S	75.84041W	Linga-Auquish	Quartz-monzodiorite
10715D	13.66571S	75.77123W	Linga-Auquish	Monzodiorite
10715E	13.66048S	75.76123W	Pampahuasi	Monzodiorite
10715F	13.63994S	75.72009W	Tiabaya	Tonalite
10715I	13.5949S	75.58416W	Gabbro	Gabbro
10715L	13.61453S	75.42432W	Incahuasi	Quartz-monzodiorite
10715M	13.60759S	75.34368W	Incahuasi	Quartz-monzodiorite
10719N	14.20803S	75.42407W	Pampahuasi	Tonalite
10719Q	14.18010S	75.38313W	Pampahuasi	Tonalite
10719R	14.17340S	75.36102W	Pampahuasi	Granodiorite
10719Z	14.06247S	75.42757W	Pampahuasi	Granodiorite
10719CC	13.97285S	75.3629W	Linga-Humay	Gabbro
10720O	14.02803S	75.62737W	Linga-Humay	Monzodiorite
10720T	13.78103S	75.50333W	Tiabaya	Granodiorite
10720U	13.75882S	75.48713W	Tiabaya	Granodiorite
10720V	13.75105S	75.48374W	Tiabaya	Granodiorite
10721D	13.84141S	75.65395W	Linga-Humay	Quartz-monzodiorite
10721K	13.78687S	75.78779W	Linga-Auquish	Granodiorite
10721M	13.75416S	75.74976W	Linga-Humay	Quartz-monzodiorite
10721N	13.74292S	75.74279W	Quilmana	Dacite
11823G	13.81709S	75.52772W	Tiabaya	Granite
11823H	13.81559S	75.52737W	Tiabaya	Granodiorite
11825A	13.83774S	75.56987W	Tiabaya	Quartz-diorite
11825G	13.74009S	75.47334W	Tiabaya	Granite
11826E	13.90717S	75.34074W	Tiabaya	Granodiorite
11828A	14.42044S	75.17647W	Tiabaya	Tonalite

11828B	14.39454S	75.16142W	Tiabaya	Tonalite
11828E	14.26018S	75.11012W	Tiabaya	Granodiorite
11829C	13.75874S	75.69473W	Gabbro	Gabbro
11829D	13.76292S	75.69561W	Gabbro	Gabbro
11830C	13.87320S	75.30364W	Tiabaya	Granite
11830D	13.84498S	75.30433W	Tiabaya	Quartz-monzodiorite
11830E	13.82603S	75.27928W	Tiabaya	Granodiorite
11830I	13.79977S	75.28555W	Tiabaya	Granodiorite
11830K	13.80459S	75.27317W	Tiabaya	Granodiorite
11831EE	13.67616S	75.32376W	Incahuasi	Granodiorite
12715A	13.92374S	75.66132W	Linga-Humay	Granodiorite
12715C	13.90900S	75.65157W	Linga-Rinconada	Granodiorite
12716F	14.17889S	75.36224W	Incahuasi	Granite
12716K	14.02594S	75.16042W	Incahuasi	Quartz-monzodiorite
12717C	13.65796S	75.75182W	Gabbro	Gabbro
12717D	13.64153S	75.72137W	Tiabaya	Tonalite
12717H	13.62511S	75.67106W	Tiabaya	Granodiorite
12719B	13.62482S	75.60254W	Incahuasi	Granodiorite
12719D	13.59757S	75.4935W	Pampahuasi	Tonalite
12719H	13.47854S	75.47002W	Tiabaya	Granite
12719I	13.48695S	75.47243W	Tiabaya	Granite
12719J	13.53151S	75.50472W	Pampahuasi	Tonalite
12719K	13.60741S	75.34363W	Incahuasi	Granodiorite
12720C	13.99534S	75.56479W	Linga-Humay	Granite
12722E	14.08006S	75.44305W	Pampahuasi	Granodiorite
12722J	14.01851S	75.36042W	Gabbro	Gabbro
12722L	14.04010S	75.35352W	Incahuasi	Granodiorite
12722T	13.96205S	75.23788W	Incahuasi	Granodiorite
12722V	13.91656S	75.19213W	Incahuasi	Granodiorite
12722Y	13.87002S	75.18557W	Incahuasi	Quartz-diorite
12723B	13.83760S	75.22997W	Incahuasi	Quartz-monzodiorite
12723C	13.83105S	75.23584W	Incahuasi	Quartz-monzodiorite
12723E	13.82604S	75.25659W	Incahuasi	Quartz-monzodiorite
12723I	13.78803S	75.3707W	Incahuasi	Granite
12723L	13.79288S	75.34314W	Incahuasi	Quartz-monzodiorite
12723M	13.80357S	75.31348W	Incahuasi	Quartz-monzodiorite
12723O	13.80322S	75.27238W	Incahuasi	Quartz-monzodiorite
12724D	13.99737S	75.62933W	Linga-Humay	Granodiorite
13820E	13.69522S	75.87918W	Linga-Auquish	Quartz-monzonite
13820J	13.7011S	75.88131W	Linga-Humay	Monzogabbro
13820M	13.70372S	75.88187W	Linga-Humay	Quartz-monzodiorite

13821C	13.69032S	75.84991W	Linga-Auquish	Monzodiorite
13821H	13.66809S	75.85394W	Linga-Auquish	Quartz-monzonite
13822A	13.72635S	75.8574W	Linga-Auquish	Granodiorite
13822C	13.7249S	75.78855W	Linga-Auquish	Granodiorite
13823A	13.64165S	75.98121W	Linga-Humay	Quartz-diorite
13823E	13.47549S	76.0281W	Linga-Humay	Granodiorite
13823I	13.44192S	75.97067W	Linga-Humay	Granodiorite
13825D	13.7034S	75.94952W	Linga-Auquish	Quartz-monzonite
13826A	13.69934S	75.82201W	Linga-Humay	Quartz-monzodiorite
13827A	13.67415S	75.79195W	Linga-Humay	Granodiorite
13827G	13.66991S	75.78868W	Linga-Auquish	Granodiorite
13828A	13.71057S	75.83787W	Linga-Auquish	Granite
13828D	13.66037S	75.76727W	Pampahuasi	Granite
13828H	13.54816S	75.68507W	Tiabaya	Granodiorite
13830B	13.99355S	75.78896W	Linga-Humay	Granodiorite
13830C	13.93927S	75.66932W	Linga-Rinconada	Granite
13830J	13.95086S	75.62944W	Linga-Humay	Granodiorite
13901E	13.88234S	75.63713W	Linga-Humay	Granodiorite
13901G	13.89267S	75.64651W	Pampahuasi	Quartz-monzodiorite
13902M	13.93131S	75.61225W	Gabbro	Quartz-diorite
13903B	13.84782S	75.75092W	Linga-Auquish	Quartz-monzonite
13903J	13.83401S	75.76089W	Linga-Auquish	Quartz-monzonite
13904D	13.99982S	75.57954W	Pampahuasi	Tonalite
13904J	13.98961S	75.56295W	Linga-Rinconada	Granite
13905C	13.88067S	75.66746W	Linga-Humay	Granodiorite
13905E	13.87881S	75.66772W	Linga-Humay	Granite
13905F	13.87463S	75.66699W	Linga-Auquish	Granodiorite
13906A	13.87219S	75.67489W	Linga-Auquish	Granite
13906B	13.87158S	75.66898W	Linga-Auquish	Granite
14710A	13.70844S	75.95422W	Quilmana	Basalt
14710C	13.62716S	75.67416W	Gabbro	Gabbro
14710G	13.61286S	75.41614W	Yura	Trachite
14713C	13.73287S	75.92406W	Linga-Humay	Monzogabbro
14714Ba	13.8570S	75.76483W	Quilmana	Trachite
14715Aa	13.9348S	75.63554W	Linga-Rinconada	Granite
14715D	13.9331S	75.62196W	Linga-Rinconada	Granite
14715F	13.93172S	75.61253W	Gabbro	Gabbro
14716A	14.03909S	75.69248W	Quilmana	Trachite
14717C	13.94179S	75.66104W	Linga-Rinconada	Granite
14724D	13.95356S	75.62752W	Linga-Rinconada	Granite
14725Ec	13.66029S	75.76186W	Pampahuasi	Granodiorite

| 14727U | 13.82762S | 75.69228W | Linga-Rinconada | Granite |
| 14727Y | 13.85073S | 75.71326W | Linga-Humay | Monzodiorite |

APPENDIX B

MAJOR ELEMENT DATA FOR SAMPLES COLLECTED FROM THE ICA-PISCO AREA OF THE PCB

LISTED AS WT%

Sample	Al_2O_3	CaO	Fe_2O_3	K_2O	MgO	MnO	Na_2O	P_2O_5	SiO_2	TiO_2	LOI	Sr	Y
10714H	15.90	5.37	7.31	2.75	2.42	0.12	3.70	0.14	56.60	0.66	0.55	307.00	27.10
10714J	14.10	3.00	4.52	3.98	1.06	0.08	3.30	0.09	65.00	0.51	0.53	202.00	36.20
10714K	17.60	7.20	9.31	1.18	3.34	0.15	3.60	0.23	52.50	0.88	1.42	395.00	24.50
10714M	17.80	6.32	8.12	2.81	2.57	0.18	3.90	0.36	54.20	0.86	0.59	469.00	30.30
10714P	15.50	5.72	7.87	1.76	2.68	0.16	3.70	0.16	56.30	0.75	0.51	329.00	37.20
10714Q	16.00	4.13	4.20	2.84	1.51	0.08	4.00	0.13	65.30	0.48	0.63	573.00	8.10
10715B	20.40	10.40	7.95	0.17	5.96	0.13	2.90	0.01	47.80	0.56	0.58	844.00	4.50
10715C	14.50	2.35	4.10	5.34	0.74	0.06	3.10	0.09	65.10	0.44	1.92	212.00	30.10
10715D	17.70	7.00	5.05	0.47	3.13	0.09	5.90	0.01	57.40	0.85	1.23	406.00	25.10
10715E	16.20	5.20	6.90	2.99	2.15	0.13	3.90	0.12	59.30	0.72	0.48	294.00	25.20
10715F	15.90	3.34	4.06	1.97	0.80	0.12	4.50	0.12	66.10	0.25	0.63	416.00	12.30
10715I	18.20	8.43	10.90	0.61	4.65	0.22	3.30	0.48	47.80	0.76	0.71	714.00	16.60
10715L	17.90	6.20	7.60	2.52	2.90	0.13	3.80	0.16	55.50	0.81	0.45	438.00	23.60
10715M	16.60	4.04	5.46	3.82	1.77	0.10	3.90	0.14	62.80	0.69	0.41	329.00	24.60
10719N	17.30	7.39	4.88	0.78	2.37	0.04	4.70	0.20	59.30	0.74	1.02	464.00	26.30
10719Q	16.60	6.02	8.21	2.51	2.68	0.15	3.40	0.15	55.60	0.77	0.21	341.00	28.40
10719R	16.00	5.41	6.66	2.49	2.13	0.14	3.80	0.23	58.40	0.74	0.58	412.00	25.00
10719Z	15.80	5.35	6.82	2.14	2.10	0.14	3.50	0.18	59.00	0.65	0.72	396.00	23.90
10719CC	20.20	10.10	9.75	0.48	4.75	0.17	2.60	0.11	49.60	0.97	1.05	538.00	13.10

10720O	15.90	6.15	7.76	2.43	2.56	0.11	3.50	0.18	55.10	0.72	0.95	379.00	29.00
10720T	17.10	4.50	3.72	2.05	1.16	0.09	4.30	0.16	62.40	0.44	0.75	659.00	7.10
10720U	15.50	4.16	3.91	2.97	1.58	0.08	3.90	0.13	64.40	0.45	0.56	565.00	6.60
10720V	15.90	4.00	3.39	2.73	1.06	0.08	3.90	0.14	64.50	0.38	0.85	585.00	7.80
10721D	14.00	3.39	5.44	4.17	1.10	0.09	3.20	0.15	63.60	0.65	0.49	206.00	43.70
10721K	14.70	3.27	5.06	4.02	1.50	0.06	3.60	0.11	61.70	0.53	1.08	181.00	40.60
10721M	15.20	5.50	7.55	2.54	2.70	0.14	3.60	0.12	57.30	0.61	1.12	301.00	31.60
10721N	14.10	3.17	4.50	1.47	1.81	0.08	3.90	0.14	67.60	0.60	0.69	250.00	35.10
11823G	15.40	3.97	3.73	2.98	1.46	0.07	4.10	0.12	65.00	0.46	0.58	502.00	7.80
11823H	16.80	5.07	5.65	3.14	2.23	0.10	3.90	0.16	59.70	0.75	0.58	498.00	19.10
11825A	19.90	5.61	5.20	1.19	1.25	0.17	5.50	0.16	58.20	0.46	0.56	543.00	6.60
11825G	13.90	2.28	2.43	3.37	0.64	0.07	3.60	0.06	68.40	0.23	0.82	243.00	8.90
11826E	14.10	2.63	2.11	2.43	0.82	0.02	4.30	0.06	70.00	0.33	1.00	225.00	17.90
11828A	16.30	5.14	6.59	1.74	1.75	0.14	3.00	0.16	61.50	0.59	0.92	276.00	22.90
11828B	17.20	6.39	7.48	1.47	2.46	0.16	3.10	0.16	58.30	0.70	0.73	340.00	24.90
11828E	16.50	4.84	3.45	2.20	1.52	0.07	4.30	0.13	63.30	0.48	0.76	582.00	7.80
11829C	20.30	10.60	9.27	0.28	3.74	0.10	3.40	0.11	47.60	1.08	0.82	483.00	13.80
11829D	19.70	11.20	10.10	0.17	7.01	0.21	1.80	0.02	47.10	0.67	0.34	440.00	5.50
11830C	14.90	2.95	3.16	4.20	1.17	0.06	3.60	0.16	64.70	0.46	0.74	389.00	14.20
11830D	16.40	5.07	5.41	3.32	2.16	0.09	3.80	0.23	59.40	0.73	0.47	515.00	16.00
11830E	16.60	5.45	6.22	2.87	2.43	0.11	3.90	0.25	58.70	0.75	0.62	515.00	20.90
11830I	16.10	4.38	6.09	3.69	1.79	0.09	3.60	0.20	60.00	0.95	0.50	356.00	22.00
11830K	15.70	5.14	5.80	2.30	2.16	0.11	3.60	0.20	60.90	0.63	0.69	325.00	24.70
11831EE	16.00	4.86	6.22	3.55	2.34	0.10	3.20	0.21	59.60	0.79	0.84	302.00	27.70
12715A	14.40	4.90	8.08	1.96	1.38	0.15	4.00	0.34	62.90	0.97	1.02	299.00	43.60
12715C	12.00	1.55	3.49	4.75	0.48	0.05	2.70	0.05	70.70	0.34	0.38	108.00	40.80

12716F	15.70	6.15	7.29	2.20	2.68	0.12	3.30	0.16	59.30	0.77	0.70	446.00	12.00
12716K	15.60	4.81	6.86	3.17	2.21	0.11	3.30	0.18	62.10	0.83	0.46	305.00	31.00
12717C	18.90	9.89	9.11	0.42	5.16	0.17	2.90	0.05	52.10	0.63	0.17	458.00	10.10
12717D	14.70	2.90	4.10	2.04	0.68	0.11	4.10	0.11	69.20	0.22	0.73	370.00	11.30
12717H	15.30	4.26	4.29	2.33	1.59	0.08	3.80	0.11	66.00	0.44	0.94	471.00	9.40
12719B	16.10	5.60	7.33	2.68	2.62	0.13	3.50	0.18	59.30	0.82	0.66	375.00	23.20
12719D	17.00	6.99	7.16	1.31	3.17	0.15	3.30	0.16	57.10	0.64	1.38	501.00	16.80
12719H	13.30	2.65	3.58	3.89	1.07	0.04	3.20	0.09	67.90	0.38	0.81	311.00	15.70
12719I	13.90	2.51	2.93	3.73	0.87	0.05	3.50	0.09	70.00	0.37	0.69	293.00	17.20
12719J	16.80	6.63	8.88	1.71	3.21	0.16	3.30	0.17	56.20	0.83	1.21	425.00	21.50
12719K	15.00	3.79	5.40	3.80	1.75	0.09	3.30	0.14	63.30	0.62	0.68	300.00	27.20
12720C	13.70	3.99	7.20	4.30	1.74	0.11	2.70	0.20	64.30	0.81	0.40	217.00	54.90
12722E	14.90	4.99	6.82	2.32	2.18	0.13	3.20	0.16	60.30	0.66	0.75	309.00	27.50
12722J	24.10	11.10	4.35	0.63	1.70	0.06	3.00	0.19	51.40	0.56	0.79	842.00	8.90
12722L	16.30	5.23	6.08	2.40	2.28	0.12	3.90	0.20	61.40	0.74	0.61	489.00	17.90
12722T	15.40	4.08	5.52	3.63	1.86	0.09	3.40	0.15	62.40	0.64	1.21	406.00	19.60
12722V	16.20	5.43	6.32	2.99	2.47	0.12	3.20	0.21	61.10	0.73	0.83	408.00	25.10
12722Y	17.20	7.72	9.44	1.80	3.98	0.21	2.80	0.23	53.20	0.85	1.34	580.00	19.30
12723B	16.40	5.63	6.89	2.65	2.53	0.12	3.70	0.20	60.40	0.77	0.55	505.00	21.30
12723C	16.60	6.46	8.02	2.37	3.00	0.14	3.50	0.23	57.10	0.88	0.70	498.00	21.20
12723E	15.70	4.47	5.37	3.27	1.94	0.09	3.70	0.16	63.20	0.67	0.62	457.00	16.90
12723I	15.10	3.50	5.36	4.36	1.47	0.09	3.40	0.18	64.00	0.75	0.71	388.00	24.30
12723L	15.40	5.57	6.51	2.16	2.50	0.11	3.40	0.20	60.10	0.68	0.61	569.00	16.90
12723M	15.30	4.94	6.62	2.90	2.25	0.11	3.60	0.24	59.70	0.86	0.49	495.00	22.20
12723O	14.20	3.88	4.69	2.90	1.57	0.09	3.20	0.10	66.70	0.48	0.70	280.00	18.60
12724D	14.00	4.23	5.69	1.03	1.73	0.05	4.50	0.09	65.10	0.46	0.98	276.00	35.70

13820E	16.70	3.38	5.74	4.61	1.37	0.04	3.88	0.20	64.80	0.54	0.50	300.00	38.90
13820J	16.30	6.84	8.88	2.27	4.03	0.11	3.95	0.10	56.40	0.71	1.57	360.00	29.10
13820M	16.30	8.66	9.06	1.83	4.78	0.17	2.94	0.07	52.60	0.67	1.91	350.00	21.70
13821C	15.80	5.60	7.83	2.84	2.67	0.17	3.42	0.21	59.70	0.68	0.97	290.00	32.50
13821H	14.80	2.09	4.92	4.90	1.24	0.10	3.50	0.10	66.00	0.44	1.20	190.00	29.70
13822A	15.30	2.59	5.12	4.29	1.29	0.06	3.91	0.11	64.40	0.49	1.57	230.00	29.10
13822C	15.40	5.07	6.84	3.34	2.30	0.10	3.26	0.13	62.80	0.53	0.93	280.00	32.70
13823A	15.70	4.62	7.31	4.11	2.31	0.11	3.70	0.60	60.20	1.23	0.28	350.00	39.90
13823E	15.60	4.34	6.79	3.34	2.25	0.14	3.62	0.16	60.50	0.62	1.96	150.00	30.80
13823I	13.20	2.68	2.06	3.17	0.44	0.03	3.77	<0.01	73.30	0.19	0.49	210.00	17.70
13825D	15.80	5.10	6.35	3.64	2.39	0.05	3.82	0.41	60.80	1.03	0.74	490.00	35.80
13826A	16.40	5.41	6.94	2.70	2.41	0.09	3.97	0.20	60.90	0.69	0.86	330.00	30.10
13827A	15.90	5.11	7.63	3.05	2.53	0.13	3.52	0.15	61.20	0.64	0.92	250.00	35.20
13827G	15.60	2.20	4.00	1.68	1.61	0.02	5.14	0.08	67.40	0.43	0.70	220.00	33.30
13828A	14.60	0.42	5.95	6.21	0.66	0.02	3.47	0.06	66.40	0.39	0.89	60.00	31.70
13828D	15.90	2.62	5.17	4.41	0.81	0.05	4.10	0.10	66.70	0.51	0.36	240.00	34.90
13828H	18.50	4.31	2.32	2.47	0.97	0.05	4.79	0.09	65.70	0.30	0.45	880.00	4.10
13830B	16.30	3.49	4.28	1.70	2.17	0.08	4.73	0.19	64.30	0.53	2.29	290.00	15.40
13830C	13.70	2.54	4.37	4.40	0.85	0.08	3.16	0.04	68.30	0.41	0.30	190.00	39.00
13830J	15.30	4.16	6.55	3.15	1.71	0.12	3.48	0.18	64.00	0.64	0.39	270.00	38.70
13901E	16.00	4.62	6.38	3.28	0.87	0.08	3.57	0.38	63.20	0.84	0.15	270.00	50.60
13901G	16.40	5.83	9.21	2.06	2.20	0.18	3.78	0.34	60.40	0.91	0.45	330.00	37.30
13902M	22.90	11.20	6.73	0.82	2.89	0.10	2.62	0.03	49.70	0.58	1.09	580.00	9.60
13903B	15.10	3.63	5.69	4.26	1.71	0.05	3.46	0.06	64.60	0.46	1.01	240.00	36.00
13903J	16.10	5.13	6.70	3.39	2.93	0.17	4.11	0.14	58.40	0.58	1.33	320.00	30.10
13904D	16.20	4.24	11.10	0.37	1.18	0.03	5.53	0.35	59.60	0.64	0.57	480.00	15.50

13904J	15.00	3.56	7.06	4.65	1.46	0.12	3.24	0.21	64.50	0.86	0.40	220.00	47.10
13905C	15.90	4.69	6.70	3.48	2.19	0.11	3.35	0.15	63.10	0.57	0.52	270.00	28.30
13905E	5.90	4.92	7.16	3.26	2.39	0.13	3.42	0.13	60.50	0.60	0.78	290.00	27.80
13905F	15.80	4.16	6.43	3.64	2.01	0.04	3.85	0.11	62.40	0.61	0.84	290.00	33.80
13906A	14.90	3.06	5.36	4.99	1.62	0.06	3.13	0.09	63.00	0.51	1.24	220.00	32.00
13906B	14.20	1.54	3.59	5.89	0.63	0.03	2.91	0.05	66.20	0.30	0.78	210.00	25.40
14710A	17.20	8.39	9.84	1.68	5.01	0.18	3.45	0.25	48.90	0.64	1.04	980.00	16.60
14710C	18.10	12.10	17.10	0.10	8.35	0.23	1.39	0.03	40.40	0.73	0.30	560.00	4.30
14710G	16.00	6.44	12.00	2.34	3.19	0.28	5.68	0.45	54.30	0.70	0.49	420.00	22.80
14713C	20.60	10.10	8.56	0.43	5.53	0.15	4.11	0.24	53.50	0.64	0.20	790.00	10.70
14714Ba	16.80	2.05	8.55	1.39	2.29	0.23	6.46	0.29	61.60	0.67	3.91	210.00	32.80
14715Aa	13.00	1.57	3.59	6.23	0.43	0.05	3.11	0.08	67.30	0.48	0.25	120.00	35.90
14715D	14.60	2.78	2.72	4.64	0.59	0.02	3.61	0.05	70.20	0.30	0.51	280.00	24.20
14715F	19.50	9.59	12.70	0.75	9.66	0.23	2.28	0.07	48.80	0.50	1.37	480.00	8.50
14716A	18.10	1.03	5.97	0.34	3.66	0.03	8.95	0.14	65.00	0.57	2.85	70.00	8.80
14717C	12.80	1.44	3.02	6.10	0.36	0.04	2.88	0.02	65.60	0.31	0.27	110.00	35.90
14724D	12.60	0.72	1.55	6.22	0.14	0.03	3.56	<0.01	67.80	0.08	0.66	100.00	20.30
14725Ec	15.40	4.42	6.24	2.53	1.92	0.13	4.01	0.13	65.70	0.59	0.71	280.00	27.20
14727U	14.30	4.17	7.12	4.60	1.55	0.13	3.10	0.27	64.60	0.94	0.66	230.00	49.90
14727Y	14.30	1.45	4.99	5.93	0.84	0.03	4.07	0.14	69.50	0.48	1.15	130.00	31.60

APPENDIX C

RARE EARTH ELEMENT DATA FOR SAMPLES COLLECTED FROM THE ICA-PISCO AREA OF THE

PCB LISTED IN PPM (METHOD ICM90A)

Sample	La	Ce	Pr	Nd	Sm	Eu	Gd	Tb	Dy	Ho	Er	Tm	Yb	Lu
10714H	22.30	47.10	6.13	25.20	5.10	1.01	4.70	0.81	4.50	0.93	2.73	0.43	2.70	0.46
10714J	28.70	59.90	7.75	31.00	6.30	0.81	5.89	0.99	5.87	1.27	3.71	0.55	3.80	0.58
10714K	14.70	31.10	4.33	19.00	4.40	1.21	4.16	0.70	4.11	0.86	2.47	0.36	2.40	0.38
10714M	37.80	78.10	10.00	41.70	8.10	1.70	6.51	1.05	5.63	1.17	3.21	0.46	3.10	0.49
10714P	27.90	56.60	7.32	29.50	6.60	1.30	6.21	1.01	6.16	1.32	4.01	0.60	3.90	0.62
10714Q	19.80	37.10	4.21	15.00	2.30	0.59	1.76	0.25	1.48	0.28	0.77	0.12	0.80	0.13
10715B	3.40	5.90	0.90	4.00	0.90	0.72	0.95	0.14	0.93	0.17	0.51	0.07	0.50	0.10
10715C	40.30	69.70	7.97	28.90	5.40	0.76	4.88	0.85	4.81	1.04	3.14	0.49	3.20	0.52
10715D	16.30	45.00	6.54	26.50	5.50	1.57	4.74	0.73	4.17	0.94	2.56	0.41	2.70	0.42
10715E	24.40	47.50	5.92	23.60	4.80	1.02	4.29	0.71	4.05	0.91	2.65	0.40	2.90	0.41
10715F	20.10	37.00	4.58	16.90	2.80	0.93	2.28	0.38	1.94	0.40	1.29	0.19	1.30	0.23
10715I	27.60	53.70	6.39	25.70	4.70	1.18	3.76	0.55	3.02	0.65	1.74	0.23	1.50	0.24
10715L	21.70	44.40	5.59	22.20	4.70	1.19	4.09	0.67	4.05	0.86	2.58	0.37	2.40	0.39
10715M	26.80	54.40	6.60	25.50	4.90	0.97	4.11	0.67	3.78	0.85	2.57	0.37	2.50	0.39
10719N	8.90	21.00	3.48	16.60	4.30	1.47	4.63	0.71	4.73	0.94	2.72	0.40	2.70	0.41
10719Q	24.20	50.10	6.37	26.30	5.50	1.04	5.08	0.81	4.88	1.03	2.96	0.44	2.90	0.50
10719R	24.40	49.40	6.41	26.00	5.40	1.25	4.80	0.77	4.15	0.90	2.55	0.40	2.50	0.43
10719Z	20.50	42.80	5.55	21.80	4.60	1.04	3.97	0.67	4.34	0.86	2.49	0.36	2.40	0.40
10719CC	10.00	20.10	2.62	11.20	2.70	0.91	2.41	0.41	2.41	0.47	1.31	0.20	1.30	0.20

10720O	19.00	45.10	6.15	26.90	5.70	0.98	5.01	0.84	5.02	1.03	2.93	0.45	2.80	0.46
10720T	16.50	31.90	3.83	14.50	2.60	0.74	1.81	0.24	1.36	0.22	0.71	0.12	0.70	0.17
10720U	17.30	29.00	3.17	11.70	2.10	0.62	1.65	0.24	1.21	0.23	0.66	0.11	0.70	0.17
10720V	19.00	33.60	3.74	13.90	2.60	0.65	1.86	0.26	1.52	0.25	0.71	0.11	0.80	0.17
10721D	39.10	80.60	10.20	39.00	8.60	1.11	7.16	1.20	7.00	1.48	4.56	0.66	4.40	0.67
10721K	36.70	78.20	9.79	37.60	7.70	0.82	6.47	1.06	6.65	1.44	4.26	0.66	4.30	0.72
10721M	26.00	51.30	6.70	26.80	5.70	1.18	5.41	0.90	5.27	1.12	3.34	0.50	3.10	0.53
10721N	28.90	59.20	7.80	31.50	6.80	1.22	5.94	1.02	6.08	1.23	3.55	0.59	3.90	0.60
11823G	20.10	35.90	4.26	15.40	2.60	0.72	1.93	0.27	1.42	0.27	0.85	0.12	0.80	0.11
11823H	25.80	54.80	7.59	30.00	6.00	1.12	4.94	0.69	3.49	0.67	2.04	0.30	1.90	0.27
11825A	19.10	30.80	3.70	13.40	2.20	1.58	1.66	0.22	1.09	0.19	0.76	0.11	0.90	0.10
11825G	24.60	41.00	4.53	15.80	2.40	0.58	1.98	0.28	1.53	0.30	0.89	0.13	0.90	0.12
11826E	14.80	35.00	4.56	17.10	3.30	0.80	3.18	0.49	2.68	0.56	1.94	0.30	2.10	0.27
11828A	20.50	41.00	5.42	21.40	4.70	1.27	4.35	0.70	3.92	0.81	2.53	0.41	2.50	0.37
11828B	21.70	43.80	5.94	24.70	5.40	1.31	5.05	0.74	4.14	0.84	2.69	0.42	2.70	0.38
11828E	17.00	31.90	4.05	15.00	2.80	0.81	2.22	0.27	1.29	0.26	0.76	0.10	0.80	0.10
11829C	8.00	15.40	2.17	9.60	2.30	1.10	2.59	0.40	2.24	0.49	1.53	0.22	1.40	0.21
11829D	2.70	5.10	0.73	3.40	0.90	0.69	0.91	0.18	0.98	0.22	0.66	0.11	0.80	0.11
11830C	36.60	64.30	7.71	26.50	4.40	0.77	3.30	0.47	2.46	0.49	1.46	0.21	1.50	0.20
11830D	23.10	46.70	6.23	24.00	4.50	1.03	3.73	0.54	2.61	0.52	1.71	0.22	1.60	0.20
11830E	26.70	54.10	7.29	28.30	5.60	1.09	4.61	0.69	3.35	0.70	2.13	0.32	2.10	0.28
11830I	39.00	75.90	9.72	36.40	6.80	1.14	5.21	0.77	3.76	0.74	2.20	0.33	2.10	0.31
11830K	33.30	57.40	6.73	24.10	4.70	1.05	4.45	0.71	3.73	0.82	2.53	0.38	2.60	0.35
11831EE	25.40	50.10	6.64	26.00	5.60	1.01	5.30	0.82	4.49	0.93	2.90	0.41	2.70	0.38
12715A	26.20	56.30	7.83	33.80	8.60	2.13	8.61	1.34	8.19	1.59	4.40	0.72	4.40	0.70
12715C	37.60	76.90	9.97	35.50	7.60	0.73	7.04	1.13	7.22	1.37	4.30	0.73	4.40	0.70

12716F	17.60	34.40	4.27	15.50	3.10	1.25	2.83	0.38	2.25	0.39	1.30	0.22	1.40	0.22
12716K	34.50	72.00	9.09	33.80	7.30	1.27	6.33	1.03	5.91	1.12	3.28	0.56	3.20	0.50
12717C	5.50	11.00	1.55	6.80	1.60	0.90	1.91	0.33	1.96	0.39	1.04	0.19	1.10	0.18
12717D	20.90	40.00	4.91	18.10	3.30	1.00	2.65	0.35	2.05	0.38	1.08	0.17	1.20	0.20
12717H	19.60	34.50	3.98	14.20	2.50	0.79	1.99	0.27	1.74	0.29	0.88	0.15	0.90	0.15
12719B	22.30	46.90	6.08	23.00	5.40	1.21	4.87	0.73	4.39	0.84	2.54	0.42	2.60	0.40
12719D	16.70	32.90	4.24	16.70	3.40	1.12	3.45	0.53	3.15	0.56	1.71	0.29	1.70	0.28
12719H	50.20	90.20	9.61	29.10	4.70	0.72	3.34	0.50	3.00	0.54	1.48	0.23	1.50	0.25
12719I	23.40	44.90	5.42	18.80	3.90	0.74	3.25	0.49	3.07	0.55	1.64	0.27	1.80	0.27
12719J	15.60	33.10	4.37	17.60	4.40	1.20	4.36	0.65	3.94	0.77	2.33	0.37	2.30	0.36
12719K	20.80	47.30	6.56	24.70	5.50	1.02	5.39	0.84	5.11	0.96	2.76	0.44	2.80	0.44
12720C	49.00	109.00	14.60	55.60	12.40	1.25	11.50	1.73	10.60	1.92	5.60	0.91	5.60	0.86
12722E	24.90	51.30	6.73	25.80	5.70	1.18	5.46	0.82	5.06	0.96	2.91	0.48	3.00	0.49
12722J	10.90	22.40	3.07	12.50	2.70	0.92	2.21	0.32	1.86	0.31	0.91	0.14	0.80	0.13
12722L	19.10	43.70	5.97	22.00	4.50	1.12	3.97	0.56	3.27	0.64	1.81	0.29	2.00	0.30
12722T	28.50	58.70	7.44	27.10	5.20	1.04	4.33	0.64	3.76	0.68	1.97	0.34	2.00	0.32
12722V	30.90	63.20	8.10	29.60	6.10	1.29	5.48	0.83	4.66	0.85	2.50	0.43	2.60	0.42
12722Y	21.20	42.90	5.62	22.20	4.90	1.43	4.46	0.67	3.84	0.73	1.95	0.32	2.00	0.34
12723B	26.20	54.80	7.09	27.60	5.50	1.21	4.51	0.68	4.13	0.73	2.03	0.37	2.10	0.36
12723C	23.90	51.50	6.95	26.80	5.50	1.28	4.69	0.69	4.10	0.78	2.23	0.37	2.20	0.35
12723E	23.00	48.90	6.20	23.60	4.60	0.95	3.92	0.57	3.25	0.62	1.74	0.27	1.90	0.29
12723I	36.40	76.30	9.79	35.20	6.90	1.11	5.56	0.83	4.71	0.87	2.40	0.42	2.60	0.42
12723L	22.80	47.80	6.30	23.70	4.90	1.09	3.69	0.53	3.39	0.58	1.72	0.22	1.60	0.27
12723M	28.90	62.20	8.22	30.60	6.20	1.19	5.26	0.78	4.17	0.80	2.20	0.37	2.30	0.36
12723O	19.30	37.70	4.67	17.70	3.90	0.90	3.55	0.57	3.43	0.62	1.91	0.33	2.10	0.32
12724D	18.30	48.50	7.32	28.80	6.80	1.16	6.13	0.98	6.31	1.23	3.61	0.65	3.90	0.64

13820E	24.40	53.20	7.68	31.20	7.80	1.58	7.29	1.16	6.72	1.38	4.43	0.65	4.20	0.62
13820J	22.40	45.30	6.21	24.50	5.90	1.22	5.55	0.84	5.03	1.02	3.18	0.48	3.20	0.48
13820M	14.30	32.20	4.62	18.00	4.50	1.09	4.30	0.66	3.92	0.77	2.46	0.33	2.20	0.31
13821C	27.80	58.80	7.95	30.50	6.70	1.38	6.13	0.97	5.54	1.14	3.58	0.54	3.50	0.51
13821H	43.20	76.90	9.26	32.00	6.10	1.20	5.51	0.85	5.04	1.04	3.27	0.51	3.30	0.51
13822A	26.50	55.50	7.11	26.20	5.70	1.19	5.36	0.84	4.87	1.01	3.15	0.49	3.20	0.45
13822C	30.80	62.00	8.09	30.20	6.70	1.19	6.33	0.94	5.69	1.17	3.50	0.54	3.60	0.53
13823A	57.60	125.00	16.40	61.90	12.60	2.14	10.30	1.43	7.81	1.41	3.97	0.59	3.80	0.56
13823E	29.00	58.60	7.69	28.60	6.30	1.35	5.94	0.91	5.22	1.09	3.36	0.50	3.30	0.51
13823I	23.40	39.60	4.40	14.40	2.80	0.74	2.61	0.44	2.66	0.57	1.97	0.31	2.20	0.30
13825D	32.60	69.00	9.48	38.90	9.10	1.68	8.43	1.18	6.35	1.23	3.58	0.53	3.30	0.51
13826A	22.30	49.00	6.75	26.10	5.90	1.36	5.69	0.86	4.92	1.02	3.19	0.48	3.10	0.46
13827A	31.40	65.70	8.68	32.70	7.20	1.35	6.67	1.01	6.00	1.20	3.70	0.59	3.60	0.55
13827G	37.50	68.70	8.49	29.20	6.30	0.95	5.41	0.83	5.33	1.14	3.90	0.64	4.30	0.65
13828A	41.00	87.50	9.50	32.30	6.50	1.06	5.82	0.92	5.39	1.12	3.54	0.55	3.70	0.54
13828D	38.20	74.90	9.63	34.60	7.20	1.50	6.49	0.97	5.67	1.21	3.81	0.59	3.90	0.58
13828H	14.40	27.00	3.28	11.50	2.00	0.89	1.45	0.18	0.90	0.14	0.40	0.05	0.40	<0.05
13830B	20.40	40.80	4.92	17.40	3.60	1.01	3.24	0.48	2.80	0.53	1.48	0.23	1.50	0.18
13830C	28.10	61.10	8.41	31.80	7.20	1.00	6.72	1.09	6.39	1.33	4.02	0.62	4.00	0.61
13830J	28.80	62.50	8.62	32.80	7.50	1.35	7.02	1.12	6.45	1.31	4.12	0.62	4.10	0.59
13901E	38.20	85.00	11.90	46.60	10.70	1.77	10.30	1.56	8.95	1.76	5.14	0.77	4.50	0.72
13901G	26.10	54.80	7.58	29.90	7.10	1.59	7.03	1.09	6.38	1.32	4.12	0.61	4.10	0.60
13902M	7.50	15.20	1.94	7.40	1.70	0.71	1.71	0.26	1.56	0.34	1.04	0.16	0.90	0.16
13903B	23.10	49.40	7.08	27.10	6.30	1.13	5.81	0.95	5.73	1.24	3.86	0.63	4.10	0.63
13903J	19.40	46.40	6.66	25.90	5.70	1.15	5.16	0.83	4.85	1.02	3.14	0.50	3.10	0.49
13904D	17.00	31.80	4.07	16.00	3.30	1.29	3.08	0.42	2.35	0.51	1.49	0.24	1.50	0.23

13904J	38.30	82.20	11.40	43.40	9.80	1.52	9.15	1.43	8.30	1.66	4.99	0.73	4.70	0.71
13905C	26.10	54.00	7.12	25.90	5.70	1.07	5.20	0.84	4.75	0.98	3.12	0.45	3.00	0.44
13905E	25.60	52.20	6.64	25.20	5.60	1.11	5.15	0.79	4.53	0.98	2.92	0.46	3.00	0.43
13905F	29.40	66.70	9.17	32.90	7.10	1.34	6.11	0.98	5.59	1.15	3.68	0.54	3.60	0.54
13906A	27.30	56.00	7.30	26.20	5.90	1.00	5.22	0.83	4.99	1.08	3.38	0.53	3.60	0.53
13906B	17.40	31.40	3.98	15.00	3.80	0.92	3.92	0.63	3.82	0.84	2.69	0.41	2.90	0.37
14710A	38.30	80.60	9.69	42.10	8.40	2.12	5.96	0.68	3.55	0.64	1.75	0.23	1.50	0.21
14710C	1.80	3.70	0.51	2.70	0.80	0.52	0.88	0.14	0.85	0.17	0.47	0.07	0.50	0.06
14710G	28.70	61.50	7.68	33.20	7.00	1.88	5.80	0.73	4.52	0.86	2.51	0.35	2.40	0.35
14713C	8.90	18.90	2.45	11.50	2.80	1.27	2.70	0.34	2.13	0.40	1.14	0.16	1.00	0.16
14714Ba	27.00	53.40	6.99	31.00	7.00	1.91	6.45	0.95	6.11	1.22	3.77	0.53	3.70	0.54
14715Aa	39.30	78.60	9.01	35.20	7.10	0.83	6.15	0.97	6.26	1.28	4.07	0.59	4.00	0.60
14715D	24.20	46.50	5.20	20.80	4.40	0.86	4.08	0.63	4.11	0.85	2.62	0.39	2.90	0.42
14715F	4.60	9.60	1.23	5.90	1.40	0.61	1.59	0.22	1.52	0.30	0.93	0.13	0.90	0.12
14716A	13.80	27.50	3.10	13.20	2.40	0.63	2.05	0.26	1.65	0.33	1.12	0.17	1.30	0.17
14717C	47.80	95.90	10.80	41.10	7.70	0.73	6.68	1.01	6.32	1.26	3.79	0.54	3.70	0.52
14724D	37.20	72.80	7.54	26.70	4.80	0.40	3.83	0.52	3.15	0.62	2.05	0.31	2.30	0.31
14725Ec	20.00	43.60	5.45	23.60	5.10	1.00	4.87	0.71	4.61	0.96	3.01	0.43	3.10	0.43
14727U	36.70	81.40	10.30	43.90	10.00	1.36	9.33	1.43	9.13	1.82	5.44	0.75	5.20	0.74
14727Y	41.50	89.20	9.21	35.50	7.00	1.10	6.23	0.91	5.86	1.10	3.18	0.44	3.10	0.44

APPENDIX D

LOCATION AND UNITS WHERE ALTERED SAMPLES WERE COLLECTED FROM THE ICA-PISCO AREA OF THE PCB. INFORMATION FROM EACH SAMPLE INCLUDE A BRIEF DESCRIPTION OF THE OUTCROP, ALTERATION MINERAL IN THIN SECTION, AND THE INFERRED TYPE OF ALTERATION

Thin section	Outcrop coordinates		Unit	Mineral association in thin section	Main type of alteration in thin section	Brief description of the outcrop from which the sample for thin section was taken
13820E	13.69522S	75.87918W	Linga-Auquish	Quartz, plagioclase, sericite K-feldspar biotite	Potassic	Outcrop located at Cerro Monte Sierpe, north of Rio Pisco. The outcrop is part of a gradational contact from gabbro to monzogabbro and monzodiorite that shows abundant cracking and jointing. The sample was taken from a spot with mafic enclaves.
13820J	13.7011S	75.88131W	Linga-Humay	Sericite, chlorite, epidote	Phyllic	Outcrop located at Cerro Monte Sierpe, north of Rio Pisco. The outcrop shows mingling probably between the monzonites and monzogabbros.
13820M	13.70372S	75.88187W	Linga-Humay	Quartz, plagioclase, sericite, K-feldspar, Biotite, chlorite,	Potassic	Outcrop located at Cerro Monte Sierpe, north of Rio Pisco. The outcrop shows quartz and calcite veins. The main lithology of the outcrop is probably monzonite.
13821C	13.69032S	75.84991W	Linga-Auquish	Quartz, plagioclase K-feldspar, Biotite, Sericite, epidote, chlorite	Potassic	Outcrop located in Quebrada Payasca, north of Rio Pisco. The lithology is probably altered monzonite. Sample was taken from a spot with abundant specular hematite.
13821H	13.66809S	75.85394W	Linga-Auquish	Quartz plagioclase, sericite, Epidote, Chlorite,	Sericitization	Outcrop located in Quebrada Payasca, north of Rio Pisco Lithology of the outcrop is probably monzonite.

Thin section	Outcrop coordinates		Unit	Mineral association in thin section	Main type of alteration in thin section	Brief description of the outcrop from which the sample for thin section was taken
13822A	13.72635S	75.8574W	Linga-Auquish	K-feldspar epidote, chlorite, sericite, opaque minerals	Propylitic	Outcrop located at Cerro Huarangal, south of Rio Pisco. The lithology is mainly Auquish monzonite. Outcrop shows elongated enclaves suggesting fluid flow in a horizontal direction.
13822C	13.7249S	75.78855W	Linga-Auquish	Quartz, plagioclase, K-feldspar, chlorite, epidote, opaques	Propylitic	Outcrop located at Quebrada la Polvareda, south of Rio Pisco. The lithology of the outcrop is mainly Auquish monzogranite. Sample was taken from a spot displaying digested enclaves.
13823A	13.64165S	75.98121W	Linga-Humay	Quartz, plagioclase, sericite, veinlets of secondary biotite cutting plagioclase	Potassic	Outcrop located at Cabeza de Toro, north of Rio Pisco. The lithology is mainly quartz-diorite.
13823E	13.47549S	76.0281W	Tiabaya	Quartz, plagioclase, sericite, chlorite, pyroxene	Phyllic	Outcrop located at Viña Vieja. The main lithology is probably monzodiorite, showing abundant jointing and cracking.
13823I	13.44192S	75.97067W	Linga-Humay	Quartz, plagioclase, sericite	Phyllic	Outcrop located close to Rio Matagentes. The main lithology is probably monzogranite.

Thin section	Outcrop coordinates		Unit	Mineral association in thin section	Main type of alteration in thin section	Brief description of the outcrop from which the sample for thin section was taken
13829B	13.76472S	75.71165W	Humay?	Plagioclase, sericite, epidote, quartz, actinolite. Shows fractures	Propylitic	Outcrop located in Mina la Bolivar. Outcrop is full of jointing. Main lithology is probably syenite.
13830B	13.99355S	75.78896W	Linga-Humay	Quartz, sericite, chlorite, epidote,	Potassic	Outcrop located in Cerro Prieto. The outcrop shows abundant K-feldspar, the main lithology is probably granodiorite.
13830D	13.94038S	75.66553W	Linga-Rinconada	Quartz, sericite, K-feldspar. Shows fractures	Phyllic	The outcrop shows intermingling and veins of felsic minerals, maybe quartz or feldspar. The main lithology is probably monzogranite.
13830J	13.95086S	75.62944W	Linga-Humay	Quartz, plagioclase sericite, actinolite, biotite	Potassic	Outcrop located in Quebrada La Mina. The outcrop shows hydrothermal veins and xenoliths. The main lithology is granodiorite which is highly weathered
13902M	13.93131S	75.61225W	Gabbro	Plagioclase, quartz, biotite, K-feldspar, epidote, chlorite	Potassic	Outcrop located in Quebrada la Yesera. The outcrop shows abundant enclaves. This is the one of the places were Linga-Rinconada intrudes Pampahuasi.
13903B	13.84782S	75.75092W	Linga-Humay	Quartz, plagioclase, K-feldspar, epidote, sericite	Phyllic	Outcrop shows a dyke of Linga-Humay intruding the Quilmana volcanics. This is one place where it is possible to observe the contact between these two Super-units.

Thin section	Outcrop coordinates		Unit	Mineral association in thin section	Main type of alteration in thin section	Brief description of the outcrop from which the sample for thin section was taken
13825D	13.7034S	75.94952W	Linga-Auquish	Plagioclase, sericite. quartz and epidote veins	Sericitization	Outcrop located close to the military area. The main lithology is probably monzodiorite
13826A	13.69934S	75.82201W	Linga-Humay	Plagioclase, K-feldspar epidote, chlorite	Propylitic	Outcrop shows abundant cracking and jointing. The main lithology is probably monzonite
13827A	13.67415S	75.79195W	Linga-Humay	Plagioclase, quartz, epidote, chlorite	Propylitic	Outcrops located in Quebrada Huaya Chica. The outcrop shows vein of quartz and calcite. The main lithology is probably granodiorite .
13828A	13.71057S	75.83787W	Linga-Auquish	Quartz, chlorite, sericite	Phyllic	Outcrop located close to Pantayco through the Rio Pisco transect. The lithology is granite. The outcrop shows sericite and mineralization veins with probably hematite or magnetite.
13828D	13.66037S	75.76727W	Pampahuasi	Quartz, plagioclase, sericite, K-feldspar	Phyllic	Outcrop located close to Letrayo in the Rio Pisco transect. The outcrop shows some quartz veins and its main lithology is probably monzodiorite.
13828F	13.66042S	75.76188W	Pampahuasi	Epidote, chlorite, actinolite. Veins and mineral alignment	Propylitic	Outcrop located close to Letrayo in the Rio Pisco transect. The outcrop shows a cumulates pipe and quartz and calcite veins.
13828H	13.54816S	75.68507W	Tiabaya	Plagioclase, quartz sericite. Multiple fractures	Phyllic	Outcrop located in Quebrada Chilcas. The outcrop shows xenolith and quartz veins. The main lithology is probably granodiorite

Thin section	Outcrop coordinates		Unit	Mineral association in thin section	Main type of alteration in thin section	Brief description of the outcrop from which the sample for thin section was taken
14711C	13.70225S	75.88208W	Linga-Humay	Quartz, plagioclase, epidote veins, chlorite, sericite calcite. Shows fractures	Propylitic	Outcrop located in a mingling zone between Linga-Humay and Linga-Auquish. The sample shows pervasive mafic enclaves probably of Humay when intruded by Auquish.
14713A	13.66404S	75.77038W	Linga-Auquish	Quartz, plagioclase, epidote, chlorite, actinolite. Quartz veins	Propylitic	Outcrop located in the Rio Pisco transect. The outcrop shows some mingling and xenoliths as well as jointing and cracking.
14714Ba	13.857S	75.76483W	Quilmana	Plagioclase, K-feldspar, biotite, clay minerals	Argillic	Outcrop located in the Quebrada Larga transect. The outcrop seems to be an andesitic flow. The sample shows abundant felsic enclaves.
14714Ca	13.84743S	75.75401W	Linga-Humay	K-feldspar, plagioclase, epidote, actinolite. Abundant fractures and veins	Potassic	Outcrop located in the Quebrada Larga transect, at the contact zone between the Linga-Humay and the Quilmana volcanics. Sample was taken from a dyke of Humay intruding the volcanics. The outcrop shows abundant jointing.
14714Cb	13.84743S	75.75401W	Quilmana	Biotite, actinolite, epidote, sericite, tremolite	Phyllic-argillic	Same location of sample 14714Ca. Sample was taken about 4 m from the contact between the Linga-Humay and the Quilmana volcanics. The outcrop shows abundant jointing.

Thin section	Outcrop coordinates		Unit	Mineral association in thin section	Main type pf alteration in thin section	Brief description of the outcrop from which the sample for thin section was taken
13903J	13.83401S	75.76089W	Linga-Humay	Quartz, plagioclase, sericite, epidote, sphene, actinolite	Propylitic-phyllic	Outcrop located in Quebrada Huarangal, close to the contact between Linga-Humay and the volcanics.
13903K	13.83264S	75.76382W	Linga-Humay	Quartz, plagioclase, epidote, chlorite, actinolite	Propylitic-phyllic	Outcrop located in Quebrada Huarangal, close to the contact between Linga-Humay and the volcanics. The outcrop shows pervasive mafic enclaves
13905F	13.87463S	75.66699W	Linga-Auquish	Quartz, plagioclase, epidote, sericite, chlorite	Propylitic	Outcrop located in mina "La Iluminada". The main lithology of the outcrop is probably syenite.
14710A	13.70844S	75.95422W	Quilmana	Plagioclase, epidote, sericite, actinolite. pyroxene	Phyllic	Outcrop located close to Dos Palmas. The outcrop shows abundant cracks and jointing and a melanocratic color suggesting dominance of mafic minerals.
14710C	13.62716S	75.67416W	Gabbro	Plagioclase, actinolite, chlorite pyroxene, K-feldspar, olivine. Oriented minerals	Propylitic	Outcrop showing a sharp contact between the gabbros and Tiabaya. One evidence for the contact is the difference between a lighter color for the Tiabaya and a darker color for the gabbros.

Thin section	Outcrop coordinates		Unit	Mineral association in thin section	Main type of alteration in thin section	Brief description of the outcrop from which the sample for thin section was taken
14714Eb	13.83944S	75.76015W	Linga-Humay	Quartz, plagioclase, K-feldspar, biotite	Potassic	Outcrop at the roof of the Humay magma chamber. The sample was taken about 4 m from the contact.
14714F	13.85554S	75.73878W	Linga-Humay	Quartz, plagioclase, K-feldspar, sericite, chlorite, epidote. Fractures and epidote veins	Propylitic	Sample taken from an outcrop located close to the contact between the Humay and the volcanics. The outcrop shows mafic enclaves
14715Aa	13.9348S	75.63554W	Linga-Humay	Quartz, actinolite, biotite amphibole. Shows fractures	Propylitic	Outcrop located in the Quebrada La Yesera, close to the contact between Linga-Rinconada and Pampahuasi. The outcrop shows abundant mingling and mafic oriented enclaves.
14715Ab	13.9348S	75.63554W	Linga-Humay	Quartz, plagioclase, biotite, actinolite, pyroxene. Shows fractures	Propylitic	Outcrop located in the Quebrada La Yesera, close to the contact between Linga-Rinconada and Pampahuasi. The outcrop shows abundant mingling and mafic oriented enclaves.
14715D	13.9331S	75.62196W	Linga-Rinconada	Quartz, plagioclase, K-feldspar, biotite, chlorite	Potassic	Outcrop at the contact between Linga-Rinconada and the Pampahuasi Super-unit. The outcrop shows abundant mafic enclaves, probably caused by the intrusion of the more felsic Rinconada monzonite into the mafic Pampahuasi diorite.

Thin section	Outcrop coordinates		Unit	Mineral association in thin section	Main type of alteration in thin section	Brief description of the outcrop from which the sample for thin section was taken
14715F	13.93172S	75.61253W	Linga-Rinconada	Quartz, epidote, chlorite, actinolite, biotite, muscovite calcite	Propylitic	Outcrop located in the Quebrada La Yesera close to the contact between Linga-Rinconada and Pampahuasi. The outcrop shows abundant felsic veins.
14716A	14.03909S	75.69248W	Quilmana	Plagioclase, sphene, sericite, chlorite, clay minerals	Propylitic-argillic	The outcrop is located at the border between the Guadalupe and the Ica quadrants. The outcrop's dark pink color suggests predominance of extrusive rocks, probably dacite.
14716Fa	13.99591S	75.56896W	Pampahuasi	Quartz, chlorite, pyroxene, amphibole, biotite, actinolite. Oriented minerals	Potassic	The outcrop shows mafic dykes and brecciation as well as quartz and epidote veins.
14716G	13.99522S	75.56576W	Linga-Humay	Quartz, plagioclase, actinolite, chlorite, biotite. Oriented minerals	Propylitic	Outcrop located in the Quebrada Cansas transect. The sample was taken from the metamorphic aureole formed by the intrusion of Humay into the volcanics. The distance to the contacts between the units is around 50 m.
14717C	13.94179S	75.66104W	Linga-Rinconada	Quartz, calcite, hornblende, biotite. Low alteration	Potassic	The main lithology of the outcrop is Rinconada monzonite.

Thin section	Outcrop coordinates		Unit	Mineral association in thin section	Main type of alteration in thin section	Brief description of the outcrop from which the sample for thin section was taken
14722Da	13.66139S	75.76941W	Pampahuasi	Plagioclase, epidote, chlorite, sericite, pyroxene, amphibole	Potassic-Propylitic	The outcrop shows a mafic jagged dike intruding monzonite. The sample was taken from the mafic dyke.
14723B	14.00293S	75.5851W	Pampahuasi	Plagioclase, K-feldspar, quartz, sericite, amphibole, epidote veins	Potassic	Outcrop located in the Quebrada Cansas transect. The sample was taken from a spot that shows ubiquitous magnetite, quartz, and epidote veins.
14723D	14.00145S	75.58366W	Pampahuasi	Quartz, epidote, biotite, chlorite. Abundant fractures	Propylitic	Outcrop located in the Quebrada Cansas transect at the contact zone between the Linga-Humay, the gabbros and the Pampahuasi Super-units. The outcrop shows strong epidotization and veins of magnetite.
14723F	14.00072S	75.58361W	Pampahuasi	Plagioclase, quartz, K-feldspar, sericite, biotite, chlorite	Propylitic	Outcrop located in the Quebrada Cansas transect. The sample was taken from an outcrop full of quartz, epidote and magnetite veins
14723L	13.99885S	75.58361W	Pampahuasi	Plagioclase, K-feldspar, sericite, chlorite, quartz. High alteration	Potassic	Outcrop located in the Quebrada Cansas transect. The sample was taken from an outcrop with pervasive magnetite, epidote and quartz veins.

Thin section	Outcrop coordinates		Unit	Mineral association in thin section	Main type of Alteration in thin section	Brief description of the outcrop from which the sample for thin section was taken
14721Aa	13.70707S	75.83489W	Linga-Auquish	Quartz, plagioclase, secondary biotite veins, sericite, clay minerals	Potassic	Outcrop located in the Rio Pisco transect. The outcrop is strongly altered. Sample was taking from a hydrothermal vein whose main mineral is probably hematite.
14721B	13.66606S	75.77181W	Linga-Auquish	Quartz, plagioclase, sericite, epidote, chlorite, actinolite, biotite. Oriented minerals and veins	Potassic	Outcrop located in the Rio Pisco transect. The outcrop shows pervasive alteration and abundant epidote and quartz veins. Sample was taken from an area containing epidote veins
14722Ab	13.6092S	76.00389W	Linga-Humay	Quartz, calcite, epidote, chlorite, clay minerals, veins. High alteration	Potassic	Outcrop located close to the military area. The outcrop shows high brecciation and abundance of quartz and calcite veins. Brecciation was probably caused by the intrusion of Humay into the volcanics.
14722Bb	13.66405S	75.77054W	Linga-Auquish	Quartz, actinolite, epidote, olivine	Potassic-propylitic	Outcrop located in the Rio Pisco transect. Sample was taken from a zone with quartz and epidote veins.
14722Cc	13.66303S	75.76998W	Linga-Auquish	Plagioclase, quartz, clay minerals, chlorite	Phyllic, argillic	Outcrop located in the Rio Pisco transect, close to the contact between Auquish and Pampahuasi. The sample was taken from a spot with quartz, epidote and K-feldspar veins

Thin section	Outcrop coordinates		Unit	Mineral association in thin section	Main type of alteration in thin section	Brief description of the outcrop from which the sample for thin section was taken
14723M	13.99824S	75.57774W	Pampahuasi	Quartz, sericite, epidote, clay minerals	Phyllic-argillic	Outcrop located in the Quebrada Cansas transect. The sample was taken from an outcrop with pervasive magnetite, quartz and epidote veins.
14723O	13.99749S	75.5764W	Pampahuasi	Calcite, epidote, actinolite, sericite	Potassic	Outcrop located in the Quebrada Cansas transect at the contact zone between the Linga-Humay, the gabbros and the Pampahuasi Super-units. The outcrop shows strong epidotization and veins of magnetite.
14724Aa	13.9544S	75.62615W	Linga-Rinconada	Quartz, epidote, chlorite, clay minerals	Phyllic-argillic	Outcrop located in the Quebrada La Mina transect. The sample was taken from a spot with pervasive malachite, azurite and epidote.
14724D	13.95356S	75.62752W	Linga-Rinconada	Plagioclase, quartz, sericite, amphibole, epidote veins	Propylitic	The outcrop is at the contact between the Rinconada-monzonite and the Linga-Humay. The sample was taken from a dyke of Humay intruding Rinconada.
14725Ea	13.66029S	75.76186W	Pampahuasi	Plagioclase, epidote, amphibole, actinolite, chlorite	Propylitic	The outcrop shows high alteration. There are pervasive K-feldspar and plagioclase cumulates as well as abundant quartz and calcite veins.
14725F	13.66006S	75.76045W	Pampahuasi	Quartz, K-feldspar, actinolite, chlorite, epidote. Oriented minerals, fractures and veins	Propylitic	Outcrop located in the Rio Pisco transect. The outcrop has pervasive quartz, epidote and calcite veins. Sample was taken from a hydrothermal vein.